UNIVERSITÀ
DEGLI STUDI
DI PADOVA

Sede Amministrativa: Università degli Studi di Padova

Dipartimento di Scienze Chimiche

CORSO DI DOTTORATO DI RICERCA IN SCIENZE MOLECOLARI
CURRICOLO SCIENZE CHIMICHE
XXXII CICLO

LIGAND-FREE WATER-BASED APPROACHES FOR THE SYNTHESIS OF METAL SULFIDES NANOSTRUCTURES

Coordinatore: Ch.mo Prof. Leonard Prins
Supervisore: Ch.ma Prof.ssa Silva Gross

Dottorando: Nicola Dengo

[…]

Though wise man at their end know dark is right,

Because their words had forked no lightning they

Do not go gentle into that good night

[…]

Dylan Thomas

List of Acronyms

BET	Brunauer-Emmett-Teller
CHFS	Continuous Flow Hydrothermal Synthesis
CMT	Charge Transfer Multiplet
DFT	Density Functional Theory
DLS	Dynamic Light Scattering
EPR	Electron Paramagnetic Resonance
EXAFS	Extended X-Ray Absorption Fine Structure
FTIR	Fourier Transform Infrared Spectroscopy
HER	Hydrogen Evolution Reaction
HRTEM	High-Resolution Transmission Electron Microscopy
HSAB	Hard and Soft (Lewis) Acids and Bases
ICP-MS	Inductively Coupled Plasma Mass Spectrometry
ifcs	Interatomic Force Constants
ITC	Isothermal Titration Calorimetry
LDA	Local Density Approximation
LED	Light Emitting Diode
MTS	(3-(4,5-dimethylthiazol-2-yl)-5-(3-carboxymethoxyphenyl)-2-(4-sulfophenyl)-2H-tetrazolium)
NAD(P)H	Nicotinamide Adenine Dinucleotide Phosphate
NP	Nanoparticle
NQR	Nuclear Quadrupole Resonance

PC	Principal Component
PCA	Principal Component Analysis
PL	Photoluminescence
SAXS	Small Angle X-Ray Scattering
SSA	Specific Surface Area
TEM	Transmission Electron Microscopy
WPPF	Whole Powder Pattern Fitting
WPPM	Whole Powder Pattern Modelling
XANES	X-Ray Absorption Near Edge Structure
XAS	X-Ray Absorption Spectroscopy
XES	X-Ray Emission Spectroscopy
XPS	X-ray Photoelectron Spectroscopy
XRD	X-Ray Diffraction

Abstract

In this Thesis, metal sulfides were synthesized through water-based and ligand-free synthetic routes. A simple batch approach was successfully employed for the synthesis of ZnS, CuS, PbS, MnS and Ag_2S in a crystalline form at a temperature near 0 °C without employing ligands or stabilizing agents. Particles dimension, crystal structure, surface composition and susceptibility to oxidation phenomena of these materials were assessed. In the case of the batch synthesis of ZnS, a SAXS (Small Angle X-Ray Scattering) *in-situ* study was also performed to elucidate the dimensional evolution of the obtained NPs (nanoparticles) as function of time. Moreover, for ZnS, the behavior in water suspension and the interaction with probe molecules at the liquid/solid interface were also assessed.

Microfluidic and CHFS (Continuous Flow Hydrothermal Synthesis) approaches were employed for the synthesis of pure and doped ZnS NPs. In the case of the pure samples, the synthesis conditions were varied in order to gain insights on the growth mechanism of the NPs and to analyze the potential over the control of dimensional and structural properties of the samples. For the doped samples, the uptake of dopants was determined and their inclusion in the ZnS matrix discussed. The functional properties of selected samples were assessed. In particular, the catalytic activity for the HER (Hydrogen Evolution Reaction) was studied for pure ZnS NPs, while PL (Photoluminescence) was measured in the doped ones. Cytotoxicity assays on doped ZnS NPs obtained with the microfluidic route were also performed in view of bioimaging applications.

The effect of thermal treatment and oxidation phenomena on ZnS NPs as a function of the NPs size was also in-depth analyzed. The study addressed the variations of size, morphology, structure, composition of the nanostructures and their effect on the photocatalytic activity.

The characterization strategy relied on the complementary use of different techniques. XRD (X-Ray Diffraction) and TEM (Transmission Electron Microscopy) analyses were performed to assess mainly dimensional and structural features of the materials, while the surface composition was analyzed combining XPS (X-ray Photoelectron Spectroscopy) and FTIR (Fourier Transform Infrared Spectroscopy). The characterization of the materials was also complemented by Raman spectroscopy.

The results showed the potential of the proposed methods to control relevant features of different materials, even without the use of stabilizing agents, and allowed to assess the surface chemistry of the synthesized naked particles.

Abstract

In questa tesi sono stati sintetizzati solfuri metallici utilizzando metodi in soluzione acquosa che non prevedono l'uso di leganti. In particolare, ZnS, CuS, PbS, MnS e Ag_2S sono stati ottenuti in forma cristallina ad una temperatura prossima a 0 °C e senza l'uso di leganti mediante un semplice metodo *batch.* Sono stati studiati la dimensione, la struttura cristallina, la composizione e i fenomeni di ossidazione delle particelle ottenute. È inoltre stato eseguito uno studio SAXS (*Small Angle X-Ray Scattering*) *in-situ* risolto nel tempo relativo alla sintesi di ZnS per valutarne la crescita nella miscela di reazione durante la sintesi *batch*. Sono inoltre stati studiati il comportamento in sospensione acquosa di particelle di ZnS e la loro interazione con sonde molecolari all'interfaccia liquido/solido.

La sintesi di nanoparticelle di ZnS pure e drogate è stata eseguita mediante un metodo microfluidico ed uno CHFS (*Continuous Flow Hydrothermal Synthesis*). Nel caso di ZnS puro, le condizioni di sintesi sono state variate per ottenere informazioni sul meccanismo di formazione del materiale e valutare le potenzialità dei metodi utilizzati per controllare le proprietà dimensionali e strutturali delle nanoparticelle. Nel caso di ZnS drogato, l'incorporazione dei droganti nel materiale è stata quantificata e discussa. Le proprietà funzionali di alcuni campioni selezionati sono state studiate. Nel caso di ZnS puro è stata quantificata l'attività fotocatalitica per la HER (*Hydrogen Evolution Reaction*), mentre per il materiale drogato sono state misurate le proprietà di fotoluminescenza. È inoltre stata determinata la citotossicità di alcuni campioni ottenuti per via microfluidica in vista di potenziali applicazioni nella diagnostica per immagini.

È stato eseguito uno studio approfondito sull'effetto di trattamenti termici e fenomeni di ossidazione sulle proprietà dimensionali, morfologiche, strutturali e composizionali delle nanostrutture e sui loro effetti sulla di attività fotocatalitica di nanoparticelle di ZnS di diversa dimensione.

La strategia di caratterizzazione si è basata sull'uso complementare di tecniche diverse, quali l'XRD (*X-Ray Diffraction*) e la microscopia TEM (*Transmission Electron Microscopy*) per lo studio di proprietà dimensionali e strutturali, mentre XPS *(X-ray Photoelectron Spectroscopy*) e FTIR (*Fourier Transform Infrared Spectroscopy*) sono state usate per la determinazione della composizione superficiale. La caratterizzazione dei campioni è stata completata dalla spettroscopia Raman.

I risultati ottenuti hanno mostrato la potenzialità dei metodi di sintesi proposti nell'ottenere il controllo di importanti proprietà dei materiali senza sfruttare l'uso di leganti superficiali, e hanno consentito lo studio della chimica della superficie esposta delle nanoparticelle sintetizzate.

Contents

List of Acronyms **1**

Abstract **3**

1. Introduction **11**

1.1 Water-based synthesis of metal sulfides 17

1.2 Continuous flow methods for NPs synthesis 21

1.2.1 Microfluidic synthesis 22

1.2.2 Continuous flow hydrothermal synthesis 25

1.3 Functionalization of colloidal transition metal sulfides nanocrystals: a fascinating and challenging playground for the chemist 28

2. Low temperature batch synthesis and characterization of uncapped ZnS NPs **69**

2.1 Crystal structure, size and morphology 70

2.2 Surface composition 74

2.3 Time resolved *in-situ* SAXS analysis 79

2.4 NPs behavior in water suspension 84

2.5 ITC characterization of the solid/liquid interface 86

3. Uncapped metal sulfides: a simplified wet-chemistry approach to CuS, PbS, MnS and Ag_2S **89**

3.1 Copper sulfide – CuS 90

3.1.1 Crystal structure, size and morphology 91

3.1.2 Surface composition 94

3.2 Lead sulfide – PbS 102

3.2.1 Crystal structure, size and morphology 102

3.2.2 Surface composition 105

3.3 Manganese sulfide – MnS 110
3.3.1 Crystal structure, size and morphology 110
3.3.2 Surface composition 112
3.4 Silver sulfide - Ag_2S 118
3.4.1 Crystal structure, size and morphology 119
3.4.2 Surface composition 121
3.5 Other metal sulfides 125
3.6 Conclusions 127

4. Room temperature microfluidic synthesis and characterization of pure and doped uncapped ZnS NPs 129
4.1 Microfluidic synthesis of small ZnS NPs 129
4.1.1 Crystal structure, size and morphology 130
4.1.2 Surface composition 137
4.1.3 NPs behavior in water suspension 140
4.1.4 Photocatalytic activity for hydrogen evolution reaction 142
4.2 Microfluidic synthesis of TM and Ln doped ZnS NPs 144
4.2.1 Composition and structure 144
4.2.2 Functional properties 151

5. Continuous hydrothermal synthesis and characterization of pure and Ln-doped defective ZnS NPs 155
5.1 Continuous hydrothermal synthesis of defective ZnS NPs 155
5.1.1 Size and morphology 158
5.1.2 Crystal structure and defectivity 159
5.1.3 Surface composition 167
5.1.4 Photocatalytic activity for hydrogen evolution reaction 168
5.2 Continuous hydrothermal synthesis of Ln-doped ZnS NPs 171
5.2.1 Size and morphology 172
5.2.2 Photoluminescence properties of Ln-doped ZnS NPs 177

6. Thermal evolution of ZnS nanostructures: effect of oxidation phenomena on structural features and photocatalytic performances 181

7. Experimental details **195**

8. Characterization methods **199**

9. Conclusions and perspectives **209**

Bibliography **213**

Publications **241**

Acknowledgments **243**

Chapter 1.

Introduction

The field of nanotechnology is one of the main driving forces for the scientific and technological development of humankind in the last 30 years, or more. Its existence as new scientific field has been formally announced in July 1990, during the *International Symposium in Nanoscience and Nanotechnology* in Baltimore. However, the story of nanotechnology and nanoscience surely starts before its formal recognition. To many, the father of the fundamental concepts of this discipline was the Nobel Prize winner Richard Feynman. With his famous talk *There's Plenty of Room at the Bottom*[1] in 1959, he surely produced the spark that flared up the scientific community and inspired countless ground-breaking achievements during the following decades. At that time, however, this new and exciting space for scientific development didn't earned already its own name. The world *nanotechnology* appeared for the first time only in 1974, introduced by the Japanese scientist Norio Taniguchi to describe his work on semiconductors processing.[2] From the time of their origin, the meaning of the world *nanotechnology* and the scope of the relative field were gradually shaped and consolidated. Nowadays, the accepted use of the term is associated to the dimensions of the studied objects, as it was established that at least one of the three spatial dimensions of the considered system must lie in the 1 – 100 nm range.[3]

This rather narrow interval is the one that bridges the atomic-realm with the world of macroscopic objects, resulting in the appearance of size-dependent properties originated from quantum effects. Consequently, nanosystems often displays functional properties that differ from their bulk counterparts, such as (opto)electronic, spectroscopic, photochemical, magnetic and/or electric features.[4,5] Among all materials studied at nanoscale, a fundamental role was played by the semiconductors. Fundamental studies on their properties led to the forge of the word *nanotechnology* itself in 1974, and the scientific interest in this class of nanomaterials has nothing but grown since then. Of course, one of the main issues and opportunities related to semiconductors is the control of their dimension, and consequently their size-related properties. Among others, the chemical bottom-up approach to the problem has received increasing attention due to the tight control on size, morphology and composition achieved.[6] The chemical synthesis of nanocrystalline semiconductors has been widely reviewed already in many dedicated articles and books.[7–14] Among all the developed methods, some gained a large popularity thanks to their outstanding capabilities to achieve significant control over the

final properties of the final product. A common feature of these methods is the central role played by surfactants or capping molecules to precisely control the nanomaterials size since their very early stages of growth from solution, providing not only narrow final size distributions and highly uniform morphologies, but also controlling surface properties and enhancing functional properties such as photoluminescence.[10] The fundamental theory that provided the basis to design and rationalize many advanced synthetical approaches was formulated by LaMer and Dinegar in 1950.[15] While heterogeneous nucleation processes are very difficult to control, as the nucleation may occur on variety sites of unknown nature, the homogeneous process described by LaMer ideally allows simultaneous and controllable nucleation of the material.

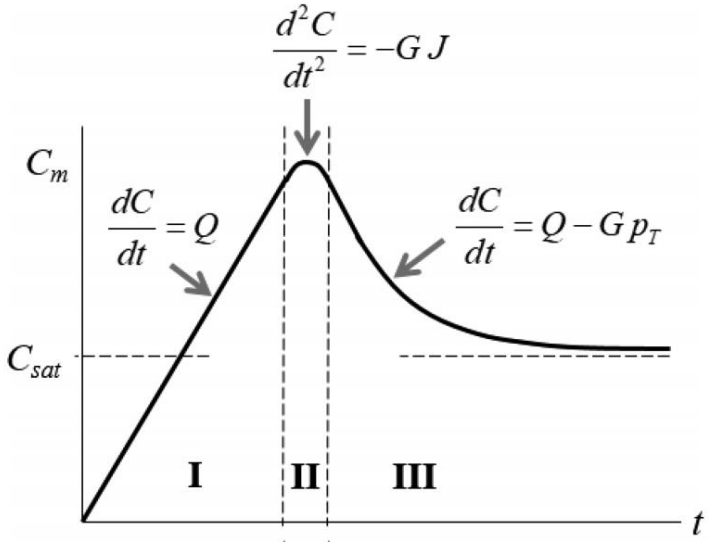

Figure 1.1 LaMer burst nucleation stages visualized as the time evolution of an ideal solute concentration and described by different kinetic equations. Adapted from Chu *et. al.*[16]

LaMer based his model on the description of a solute concentration profile over the course of time during particles formation. The final single particle is viewed as a concerted assembly of individual building blocks represented by the solute, as portrayed in Figure 1.1. The three stages he identified were: *I.* the initial growth of solute concentration, as it is provided to the solution over its solubility limit into a metastable state of supersaturation; *II*. the fast nucleation (burst), consisting in the formation of a massive amount of small individual particles nuclei in a short timeframe; *III*. the growth of particles starting from the formed nuclei until the saturation concentration of the solute is reached. Nanoparticles (NPs) dimension may also evolve further by Ostwald ripening[17] or coalescence[18], but these were not regarded in the LaMer model. This qualitative model was validated by many experimental reports[19–21] and was employed to attempt the quantitative kinetic description of the process. The main contribution to the latter was firstly provided by Sugimoto,[22,23] and very recently refined by Chu *et al.*[16] These authors started from a straightforward interpretation of the kinetic

equation describing the consumption of the solute $C(t)$ overtime, accounting for three concurring factors: solute supply, nucleation rate and growth rate.

$$\frac{dC}{dt} = Q - Jn* - Gp_T \tag{1.1}$$

$$\frac{dp_T}{dt} = J \tag{1.2}$$

In equation (1.1) Q is the solute supply rate per volume, $n*$ is the critical nucleus size, J is the nucleation rate, p_T is the number of post-critical nuclei per unit of volume and G is the growth rate. The definition of nucleation rate is provided by equation (1.2) as the rate of formation of post-critical nuclei. By solving equation (1.1) is theoretically possible to model the final average size and size distribution formed in each homogeneous burst nucleation reaction. However, several approximations are needed, that of course limits the validity and the predictive power of the obtained results. The most advanced elaboration of this problem is the one provided by Chu *et al.*,[16] who assumed that the growth rate G was size and concentration independent, that the dC/dt term vanishes, and that the nucleation rate variation is zero ($dJ/dt = 0$) when the solute concentration reaches its maximum value. From these assumptions, Chu derived that *i.* the total number of generated nuclei (and therefore their final size) depend from the ratio $2Q/G$, thus it is counterintuitively independent from the nucleation rate; *ii.* the particle size distribution is governed by the nucleation rate J, since it controls the critical time and concentration at the supersaturation burst. This interpretation established the theoretical background to validate the qualitative but sound concept of nucleation – growth separation. Intuitively, to obtain small monodispersed nanocrystals, the nucleation burst producing the initial nuclei needs to be temporally separated by the growth. This allows the nuclei to further evolve simultaneously and in principle with the same growth rate, thus leading to a unique final size. If, on the contrary, the two processes are both relevant in the same timeframe, different nuclei will grow for a different time until the saturation concentration of the solute is reached, leading to a polydispersed population of particles. Following this simple concept, many synthetic approaches were developed, employing the self-regulating nature of the homogeneous nucleation. Indeed, in homogeneous nucleation a very high energy barrier needs to be surpassed before the process commences, and therefore a high level of supersaturation is required. After the initial burst, the nucleation rapidly terminates itself, leaving the growth process to consume the excess solute.[11]

$$\Delta G_N = \frac{4}{3}\pi r^3 \Delta G_V + 4\pi r^2 \gamma \quad (1.3)$$

For spherical particles, the energy barrier for the homogeneous nucleation can be calculated as the free energy change ΔG_N in equation (1.3), where ΔG_V is the change in free energy per unit volume, γ is the particle interfacial energy, and r is the radius of the formed particle.[24]

Two of the most popular approaches suited for the synthesis of small monodispersed semiconductors NPs surely are the *hot-injection* and the *heat-up* methods.[11] Hot-injection is widely applicable to a wide variety of materials, and consists in the rapid injection of the precursors in a hot (often 300 °C or higher) solution containing surfactants. The high temperature leads to a rapid decomposition of the precursors with the related fast supersaturation of the solution and consequent nucleation of nanocrystals. The surfactants added to the solution prevent NPs agglomerations and provide steric colloidal stability to the product. In the heat-up approach, the precursors are already introduced in the same solution of the surfactants, and the solution is gradually heated until the decomposition of precursors commences.[11] Noticeably, the heat-up approach is not specifically designed to produce a simultaneous nucleation of the nanocrystals, but it was successfully employed to produce monodispersed particles of a variety of materials.[11]

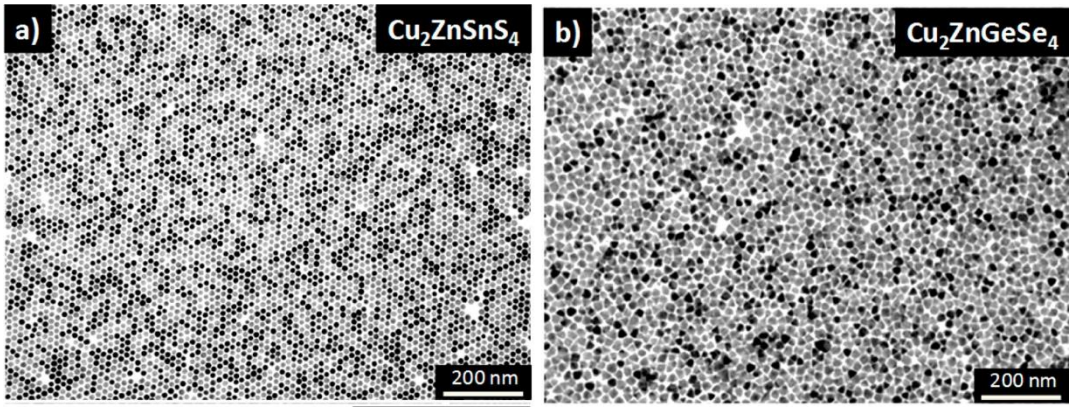

Figure 1.2 TEM micrographs of quaternary metal chalcogenides nanocrystals obtained from (a) heat-up and (b) hot-injection syntheses. Adapted from Kovalenko *et. al.*[10]

In this Thesis, the synthesis of metal sulfides is considered, as a sub-class of emerging and important semiconductors showing a variety of structures, properties and applications. Metal sulfides are extremely relevant for the development of quantum dots,[25–27] in particular for the field of bioimaging devices[28] or the development of LEDs[28] and solar cells.[28] Among the synthesis methods applied to metal sulfides, the hot-injection has achieved a high stage of development, allowing a size control that reached the single layer of surface atoms.[29] An example of an advanced but general method for the

synthesis of metal sulfides can be found in the recent work of Hendricks *et al.*,[29] who exploited the linear relationship, described by Chu *et al.,*[16] of the final NPs size with the solute supply rate to develop a library of substituted thiourea molecules with specific decomposition kinetics for the release of sulfur precursor in solution. Consequently, the supply rate of the sulfur precursor was finely tuned allowing a tight size control over a wide variety of nanosized metal sulfides.

Despite this extremely high level of development, these methods commonly share some relevant drawbacks. The syntheses are often performed at relatively high temperature (from 200 to over 350 °C), in high boiling organic solvents (e.g. octadecene[30] or oleylamine[31]), often employing specifically synthetized precursors (e.g. thioureas,[29] thiocarbamates[30] and metal oleates[29]), and with the employment of one or more surfactants (e.g. amines, carboxylates, and phosphonates[29]). All these conditions are clearly and profoundly misaligned with to the principles of the green chemistry,[32] as a rather large amount of special derivatives and waste is produced, while hazardous chemicals are often employed along with a considerable amount of energy.[33] Even leaving the environmental issues aside, other limitations can be considered the relatively high complexity of the synthetic protocols, often requiring a glove-box or specialized labware, and the difficulty of scaling up these methods to an industrial level. Another limitation, often underestimated, is the inherent complexity of studying the surface properties of these materials, with relation of the true properties of the naked surface and not to the properties related to the adsorbed ligands. Indeed, these syntheses produces NPs having tightly bound molecules on the surface that cannot be easily removed. Calcination treatments, for example, are commonly employed in materials chemistry to release organics from the surface, but their employment also lead to the alteration of the NPs features like size, crystal structure and composition.[34] Consequently, the surface chemistry of nanocrystals is often regarded as the chemistry of their capping ligands and the influence they have on functional properties, more than the properties of the pristine exposed surface.[35]

In this Thesis, a very different approach to the problem of the synthesis of nanosized metal sulfides were explored, accepting the challenge of studying the obtainment of nanosized metal sulfides employing a radically simplified and green-oriented method, while considering its limitations and advantages. Since no surfactants were used, the obtainment of uncapped particles also disclosed the opportunity to evaluate the surface of the material, and in particular to study the effect of oxidation phenomena on sulfides.

To tackle this challenge, the synthetic approach was firstly redesigned starting from the simple water-based precipitation of the material, while aiming to gain a high level of control over the reaction conditions without further adding ligands or surfactants. This approach was firstly developed for ZnS, that was chosen for its relevance, and then extended to other metal sulfides. To pursue further control

over the reaction conditions and pave the way to the scale up of the processes, two different flow chemistry approaches were also developed. By using microfluidics, a better degree of control over the room temperature mixing of the precursors was specially investigated, while a continuous hydrothermal setup was designed and realized to explore the influence of different temperature, pressure and chemico-physical properties of water as a solvent on the crystallization process of the material. Moreover, the inclusion of dopants was also studied with these synthetic approaches to disclose the possibility to obtain luminescent functional materials for potential applications.

A wide array of different characterization techniques was identified to provide a detailed description of the obtained samples from the compositional, dimensional, morphological and structural points of view. These techniques provided a detailed evaluation of the effects of the different synthetic strategies over the final features and properties of the samples. Moreover, being the obtained particles ligands-free by design, a detailed assessment of the surface chemistry was carried out along with a study of the effects of oxidation phenomena on the materials. These analyses were mainly based on the complementarity of different spectroscopic techniques (XPS, FTIR and Raman) to gain a sound description of the studied surfaces. In the case of ZnS, the obtainment of ligand-free water suspensions and the interactions occurring at the unhindered solid/liquid interface were also thoroughly assessed by ITC. Finally, selected functional properties (i.e. photocatalytical activity and luminescence) were studied to elucidate the possible presence of correlations with the obtained features of the synthesized samples, and in view of application of the optimized nanomaterials.

1.1 Water-based synthesis of metal sulfides

The field of aqueous synthesis of nanostructured metal sulfides was fundamentally started by the efforts of Prof. Arnim Henglein and coworkers.[32] One of the earlier recognized and more straightforward advantages of water-based approaches was not only the greener choice in comparison to the nonaqueous counterparts, but also the easier scale-up for larger productions and a better cost-effectiveness. Moreover, the usage of water allowed an easier solubilization of the precursors and a considerable extension of the choice of available capping ligands and surfactants, enabling the inclusion of relevant biomolecules that paved the way for applications of nanocrystals to the biomedical field.[36] The development of a water-based route is however complicated by the acid-base properties of water, that extends the amount of parameters that kinetically and thermodynamically need to be considered. Water itself, due to its polarity, heavily influences the nucleation and growth stages of the material, altering the dynamics of precursors and eventually affecting structural and functional features of the NPs (e.g. favoring the formation of surface traps in quantum dots).[36]

Table 1.1 HSAB chart for the water-based synthesis of metal chalcogenides proposed by Jing *et al.*[36]

Hard	Borderline	Soft
	Acids	
H^+, Na^+, In^{3+}, Mn^{2+}, Ln^{3+}	Cu^{2+}, Zn^{2+}, Pb^{2+}	Cu^+, Ag^+, Cd^{2+}, Hg^{2+}
	Bases	
Cl^-		H_2S, HS^-, S^{2-}
H_2O, OH^-, O^{2-}		RSH, RS^-
ROH, $RCOO^-$, RO^-		Se^{2-}, Te^{2-}
NO^{3-}, ClO^{4-}		
NH_3, RNH_2, N_2H_4		

From a thermodynamic point of view, three main parameters play a fundamental role in the synthesis of metal sulfides from water: the solubility constant, the oxygen affinity of the metal (either to water or to the hydroxyl ion) and the solution pH. In the common case of a ligand or surfactant-assisted synthesis, the binding affinity of these moieties towards the metal and the formed NPs also plays a central role. In this framework, the hard and soft (Lewis) acids and bases theory (HSAB)[37,38] can be used as a harmonized but qualitative approach to estimate the influence of each of the aforementioned thermodynamic parameters in determined chemical environment. HSAB theory classifies Lewis acids and bases in *hard*, which are non-polarizable, weak electron-pair acceptors and donors and mainly interacts through electrostatic interactions, and *soft*, which are polarizable, strong electron-pair acceptors and establish interaction dominated by a covalent character. From here, the general

tendency of forming *hard-hard* and *soft-soft* interaction can be considered when evaluating the possible interaction occurring during a synthesis. An additional class was also introduced for those acid and bases that did not display a clear preference to interact with either hard or softs counterparts, referred as *borderline*.

Considering S^{2-}, Se^{2-} and Te^{2-}, the HSAB theory correctly predicts the low solubility constant of many metal chalcogenides, as many metal ions behave like soft or borderline acids, depending on the oxidation state. Therefore, the formed bonds will be characterized by a relevant covalent character (coherently with the semiconducting properties of the compounds). The stabilization provided from these formed bond more than compensates the lost hard-soft interactions of the solvated ions. On the other side, typical salts used as precursors for the synthesis of these compounds in water, such as metal nitrates or Na_2S, are made of hard-soft combinations of ions. This accounts for their great solubility in water and the relative minor interference of counter ions in the formations of the metal chalcogenides, both usually desirable for a good precursor.

Other than the solubility, another important parameter is represented by the pH of the solution.[39] Since OH^- is a hard base, by principle, the higher the solution pH is, the more the formation of hydroxides compounds or soluble complexes will be favored. Thus, a high pH generally introduces the problem of the competition of the desired sulfide with these compounds. This gets more relevant the harder the considered metal ion is. For example, lanthanides are known for their oxophilicity, and indeed they are regarded as hard acids in the HSAB theory, as also showed in Table 1.1. Thus, the obtainment from water solutions of the lanthanides sulfides may represent an issue. Considering borderline metals like Zn^{2+} and Cd^{2+}, on the basis of the HSAB theory, a proper control on the pH would be predicted to be necessary to avoid the formation of hydroxides. Indeed, the issue of $Zn(OH)_2$ formation was reported for the synthesis of zinc chalcogenides.[40,41] In the case of soft metals, the influence of the pH can be often ignored in its thermodynamic contribution.

From a methodological point of view, the synthesis of metal sulfides in water can be almost always seen as an easy precipitation starting from the precursors ions M^{n+} and SH^- in solution, normally assisted by the presence of ligands to stop the growth of the particles in the nanorange. While in the case of the metal precursor simple inorganic salts are often employed, the choice of the sulfur precursor can be either the direct supply of SH^- through a soluble salt or the formation of these ions *in-situ* through the decomposition of a sulfur-bearing molecule. The second case can be generally regarded as way to control the supply of SH^- to the solution. In water solution is sufficient to account for the presence of SH^-, since the S^{2-} ion cannot play a role, as its presence in water solutions was ruled out over 30 years ago.[42] Despite this, its occurrence can still be found reported in thermodynamic charts[43] as well as in countless research articles. This was caused by the widespread of overestimated

values for the SH^- acid dissociation constant determined in the early years of the last century.[42] The current accepted pK_a estimation of the acid dissociation of SH^- is ≥ 17, while May *at al.*[44] also demonstrated the absence of S^{2-} even in hyper-concentrated basic solutions of NaOH and CsOH. Historically, H_2S was also a largely employed source for the sulfur ions, but this strategy was later mostly abandoned due to the difficult handling of the gaseous compound and the severe health risks associated with accidental exposures.[45]

To control the syntheses, a wide variety of molecules was employed, but the more recurrent choices were sulfur-based ligands such as thioglycerol (TG), thioglycolic acid (TGA), 3-mercaptopropionic acid (MPA) and glutathione (GSH).[36] The choice of a sulfur interacting moieties is related to the stability of the ligand-NP interaction predictable using the HSAB theory. The role of these moieties goes beyond the size control of the product and the colloidal stability of the obtained suspension, as functional properties can be also strongly affected, e.g. dramatically increasing the quantum yield of quantum dots.[46,47]

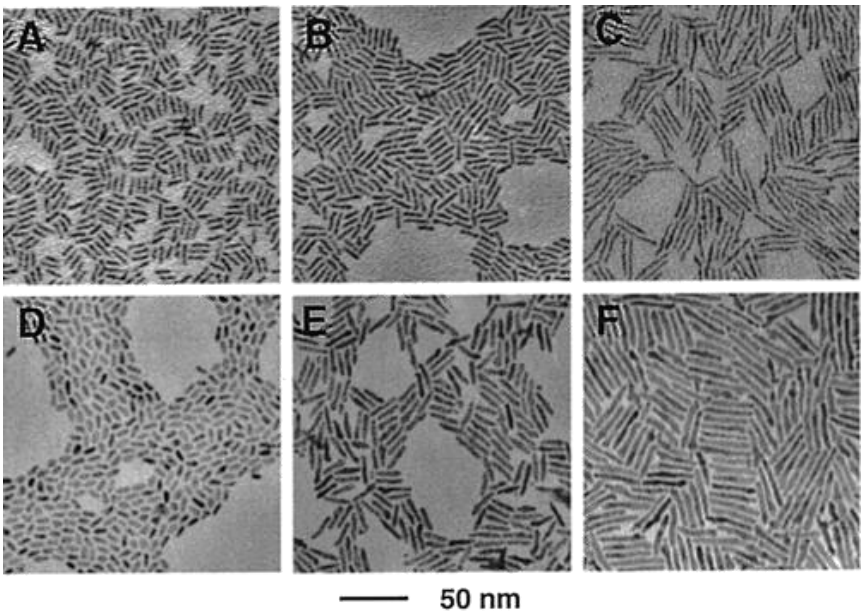

Figure 1.3 CdSe anisotropic nanocrystals obtained with different choices of organic surfactant molecules. Reprinted from Li *et. al.*[48]

To describe the growth of NPs in solution the LaMer theory is generally considered.[15] The growth phase, after the nucleation one, can be modelled in two ways, depending on the realized synthesis conditions: diffusion-controlled growth[49,50] or reaction-controlled growth.[51–53] In the first, the growth is controlled by the diffusion of a *monomer* (either the solvated ions or more complicated species) towards the NPs. In the second, precipitation and dissolution equilibria of the *monomer* exist, which eventually control the growth kinetics. While the first is regarded as a size-focusing process (i.e. it leads to a relatively monodispersed distribution of NPs), the second often generates a wider polydispersity.

Talapin *et al.*[51] developed a theoretical framework for these phenomena, accounting for the simultaneous occurrence of both during the precipitation of NPs. In his work, the rate of change of a growing particle depends from both processes, where the relative contribution of the two is ultimately regulated by the dimensionless parameter K.

$$K = \frac{RT}{2\gamma V_m}\frac{D}{k_g^{flat}} \tag{1.4}$$

According to Talapin *et al.*[51] K is defined as in equation (1.4), where γ is the surface tension of the NP, V_m represents the molar volume of the solid, D is the diffusion coefficient of the monomer and k_g^{flat} is the first-order reaction rate constant for the addition of a monomer at a flat surface. For $K > 100$ the growth can be considered fully reaction-controlled, while for $K < 0.01$ the diffusion regime prevails. Thus, the estimation of this parameter can be employed to understand the kinetic regime in a synthesis, and to further refine the experimental conditions to drive the reaction toward the formation of an ensemble of small monodispersed NPs. In the case of a diffusion-controlled regime, such as the direct addition of the metal precursor to SH^- (or vice versa) where the reaction between the precursor is extremely rapid, the monomer is almost immediately depleted and the growth process enters in the Ostwald ripening regime.[51]

In the kinetic control of the growth process, ligands can play a twofold role. The attachment/detachment dynamics of ligands influences the attachment of monomers on the growing NPs,[54,55] but also influences the later Ostwald ripening regime.[51] As different NP facets can display different binding affinity towards the same ligand, the choice of the latter can also lead to different competing dynamics on different facets. Consequently, the NPs growth may occur differently towards different crystallographic directions, leading to anisotropic NPs.[54]

1.2 Continuous flow methods for NPs synthesis

While chemistry has immensely evolved in the last centuries, the evolution of the standard equipment of a chemist in the lab has proceeded at a much slower pace, as the focus was put in the flask content rather than on the flask itself. Considering the results, this approach can indeed be considered extremely successful. However, outside the lab, and particularly in the chemical industrial production, a very different approach has established to meet analogously different needs: the flow chemistry.[56] At the cost of a more elaborate setup with respect to a simple stirred vessel, flow methods can disclose several important advantages.[57] Flow processes are more easily automated, generally safer, and allow a better reproducibility of the reaction conditions, making the process more reliable. Indeed, the control over reaction time and temperature, along with the control of reactants concentration and mixing, can be easily assured.[57] Using a batch approach, the molar ratio of the precursors is ultimately determined by the volumetric ratio of the solutions employed. In the flow techniques, the flow rates also determine the precursors relative amounts at the mixing points. The discontinuous nature of the batch process also limits the production, as syntheses needs to be cyclically repeated to accumulate the product, while in a continuous synthesis the product is simply accumulated in any reasonable amount just by maintaining the setup operative for enough time. The concept of reaction time also differs. In batch it can be simply considered as the time interval that separates the mixing of the precursors from the end of the reaction. In a flow method the reaction time reflects the residence time in the reactor, that is determined by the ratio of the reactor volume and the total flow rate, the latter given by the sum of the individual flow rates of solutions fed in the reactor.[57] This also establishes a precise time-space correlation, in which different reaction times are accessible simply considering a different length of the reactor after the point where the reaction starts (usually the mixing point). Therefore, it is possible to probe different reaction times simply moving across the reactor length. This concept was proven extremely powerful to perform *in-situ* time-resolved studies, especially to access extremely short reaction times.[58,59] The time-space correlation can also be used to develop multi-step processes, where different reactants are added in successive steps, or different reaction conditions are employed. At the cost of an intensive optimization of the set-up, this advantage discloses the opportunity to transform a long and elaborate multi-step synthesis, involving the isolation of the intermediates, to a single input-output process that already delivers the final product.

In recent times, reactors miniaturization towards meso- (500 µm to few mm) and microfluidic (10 – 500 µm)[57,60] setups has not only made the flow chemistry more compatible with the lab scale, but has greatly improved the control over heat transfer and reactants mixing. Moreover, high temperature and pressure methods were also developed, allowing even normally time-consuming process like batch hydro- and solvothermal synthesis, to be performed in-flow and with shorter reaction time. The latter technique is generally referred as Continuous Flow Hydrothermal Synthesis (CHFS).[61]

In this Thesis, microfluidic and CHFS approaches were employed to test the transition toward flow techniques of the synthesis of metal sulfides, and in particular of ZnS, starting from both a pre-designed simple batch and the available literature.

1.2.1 Microfluidic synthesis

Microfluidics is the science and the technology of handling small amount of fluids in channels with dimensions ranging from 10 to 500 µm.[57,60] Initially developed mainly for analytical purposes, microfluidics has already found many successful applications to design flow synthesis methods,[60,62–64] even at the industrial scale.[60] The main advantage of a microfluidic approach is the superior control over mass and heat transfer granted by the small dimension of the employed reactors. Thus, the reduced size represents the key factor, since it allows the device to operate maintaining a laminar flow regime with a Reynolds[a] number below 250. This consents a regular parallel flow of the liquids in the channels, that are mainly mixed just by lateral diffusion. The absence of turbulence and the fast flow rate also inhibits back-mixing phenomena.[60] The rapid mixing of the reactants is achieved due to the small size of the channels, or alternatively it can be induced employing a dedicated mixing sections. A wide variety of microfluidic mixing techniques have already been developed, since the small scale allows to simply design and realize special mixers tailored for specific pourposes.[65,66] Compared to a batch process, the microfluidic mixing strategies allow a high level of control and a remarkably higher homogeneity. The improved control over the reaction temperature and the stable flow conditions allow the abatement of concentration and thermal gradients in the reaction mixture, ultimately ensuring stable reaction conditions.[65,66] In the view of NPs synthesis, and considering the LaMer model[15,16,23] of a homogeneous nucleation reaction, these advantages can be exploited to achieve highly defined and reproducible nucleation conditions, promoting the nucleation-growth separation and resulting in the improvement of final NPs size distribution.[63] Moreover, following the Sugimoto[23]

[a] The Reynolds number (R_e) is an adimensional quantity that quantifies the relative contribution of inertial and viscous forces in a flowing liquid. With a circular cross section: $R_e < 2300$ laminar flow; $2300 < R_e < 4000$ transitional flow; $R_e > 4000$ turbulent flow.

and Chu[16] theories, the controllable flow rate can also be employed to tune the supply rate of the precursors, affecting the final size of NPs. The time-space correlation in a flow technique, associated with the small and versatile setup and the high flux rate, constitute a unique occasion to introduce many in-line analytical techniques like UV,[67] IR[68,69], Raman[68,70] or NMR[71] spectroscopies (Figure 1.4). This unlocks the unique advantage of simplifying *in-situ* studies, allowing an easier optimization of the synthesis.[60]

The small size of the channels may induce into thinking that the scale-up of a microfluidic is, in fact, impossible, as any increase of the device size may lead to the loss of the optimized reaction parameters and ultimately to the loss of the advantages that makes microfluidic devices unique.

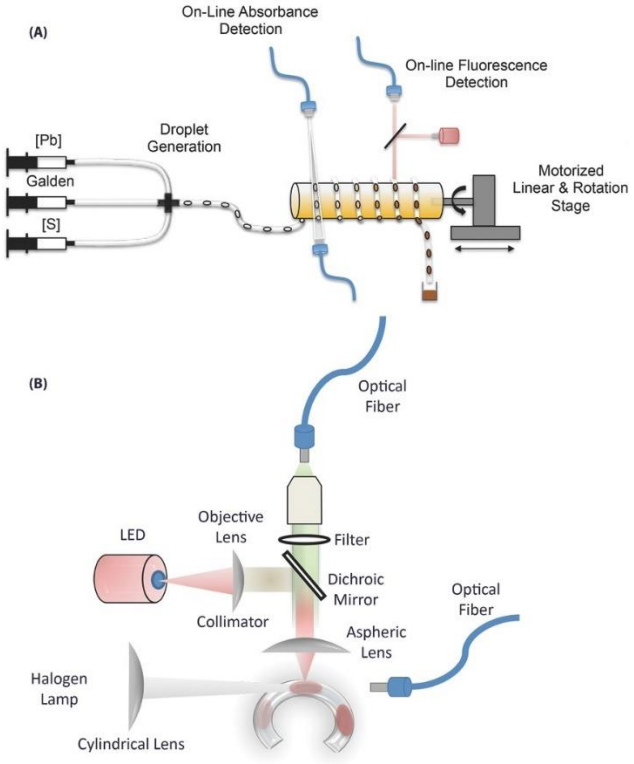

Figure 1.4 Schematic of a droplet-based microfluidic setup for the kinetic study of the synthesis of PbS. The setup is equipped with both online absorbance and fluorescence detections. Reprinted from Lignos *et al.*[72]

Indeed, a different approach was necessary to enlarge the production capabilities of the microfluidic technology while maintaining the reduced sizes of the singular channels. Instead of simply creating a larger system, like in the regular batch scale-up approach, the strategy of numbering-up was introduced. Many individual devices can work in parallel, allowing to keep the microfluidic conditions and simultaneously multiplying the product output.[60] In the view of making chemistry greener, this

technology grants the reduction of energy consumption thanks to the optimized heat transfer, and the intensification of the production in unit of space. Moreover, as a multistep process is concerned, the elimination of steps for the purification and isolation of intermediate products also allows a significant reduction of the chemicals employed, connected with a waste reduction of the overall process, in compliance of the green chemistry paradigms.[33]

The initial development of the microfluidic approach applied to the synthesis of nanocrystals has to be attributed to the pioneeristic work of Andrew J. DeMello and coworkers, initially focused on the synthesis of CdS quantum dots.[73]

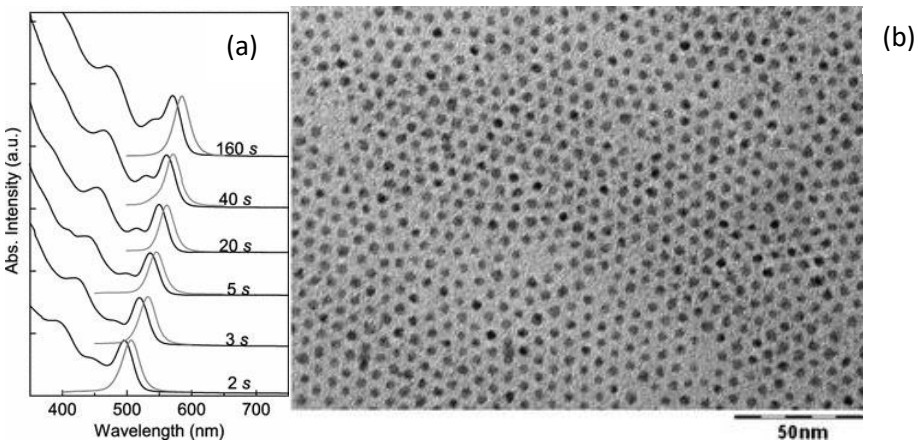

Figure 1.5 (a) Adsorption and emission spectra of CdS NPs synthesized at 280 °C at different residence times, using the oleylamine-assisted technique employed by Yang *et. al.*[74] (b) TEM micrographs of the same NPs CdS synthetized at 160 s. Reprinted from Yang *et. al.*[74]

In his original work, a simple water-based approach was used, but the potentiality of in-line monitoring of the reaction product was immediately exploited, making the team capable to recognize that the final polydispersion of the quantum dots was directly connected with the flow rate employed in the device. To now, the potentiality of the method was extended to many crystalline NPs, pursuing a high degree of structural, morphological and compositional control. Successful development of these NPs synthesis techniques was obtained for metals (e.g. Ag, Au, Co), oxides (e.g. TiO_2, SiO_2, Fe_xO_y) and chalcogenides (e.g. CdS, CdSe, InP). More complex structures like core-shell NPs were also successfully obtained.[73]

In this Thesis a microfluidic approach was employed to test the synthesis of pure and doped ZnS NPs using a simple ligand-free precipitation strategy.

1.2.2 Continuous flow hydrothermal synthesis

Continuous flow hydrothermal synthesis (CHFS) was developed to couple the unique features of the high-temperature high-pressure hydrothermal approaches with the advantages of a flow synthesis.[61] These reaction conditions made the transition rather technologically challenging. Nonetheless, CHFS now almost celebrates 30 years of development and can be considered an established approach of both scientific and industrial interest.[61] Despite both organic solvents and water can be in principle used with little variations of the setups, the second is a more widely studied and generally preferred alternative that allows greener processes. In CHFS, water is pumped at high pressure (up to 30 MPa) and pre-heated at high temperature (up to 500 °C). Since the critical point of water is reached at 374 °C and 22.1 MPa, this approach normally exploits supercritical water. In this physical state, profound variations of the physico-chemical properties occur. The hydrogen bond network formed in liquid water breaks down when the critical point is reached. As consequence, the density decreases from 1 g ml^{-1} in regular conditions to 0.332 g ml^{-1}, while the viscosity is also strongly reduced.[61] At the same time, water autoprotolysis increases, making approximatively a 30-fold increase in $[H^+]$ and $[OH^-]$ ions concentration.[61] The dielectric constant drops from 80 to only 2 at 500 °C,[75] making water in these conditions turning from a polar solvent to a nonpolar one, thus making electrolytes far less soluble in the solvent as the solvation sphere of ions is destroyed.[75] The latter effect is of primary importance in this technology, as the nearest neighbors of cations (before solvated) became constituted by anions instead of water molecules.[75] This causes a rapid association of opposite ions from their fast dehydration, ultimately leading to nucleation and growth of the materials. Therefore, in the framework of the LaMer theory,[15] the supersaturation is here obtained altering the solvent properties rather that quickly providing a solute to the solution. To obtain a clean and fast nucleation, the precursors solution is not pre-heated, but instead is kept at room temperature and later mixed with supercritical water though an engineered mixer. This causes the abrupt supersaturation of the solution, leading to the fast nucleation needed to contain NP polydispersity.

An important role in the process is interpreted by the mixer design, as the mixing fluid dynamics alters the time and temperature of exposure of the precursors to the supercritical water.[76] One of the main problems that needs to be addressed through a competent design of the mixer is its clogging, mainly caused by the pre-heating of the precursors solution before the contact with supercritical water is made.[76] Different designs characterized by a different complexity were proposed, ranging from simple T-junctions to more complex counter-current mixers (or nozzle reactors) and confine jet mixers.

The main advantage of the last design is the flexibility towards different flow rates, that can be varied in a wide range while allowing the good contact of the precursors with supercritical water and short mixing time.[77] The scale-up of a CHFS systems can be achieved increasing the size of the apparatus, often requiring the re-design or re-adaptation of technical parts and synthesis protocols. The necessary size increase to obtain a pilot-plant is limited in comparison to the scale-up of a batch process, since the increased productivity can also be obtained increasing the flow rates.[77]

Compared to a batch hydrothermal approach, in CHFS heating time is highly reduced, allowing to reach supersaturation conditions in a shorter time. The cool-down time is also greatly reduced, as the reaction mixture is flowed through a cooler after a certain residence time, providing the fast abatement of the temperature below the boiling point of water to allow the reaction product to be collected at ambient pressure.

The CHFS method was firstly developed for the synthesis of nanostructured metals oxides, which largely benefits from the supercritical conditions, but it was extended to an extremely wide variety of other compounds[61] such as sulfides[78], silicates[79] and phosphates.[76] Syntheses can be performed either by directly mixing the precursors salts to supercritical water or introducing more additives, like oxidizing or reducing agents to control the final oxidation state of the products.

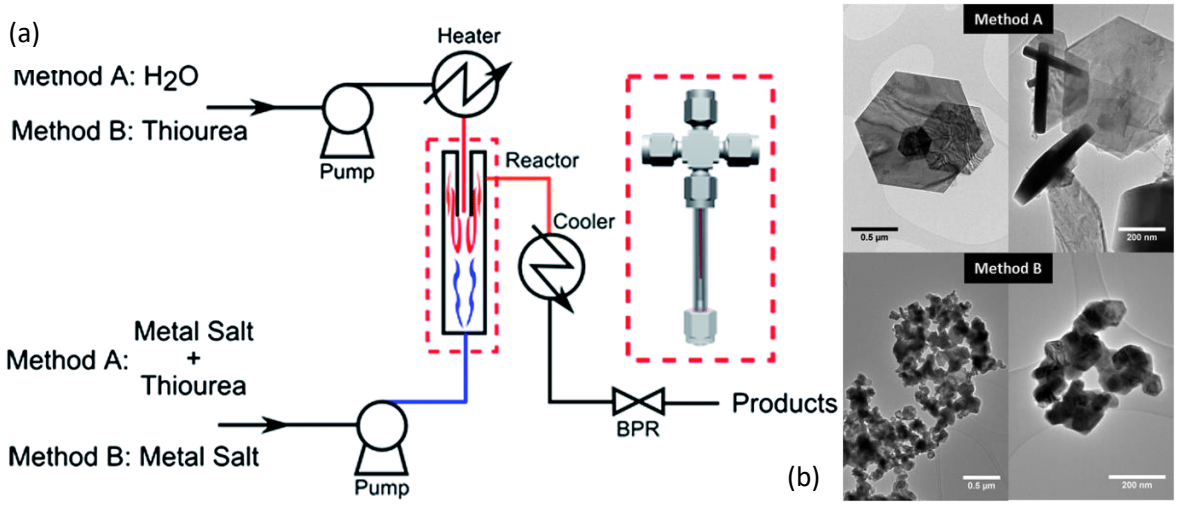

Figure 1.6 (a) CHFS setup developed by Dunne et. al.[78] for the synthesis of ZnS, CdS, PbS, CuS, $Fe_{(1-x)}S$ and Bi_2S_3. (b) $Fe_{(1-x)}S$ NPs obtained from the same setup employing two synthesis methods.

The CHFS of sulfides was pioneered by Dunne *et. al.*,[78] who obtained nanocrystalline ZnS, CdS, PbS, CuS, $Fe_{(1-x)}S$ and Bi_2S_3. In his approach, the sulfur precursor was introduced in the reactor as thiourea, that was quickly thermally decomposed upon contact with supercritical water releasing SH^- in solution.[80] From this strategy, Dunne *et. al.*[78] develop two distinct methods (Figure 1.6a). In the first, thiourea was mixed with the metal salt precursor to from a single solution. This solution was then

mixed to supercritical water causing thiourea to decompose in the presence of the metal ions, leading to the NPs nucleation and growth. In the second method, thiourea was directly dissolved into the heated water flow, causing its decomposition prior to be mixed with the metal precursors solution. While the first method was found to require a temperature of at least 400 °C to allow a sufficient SH^- formation from thiourea prior to the quenching of the reaction mixture, the second allowed him to explore reaction temperatures from 250 °C to 400 °C, that led to the obtainment of particles of different sizes.

In this Thesis, the approach proposed by Dunne *et. al.*[78] was modified by developing a double mixer strategy that was employed to test the synthesis of pure and doped ZnS NPs.

1.3 Functionalization of colloidal transition metal sulfides nanocrystals: a fascinating and challenging playground for the chemist

The reliable functionalization for nanosized metal sulfides represents one of the most challenging tasks in the field of the inorganic nanomaterial. The surface modification is an important step for many applications. As example, to develop quantum dots for *in vivo* applications in the bioimaging field, NPs need to be dispersible in a physiological solution, to be stable against coagulation and often to be capable of selectively recognize a target tissue. All these features can be obtained employing a proper functionalization procedure.[81] While this was largely studied and can be considered established for many metals and metal oxides NPs,[82] still many open questions remain unanswered when metal sulfides are concerned. The reason might be related to a gap in the knowledge about the surface chemistry of metal sulfides, which prevents the development of reliable functionalization strategies. F

The study of pure metal sulfides was one of the main reasons that inspired the synthesis of organic-free uncapped metal sulfide NPs in this Thesis. Indeed, the surface composition was analyzed, and the oxidation sensitivity of the obtained materials was discussed. Moreover, a study focused on the size-dependent oxidation phenomena, focusing on dimensional, structural, compositional and functional (photocatalytic activity) properties.

Here, the state-of-the-art in colloidal metal sulfides NPs functionalization was reviewed in relation to the current knowledge about the surface chemistry.

crystals

Review

Functionalisation of Colloidal Transition Metal Sulphides Nanocrystals: A Fascinating and Challenging Playground for the Chemist

Silvia Gross [1,2,*], Andrea Vittadini [1,2] and Nicola Dengo [1,2]

1 Istituto di Chimica della Materia Condensata e di Tecnologie per l'Energia, ICMATE-CNR, via Marzolo 1, I-35131 Padova, Italy; andrea.vittadini@unipd.it (A.V.); nicola.dengo@phd.unipd.it (N.D.)
2 Dipartimento di Scienze Chimiche, Università degli Studi di Padova and INSTM, UdR Padova, via Marzolo 1, I-35131 Padova, Italy
* Correspondence: silvia.gross@unipd.it; Tel.: +39-049-827-5736

Academic Editor: Roberto Comparelli
Received: 27 December 2016; Accepted: 24 March 2017; Published: 14 April 2017

Abstract: Metal sulphides, and in particular transition metal sulphide colloids, are a broad, versatile and exciting class of inorganic compounds which deserve growing interest and attention ascribable to the functional properties that many of them display. With respect to their oxide homologues, however, they are characterised by noticeably different chemical, structural and hence functional features. Their potential applications span several fields, and in many of the foreseen applications (e.g., in bioimaging and related fields), the achievement of stable colloidal suspensions of metal sulphides is highly desirable or either an unavoidable requirement to be met. To this aim, robust functionalisation strategies should be devised, which however are, with respect to metal or metal oxides colloids, much more challenging. This has to be ascribed, *inter alia*, also to the still limited knowledge of the sulphides surface chemistry, particularly when comparing it to the better established, though multifaceted, oxide surface chemistry. A ground-breaking endeavour in this field is hence the detailed understanding of the nature of the complex surface chemistry of transition metal sulphides, which ideally requires an integrated experimental and modelling approach. In this review, an overview of the state-of-the-art on the existing examples of functionalisation of transition metal sulphides is provided, also by focusing on selected case studies, exemplifying the manifold nature of this class of binary inorganic compounds.

Keywords: metal sulfides; transition metal sulfides; colloids; nanocrystals; functionalization; surface chemistry; bioimaging; derivatization; modelling; zinc sulfides; molybdenum sulfides

1. Introduction

The present review aims at providing a broad, though not comprehensive, overview of the functionalisation of metal (and in particular transition metal) sulphides, focusing on colloidal sulphide nanocrystals (NC). This wide and diversified class of inorganic materials has been the topic of several contributions, addressing their synthesis and characterisation [1–36], functionalisation [37–40], surface chemistry and eventually applications [1,6–11,15,27,30,33,35,41–49].

Nanocrystals present features which are different from those of bulk materials, particularly at the surface. With respect to bulk surfaces, nanocrystals present different and/or additional properties as a results of reduced size. In fact, a bulk solid contains only a small percentage of surface atoms; as a result, broken chemical bonds on the outer part contribute only minimally to material properties [50]. The surface-to-volume ratio increases inversely with shrinking size, and consequently the surface contribution increases in relevance, eventually becoming dominant. At the nanoscale, reduced size

can significantly alter some properties (for example optical properties) and generate completely new effects (such as surface plasmon resonance or size-dependent catalytic activity [51–56].

The review will therefore provide an overview on metal sulphide NCs surface chemistry and on the functionalisation of these surfaces, with particular emphasis on functionalisation strategies for biomedical applications, though other application fields will be also mentioned. Ligands exchange strategies will also be shortly surveyed, though this is not the main focus of the contribution.

Using the above reported state of the art as a starting point, the present work will aim not only at covering and updating the information addressed by the above quoted references, but also at complementing the topics addressed by these reviews from three points of view. In particular, compared to the aforementioned extended reviews, this work will focus on aspects such as:

1. efforts toward the unambiguous characterisation and assessment of metal sulphides surfaces, which is still an open issue, and a lively debate on it is present in the literature.
2. the development of effective functionalisation strategies for metal sulphides surfaces which requires a careful consideration of the former point;
3. survey the combination of experimental and computational tools to unravel the exact nature of functional groups and moieties present on the sulphide surface.

Accordingly, due to the vastness of the topic and to space constraints, in this Review, which has not the goal to provide a thorough and comprehensive coverage of this huge and widespread field, only a selection of case studies will be addressed. The whole *corpus* of works on the topic will be not considered, as it is extensively reviewed in the aforementioned given references, to which interested readers are referred.

Nevertheless, a few significant examples of convincingly performed functionalisations will be reviewed and discussed. The selection has been performed on two levels:

- selected different substrates (i.e., molybdenum, iron, copper and zinc sulphide) were chosen as examples of functionalised metal sulphides;
- selected functionalisation routes and moieties.

The structure of the Review entails a general introduction on metal sulphides and in particular on transition metal sulphides, as well as a discussion on the most relevant analogies and differences with respect to the homologues oxides. This latter part is relevant and functional also to the following discussion on the comparison of the functionalisation strategies for these two classes of inorganic colloids, being those for the latter ones (i.e., oxides) well established and thoroughly reported in the literature. The state-of-the-art in the corresponding field for the sulphides is instead not homogeneous, incomplete and in many cases contradictory, as explained in Sections 2.2 and 2.4 of this review. A section dealing with functionalisation of these compounds is then presented. The Section 2.3 deals with nanocrystals-ligands interactions.

The penultimate (Section 3) is devoted to an overview on selected case studies chosen to demonstrate the various solutions developed to stabilise transition metal sulphides colloids.

For each analysed substrate (i.e., metal sulphide), a brief description of the most relevant properties and applications (mainly in the field of bio-related applications such as bioimaging, in the field of inks and thin films, and in the field of electronics and opto-electronics) of the considered chalcogenide is provided, followed by relevant state-of-the-art examples. These are indeed selected to present in the most comprehensive fashion the manifold variability in terms of chemical nature of the surface and of the moieties used to strongly interact with it. Finally, the last part of the review is devoted to draw some conclusions, but chiefly to outline possible developments and perspectives in this highly fascinating field of research.

2. Transition Metal Sulphides: General Features and Surface Chemistry

In this section, we address firstly (Section 2.1) the main chemical and structural features of metal sulphides, by outlining the differences and analogies with respect to the homologues with oxygen, i.e., metal oxides. In the following (Section 2.2), the features of surface of transition metal sulphides, both as bulk materials as well as nanocrystals are surveyed, by discussing main model systems. A third sub-chapter, Section 2.3, is devoted to the description of some relevant example and on the main findings concerning the complex nature of interactions between ligands and nanocrystals surface. This is a more general part, mostly dealing with oxide NCs, though many considerations and methodological approaches can be extended to sulphides. In the last Section 2.4, applications of transition metal sulphides and the main functionalisation approaches to pursue these applications are reviewed.

2.1. Transition Metal Sulphides: Analogies and Differences with Respect to Transition Metal Oxides

Metal sulphides are a very broad and variable class of binary materials, having the general formula M_xS_y [57–61].

The structures and properties of most metal sulphides are remarkably different from those of the parent metal oxides. This has partially to be ascribed to the stronger covalence of the metal-sulphur bond, as extensively described in the following (*vide infra*), which reflects in a broader variety of accessible structures. For instance, contrary to the oxides homologues, sulphides present also stable structures characterised by the metal in trigonal-prismatic coordination and by the formation of S-S bonds, which are instead not observed in the metal oxides [57]. As thoroughly discussed in the following, the higher polarisability of the sulphide anion with respect to the harder (in Pearson's terms, [62]) oxide counterparts enables also the formation of layered structures, such as MoS_2 or WS_2, based on van der Waals interactions among the layers.

The main differences in terms of chemical reactivity and properties between metal oxides [63] and metal sulphides may be rationalised by referring to the different atomic numbers and sizes of oxygen and sulphur atoms and of the corresponding negative divalent anions (the ionic radius of the oxide ion ranges between 1.35 and 1.42 Å [64], while the S^{2-} ionic radius amounts to 1.84 Å [64,65]. As a consequence of the larger size of the atoms, sulphur is also characterised by a much higher average polarisability (α_S = 2.90 in units of 10^{-24} cm^3) with respect to oxygen (α_O = 0.802 in units of 10^{-24} cm^3) [66], which allows to classify S and O donor atoms as soft and hard, respectively [62]. In this regard, it can be also useful to remind that the Pauling sulphur electronegativity (2.5) is significantly lower that the O one (3.5) [67] thus indicating a M–S bond much more covalent than the M–O one. A further important consequence of the lower electronegativity of sulphur is its lower tendency to form hydrogen bonds. The higher covalent character of the M–S interaction in M_xS_y binary compounds has important consequences on the structures and chemical properties of M sulphides. A thorough discussion of the structural chemistry in metal and transition metal sulphides is reported in general inorganic textbooks [57–61].

In some cases, the M_xS_y structures are quite similar to those of the corresponding oxides (for instance, the cubic MnO and the most stable polymorph of MnS have the same structure (rock salt), but quite different chemical and functional features). On the other side, there are several further oxides and sulphides which, even though characterised by the same stoichiometry, show striking structural differences. For instance, in the case of Cu(II), the oxide tenorite and the corresponding sulphide covellite (i.e., CuO vs. CuS) [57,59], though characterized by the same formal 1:1 stoichiometry, feature very different structural arrangements, the latter compound presenting also S-S disulphide bonds [68].

Transition metal (TM) sulphides are particularly fascinating because of the structural variability and highly interesting functional properties [57–59,61], deriving not only by the nature of the involved transition metal, but also from variability in structure and stoichiometry. In fact, some of them present very complex structures not displaying a unique stoichiometry, for instance determined by other factors, such as atomic sizes and the possibility to form S-S bridges. The broad class of sulfur-rich

metal sulphides is characterised by the presence of S_n^{2-} polysulphide anions. Besides well know polysulphides of alkaline and earth alkaline metals, having a M_2S_n stoichiometry (n = 2 for Na, n = 2–6 for K, n = 6 for Cs) or BaS_n (n = 2, 3, 4), there are also TM polysulphides, such as VS_4, Re_2S_7 and the trisulfide TiS_3, ZrS_3, HfS_3, formally written as $M^{4+}S^{2-}(S_2)^{2-}$ and based on both sulphide and disulphide ions and displaying unusual structures [57,59].

Metal disulphides, having the formal stoichiometry MS_2, are a relevant class of TM sulphides, also from the technological point of view. They crystallise in three different structures (CdI_2-type, MoS_2-type, pyrite-type, e.g., Fe_2S) [57]. Metal disulphides of the groups 4, 5, 6 form layered structures in which the metal atoms occupy trigonal anti-prismatic or trigonal-prismatic voids. The structures are built up of different layers characterised by S–M–S bonds. [35,48]. Chalcogenide atoms in two hexagonal planes are separated by a plane of metal atoms, and the formal valence states of metal (M) and chalcogen (X) atoms are +4 and −2, respectively.

As a further function-relevant feature, some transition metal chalcogenides systems are characterised by either small (such as in the case of ZnS) or large deviation from the formal stoichiometry [69]. In the former case, the deviations from 1:1 stoichiometry result from lattice disorder arising from the presence, in small concentrations, of vacancies or interstitials. The latter case is instead much more represented among transition metal sulphides, which can exist as homogeneous phases over rather large composition ranges. This range usually, but not always, encompasses some simple stoichiometric composition. This stoichiometry variability is made possible by the presence of native structural defects built into the crystalline lattice.

In this regard, the structures of different iron and copper sulphides characterized by different S:M stoichiometry are depicted in Figure 1.

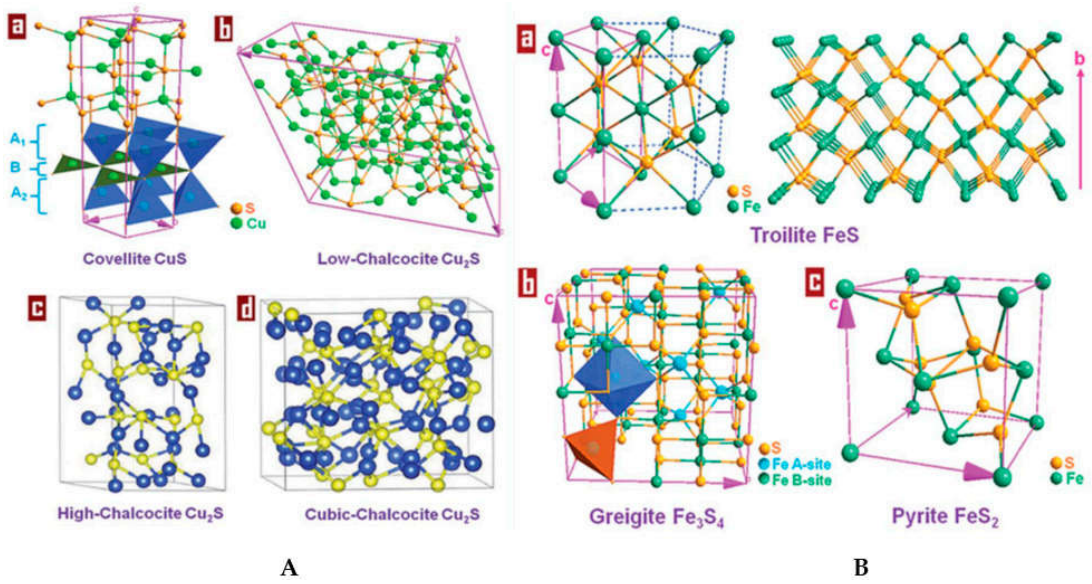

Figure 1. (**A**) Crystal structures of (**a**) covellite CuS consisting of layers triangular CuS_3 units (layer B) surrounded by CuS_4 tetrahedra (layers A1 and A2), (**b**) low-chalcocite (monoclinic), (**c**) high-chalcocite (hexagonal) and (**d**) cubic-chalcocite (cubic) Cu_2S. (**B**) Crystalline structures of stoichiometric (**a**) troilite FeS along different directions, (**b**) greigite Fe_3S_4, and (**c**) pyrite FeS_2. Taken from Ref. [27]. Reproduced with permission of Royal Society of Chemistry.

For a thorough and comprehensive description of the rich chemistry of metal sulphides, the interested reader is referred to inorganic chemistry textbooks [57–61] and to the cited dedicated reviews.

Synthetic routes for the reproducible and phase-controlled preparation of metal sulphide colloids are of fundamental interest for the study of the mentioned properties at the nanoscale level. Limiting the attention to wet chemistry approaches, a wide plethora of synthetic routes has

been proposed in the literature to prepare metal sulphide colloids ranging from non-aqueous sol-gel routes [70–73], hydro/solvothermal [24,74–86], to sono- [19,87–110] and radiochemistry [111–117], laser ablation [118,119], micro- [120–130] and miniemulsion synthesis [131–138], seeded-growth [139] and nucleation/growth and general colloidal and precipitation/co-precipitation approaches [13,82,140–153]. Recently, microbial, biomimetic and biogenic environmentally friendly synthesis of metal sulphide nanoparticles by using microbacteria, fungi, yeast has been also explored and thoroughly reviewed [5,9,15,154–159].

A comprehensive collection of wet-chemistry routes to metal sulphides is reported in the cited review papers [6,15,47,123,160–162] and in the above given specific references. In reference [161], a comprehensive table is reported, collecting many of the wet chemistry routes used to produce, *inter alia*, different sulphides and other chalcogenides. Transition metal sulphides such as Ag_2S, CuS, CdS, and ZnS, FeS_2, which can be formed either directly from their precursors ions or indirectly by sulphide ion-assisted conversion of the corresponding metal oxide, typically under anaerobic conditions, have been the focus of recently appeared review [163].

Metal sulphides NCs can be also produced in a controlled fashion by reaction of metal salts with tailor-made sulphide precursors, such as bis-(trimethylsilyl) sulfide [$(TMS)_2S$], phosphines sulphides (R_3P = S, where R indicates an alkyl or aryl group), and hydrogen sulfide produced by heating elemental sulfur in alkane or amine solvents. By following this precursor-based approach, the synthesis of size-controlled sulphide NCs (lead sulfide, cadmium sulfide, zinc sulfide, and copper sulfide) has been recently afforded by Owen and co-workers [13] by using a library of tri-substituted thioureas. The conversion reactivity to the targeted sulphide was determined by the substitution degree and in particular by the electronic and steric features of the substituents in the thiourea. By controlling the monomer supply kinetics, the extent of nucleation in syntheses of the NCs and the size distribution could be controlled.

2.2. The Surface of Transition Metal Sulphides: Bulk and Nanocrystals

Surface chemistry of metal sulphide, as already outlined above, is not so widely explored and studied as the one of the oxides homologues. As Balantseva et al. [164] pointed out, whereas literature concerning in situ infrared studies of surface of oxide materials is very abundant [165–167], the one on sulphides is instead quite limited. Some works were reported about the surface properties of unsupported or supported MoS_2, an increasingly studied catalyst for hydrodesulphurisation [168].

Progress in the knowledge of metal sulphides surface chemistry has been spurred by the need of improved mineral processing technologies. In this regard, it suffices to cite the separation of sphalerite ZnS from less valuable mineral by froth flotation, which is hampered by the presence of undesirable components such as pyrite. Further interest on the surface reactivity of metal sulphides has been recently driven by concerns on the impact of the products of mining operations, by catalysis (most notably desulphurization), and by the self-assembly and functionalization of organic molecules [45].

As outlined in previous reports on the topic [164], one of the reasons for this lack or scarcity of information on the surface chemistry of metal sulphides could be ascribed to the intrinsic difficulties in handling this class of materials. Whereas in the case of oxides, in situ surface studies are usually carried out on clean surfaces, obtained by removing species adsorbed from the atmosphere or residual synthetic reactants by calcination/oxidation treatments in flow or static conditions, the same cannot be stated for sulphides. A very general tendency of most metal sulphide, making the study of their surface chemistry even more challenging, is the possibility to get easily oxidised to oxides or sulphates [45,61,169,170], as extensively reported in the given references. It is for instance well-known that calcination at temperatures as high as 773 K promotes the transition from ZnS to ZnO. Even if oxidation is carried out in controlled conditions, by avoiding the complete ZnS/ZnO phase transition, treatment with oxygen or water vapour was shown to cause the formation of surface sulfate (SO_4^{2-}) and sulfite (SO_3^{2-}) species. This in turn further complicates the handling of sulphide surfaces, since no univocal model surface can be adopted, being the chemistry ruled by several further parameters, both

in the solid/gas phase (i.e., nanoparticles exposed to air) or in the liquid/solid phase (i.e., suspensions of nanoparticles).

The surface properties of bulk transition metal sulphides are best discussed by classifying the compounds according to the bulk structure. The discussion can be started by examining the case of transition metal monosulphides, which generally prefer hexagonal structures, *viz.* the NiAs structure, adopted by NiS and FeS. ZnS can also be found in nature in a hexagonal structure, namely wurtzite, but attention is now focused on the most typical sphalerite case, which is a cubic structure. As it is usual for all II-VI semiconductors, the most stable and abundant surface is the (110) one [164,171,172]. Surface relaxation essentially involve inward and outward displacements of cations and anions, respectively. The stability of the (110) surface is reflected in the theoretical equilibrium shape of the ZnS crystal. In fact, the minimization of the surface Gibbs free energy as performed in the Wulff construction, generates a dodecahedron exposing only (110) facets [171], as shown in Figure 2.

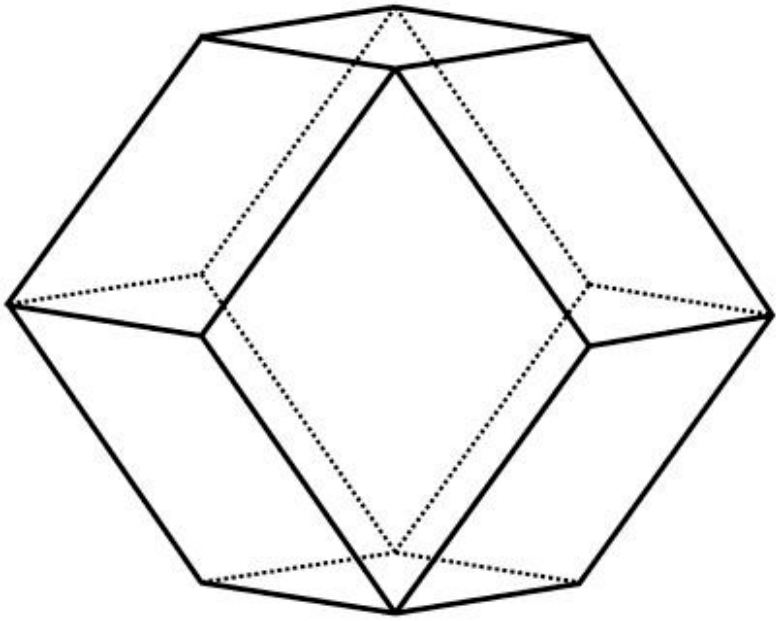

Figure 2. Calculated morphology of the cubic phase of ZnS, as obtained by relaxed surface energies. The only surface to appear is the (110). Taken from Ref. [171]. Copyright American Chemical Society.

Experimentally, other surfaces are also observed, including the non-polar ($\bar{4}$31) and (431) surfaces and the polar (111) surface. The (111) surface, both cation- and anion-terminated, is in principle unstable, being a type III surface for the Tasker rules [173]. However, the macroscopic electric field perpendicular to the surface can be compensated by suitable stoichiometric defects. Particularly favoured is the formation of vacancies in the terminal cation/anion layers [171]. The surface properties of FeS in the troilite structure has been studied by Wells et al. [174]. Only the (100) surface was considered, finding that it tends to reconstruct in such a way to form triangles of iron atoms "capped" with a sulphur atom.

The case of layered disulphides, which contain monoatomic S anions, and that are formed by the early transition elements of each period (e.g., TiS_2, MoS_2) is a peculiar one. As it is common for layered compounds, the (001) surface is very stable and practically inert, so that most interest has been devoted to the so-called "edge surfaces", which terminate the MoS_2 nanoribbons. In general, these edge surfaces are characterized by strong rearrangements due to the breaking of S-S bonds. After the pioneering work by Raybaud et al. [168] the MoS_2 edge surfaces have been systematically studied and compared theoretically by Spirko et al. [175], Figure 3.

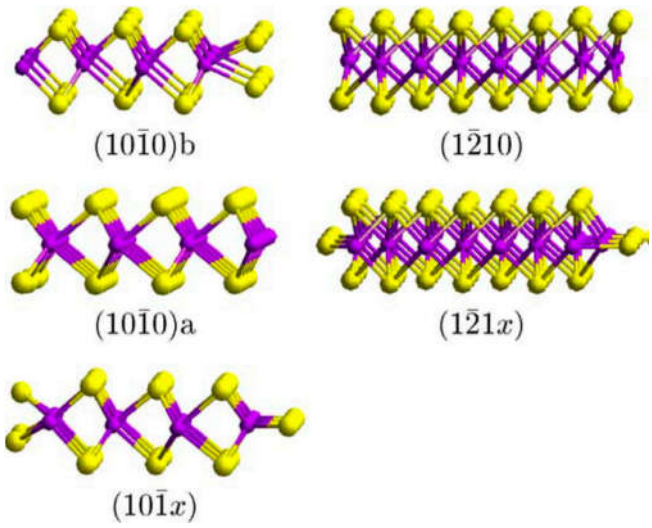

Figure 3. Side views along the relaxed MoS_2 edges rearrangement. Taken from Ref. [175], with permission by Elsevier.

The most stable are the $(10\bar{1}0)$ "diagonally" cut in such a way to include half of the terminal S ions, followed by $(1\bar{2}10)$ edges cut in an analogous way. These diagonal cuts allow an efficient reconstruction, which substantially lowers the system energy.

Disulphides of late transition elements are characterised by the presence of S_2^{2-} ions, and may be observed in rock-salt (pyrite), rutile (marcasite) and in the arsenopyrite structures. Particular attention has been devoted to Fe(II), compounds, such as chalcopyrite $CuFeS_2$ and pyrite FeS_2. The most common natural surfaces of FeS_2 are the (100), (110), (111), and (210) ones. The stability as well as the structural and electronic properties of these surfaces have been investigated by first principles calculations by Hung et al. [176]. Ion relaxations are generally weaker than in the above examined cases, which is explained by the rock-salt structure of pyrite. However, reconstruction such as micro-facetting has been theoretically predicted to be relevant, and able to make the (110) surface even more stable than the (100) one. In general, apparent relationship between overall surface Fe coordination and surface energy, with the presence of lower-coordinated species resulting in higher dangling bond density and therefore higher energy, less stable surfaces, are evidenced.

Among disulphides, MoS_2 is interesting both as a hydro-treating and as a desulphurisation catalyst. The complicated chemistry of its edge surfaces has stimulated several theoretical and experimental investigations [177–182]. More systematic studies involving a broader range of metal sulphides [183] are also reported. These studies allowed to prove, through the use of Sabatier analysis, that Co and Ni almost optimally promote the catalytic activity of MoS_2 by weakening the HS binding energy. As pointed out above, the basal (001) surface of MoS_2 is generally considered to be inert. Very recently, however, it has been pointed out that a careful combination of strain and S-vacancies can greatly enhance the activity of MoS_2 for the hydrogen evolution reaction, as predicted by theoretical calculations [184]. The surface of MoS_2 has also been the topic of detailed FT-IR studies [185,186].

As one of the chosen model systems, ZnS crystals undergo surface modification by reacting with the environment. By studying several samples composed of sphalerite and/or wurtzite ZnS crystals, Hertl [38] has hypothised the presence of -OH and -SH groups and of molecularly adsorbed water as well as a significant surface oxidation, revealed by the presence of sulphite and sulphate species.

In a further study on the high temperature (823 K) reaction of water vapour with the ZnS surface, mainly sulphite and additionally adsorbed water, hydrogen sulphide and adsorbed sulphur oxides were detected by FT-IR analysis. Exposure to oxygen determined the formation also of sulphate species [187]. In a very comprehensive experimental and computational study by Balantseva et al. [164], a combined theoretical and experimental work was carried out to unveil details on the ZnS surface

chemistry. ZnS nanoparticles were prepared by an easy precipitation method and activated in vacuum in order to clean the surface without affecting the stability of the cubic ZnS phase. The results were also compared to those of a commercial bulk ZnS sample (particle size < 10 μm). The combined approach allowed to evidence as the strength of Zn^{2+} Lewis acidity in ZnS is considerably lower than in ZnO and more comparable to those of other oxides like TiO_2 ($\Delta E_{ads} = -0.22$ eV) and MgO ($\Delta E_{ads} = -0.11$ eV) as well as the surface Lewis acidity of Zn^{2+} sites in ZnS nanocrystals appears significantly different with respect to the same sites in bigger microcrystals. The paper also outlines as, though the intense research activity on the synthesis and properties of nanostructured ZnS materials, very little information is available about their surface structure, which however can play an outstanding role in controlling ZnS crystal growth. This includes the presence of defects or disorder and of surface ligands or adsorbed species, which can determine important properties, including optical absorption threshold position and photoluminescence efficiency. Furthermore, a description of the surface from an atomic point of view could be crucial for a thorough understanding of photocatalytic processes.

Concerning iron, the surface reactivity of FeS_2 has been studied in UHV by several authors, with contrasting results. This has been ascribed to the difference between pyrite surfaces obtained by crystal fracturing and those grown and cleaned in vacuum. In fact, whereas the former is found to react with O_2 [188], the latter is non-reactive [189–191]. Arsenic is a common contaminant of pyrite, which may rise concerns about the environmental impact of this mineral. DFT calculations however show that there is no tendency for As impurities to segregate at the surface [192].

Focusing instead on nanocrystals, a very exciting class of systems [36,41,50,139,150,193–247] in which the relevance of surface becomes important and the properties transition with respect to the bulk is particularly noticeable [208,241,248,249], their surface chemistry has been the topic of extensive research and contributions, mostly on oxide NCs [36,41,50,202,209,210,215,219,221,222,240,246,250–260]. Little attention has been instead paid to sulphide NCs, though some contribution focus on both their synthesis [261–267] as well as on their surface chemistry [152,262,268–273].

Concerning the main differences with respect to the oxide counterparts, sulphides are typically cation-rich, which enhances the adsorption of, *inter alia*, negatively charged carboxylates. Conversely, the homologue oxides are typical stoichiometric and have dissociatively adsorbed carboxylic acids on their surface [251]. In this regard, in a study by Hens et al. [274], the ligand composition and dynamics of monodisperse suspensions PbS quantum dots was effectively investigated with nuclear magnetic resonance (NMR) spectroscopy. This study evidenced how oleate ions strongly bind to the cation-rich surface of the sulphide. The ligand exchange and the stoichiometry of metal chalcogenide nanocrystals were spectroscopically investigated outlining an easy metal-carboxylate displacement and binding [211]. In particular, the authors demonstrated as metal carboxylate complexes (L-M$(O_2CR)_{(2)}$, R = oleyl, tetradecyl, M = Cd, Pb) are readily displaced from carboxylate-terminated metal chalcogenides (ME) nanocrystals (ME = CdSe, CdS, PbSe, PbS) by various Lewis bases, the relative displacement efficiency being assessed by ^{1}H NMR spectroscopy and being strongly dependent on geometric factors such as steric arrangement and chelation. The results presented in the cited work suggest as ligands displace L-M$(O_2CR)_{(2)}$ by cooperatively complexing the displaced metal ion as well as the nanocrystal. The results demonstrate that nanocrystals cannot be defined by a single chemical formula, but are instead better described as dynamic structures with concentration-dependent compositions. The presented outputs are noticeable, since they have a relevant importance for the synthesis and purification of nanocrystals as well as ligand exchange reactions.

De Roo et al. [250] highlighted as NCs might also serve as suitable model systems to understand the interaction of organic molecules with macroscopic, inorganic material, e.g., solid-state membranes or mesoporous materials and they can also effectively used as model systems can also be used to revisit existing theories of NC nucleation and growth.

2.3. Nanocrystal-Ligand Interactions and Ligands Exchange Dynamics

Manipulating and tailoring nanocrystal surface ligands is a crucial step for their practical application as optoelectronic devices and fluorescent labels for biological imaging. The ligand exchange between the existing ligand and a new one is generally based on a two-step stripping route in which the existing ligand is replaced by the new once, typically displaying higher affinity and stronger binding to the targeted surface. Ligand exchange [6,195,211,222,240,251,255,275–284] is required to replace insulating organic surfactants and allow charge transport in nanocrystal solids as well as to prepare water-soluble nanocrystals that target specific cellular sites.

In an interesting contribution on shape-control through tailoring of surface-ligand interactions, Hennig [214] et al. outline as a deep understanding of NC surface chemistry is increasingly recognised to be critical for the comprehension of a broad range of phenomena and issues, including charge transport, solubility, functionalisation (e.g., for biological systems), optical properties (e.g., quantum yield), and the assembly of NCs into ordered super-structures and arrays [208,285,286]. Unravelling the effect of ligands on the NC properties and behaviour is better accomplished through atomistic computational methods, whereas it can be hardly pursued through standard analytical tools, typically more suited for the characterisation of well-defined planar interfaces. The NC shape is eventually controlled by the thermodynamics and growth kinetics of the dynamic system composed of the inorganic core, the ligands, and the solution containing both NC chemical precursors and ligand species. In this case, DFT calculations allowed to determine surface and binding energies for PbSe {100} and reconstructed {111} surfaces, capped with $Pb(OAc^{-})_2$ for a range of coverages. The authors of these studies concluded as, through the consideration of the surface/ligand interactions in the PbSe NC system, a model can be obtained. This model allows to predict that the facet-dependent interactions between core and ligand capping layer can be exploited, through the variation of the ligand concentration, to control the morphology and shape evolution not only of single NCs, but also of their assembly.

As outlined by some authors, as for instance the quoted work by Hens et al. [253], ligand exchange approaches are valuable tools to (i) adjust the interaction of the NC with their environment for instance modulating their solubility in either polar or apolar solvents; to (ii) enable the use of NC as biolabels, bioimaging probes or biosensors, through exchange with biomolecules; or to (iii) pursue the assembly of NC arrays, by replacing the original monofunctional ligand with bi- or polyfunctional ones.

To this aim, the understanding of NC-ligand interactions is mandatory also to develop successful ligand exchange strategies. In this framework, the NC-ligand exchange can also be effectively be followed by solution NMR, as extensively reported by Hens and Martins [253], also by using an in situ approach. For instance, in the case of oxides, in particular hafnia [251] surface chemistry of NC, has been studied through a multitechnique approach encompassing different NMR methods (Nuclear Overhauser Effect Spectroscopy (NOESY, Diffusion Ordered Spectroscopy (DOSY)) and FT-IR spectroscopy.

In a contribution by Mews [255], the ligand exchange on NC surface was investigated by Fluorescence Resonance Energy Transfer (FRET). In this study, the NC-ligand interaction was proven to influence the electronic properties of the NCs and also fluorescence in semiconductor NCs due to the weak binding of ligands. In fact, exchange with different polymeric ligands showed to influence not merely the colloidal stability, but also the fluorescence quantum yield. Furthermore, the strength of the binding was found to be enhanced by multi-dentate ligands, in that specific case amines.

Again concerning ligand dynamics, Owen and coworkers demonstrated that the surface layer of excess metal ions is labile and reversibly binds to and dissociates from nanocrystal surfaces as carboxylate complexes ($M(O_2CR)_2$); denoted as a Z-type ligand. They also adopted a rational ligand labelling, based on the covalent bond classification method developed by M. L. H. Green [287], in which L-type ligands are two-electron donors (neutral Lewis bases, dative covalent bonds), X-type ligands are one-electron donors (anionic, normal covalent bonds), and Z-type ligands are two-electron acceptors (Lewis acids).

PbS colloids have been used by Giansante et al. [252] to investigate the dynamics at organic/inorganic interfaces (Figure 4).

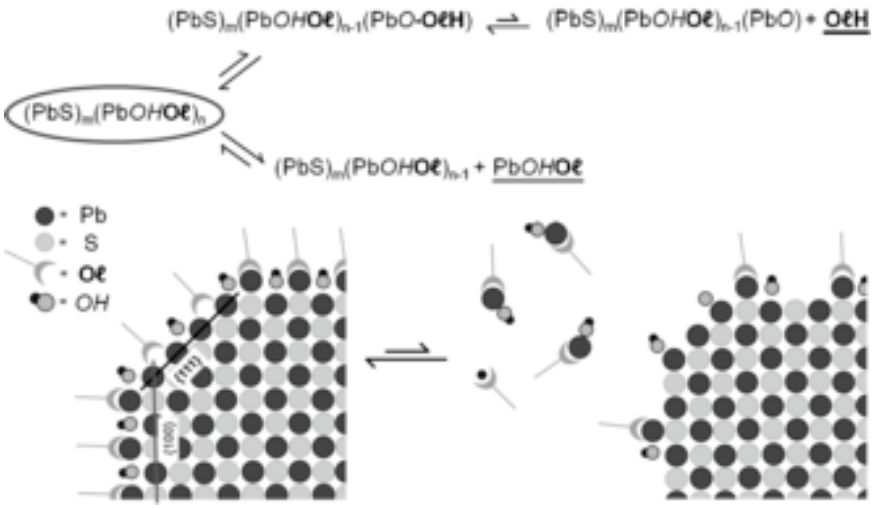

Figure 4. Simplified chemical formula of colloidal PbS Quantum Dots (QDs) and schematic representation of the dynamic equilibria involving oleic acid (OℓH) and Pb oleate (PbOHOℓ) as ligands at the {111} and {100} facets of the QD. Taken from Ref. [252] with permission of Wiley VCH.

It turned out that the organic/inorganic interface markedly affects forms and functions of the quantum dots, therefore its description and control are important for effective application. The authors showed that model sulphide NCs, i.e., PbS colloids, adapt their interface to the surroundings, thus existing in solution phase as equilibrium mixtures with their (metal-)organic ligand and inorganic core components. The interfacial equilibria are ruled by solvent polarity and concentration, show striking size dependence (leading to more stable ligand/core adducts for larger quantum dots), and selectively involve nanocrystal facets. The understanding of this ligand/core dynamic equilibrium is relevant not only to develop new synthetic paths but also to implement successful functionalisation and surface-chemistry strategies.

In the study of the interplay between the organic ligand shell and the inorganic core, magic-sized clusters [288], which are predominately surface atoms, provide a promising tool to clarify these critical surface interactions. This model system has been used to unveil the complex interactions ruling the surface chemistry of cadmium sulphide nanoparticles. These interactions affect the surface of both nanoparticles and magic-sized clusters and the results presented by Douglas et al. highlight the utility of the clusters as a probe of ligand–surface interactions.

The covalent bond classification has been also adopted by Van Driessche, De Roo et al. [250] to rationalise and classify in a logical fashion different binding motifs. The model additionally allows to effectively predict and to rationalise ligand exchange and ligand displacement reactions, therefore disclosing new applications for NCs in the field, *inter alia*, of opto-electronics, photovoltaics and catalysis, to mention the most relevant ones. Although the surface chemistry of several semiconductors and metal oxide nanocrystals are currently well-understood, more efforts are needed to unravel the ligand–NC interactions in the other materials. In fact, the general approach has been so far chiefly applied to oxides, but its adjustment and application to sulphides can be envisioned.

Ligands can be also used to direct the growth of the forming NCs [289–292]. In the ligand-assisted growth of NCs, the surface ligand dynamics is affected by the growth temperature, the ligand concentration and the ligand chain length, as outlined by Peng et al. [240], and as shown in Figure 5. Also the intermolecular interactions among the ligands can affect the growth of the NCs. These complex dynamic phenomena have been proven to influence also the final shape and morphology on the resulting colloids.

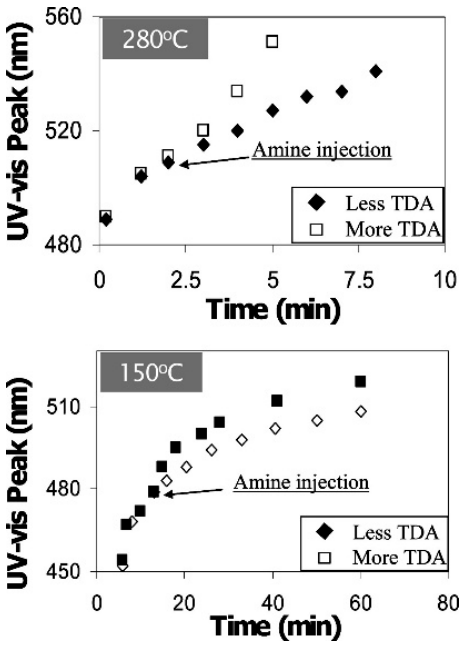

Figure 5. Impact of tetradecylamine (TDA) concentration on the growth of CdSe nanocrystals at 280 °C (above the bp for TDA) (top plot) and 150 °C (below the bp of TDA) (bottom plot). Taken from Ref. [240] with permission of the American Chemical Society.

Surface chemistry additionally rules the self-assembly behaviour of NCs, which can be used to obtain NC superlattices. In fact, as outlined by Hanrath and coworkers [214], the assembly of colloidal nanocrystals (NCs) into superstructures with long-range translational and orientational order is sensitive to the molecular interactions between ligands bound to the NC surface. In their study (see Figure 6, referring to the equilibrium form), the authors show as ligand coverage on colloidal PbS NCs can be exploited as a tunable parameter to direct the self-assembly of superlattices with given symmetry.

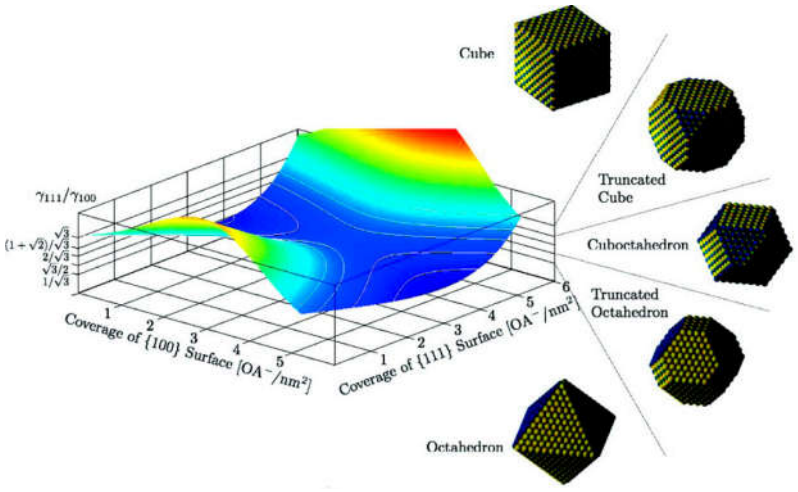

Figure 6. Surface energies and equilibrium shape of PbSe NC as a function of surface coverage with oleic acid molecules. (a) Ratio of the surface energies $\gamma 111/\gamma 100$ as a function of the coverages of the {100} and {111} surfaces. The ratios $\gamma 111/\gamma 100 = \sqrt{3}$, $(1+\sqrt{2})/\sqrt{3}$, $2/\sqrt{3}$, $\sqrt{3}/2$, and $1/\sqrt{3}$ are plotted as contours on the surface and correspond to NC cores with the equilibrium shape of a cube, uniform truncated cube, cuboctahedron, uniform truncated octahedron, and octahedron, respectively. Adapted from Ref. [214] with permission of the American Chemical Society.

The study additionally evidenced how the interplay of different analytical and theoretical tools is effective in thoroughly characterising these complex supramolecular systems. In particular, surface chemistry characterization encompassing FT-IR, XPS and Grazing Incidence SAXS (GI-SAXS) combined with density functional theory calculations suggest that the loss of ligands occurs preferentially on {100} than on reconstructed {111} NC facets.

2.4. Applications-Oriented Functionalisation of Transition Metal Sulphides

Most metal sulphides, in analogy with the oxide counterparts [63], feature exciting as well as diverse chemico-physical properties. Their electric behaviour ranges from insulating, through semiconductive to metallic. Likewise, they can be diamagnetic, paramagnetic, ferromagnetic or antiferromagnetic [1,44,293–296]. A relevant functional property displayed by some metal sulphides, particularly upon doping, is luminescence [46], which is broadly used also in optical bioimaging applications of these compounds [1,10,44,297–300]. Sulphide-based luminescent materials have attracted much attention for a wide range of photo-, cathodo- and electroluminescent applications. Upon doping with lanthanides or transition metal ions such as Mn^{2+} or Cu^{2+}, the luminescence can be tuned over the entire visible region by appropriately choosing the composition of the sulphide host. Among the wide range of applications, flat panel displays based on electroluminescent thin film, field emission displays and ZnS-based phosphors [46,262,301,302] and electroluminescent powders for backlights are worth to be mentioned.

By exploiting their interesting optical and electronic properties, transition metal sulphides can be used additionally for the development of devices in electronic and energy applications, in which the surface functionalisation of nanoparticles with specific ligands are relevant to ensure the charge transport properties of nanoparticles arrays.

In this regard, a novel and fascinating approach for the post-functionalisation of nanocrystals, among which also metal sulphide colloids, is based on the use of inorganic ligands [279]. In particular, various inorganic anions including metal-free chalcogenides, oxoanions/oxometallates, and halides/pseudohalides/halometallates have been employed to replace the original long-chain organic ligands on NCs. These ligands, with respect to single NC functionalised with insulating organic ligands, can passivate surface traps, are electronically transparent and can enhance the interparticle charge transport. This approach based on inorganic ligands broaden the functionality of NCs by tailoring their electro-optical properties or generating new inorganic phases through chemical reactions between nanomaterials and their surface ligands. Especially promising are the electronic, optoelectronic, and thermoelectric applications of solution-processed and inorganically-capped colloidal NCs, which substantially outperform their organically-capped counterparts.

A further example reported in the literature [16] and again involving cooperative effects, is instead concerned with absence of ligands in inorganic nanocrystals designed to exhibit negative charges and, therefore, electrostatically stabilised to give a colloidal dispersion in polar solvents. Undoped and Mn-doped $Zn_xCd_{1-x}S$ nanocrystals were studied, the latter showing strong luminescence. Also in this case, the possibility of surface-mediated electronic coupling between ligand-free sulphide nanocrystals was evidenced, which make them more suitable for electronic and optoelectronic applications compared to organic-capped nanocrystals.

The luminescent properties, combined with low or absent cytoxicity [158,299], (except for cadmium chalcogenides, broadly used as luminescent quantum dot [20,258,303–311]), make transition metal sulphide appealing candidate probes for optical bioimaging applications and further related bio-applications (e.g., photothermal and/or photodynamic applications [10,312,313]). As we shall extensively discuss in the next section, all these applications require a chemical, photochemical and thermal stable functionalisation. Nevertheless, they are not the only applications requiring functionalisation. Dispersions of transition metal sulphide nanoparticles in liquid media can find wide applications as precursors for nanocomposites or films with tailored functional and structural properties [140,314,315], or for stable suspensions for inks and paints.

Whereas in the cases of metallic and metal oxide nanoparticles (NPs) well-established and reliable functionalisation protocols have been developed and optimised (see the most remarkable reactions listed in Figure 7) [220,276,316–318], the development of effective surface-derivatisation methods for metal sulphide-based analogues has not been fully met so far by synthetic chemists, and reports retrieved in the literature fail, in several cases, either to convincingly demonstrate the stable functionalisation of metal sulphides or to prove the actual chemical nature of the sulphide surface, as also outlined by other authors [164,172].

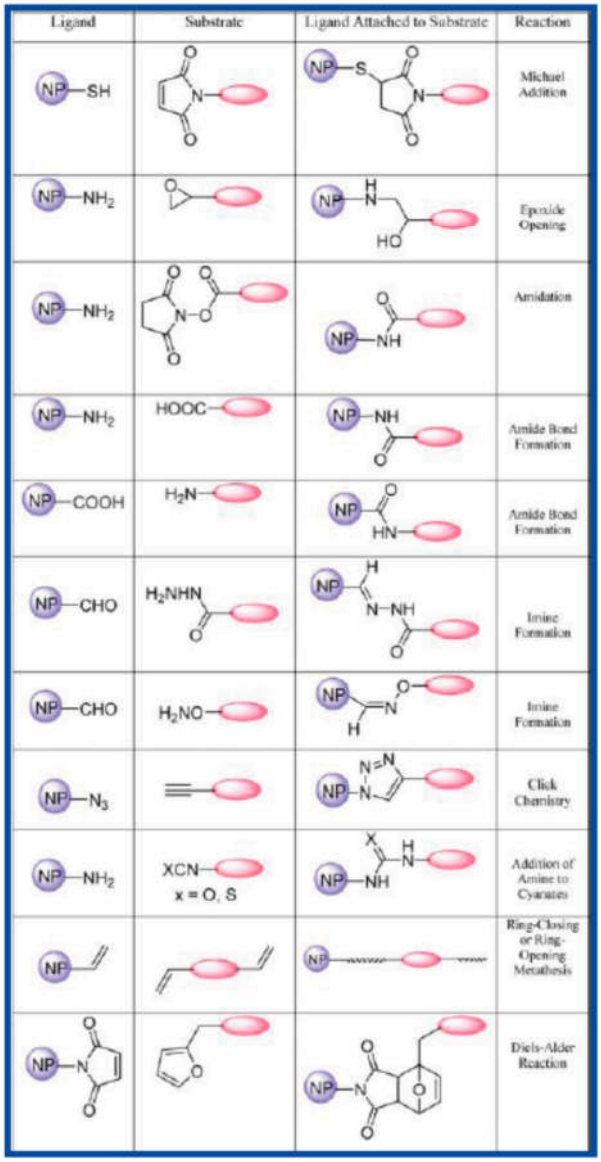

Figure 7. Functionalisation strategies for inorganic nanoparticles. Reprinted with permission from Ref. [318]. Copyright 2012 American Chemical Society.

The functionalisation strategy for an inorganic colloid is tightly related to the nature of the colloid, and hence to the synthetic route chosen to prepare it. Inorganic colloids and nanoparticles can chiefly be approached by two main strategies, involving either (i) hydrophobic conditions or (ii) direct synthesis in aqueous phase, resulting in hydrophobic and hydrophilic colloids, respectively. Several colloidal-based methods are based on the use of surfactants, which yield the formation of stable particles and/or emulsions, therefore these methods deliver nanoparticles which are inherently

hydrophobic, causing insolubility in water and preventing further functionalisation. However, since stable water dispersions are mandatory for many applications, ranging from bio-oriented ones to inks and paints production, functionalisation is a key step prior to the applications of NPs. Effective derivatisation chemistry becomes therefore critical toward colloidally stable, water-soluble NPs with flexible surface chemistry. The robust, steric stabilisation of inorganic nanocolloids within aqueous and physiological media via an appropriate chemical functionalisation stands as a fundamental requirement to enable their application in the biomedical field, particularly for the designing of novel bioimaging systems.

In the literature, hundreds of different functionalisation approaches are reported. They can be classified starting from the nature of chemical reactions involved, as reported in Figure 7, or they can be more easily sorted into three general typologies [220,276,316–318]:

(i) direct encapsulation of the hydrophobic NPs by hydrophilic polymers [289,319,320],
(ii) ligand exchange of the original surfactant with hydrophilic ligands [211,222,275–277,280,281,283, 320,321],
(iii) formation of an interdigitated bilayer between amphiphilic molecules or polymers and the passivating surfactant layer on the NP surface.

It should however be highlighted that the general functionalisation strategies reported in Figure 7, could be applicable to any suitable inorganic system, either metal sulphides or oxides, once the nature of the interacting moieties on the surface is identified or speficifically provided within a previous derivatisation step.

Among the most employed ligands for metal nanoparticles, thiols [39,322–328] have to be mentioned, whereas metal oxides NP can be conveniently derivatised by carboxylates or, even stronger, by multifunctional ligands such as dopamine-derivatives and cathecols [280,283,292,329–331]. A further distinction can be carried out accordingly to the chemical nature of the surface to be derivatised, which can be noble metal NPs [9,141,163,269,318,332–368] or metal oxides, the most commonly functionalised colloids, but also of other composition (halogenides, chalcogenides, phosphates, carbonates etc.).

Viable strategies to functionalise a nanostructure may also be classified depending on the interaction between ligand and surface, being either covalent (or coordinative) and non-covalent. The former, also based on multifunctional molecules, have enabled the development of stable systems also in harsh conditions such as extremely low (1) or high (14) pH values [369]. The latter discloses instead the possibility to apply rapid and easy self-assembly procedures involving the inorganic substrate and the organic ligand.

As far as the most explored application field is concerned, i.e., biomedicine , the robust, typically steric stabilisation of inorganic colloids within aqueous and physiological media via an appropriate chemical functionalisation stands as a fundamental step to enable their application, particularly for the design of novel bioimaging systems.

Surface derivatisation for bioimaging purposes of inorganic fluorophores is typically pursued by chemisorptions of selected molecules, which convey, with respect to physisorption, more robust bond and more stable surface functionalisation, hence ensuring an effective bioconjugation. The use of inorganic NP as fluorophores is motivated by different reasons. Compared to the homologue organic fluorescent dyes, inorganic colloids are endowed with better performances and stability. In fact, by combining suitable semiconductor nanocrystals with biomolecules it is possible to prepare new advanced systems with enhanced resolution and specific fluorescence detection capability [1,125,276,346,370,371]. Commonly used organic fluorophores have two significant limitations: (1) they cannot fluoresce continuously over long periods (long term imaging) and (2) they are not optimised for multicolour applications (multiplexing) [372], i.e., simultaneous, not sequential, detection of multiple signals. The unique optical properties of inorganic colloids, in many case referred to as Quantum Dots (QD) [20,39,44,46,163,210,307,311,373–377], make them instead appealing

as in vivo and in vitro fluorophores in a variety of biological investigations because they are able to overcome problems of long-term stability and multi-signal detection [105,372,378]. Nevertheless, one of the most significant drawbacks is the toxicity of QDs. Among QD, increasingly used are metal sulphides, characterised by low or absent toxicity such as ZnS [299,300].

3. Functionalisation of Transition Metal Sulphides: Case Studies

In this section, selected transition metal sulphides were chosen (i.e., ZnS, Cu_xS (x = 1, 2), Fe_xS_y (x = 0, 1, 2; y = 2, 3), MoS_2) to describe the manifold possibilities to address the functionalisation of these peculiar surfaces. The choice was driven mostly by three factors:

i relevance and wide applicability of the sulphide;
ii broadest differences among the chemistry, the structural and electronic features of the selected sulphides;
iii broadest differences among the chemistry and the structural features of the selected ligands as well as of their interaction with the sulphide surface.

CdS was deliberately not considered, due to the well-known toxicity, limiting its applications in bio-related fields. References on CdS nanoparticles are provided for interested readers [49,265,306,307,310,379–385].

In the following, the different sulphides substrates are concisely described, and an overview of their most relevant surface features is provided. The following section of each paragraph outlines instead the state-of-the-art relative to the selected examples concerning their functionalisation.

3.1. Zinc Sulphide

Among the metal sulphides, zinc sulphide (ZnS) [8,33,38,386] is one of the most investigated. It has been especially studied because of its appealing electronic properties, i.e., a wide band gap (3.7 eV) and a high exciton binding energy (40 meV). Zinc sulphide is among the most appealing semiconducting materials for the development of electroluminescent devices [46,301,387], which enables the direct conversion of electric energy into visible light, without generating heat, or requiring chemical or mechanical triggers. Additionally, ZnS can be easily doped by multiple ions (multiplexing), making it a suitable starting material for the development of optical and optoelectronic devices. Its intrinsic luminescence and the possibility of easy doping disclose its application in optoelectronics and related fields [8]. Moreover, it is environmental friendly and not-cytotoxic [298,299], thus suggesting possible applications also in biomedicine. In fact, combining the biocompatibility and the luminescence, optical bioimaging applications can be pursued [298,299]. For all these reasons and thanks to ZnS non-toxicity and intrinsic photoluminescence, ZnS NPs can be envisioned as high-performance and biocompatible bioimaging probes, although their stable dispersion in aqueous media still remains an open challenge, as discussed in the following.

The phase diagram defining the conditions of existence of the different polymorphs (sphalerite and wurtzite being the most relevant ones) has been obtained and reported along with main thermodynamic and structural data on the compound [388], whereas the pressure-induced structural changes in ZnS have been investigated by Desgreniers et al. [389].

Surface effects in ZnS are particularly interesting: Banfield et al. [273] have outlined as, whenever the surface of a ZnS nanoparticle gets wet, the whole crystal structure rearranges to become more ordered, closer to the structure of bulk ZnS. The same authors reported [390] that very small zinc sulphide nanoparticles display a disordered crystal structure that puts them under constant strain, increasing the stiffness of the particles. Surface chemical properties of zinc sulphide play a critical role in these phenomena. When zinc sulphide nanocrystals are put into water or either aqueous solution, surface hydration takes place, and the adsorption of proton and hydroxide ions make the surface either positively or negatively charged, in the absence of foreign preferentially adsorbed ions. Due to the sensitivity of sulphide ions to oxygen, redox reactions at the surfaces may occur as well.

As also outlined in Section 2.2, the zinc sulphide surface is characterised by a rich chemistry, which is influenced by the overall equilibrium of surface and solution chemical reactions, encompassing redox, acid-base, surface complexation, precipitation and dissolutions [271]. A comprehensive list of all possible occurring reactions is reported in ref. [271], which collects relevant chemical reactions and corresponding equilibrium constants, as retrieved from a comprehensive literature on the topic. The interplay of all these equilibria involving sulphides, hydrogensulphides, sulphates, is obviously determined by pH, concentration and different reactions can occur simultaneously in dependence of these factors. Based on this complex coexistence of equilibria, E-pH diagram can be plotted (Figure 8), defining the boundary of existence of the different species, and outlining as, between pH 3–11, when the concentration of Zn^{2+} and $S^{=}$ are equal, ZnS results the dominating species.

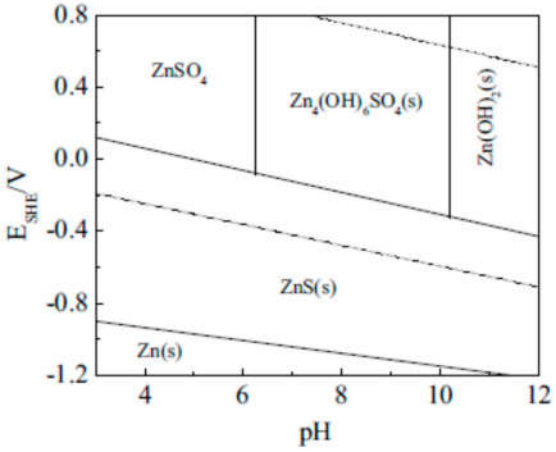

Figure 8. Predominant areas in E-pH diagram in Zn^{2+}–HS^{-} and H_2O system (Zn^{2+} = 0.1 M; HS^{-} = 0.1 M). Reprinted with permission from Ref. [271]. Copyright 2011 Chemistry Central Journal.

The same paper discusses further, based on potentiometric titration, adsorption and solution speciation modelling, the nature of the ZnS surface. Surface acidity, surface stoichiometry and surface proton binding sites are thoroughly analysed. The results show that, for stoichiometric surfaces of zinc sulphide, the proton and hydroxide determine the surface charge, whereas for the nonstoichiometric surfaces, the surface charge is controlled by proton, hydroxide, zinc and sulphide ions depending on specific conditions. Analogously, a distribution of the different species as a function of relative concentrations and pH is provided in the same paper (Figure 9). These are all aspects of the surface chemistry to be taken into account when planning an effective functionalisation. At the same time, this data evidences how complex and multifaceted is the surface chemistry of this sulphide. An important conclusion of the mentioned paper is that the surface stoichiometry strongly affects the surface properties of zinc sulphide; either zinc rich or sulphur rich surface determine different acid base properties, i.e., different surface acidity constants, ruling also the kind of functionalisation strategy to be implemented.

Nevertheless, a comprehensive, systematic and unambiguous characterisation of the precise surface composition of ZnS NPs (following the diverse synthetic pathways to obtain them) has not been provided so far, therefore hampering the identification of an effective functionalisation protocol and making the choice of a robust anchoring chemistry a challenging task. Although in several experimental and theoretical studies, it has been proposed that the ZnS surface could feature either oxidised species (SO_4, SO_3, ZnO) or reduced (SH, ZnOH) moieties [38], no unequivocal evidence of the chemical nature of these surfaces has been provided yet. Hence, a coherent proof of the selective ZnS surface-derivatisation by adsorbates presenting appropriate organic anchors remains still a partially unaccomplished issue in the recent literature. Additionally, it remains still open the question whether actually ZnS is the surface to be functionalised or rather partially or completely oxidised.

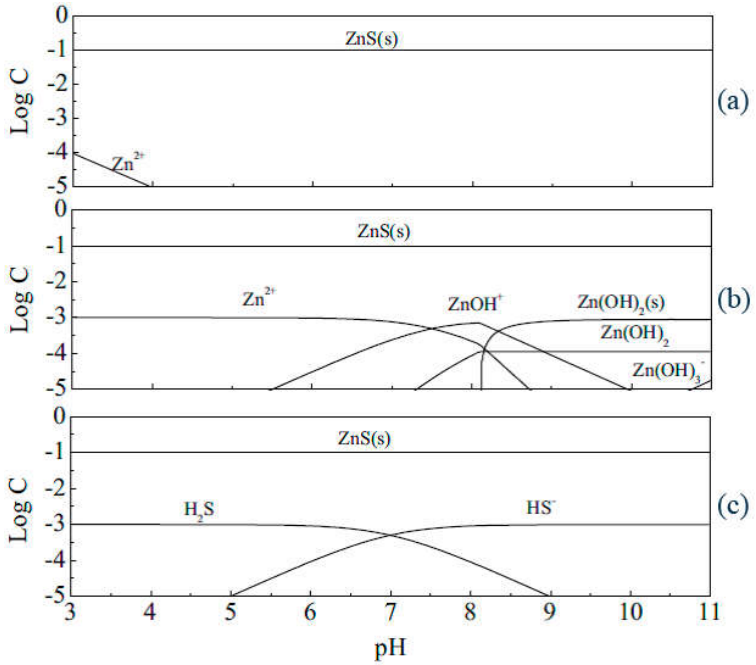

Figure 9. Distribution of zinc species in Zn^{2+}-HS^{-}-H_2O system as a function of pH in the presence of: (**a**) 100 mM Zn^{2+}, 100 mM HS^{-}; (**b**) 101 mM Zn^{2+}, 100 mM HS^{-}; (**c**) 101 mM HS^{-}, 100 mM Zn^{2+}.Adapted with permission from Ref. [271]. Copyright 2011 Chemistry Central Journal.

In the literature are however reported several examples of stable derivatisation of ZnS colloids, and hereafter some of the most meaningful ones are reported. Recently, the incorporation of ZnS:Mn NPs into polymeric matrix (polyacrylic acid and polymethylmethacrylate) to convey luminescent properties to plastics was investigated [391–393], although no specific functions by the polymers were demonstrated to enhance the interactions with the NPs. Alternatively, semiconductor nanocrystals (entirely or partially constituted by sulphides) were successfully incorporated into polymeric matrices [394] or derivatised with oleic acid and hexadecyl- trimethylammonium bromide to allow their dispersion in organic phases. Also in these cases, no detailed description of the characteristics of the coated surface and a proof of the effective functionalisation were provided.

A further elegant route to surface-functionalized ZnS nanoparticles (NPs) to be embedded in polymer matrix was based on a facile ligand exchange approach of mercaptoethanol with 5-(2-methacryloylethyloxymethyl)-8-quinolinol (MQ) [278]. By exploiting in situ bulk polymerization, the functionalised MQ-ZnS NPs were successfully incorporated into the polymer matrix to fabricate transparent bulk nanocomposites with good thermal stability and processability.

In this case, different coordination modes of the ligand to the surface were proposed, as sketched in Scheme 1, and the ligand exchange as well as the coordination of MQ to the ZnS surface could be convincingly demonstrated by NMR.

Functionalisation of ZnS could be pursued also by hexamethylenetetramine [395], enhancing the optical properties and thermal stability of ZnS nanoparticles. In this case, by HR-TEM coupled with SAED, a convincing demonstration of ZnS cubic structure in very small (ca. 2 nm) nanoparticles was provided. Therefore, the actual attachment of the hexamethylenetetramine on the surface could be inferred, probably mediated by the interaction of the amine group and the Zn^{2+} ions on the surface, as shown by FT-IR data. This latter was also evidencing Zn-S vibrations of the ZnS nanocrystals. A similar spectroscopic evidence is reported as a proof of successful functionalisation also in the paper of Taherian, where the S-H vibration of the thiol ligands glutathione and thioglycolic acid at 2550–2670 cm^{-1} is not observed anymore upon capping of the ZnS nanoparticles [396], therefore

indicating successful anchoring of the ligand. In this study, the effect of ligand chemistry on the microstructural properties and photo-physical properties, in particular the UV absorption is discussed.

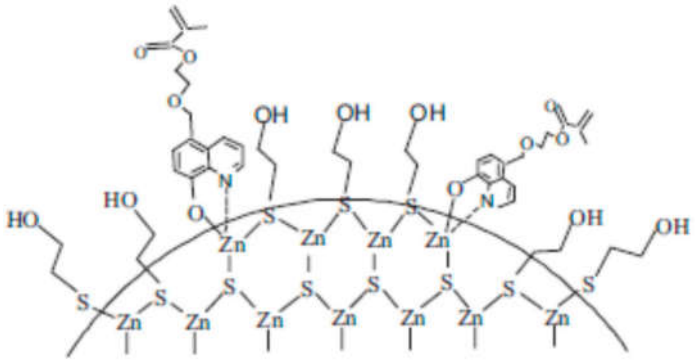

Scheme 1. Possible coordination structure of MQ on the surface of MQ–ZnS NPs. Reprinted with permission from Ref. [278]. Copyright 2008 Wiley VCH.

Folic acid (FA) conjugated carboxymethyl chitosan coordinated to manganese doped zinc sulphide quantum dot (FA–CMC–ZnS:Mn) nanoparticles for targeting, controlled drug delivery and also imaging of cancer cells was the topic of a comprehensive work of Mathew et al. [300]. The prepared nanoparticles were characterized using SEM, AFM, FT-IR, UV and DLS. Also in this further case, vibrational data were brought as demonstration of the successful occurred conjugation. Manzoor reported a further example of successful functionalization of ZnS with folic acid for targeted cancer imaging [299].

As a further example of functionalisation with folic acid, in another study [397], the synthesis of fluorescent-doped core/shell quantum dots of water-soluble manganese-doped zinc sulphide was addressed by a nucleation doping strategy, with 3-mercaptopropionic acid as stabiliser at 90 °C in aqueous solution. The manganese-doped zinc sulphide nanoparticles exhibit strong orange fluorescence under UV irradiation, resistance to photo-bleaching, and low-cytotoxicity to HeLa cells. In this case, the manganese-doped zinc sulphide nanoparticles were conjugated with folic acid using 2,20-(ethylenedioxy)-bis-(ethylamine) as the linker. The covalent binding of both 2,20-(ethylenedioxy)-bis-(ethylamine) and folic acid on the surface of manganese-could be probed by FT-IR detection.

Bioconjugation can be effectively accomplished by *N*-hydroxysuccinimide (NHS) chemistry. Generally, colloids prepared in non-aqueous medium need to be first solubilised in water through a ligand exchange reaction with thiol, amine, or carboxyl groups and then reacted with an *N*-(3-dimethylaminopropyl)-*N* ethylcarbodiimide (EDC) and *N*-hydroxysuccinimide (NHS) pair to create reactive species of NHS–carboxylates to connect with the functional groups in the folic acid [398]. In the case of ZnS, a direct functionalisation with folic acid has been reported [399], by simply reacting ZnS with folic acid, in aqueous medium, at room temperature.

In several other reports, the functionalisation of ZnS NPs was achieved by means of adsorbates presenting cysteine functions, suggesting the formation of S-S linkages with the sulphur present on the NP surface, even though the study of the stability of the obtained suspensions was not addressed in these reports. In one of this, the development of biotin tagged avidin functionalised zinc sulphide nanocrystals through a simple aqueous chemistry route at room temperature for targeted imaging applications is reported [400]. Surface functionalisation of manganese doped ZnS nanocrystals with L-cysteine provided functional groups that facilitated its conjugation to avidin. Further biotinylation of these particles through the strong non-covalent interaction between biotin and avidin enabled highly specific labelling of the biotin receptors on human hepatocellular carcinoma cells.

Narayanaswamy and co-workers reported the synthesis of L-cysteine-capped ZnS QDs and used them for Cu detection [401]. Cysteine is a water-soluble amino acid and frequently used as a capping

agent for ZnS QDs. The surface modification of ZnS QDs with cysteine prevents the aggregation of nanoparticles and makes them available for the interaction with the target materials. Furthermore, it increases the emission quantum yields of QDs and also stabilises the nanoparticles.

In a further paper [402], the authors report that ZnS nanoparticles were coated with a silica shell by exploiting the formation of Zn–O–Si bonds, as a result of the interaction of positively charged Zn^{2+} ions and of the silanol produced by the hydrolysis of alkoxysilane. Upon heating, condensation reaction of two adjacent silanol groups and release one water molecule occurred, thus forming siloxane bonds. In this peculiar case, conditions should be properly optimised to favour a very slow polymerisation process around the nanospheres, therefore minimising the inter-particles cross-linking. Among these conditions, the temperature plays a relevant important factor: mild temperature favours van der Waals force between silanol bridges, hence promoting a later condensation reaction to form covalent siloxane bonds (-Si-O-Si-). In general, this adaptation of the Stöber process [403] has been reported to be effective in coating different kinds of inorganic NP, some of them described in the following case studies, and of CdS. This is not strictly a functionalisation, but the approach was effective in providing the particles long term colloidal stability.

3.2. Copper Sulphide

Copper (II) sulphide (CuS) [10,12,32,404] has attracted considerable interest for its potential use as a material for transparent conductive films [12] able to transmit only the visible part of the solar spectrum, as a catalyst [405] and as a filler to enhance conductivity or wear resistance of polymeric materials. Doping with CuS was also reported to raise the critical temperature of some superconductors. Additionally, CuS is attracting a growing interest for application in photothermal therapy and in general in theranostics [10].

The crystalline hexagonal phase (covellite) of CuS, displaying an interesting and unusual structure envisioning the presence of both Cu^{I} and Cu^{II} and both trigonal and tetrahedral coordination of copper [406], is often described as a semiconductor and its reported band gap values, obtained from UV-Vis-NIR absorption spectra, range between 1.4 eV and 2.2 eV. Modelling of the CuS electronic structure also suggests a metallic behaviour. Such different results about metallic and semiconductive behaviour of CuS can be explained by considering that, even if the bulk solid behaving like a metal, a band gap can still be originated due to size confinement effects in nanocrystalline samples.

Different routes for the synthesis of CuS nanoparticles were developed, including the use of nucleation from solution, hydrothermal conditions, microemulsions, use of chelating agents, sonochemical methods, as reported in some of the already mentioned reviews and relevant papers on the topic [10,31,140,161,407–410].

As far as functionalisation is concerned, in the case of copper sulphide, very few examples could be retrieved in the literature in this regard.

In a contribution by Ang et al. [120], heterostructured CuS-ZnS nanocrystals (NCs) and Cu-doped ZnS (ZnS:Cu) NCs synthesized by two different protocols were investigated. These NCs were coated with a thin silica shell by using (3-mercaptopropyl)triethoxysilane in a reverse microemulsion to make them water soluble. Cytotoxicity experiments showed that these silica-coated NCs displayed low toxicity on both cancerous HeLa and noncancerous Chinese hamster ovary cells. The labelling of cancerous HeLa cells was also demonstrated.

In a paper by Kryukov et al., copper(II) sulphide stabilised in aqueous solutions by sodium polyphosphate [411] was reported, though also in this case no clear evidence of the interaction between the covellite nanoparticles and the stabiliser was provided.

Analogously to the previously discussed ZnS case study, chitosan functionalized CuS nanoparticles around 15 nm were prepared by employing the hydrothermal method. The modification of CuS nanoparticles with chitosan led to higher physiological stability and biocompatibility [412].

In a further example, manganese (II) chelate functionalized copper sulphide nanoparticles (CuS@MPG NPs) were successfully prepared using a facile hydrothermal method and employed

for their excellent photothermal effect and photoaoustic activity [413]. In this case, no clear evidence regarding neither the actual chemical nature of the surface (CuS or either oxidized species) nor the chemical nature of the functionalisation was provided, and the authors only stated that "The powdery CuS@MPG NPs were quite stable and could be stored for several months without any obvious change" without reporting any experimental data in this regard, which makes the assessment difficult.

3.3. Iron Sulphide

Iron sulphides (FeS, FeS_2, Fe_2S_3) are fewer in number than the corresponding oxides and based on lower oxidation states, being also the pyrite mineral built of Fe^{II} and S_2^{2-} ions in a distorted rock-salt structure. Concerning iron sulphides, very few examples could be retrieved in the literature, dealing with their derivatisation. Among these ones, some [414–416] report on iron sulphide which was stabilised by using carboxymethyl cellulose as stabilising ligand. In one case [416], the nanoparticles were prepared using a low-cost, food-grade cellulose (sodium carboxymethyl cellulose, CMC) as the stabiliser. The hydrodynamic diameter of fresh FeS-CMC nanoparticles was measured to be about 40 nm. In this case, the successful formation of CMC-FeS could be only indirectly assessed by verifying the very low polydispersity index, suggesting a quite monodisperse system. In a previous paper on the topic [414], evidence that attachment of CMC onto the surface of FeS particles induced strong electrostatic repulsion between the negatively charged particles was also provided based on zeta potential measurements [414]. Furthermore, when stored in sealed vials under anaerobic conditions at room temperature, the CMC-FeS NP did not display any visual sedimentation over a period of several weeks. However, the nanoparticles were quickly oxidised when coming in contact with air, turning the black suspension into a yellowish-orange coloured solution. In a further paper, adsorption of cetylpyridinium chloride (CPC), a cationic surfactant, on pyrite surface was investigated in its suspension, showing a CPC adsorption capacity dependence upon pH [268] (see Figure 10). Zeta potential of pyrite surface changed from positive to negative value by the addition of NaCl. Though the absorption cannot be considered a stable functionalisation, this study provides basic understanding of the adsorption mechanism of cationic surfactant on pyrite surface at different pH conditions.

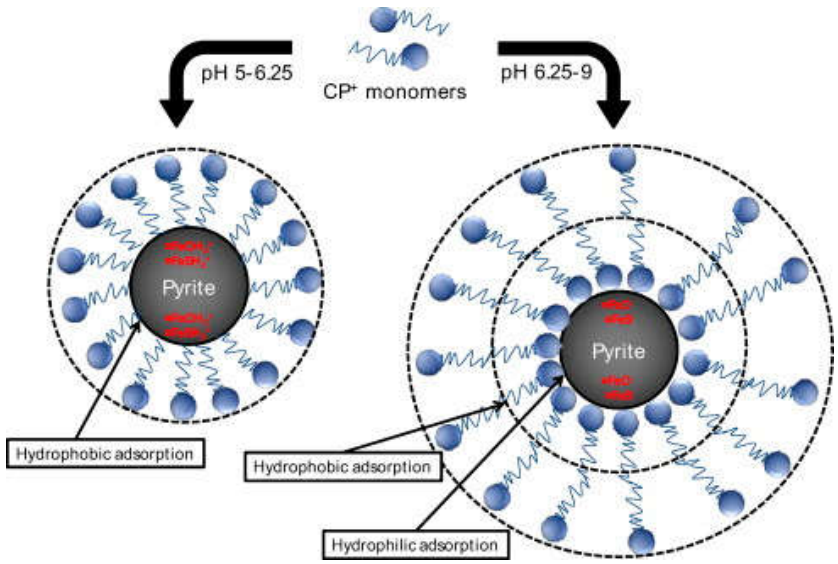

Figure 10. Schematic illustration for adsorption of cetylpyridinium chloride (CPC) on pyrite surface at different pH ranges. Taken from Ref. [268]. Copyright 2012 Elsevier.

3.4. Molybdenum Sulphide

Molybdenum disulphide, MoS_2, is a very interesting transition metal chalcogenide, and the most stable among Mo sulphides. It displays a peculiar structure, elucidated by Pauling in 1923 [417], consisting of layers of MoS_2 in which Mo atoms are each coordinated to 6 sulphide atoms, forming not the usual octahedron, but rather a trigonal prism [58]. The layered structure favours the easy cleavage along the planes, thus explaining also the lubricants properties. Indeed, being well investigated as lubricant [418], MoS_2 has recently attracted attention also as interesting material for the development of catalysts in many hydrogenation and in general catalytic reactions [419,420]. By activating the MoS_2 basal plane, the hydrogen evolution reaction (HER) could be further enhanced. Theoretical and experimental results show that the S-vacancies are the catalytic sites in the basal plane, where gap states around the Fermi level allow hydrogen to bind directly to exposed Mo atoms. Molybdenum-sulphide-based catalysts has also found potential application in lithium-ion batteries (LIBs) and supercapacitors (SCs) applications [27].

Also in this case, few papers dealing with functionalisation of this sulphide could be retrieved, also because applications in bio-related disciplines have not yet been assessed. One of the most relevant paper on derivatisation is one reporting on the synthesis of edge-oriented MoS_2 nanosheets by the evaporation of a single source precursor [40]. The surface chemistry of the MoS_2 nanosheets has been studied in order to evaluate the chemical reactivity of the basal planes and edges. In this case, the functionalisation of the basal plane with 1-pyrene acetic acid allows the immobilization of DNA and immunoglobins on the MoS_2 basal plane for biosensing purposes. In particular, the MoS_2 film was treated with 1-pyrene acetic acid in order to introduce COOH groups on the basal planes of the MoS_2 for tethering to NH_2-terminal DNA and proteins. 1-Pyrene acetic acid has four six-membered rings which can adsorb via van der Waals bonding on graphitic-like planes. Evidence of the occurred anchoring was provided by FT-IR showing that following treatment with 1-pyrene acetic acid and washing with buffer solution. Distinct peaks at 1700 and 1650 cm^{-1} assignable to the C=O and C–C stretching could be evidenced. Afterwards, EDC was used to activate the COOH groups of the MoS_2 samples to facilitate the formation of amide bonds with theNH_2-DNA probe. The DNA-immobilized MoS_2 was then used to assay for the labelled complementary DNA. By using the different emission filters, the NH_2-DNA probes and labelled targets were imaged separately, showing effectiveness of the functionalisation procedure.

4. Conclusions

This review has collected the most relevant examples retrieved in the state of the art on nanostructured transition metal sulphide surface chemistry and on selected case studies dealing with their functionalisation. The main goal of this contribution was to provide an overview on the still inhomogeneous and sometimes contradictory state-of-the-art in this field as well as to try to unify the picture on the complex surface chemistry of this peculiar class of inorganic compounds. Endeavours towards a deeper understanding of the presence and nature of different species on the sulphide surface, their dependence on experimental factors (pH, temperature, potential, solvent etc.) and to the development of effective functionalisation strategies leading to stable and robust anchoring of the functionalising moieties, are challenging but worth to be pursued, since the establishment of effective derivatisation strategies would enable to further widen the functional applications of metal sulphides. This collection of relevant examples has also pointed out as, to address a systematic and reliable investigation of metal sulphides surface, the combination of different analytical approaches and theoretical tools is highly desired.

As outlined by Balantseva et al. [164], very few techniques are available to study the surface properties of sulphide colloids, so that often indirect methods and combination of different analytical tools are necessary. Among these, the use of in situ infrared spectroscopy has been proven, also in the case of oxides, to be a very powerful tool, especially when coupled to theoretical modelling allowing the calculation of energy, structure, and vibrational frequencies of simple molecules weakly interacting

with the surface. Adsorption of small molecules, followed by DRIFT, has also demonstrated to be useful to unveil acid/base properties of surfaces [421–425].

As outlined in Section 2.3, a further valuable tool in the understanding of NC/ligands interactions is offered also by NMR spectroscopy. The possibilities offered by ^{1}H solution NMR for the study of colloidal nanocrystal ligands have been reviewed by Hens and Martins [253] and De Roo [251]. Using CdSe and PbSe nanocrystals with tightly bound oleate ligands as examples, solution NMR for ligand analysis was used. In particular, the authors explored the capabilities of diffusion ordered (DOSY) and nuclear Overhauser effect (NOESY) spectroscopy as NMR-related techniques which enable bound ligands to be distinguished from free ligands.

Additionally, as witnessed by the literature surveyed in this review, analytical methods to study colloids such as zeta-potential measurements, combined with potentiometric titration, adsorption and solution speciation modelling, could enable to unravel the effective nature of even complex surfaces (in terms of surface acidity, surface stoichiometry and surface proton binding site), whose chemistry has been shown to be affected, *inter alia*, by species concentration, pH, temperature, surrounding environment.

In this regard, a still open challenging task for the chemist is to better understand the surface chemistry of metal sulphides, its dependence from experimental parameters, and to design new functionalisation strategies to effectively address their long-term stabilisation. In this endeavour, the preparative chemist need to be supported also by theoreticians who are able to reliably model the surface.

Author Contributions: S.G. conceived the topic and structure of the review; N.D. performed carefully literature survey and its organisation. A.V. wrote the part on surface chemistry of sulphides, S.G. wrote the rest of the paper. A.V. and N.D. critically revised the whole text and added some sections.

Conflicts of Interest: The authors declare no conflict of interest.

References

1. Biju, V.; Itoh, T.; Anas, A.; Sujith, A.; Ishikawa, M. Semiconductor quantum dots and metal nanoparticles: Syntheses, optical properties, and biological applications. *Anal. Bioanal. Chem.* **2008**, *391*, 2469–2495. [CrossRef] [PubMed]
2. Bilecka, I.; Niederberger, M. New developments in the nonaqueous and/or non-hydrolytic sol-gel synthesis of inorganic nanoparticles. *Electrochim. Acta* **2010**, *55*, 7717–7725. [CrossRef]
3. Bowles, K.C.; Bell, R.A.; Ernste, M.J.; Kramer, J.R.; Manolopoulos, H.; Ogden, N. Synthesis and characterization of metal sulfide clusters for toxicological studies. *Environ. Toxicol. Chem.* **2002**, *21*, 693–699. [CrossRef] [PubMed]
4. Bruehwiler, D.; Seifert, R.; Calzaferri, G. Quantum-Sized Silver Sulfide Clusters in Zeolite A. *J. Phys. Chem. B* **1999**, *103*, 6397–6399. [CrossRef]
5. Da Costa, J.P.; Girao, A.V.; Trindade, T.; Costa, M.C.; Duarte, A.; Rocha-Santos, T. Biological synthesis of nanosized sulfide semiconductors: Current status and future prospects. *Appl. Microbiol. Biotechnol.* **2016**, *100*, 8283–8302. [CrossRef] [PubMed]
6. Dahl, J.A.; Maddux, B.L.S.; Hutchison, J.E. Toward Greener Nanosynthesis. *Chem. Rev.* **2007**, *107*, 2228–2269. [CrossRef] [PubMed]
7. Dunne, P.W.; Munn, A.S.; Starkey, C.L.; Huddle, T.A.; Lester, E.H. Continuous-flow hydrothermal synthesis for the production of inorganic nanomaterials. *Philos. Trans. R. Soc. a-Math. Phys. Eng. Sci.* **2015**, *373*, 20150015. [CrossRef] [PubMed]
8. Fang, X.; Zhai, T.; Gautam, U.K.; Li, L.; Wu, L.; Bando, Y.; Golberg, D. ZnS nanostructures: From synthesis to applications. *Prog. Mater. Sci.* **2011**, *56*, 175–287. [CrossRef]
9. Faramarzi, M.A.; Sadighi, A. Insights into biogenic and chemical production of inorganic nanomaterials and nanostructures. *Adv. Colloid Interface Sci.* **2013**, *189*, 1–20. [CrossRef] [PubMed]
10. Goel, S.; Chen, F.; Cai, W. Synthesis and biomedical applications of copper sulfide nanoparticles: From sensors to theranostics. *Small* **2014**, *10*, 631–645. [CrossRef] [PubMed]

11. Gong, Y.Y.; Tang, J.C.; Zhao, D.Y. Application of iron sulfide particles for groundwater and soil remediation: A review. *Water Res.* **2016**, *89*, 309–320. [CrossRef] [PubMed]
12. Grijalva, H.; Inoue, M.; Boggavarapu, S.; Calvert, P. Amorphous and crystalline copper sulfides, CuS. *J. Mater. Chem.* **1996**, *6*, 1157–1160. [CrossRef]
13. Hendricks, M.P.; Campos, M.P.; Cleveland, G.T.; Jen-La Plante, I.; Owen, J.S. A tunable library of substituted thiourea precursors to metal sulfide nanocrystals. *Science* **2015**, *348*, 1226–1230. [CrossRef] [PubMed]
14. Hendricks, M.P.; Campos, M.P.; Cleveland, G.T.; Owen, J.S. Rapid access to substituted thioureas: A tunable library of precursors for metal sulfide nanocrystals. In *Abstracts of Papers of the American Chemical Society (vol. 248). 1155 16TH ST, NW*; American Chemical Society: Washington, DC, USA.
15. Hosseini, M.R.; Sarvi, M.N. Recent achievements in the microbial synthesis of semiconductor metal sulfide nanoparticles. *Mat. Sci. Semicond. Proc.* **2015**, *40*, 293–301. [CrossRef]
16. Kadlag, K.P.; Rao, M.J.; Nag, A. Ligand-Free, Colloidal, and Luminescent Metal Sulfide Nanocrystals. *J. Phys. Chem. Lett.* **2013**, *4*, 1676–1681. [CrossRef] [PubMed]
17. Kowshik, M.; Deshmukh, N.; Vogel, W.; Urban, J.; Kulkarni, S.K.; Paknikar, K.M. Microbial synthesis of semiconductor CdS nanoparticles, their characterization, and their use in the fabrication of an ideal diode. *Biotechnol. Bioeng.* **2002**, *78*, 583–588. [CrossRef] [PubMed]
18. Kristl, M.; Drofenik, M. Sonochemical synthesis of nanocrystalline mercury sulfide, selenide and telluride in aqueous solutions. *Ultrason. Sonochem.* **2008**, *15*, 695–699. [CrossRef] [PubMed]
19. Kristl, M.; Hojnik, N.; Gyergyek, S.; Drofenik, M. Sonochemical preparation of copper sulfides with different phases in aqueous solutions. *Mater. Res. Bull.* **2013**, *48*, 1184–1188. [CrossRef]
20. Kuzyniak, W.; Adegoke, O.; Sekhosana, K.; D'Souza, S.; Tshangana, S.C.; Hoffmann, B.; Ermilov, E.A.; Nyokong, T.; Hopfner, M. Synthesis and characterization of quantum dots designed for biomedical use. *Int. J. Pharm.* **2014**, *466*, 382–389. [CrossRef] [PubMed]
21. Lu, F.; Zhou, M.; Li, W.R.; Weng, Q.H.; Li, C.L.; Xue, Y.M.; Jiang, X.F.; Zeng, X.H.; Bando, Y.; Golberg, D. Engineering sulfur vacancies and impurities in $NiCo_2S_4$ nanostructures toward optimal supercapacitive performance. *Nano Energy* **2016**, *26*, 313–323. [CrossRef]
22. Pileni, M.P. Colloidal assemblies used as templates to control the size, shape and self organization of nanoparticles. *PCCP* **1997**, *101*, 1578–1587. [CrossRef]
23. Pouretedal, H.R.; Norozi, A.; Keshavarz, M.H.; Semnani, A. Nanoparticles of zinc sulfide doped with manganese, nickel and copper as nanophotocatalyst in the degradation of organic dyes. *J. Hazard. Mater.* **2009**, *162*, 674–681. [CrossRef] [PubMed]
24. Qian, X.F.; Zhang, X.M.; Wang, C.; Wang, W.Z.; Xie, Y.; Qian, Y.T. Solvent-thermal preparation of nanocrystalline tin chalcogenide. *J. Phys. Chem. Solids* **1999**, *60*, 415–417. [CrossRef]
25. Ramasamy, K.; Malik, M.A.; Revaprasadu, N.; O'Brien, P. Routes to Nanostructured Inorganic Materials with Potential for Solar Energy Applications. *Chem. Mater.* **2013**, *25*, 3551–3569. [CrossRef]
26. Rickard, D.; Luther, G.W. Chemistry of iron sulfides. *Chem. Rev.* **2007**, *107*, 514–562. [CrossRef] [PubMed]
27. Rui, X.H.; Tan, H.T.; Yan, Q.Y. Nanostructured metal sulfides for energy storage. *Nanoscale* **2014**, *6*, 9889–9924. [CrossRef] [PubMed]
28. Sadovnikov, S.I.; Rempel, A.A. Synthesis of nanocrystalline silver sulfide. *Inorg. Mater.* **2015**, *51*, 759–766. [CrossRef]
29. Shiri, L.; Ghorbani-Choghamarani, A.; Kazemi, M. Sulfides Synthesis: Nanocatalysts in C-S Cross-Coupling Reactions. *Aust. J. Chem.* **2016**, *69*, 585–600. [CrossRef]
30. Teranishi, T.; Saruyama, M.; Kanehara, M. Seed-mediated synthesis of metal sulfide patchy nanoparticles. *Nanoscale* **2009**, *1*, 225–228. [CrossRef] [PubMed]
31. Tolia, J.; Chakraborty, M.; Murthy, Z.V.P. Synthesis and characterization of semiconductor metal sulfide nanocrystals using microemulsion technique. *Cryst. Res. Technol.* **2012**, *47*, 909–916. [CrossRef]
32. Van der Stam, W.; Berends, A.C.; Donega, C.D. Prospects of Colloidal Copper Chalcogenide Nanocrystals. *Chemphyschem* **2016**, *17*, 559–581. [CrossRef] [PubMed]
33. Wang, X.F.; Huang, H.T.; Liang, B.; Liu, Z.; Chen, D.; Shen, G.Z. ZnS Nanostructures: Synthesis, Properties, and Applications. *Crit. Rev. Solid State Mater. Sci.* **2013**, *38*, 57–90. [CrossRef]
34. Zhang, F.; Wong, S.S. Controlled synthesis of semiconducting metal sulfide nanowires. *Chem. Mater.* **2009**, *21*, 4541–4554. [CrossRef]

35. Wang, D.-S.; Zheng, W.; Hao, C.-H.; Peng, Q.; Li, Y.-D. A Synthetic Method for Transition-Metal Chalcogenide Nanocrystals. *Chem. Eur. J.* **2009**, *15*, 1870–1875. [CrossRef] [PubMed]
36. Chemseddine, A. *Metal-Oxide and -Sulfide Nanocrystals and Nanostructures*; Wiley-VCH Verlag GmbH: Weinheim, Germany, 2000; pp. 315–352.
37. Hiratani, T.; Konishi, K. Functionalization of inorganic nanoclusters based on the molecular recognition events at the heterogeneous interface. *J. Synth. Org. Chem. Jpn.* **2008**, *66*, 239–248. [CrossRef]
38. Hertl, W. Surface chemical properties of zinc sulfide. *Langmuir* **1988**, *4*, 594–598. [CrossRef]
39. Lee, C.M.; Jang, D.; Cheong, S.J.; Kim, E.M.; Jeong, M.H.; Kim, S.H.; Kim, D.W.; Lim, S.T.; Sohn, M.H.; Jeong, H.J. Surface engineering of quantum dots for in vivo imaging. *Nanotechnology* **2010**, *21*, 285102. [CrossRef] [PubMed]
40. Zhang, H.; Loh, K.P.; Sow, C.H.; Gu, H.R.; Su, X.D.; Huang, C.; Chen, Z.K. Surface modification studies of edge-oriented molybdenum sulfide nanosheets. *Langmuir* **2004**, *20*, 6914–6920. [CrossRef] [PubMed]
41. Buonsanti, R.; Milliron, D.J. Chemistry of Doped Colloidal Nanocrystals. *Chem. Mater.* **2013**, *25*, 1305–1317. [CrossRef]
42. Chen, J.-H.; Long, X.-H.; Zhao, C.-H.; Kang, D.; Guo, J. DFT calculation on relaxation and electronic structure of sulfide minerals surfaces in presence of H_2O molecule. *J. Cent. South Univ.* **2014**, *21*, 3945–3954. [CrossRef]
43. Luther, G.W.; Rickard, D.T. Metal sulfide cluster complexes and their biogeochemical importance in the environment. *J. Nanop. Res.* **2005**, *7*, 389–407. [CrossRef]
44. Mal, J.; Nancharaiah, Y.V.; van Hullebusch, E.D.; Lens, P.N.L. Metal chalcogenide quantum dots: Biotechnological synthesis and applications. *RSC Adv.* **2016**, *6*, 41477–41495. [CrossRef]
45. Rosso, K.M. Reactivity of Sulfide Mineral Surfaces. *Rev. Mineral. Geochem.* **2006**, *61*, 557–607. [CrossRef]
46. Smet, P.F.; Moreels, I.; Hens, Z.; Poelman, D. Luminescence in sulfides: A rich history and a bright future. *Materials* **2010**, *3*, 2834–2883. [CrossRef]
47. Zhang, H.; Hyun, B.-R.; Wise, F.W.; Robinson, R.D. A Generic Method for Rational Scalable Synthesis of Monodisperse Metal Sulfide Nanocrystals. *Nano Lett.* **2012**, *12*, 5856–5860. [CrossRef] [PubMed]
48. Sorkin, V.; Pan, H.; Shi, H.; Quek, S.Y.; Zhang, Y.W. Nanoscale Transition Metal Dichalcogenides: Structures, Properties, and Applications. *Crit. Rev. Solid State Mater. Sci.* **2014**, *39*, 319–367. [CrossRef]
49. Acar, C.; Dincer, I.; Naterer, G.F. Review of photocatalytic water-splitting methods for sustainable hydrogen production. *Int. J. Energy Res.* **2016**, *40*, 1449–1473. [CrossRef]
50. Boles, M.A.; Ling, D.; Hyeon, T.; Talapin, D.V. The surface science of nanocrystals. *Nat. Mater.* **2016**, *15*, 141–153. [CrossRef] [PubMed]
51. Cuenya, B.R.; Behafarid, F. Nanocatalysis: Size- and shape-dependent chemisorption and catalytic reactivity. *Surf. Sci. Rep.* **2015**, *70*, 135–187. [CrossRef]
52. Frank, M.; Baumer, M. From atoms to crystallites: Adsorption on oxide-supported metal particles. *Phys. Chem. Chem. Phys.* **2000**, *2*, 3723–3737. [CrossRef]
53. Hebie, S.; Napporn, T.W.; Morais, C.; Kokoh, K.B. Size-Dependent Electrocatalytic Activity of Free Gold Nanoparticles for the Glucose Oxidation Reaction. *Chemphyschem* **2016**, *17*, 1454–1462. [CrossRef] [PubMed]
54. Liu, Y.L.; Gao, P.F.; Huang, C.Z.; Li, Y.F. Shape- and size-dependent catalysis activities of iron-terephthalic acid metal-organic frameworks. *Sci. China-Chem.* **2015**, *58*, 1553–1560. [CrossRef]
55. Mondal, J.; Trinh, Q.T.; Jana, A.; Ng, W.K.H.; Borah, P.; Hirao, H.; Zhao, Y.L. Size-Dependent Catalytic Activity of Palladium Nanoparticles Fabricated in Porous Organic Polymers for Alkene Hydrogenation at Room Temperature. *ACS Appl. Mater. Interfaces* **2016**, *8*, 15307–15319. [CrossRef] [PubMed]
56. Rozanska, X.; Fortrie, R.; Sauer, J. Size-Dependent Catalytic Activity of Supported Vanadium Oxide Species: Oxidative Dehydrogenation of Propane. *J. Am. Chem. Soc.* **2014**, *136*, 7751–7761. [CrossRef] [PubMed]
57. Alsfasser, R.; Janiak, C.; Klapötke, T.M.; Meyer, H.-J. *Moderne Anorganische Chemie*, 4th ed.; Walter de Gruyter: Berlin, Germany, 2012.
58. Greenwood, N.N.; Earnshaw, A. *Chemistry of the Elements*, 2nd ed.; Pergamon Press: Cambridge, UK, 1998.
59. Wells, A.F. *Structural Inorganic Chemistry*, 3rd ed.; Oxford University Press: Oxford, UK, 1962.
60. Müller, U. *Anorganische Strukturchemie*, 2nd ed.; Teubner Studienbuecher Chemie: Stuttgart, Germany, 1992.
61. Holleman, A.F.; Wiberg, E. *Lehrbuch der Anorganischen Chemie*, 101th ed.; W. de Gruyter & Co: Berlin, Germany, 1985.
62. Pearson, G. Hard and Soft Acids and Bases. *J. Am. Chem. Soc.* **1963**, *85*, 3533–3539. [CrossRef]

63. Cox, P.A. *Transition Metal Oxides: Introduction to Their Electronic Structure and Properties*; Oxford University Press: Oxford, UK, 1995; p. 272.
64. Shannon Radii—Atomistic Simulation Group. Available online: http://abulafia.mt.ic.ac.uk/shannon/ptable.php. (accessed on 10 December 2016).
65. Shannon, R.D. Revised Effective Ionic Radii and Systematic Studies of Interatomie Distances in Halides and Chaleogenides. *Acta Crystallogr.* **1976**, *32*, 751–767. [CrossRef]
66. Miller, T.M.; Bederson, B. Atomic and molecular polarizabilities—A review of recent advances. *Adv. At. Mol. Phys.* **1978**, *13*, 1–55.
67. Lide, D.R. *CRC Handbook of Chemistry and Physics*, 53rd ed.; CRC Press: Boca Raton, FL, USA, 1995.
68. Evans, H.T.; Konnert, J.A. Crystal structure refinement of covellite. *Am. Mineral.* **1976**, *61*, 996–1000.
69. Prener, J.S. *Nonstoichiometry in Chalcogenide Systems*; American Chemical Society: Washington, DC, USA, 1963.
70. Pedoussaut, N.M.; Lind, C. Facile Synthesis of Troilite. *Inorg. Chem.* **2008**, *47*, 392–394. [CrossRef] [PubMed]
71. Geng, B.; Liu, X.; Ma, J.; Du, Q. A new nonhydrolytic single-precursor approach to surfactant-capped nanocrystals of transition metal sulfides. *Mater. Sci. Eng. B* **2007**, *145*, 17–22. [CrossRef]
72. Geng, B.; Liu, X.; Du, Q.; Ma, J.; Liu, X. Size-dependent blue luminescent CdS nanocrystals synthesized through a single-source molecular precursor route. *Mater. Res. Bull.* **2008**, *43*, 1093–1098. [CrossRef]
73. Ludi, B.; Olliges-Stadler, I.; Rossell, M.D.; Niederberger, M. Extension of the benzyl alcohol route to metal sulfides: "Nonhydrolytic" thio sol-gel synthesis of ZnS and SnS_2. *Chem. Commun.* **2011**, *47*, 5280–5282. [CrossRef] [PubMed]
74. Qian, Y.; Su, Y.; Xie, Y.; Chen, Q.; Chen, Z. Hydrothermal preparation and characterization of nanocrystalline powder of sphalerite. *Mater. Res. Bull.* **1995**, *30*, 601–605.
75. Chen, Q.; Qian, Y.T.; Chen, Z.Y.; Shi, L.; Li, X.G.; Zhou, G.E.; Zhang, Y.H. Preparation of zinc sulfide thin films by the hydrothermal method. *Thin Solid Films* **1996**, *272*, 1–3. [CrossRef]
76. Chen, Q.; Li, X.; Qian, Y.; Zhu, J.; Zhou, G.; Zhang, W.; Zhang, Y. Photoluminescence in ultrafine zinc sulfide thin film. *Appl. Phys. Lett.* **1996**, *68*, 3582–3584. [CrossRef]
77. Li, Y.; Yi, D.; Yue, Z.; Qian, Y. Photophysical properties of ZnS quantum dots. *J. Phys. Chem. Solids* **1998**, *60*, 13–15. [CrossRef]
78. Zhang, H.; Wei, B.; Zhu, L.; Yu, J.; Sun, W.; Xu, L. Cation exchange synthesis of ZnS-Ag_2S microspheric composites with enhanced photocatalytic activity. *Appl. Surf. Sci.* **2013**, *270*, 133–138. [CrossRef]
79. Yu, S.-H.; Yang, J.; Wu, Y.-S.; Han, Z.-H.; Lu, J.; Xie, Y.; Qian, Y.-T. A new low temperature one-step route to metal chalcogenide semiconductors: PbE, Bi_2E_3 (E = S, Se, Te). *J. Mater. Chem.* **1998**, *8*, 1949–1951. [CrossRef]
80. Chen, X.; Wang, Z.; Wang, X.; Zhang, R.; Liu, X.; Lin, W.; Qian, Y. Synthesis of novel copper sulfide hollow spheres generated from copper (II)–thiourea complex. *J. Cryst. Growth* **2004**, *263*, 570–574. [CrossRef]
81. Roy, P.; Srivastava, S.K. Hydrothermal Growth of CuS Nanowires from Cu−Dithiooxamide, a Novel Single-Source Precursor. *Cryst. Growth Des.* **2006**, *6*, 1921–1926. [CrossRef]
82. Liu, Z.; Peng, S.; Xie, Q.; Hu, Z.; Yang, Y.; Zhang, S.; Qian, Y. Large-scale synthesis of ultralong Bi_2S_3 nanoribbons via a solvothermal process. *Adv. Mater.* **2003**, *15*, 936–940. [CrossRef]
83. Qian, Y.; Yu, D.; Liu, Z. Solvothermal synthesis route to one-dimensional nanostructures. *Trans. Mater. Res. Soc. Jpn.* **2004**, *29*, 2233–2238.
84. Qian, Y.T. Solvothermal synthesis of nanocrystalline III-V semiconductors. *Adv. Mater.* **1999**, *11*, 1101–1102. [CrossRef]
85. Li, Y.; Liao, H.; Ding, Y.; Fan, Y.; Zhang, Y.; Qian, Y. Solvothermal Elemental Direct Reaction to CdE (E = S, Se, Te) Semiconductor Nanorod. *Inorg. Chem.* **1999**, *38*, 1382–1387. [CrossRef]
86. Yang, J.; Zeng, J.-H.; Yu, S.-H.; Yang, L.; Zhou, G.-E.; Qian, Y.-T. Formation Process of CdS Nanorods via Solvothermal Route. *Chem. Mater.* **2000**, *12*, 3259–3263. [CrossRef]
87. Amiri, O.; Salavati-Niasari, M.; Sabet, M.; Ghanbari, D. Sonochemical method for preparation of copper indium sulfide nanoparticles and their application for solar cell. *Comb. Chem. High Throughput Screen.* **2014**, *17*, 183–189. [CrossRef] [PubMed]
88. Bang, J.H.; Suslick, K.S. Applications of Ultrasound to the Synthesis of Nanostructured Materials. *Adv. Mater.* **2010**, *22*, 1039–1059. [CrossRef] [PubMed]
89. Baranchikov, A.Y.; Ivanov, V.K.; Tretyakov, Y.D. Sonochemical synthesis of inorganic materials. *Russ. Chem. Rev.* **2007**, *76*, 133–151. [CrossRef]

90. Behboudnia, M.; Khanbabaee, B. Conformational study of CdS nanoparticles prepared by ultrasonic waves. *Colloids Surf. A Physicochem. Eng. Asp.* **2006**, *290*, 229–232. [CrossRef]
91. Wang, S.F.; Gu, F.; Lü, M.K.; Zhou, G.J.; Zhang, A.Y. Sonochemical synthesis of PbS nanocubes, nanorods and nanotubes. *J. Cryst. Growth* **2006**, *289*, 621–625. [CrossRef]
92. García-Gómez, N.A.; de la Parra-Arcieniega, S.M.; Garza-Tovar, L.L.; Torres-González, L.C.; Sánchez, E.M. Ionic liquid-assisted sonochemical synthesis of SnS nanostructures. *J. Alloy. Compd.* **2014**, *588*, 638–643. [CrossRef]
93. Gedanken, A. Using sonochemistry for the fabrication of nanomaterials. *Ultrason. Sonochem.* **2004**, *11*, 47–55. [CrossRef] [PubMed]
94. Hao, L.-X.; Chen, G.; Yu, Y.-G.; Zhou, Y.-S.; Han, Z.-H.; Liu, Y. Sonochemistry synthesis of Bi_2S_3/CdS heterostructure with enhanced performance for photocatalytic hydrogen evolution. *Int. J. Hydrog. Energy* **2014**, *39*, 14479–14486. [CrossRef]
95. Hosseini, Z.; Azizian-Kalandaragh, Y.; Khodayari, A.; Nedaee-Shakarab, B. Sonochemically prepared PbS nanostructures and investigation of their optical and structural properties. *Optoelectron. Adv. Mater.* **2014**, *8*, 201–203.
96. Kis-Csitári, J.; Kónya, Z.; Kiricsi, I. Sonochemical Synthesis of Inorganic Nanoparticles. In *Functionalized Nanoscale Materials, Devices and Systems. NATO Science for Peace and Security Series B: Physics and Biophysics*; Vaseashta, A., Mihailescu, I.N., Eds.; Springer: Dordrecht, The Netherlands, 2008; pp. 369–372.
97. Kumar, R.V.; Palchik, O.; Koltypin, Y.; Diamant, Y.; Gedanken, A. Sonochemical synthesis and characterization of Ag_2S/PVA and CuS/PVA nanocomposite. *Ultrason. Sonochem.* **2002**, *9*, 65–70. [CrossRef]
98. Lee, G.-J.; Anandan, S.; Masten, S.J.; Wu, J.J. Sonochemical Synthesis of Hollow Copper Doped Zinc Sulfide Nanostructures: Optical and Catalytic Properties for Visible Light Assisted Photosplitting of Water. *Ind. Eng. Chem. Res.* **2014**, *53*, 8766–8772. [CrossRef]
99. Lopes, P.A.L.; Santos, M.B.; Mascarenhas, A.J.S.; Silva, L.A. Synthesis of CdS nano-spheres by a simple and fast sonochemical method at room temperature. *Mater. Lett.* **2014**, *136*, 111–113. [CrossRef]
100. Murcia, M.J.; Shaw, D.L.; Woodruff, H.; Naumann, C.A.; Young, B.A.; Long, E.C. Facile Sonochemical Synthesis of Highly Luminescent ZnS−Shelled CdSe Quantum Dots. *Chem. Mater.* **2006**, *18*, 2219–2225. [CrossRef]
101. Nowak, M.; Kauch, B.; Szperlich, P.; Stróz, D.; Szala, J.; Rzychoń, T.; Bober, Ł.; Toroń, B.; Nowrot, A. Sonochemical preparation of $SbS_{(1-x)}Se_{(x)}I$ nanowires. *Ultrason. Sonochem.* **2010**, *17*, 487–493. [CrossRef] [PubMed]
102. Park, J.; Song, M.; Jung, W.M.; Lee, W.Y.; Kim, H.; Kim, Y.; Hwang, C.; Shim, I.-W. Syntheses of Cu_2SnS_3 and Cu_2ZnSnS_4 nanoparticles with tunable Zn/Sn ratios under multibubble sonoluminescence conditions. *Dalton Trans.* **2013**, *42*, 10545–10550. [CrossRef] [PubMed]
103. Salinas-Estevané, P.; Sánchez, E.M. Preparation of Sb_2S_3 Nanostructures by the Ionic Liquid-Assisted Sonochemical Method. *Cryst. Growth Des.* **2010**, *10*, 3917–3924. [CrossRef]
104. Wang, G.Z.; Geng, B.Y.; Huang, X.M.; Wang, Y.W.; Li, G.H.; Zhang, L.D. A convenient ultrasonic irradiation technique for in situ synthesis of zinc sulfide nanocrystallites at room temperature. *Appl. Phys. A* **2003**, *77*, 933–936. [CrossRef]
105. Wang, H.; Zhang, J.-R.; Zhao, X.-N.; Xu, S.; Zhu, J.-J. Preparation of copper monosulfide and nickel monosulfide nanoparticles by sonochemical method. *Mater. Lett.* **2002**, *55*, 253–258. [CrossRef]
106. Wu, G.S.; Yuan, X.Y.; Xie, T.; Xu, G.C.; Zhang, L.D.; Zhuang, Y.L. A simple synthesis route to CdS nanomaterials with different morphologies by sonochemical reduction. *Mater. Lett.* **2004**, *58*, 794–797. [CrossRef]
107. Yadav, R.S.; Mishra, P.; Mishra, R.; Kumar, M.; Pandey, A.C. Growth mechanism and optical property of CdS nanoparticles synthesized using amino-acid histidine as chelating agent under sonochemical process. *Ultrason. Sonochem.* **2010**, *17*, 116–122. [CrossRef] [PubMed]
108. Zhou, S.-M.; Zhang, X.-H.; Meng, X.-M.; Fan, X.; Lee, S.-T.; Wu, S.-K. Sonochemical synthesis of mass single-crystal PbS nanobelts. *J. Solid State Chem.* **2005**, *178*, 399–403. [CrossRef]
109. Zhu, J.; Liu, S.; Palchik, O.; Koltypin, Y.; Gedanken, A. A Novel Sonochemical Method for the Preparation of Nanophasic Sulfides: Synthesis of HgS and PbS Nanoparticles. *J. Solid State Chem.* **2000**, *153*, 342–348. [CrossRef]
110. Zhu, Y.-P.; Li, J.; Ma, T.-Y.; Liu, Y.-P.; Du, G.; Yuan, Z.-Y. Sonochemistry-assisted synthesis and optical properties of mesoporous ZnS nanomaterials. *J. Mater. Chem. A* **2014**, *2*, 1093. [CrossRef]

111. Kharazmi, A.; Saion, E.; Faraji, N.; Hussin, R.M.; Yunus, W.M.M. Structural, optical and thermal properties of PVA/CdS nanocomposites synthesized by radiolytic method. *Radiat. Phys. Chem.* **2014**, *97*, 212–216. [CrossRef]
112. Mostafavi, M.; Liu, Y.; Pernot, P.; Belloni, J. Dose rate effect on size of CdS clusters induced by irradiation. *Radiat. Phys. Chem.* **2000**, *59*, 49–59. [CrossRef]
113. Souici, A.H.; Keghouche, N.; Delaire, J.A.; Remita, H.; Mostafavi, M. Radiolytic synthesis and optical properties of ultra-small stabilized ZnS nanoparticles. *Chem. Phys. Lett.* **2006**, *422*, 25–29. [CrossRef]
114. Evans, J.E.; Jungjohann, K.L.; Browning, N.D.; Arslan, I. Controlled growth of nanoparticles from solution with in situ liquid transmission electron microscopy. *Nano Lett.* **2011**, *11*, 2809–2813. [CrossRef] [PubMed]
115. Hayes, D.; Micic, O.I.; Nenadovic, M.T.; Swayambunathan, V.; Meisel, D. Radiolytic production and properties of ultrasmall cadmium sulfide particles. *J. Phys. Chem.* **1989**, *93*, 4603–4608. [CrossRef]
116. Swayambunathan, V.; Hayes, D.; Schmidt, K.H.; Liao, Y.X.; Meisel, D. Thiol surface complexation on growing cadmium sulfide clusters. *J. Am. Chem. Soc.* **1990**, *112*, 3831–3837. [CrossRef]
117. Ni, Y.; Ge, X.; Liu, H.; Xu, X.; Zhang, Z. γ-Irradiation preparation of CdS nano-particles and their formation mechanism in non-water system. *Radiat. Phys. Chem.* **2001**, *61*, 61–64. [CrossRef]
118. Ullrich, B.; Ezumi, H.; Keitoku, S.; Kobayashi, T. Luminescence properties of p-type thin CdS films prepared by laser ablation. *Mater. Sci. Eng. B Solid State Mater. Adv. Technol.* **1995**, *35*, 117–119. [CrossRef]
119. Zhang, D.S.; Goekce, B.; Barcikowski, S. Laser Synthesis and Processing of Colloids: Fundamentals and Applications. *Chem. Rev.* **2017**, *117*, 3990–4103. [CrossRef] [PubMed]
120. Ang, H.X.; Bosman, M.; Thamankar, R.; Zulkifli, M.F.B.; Yen, S.K.; Hariharan, A.; Sudhaharan, T.; Selvan, S.T. Highly Luminescent Heterostructured Copper-Doped Zinc Sulfide Nanocrystals for Application in Cancer Cell Labeling. *Chemphyschem* **2016**, *17*, 2489–2495. [CrossRef] [PubMed]
121. Boutonnet, M.; Kizling, J.; Stenius, P.; Maire, G. The preparation of monodisperse colloidal metal particles from microemulsions. *Colloids Surf.* **1982**, *5*, 209–225. [CrossRef]
122. Chander, H. Development of nanophosphors—A review. *Mater. Sci. Eng. R Rep.* **2005**, *49*, 113–155. [CrossRef]
123. Cushing, B.L.; Kolesnichenko, V.L.; O'Connor, C.J. Recent Advances in the Liquid-Phase Syntheses of Inorganic Nanoparticles. *Chem. Rev.* **2004**, *104*, 3893–3946. [CrossRef] [PubMed]
124. Gao, L.; Wang, E.; Lian, S.; Kang, Z.; Lan, Y.; Wu, D. Microemulsion-directed synthesis of different CuS nanocrystals. *Solid State Commun.* **2004**, *130*, 309–312. [CrossRef]
125. Selvan, S.T.; Tan, T.T.Y.; Yi, D.K.; Jana, N.R. Functional and multifunctional nanoparticles for bioimaging and biosensing. *Langmuir ACS J. Surf. Colloids* **2010**, *26*, 11631–11641. [CrossRef] [PubMed]
126. Xu, S.J.; Chua, S.J.; Liu, B.; Gan, L.M.; Chew, C.H.; Xu, G.Q. Luminescence characteristics of impurities-activated ZnS nanocrystals prepared in microemulsion with hydrothermal treatment. *Appl. Phys. Lett.* **1998**, *73*, 478–480. [CrossRef]
127. Zhang, P.; Gao, L. Copper sulfide flakes and nanodisks. *J. Mater. Chem.* **2003**, *13*, 2007–2010. [CrossRef]
128. Agostiano, A.; Catalano, M.; Curri, M.L.; Della Monica, M.; Manna, L.; Vasanelli, L. Synthesis and structural characterisation of CdS nanoparticles prepared in a four-components "water-in-oil" microemulsion. *Micron* **2000**, *31*, 253–258. [CrossRef]
129. Curri, M.L.; Agostiano, A.; Manna, L.; Della Monica, M.; Catalano, M.; Chiavarone, L.; Spagnolo, V.; Lugara, M. Synthesis and characterization of CdS nanoclusters in a quarternary microemulsion: The role of the cosurfactant. *J. Phys. Chem. B* **2000**, *104*, 8391–8397. [CrossRef]
130. Fini, P.; Curri, M.L.; Castagnolo, M.; Ciampi, F.; Agostiano, A. Calorimetric study of US nanoparticle formation in w/o microemulsions. *Mater. Sci. Eng. C Biomim. Supramol. Syst.* **2003**, *23*, 1077–1081. [CrossRef]
131. Bechthold, N.; Tiarks, F.; Willert, M.; Landfester, K.; Antonietti, M. Miniemulsion polymerization: Applications and new materials. *Macromol. Symp.* **2000**, *151*, 549–555. [CrossRef]
132. Dolcet, P.; Maurizio, C.; Casarin, M.; Pandolfo, L.; Gialanella, S.; Badocco, D.; Pastore, P.; Speghini, A.; Gross, S. An Effective Two-Emulsion Approach to the Synthesis of Doped ZnS Crystalline Nanostructures. *Eur. J. Inorg. Chem.* **2015**, *2015*, 706–714. [CrossRef]
133. Landfester, K. Synthesis of colloidal particles in miniemulsions. *Annu. Rev. Mater. Res.* **2006**, *36*, 231–279. [CrossRef]
134. Landfester, K. Miniemulsions for nanoparticle synthesis. *Top. Curr. Chem.* **2003**, *227*, 75–123.
135. Landfester, K. Recent developments in miniemulsions—Formation and stability mechanisms. *Macromol. Symp.* **2000**, *150*, 171–178. [CrossRef]

136. Landfester, K. The Generation of Nanoparticles in Miniemulsions. *Adv. Mater.* **2001**, *13*, 765–768. [CrossRef]
137. Landfester, K. Miniemulsions for Nanoparticle Synthesis. In *Colloid Chemistry II*; Antonietti, M., Ed.; Springer: Berlin/Heidelberg, Germany, 2003; Volume 227, pp. 75–123.
138. Muñoz-Espí, R.; Weiss, C.K.; Landfester, K. Inorganic nanoparticles prepared in miniemulsion. *Curr. Opin. Colloid Interface Sci.* **2012**, *17*, 212–224. [CrossRef]
139. Carbone, L.; Cozzoli, P.D. Colloidal heterostructured nanocrystals: Synthesis and growth mechanisms. *Nano Today* **2010**, *5*, 449–493. [CrossRef]
140. Armelao, L.; Camozzo, D.; Gross, S.; Tondello, E. Synthesis of copper sulfide nanoparticles in carboxylic acids as solvent. *J. Nanosci. Nanotechnol.* **2006**, *6*, 401–408. [CrossRef] [PubMed]
141. Grzelczak, M.; Liz-Marzan, L.M. The relevance of light in the formation of colloidal metal nanoparticles. *Chem. Soc. Rev.* **2014**, *43*, 2089–2097. [CrossRef] [PubMed]
142. Kwon, S.G.; Hyeon, T. Colloidal Chemical Synthesis and Formation Kinetics of Uniformly Sized Nanocrystals of Metals, Oxides, and Chalcogenides. *Acc. Chem. Res.* **2008**, *41*, 1696–1709. [CrossRef] [PubMed]
143. Leon-Velazquez, M.S.; Irizarry, R.; Castro-Rosario, M.E. Nucleation and Growth of Silver Sulfide Nanoparticles. *J. Phys. Chem. C* **2010**, *114*, 5839–5849. [CrossRef]
144. Lewis, A.E. Review of metal sulphide precipitation. *Hydrometallurgy* **2010**, *104*, 222–234. [CrossRef]
145. Mudring, A.-V.; Alammar, T.; Baecker, T.; Richter, K. Nanoparticle synthesis in ionic liquids. *ACS Symp. Ser.* **2009**, *1030*, 177–188.
146. Muñoz-Espì, R.; Mastai, Y.; Gross, S.; Landfester, K. Colloidal systems for crystallization processes from liquid phase. *CrystEngComm* **2013**, *15*, 2175–2191. [CrossRef]
147. Najmaei, S.; Lou, J. Synthesis, Characterization and Engineering of Two-Dimensional Transition Metal Dichalcogenides. In Proceedings of the 2014 IEEE 14th International Conference on Nanotechnology (IEEE-Nano), Toronto, ON, Canada, 18–21 August 2014; pp. 616–619.
148. Palberg, T. Crystallization kinetics of colloidal model suspensions: Recent achievements and new perspectives. *J. Phys. Condens. Matter* **2014**, *26*, 333101. [CrossRef] [PubMed]
149. Rempel, J.Y.; Bawendi, M.G.; Jensen, K.F. Insights into the Kinetics of Semiconductor Nanocrystal Nucleation and Growth. *J. Am. Chem. Soc.* **2009**, *131*, 4479–4489. [CrossRef] [PubMed]
150. Tao, A.R.; Habas, S.; Yang, P.D. Shape control of colloidal metal nanocrystals. *Small* **2008**, *4*, 310–325. [CrossRef]
151. Thanh, N.T.K.; Maclean, N.; Mahiddine, S. Mechanisms of Nucleation and Growth of Nanoparticles in Solution. *Chem. Rev.* **2014**, *114*, 7610–7630. [CrossRef] [PubMed]
152. Warad, H.C.; Ghosh, C.K.; Hemtanon, B.; Thanachayanont, C.; Dutta, J. Luminescent nanoparticles of Mn doped ZnS passivated with sodium hexametaphosphate. *Sci. Technol. Adv. Mater.* **2005**, *6*, 296. [CrossRef]
153. Burda, C.; Chen, X.; Narayanan, R.; El-Sayed, M.A. Chemistry and Properties of Nanocrystals of Different Shapes. *Chem. Rev.* **2005**, *105*, 1025–1102. [CrossRef] [PubMed]
154. Dharsana, U.S.; Varsha, M.; Behlol, A.A.K.; Veerappan, A.; Thiagarajan, R. Sulfidation modulates the toxicity of biogenic copper nanoparticles. *RSC Adv.* **2015**, *5*, 30248–30259. [CrossRef]
155. Gonzalez-Estrella, J.; Puyol, D.; Sierra-Alvarez, R.; Field, J.A. Role of biogenic sulfide in attenuating zinc oxide and copper nanoparticle toxicity to acetoclastic methanogenesis. *J. Hazard. Mater.* **2015**, *283*, 755–763. [CrossRef] [PubMed]
156. Lee, J.H.; Kennedy, D.W.; Dohnalkova, A.; Moore, D.A.; Nachimuthu, P.; Reed, S.B.; Fredrickson, J.K. Manganese sulfide formation via concomitant microbial manganese oxide and thiosulfate reduction. *Environ. Microbiol.* **2011**, *13*, 3275–3288. [CrossRef] [PubMed]
157. Rubilar, O.; Rai, M.; Tortella, G.; Diez, M.C.; Seabra, A.B.; Duran, N. Biogenic nanoparticles: Copper, copper oxides, copper sulphides, complex copper nanostructures and their applications. *Biotechnol. Lett.* **2013**, *35*, 1365–1375. [CrossRef] [PubMed]
158. Suresh, A.K.; Doktycz, M.J.; Wang, W.; Moon, J.W.; Gu, B.H.; Meyer, H.M.; Hensley, D.K.; Allison, D.P.; Phelps, T.J.; Pelletier, D.A. Monodispersed biocompatible silver sulfide nanoparticles: Facile extracellular biosynthesis using the gamma-proteobacterium, Shewanella oneidensis. *Acta Biomater.* **2011**, *7*, 4253–4258. [CrossRef] [PubMed]
159. Jacob, J.M.; Lens, P.N.L.; Balakrishnan, R.M. Microbial synthesis of chalcogenide semiconductor nanoparticles: A review. *Microb. Biotechnol.* **2016**, *9*, 11–21. [CrossRef] [PubMed]
160. Mitzi, D.B. *Solution Processing of Inorganic Materials*; John Wiley & Sons: New York, NY, USA, 2009.

161. Diodati, S.; Dolcet, P.; Casarin, M.; Gross, S. Pursuing the Crystallization of Mono- and Polymetallic Nanosized Crystalline Inorganic Compounds by Low-Temperature Wet-Chemistry and Colloidal Routes. *Chem. Rev.* **2015**, *115*, 11449–11502. [CrossRef] [PubMed]
162. Mitzi, D.B. Solution-processed inorganic semiconductors. *J. Mater. Chem.* **2004**, *14*, 2355–2365. [CrossRef]
163. Sharma, V.K.; Filip, J.; Zboril, R.; Varma, R.S. Natural inorganic nanoparticles—Formation, fate, and toxicity in the environment. *Chem. Soc. Rev.* **2015**, *44*, 8410–8423. [CrossRef] [PubMed]
164. Balantseva, E.; Berlier, G.; Camino, B.; Lessio, M.; Ferrari, A.M. Surface Properties of ZnS Nanoparticles: A Combined DFT and Experimental Study. *J. Phys. Chem. C* **2014**, *118*, 23853–23862. [CrossRef]
165. Busca, G. The surface acidity of solid oxides and its characterization by IR spectroscopic methods. An attempt at systematization. *Phys. Chem. Chem. Phys.* **1999**, *1*, 723–736. [CrossRef]
166. Busca, G.; Lorenzelli, V. Infrared spectroscopic identification of species arising from reactive adsorption of carbon oxides on metal oxide surfaces. *Mater. Chem.* **1982**, *7*, 89–126. [CrossRef]
167. Ramis, G.; Busca, G.; Lorenzelli, V. Low-temperature CO_2 adsorption on metal oxides: Spectroscopic characterization of some weakly adsorbed species. *Mater. Chem. Phys.* **1991**, *29*, 425–435. [CrossRef]
168. Dinter, N.; Rusanen, M.; Raybaud, P.; Kasztelan, S.; da Silva, P.; Toulhoat, H. Temperature-programed reduction of unpromoted MoS_2-based hydrodesulfurization catalysts: Experiments and kinetic modeling from first principles. *J. Catal.* **2009**, *267*, 67–77. [CrossRef]
169. Vaughan, D.J.; Becker, U.; Wright, K. Sulphide mineral surfaces: Theory and experiment. *Int. J. Miner. Process.* **1997**, *51*, 1–14. [CrossRef]
170. Emin, S.; Lisjak, D.; Pitcher, M.; Valant, M. Structural and morphological transformations of textural porous zinc sulfide microspheres. *Microporous Mesoporous Mater.* **2013**, *165*, 185–192. [CrossRef]
171. Hamad, S.; Cristol, S.; Catlow, C.R.A. Surface structures and crystal morphology of ZnS: Computational study. *J. Phys. Chem. B* **2002**, *106*, 11002–11008. [CrossRef]
172. Balantseva, E.; Camino, B.; Ferrari, A.M.; Berlier, G. Effect of Post-Synthesis Treatments on the Properties of ZnS Nanoparticles: An Experimental and Computational Study. *Oil Gas Sci. Technol. Revue d'IFP Energies Nouvelles* **2015**, *70*, 817–829. [CrossRef]
173. Tasker, P.W. The stability of ionic crystal surfaces. *J. Phys. C* **1979**, *12*, 4977–4984. [CrossRef]
174. Wells, S.; Alfe, D.; Blanchard, L.; Brodholt, J.; Calleja, M.; Catloe, R.; Price, D.; Tyler, R.; Wright, K. Ab-initio simulations of magnetic iron sulphides. *Mol. Simul.* **2005**, *31*, 379–384. [CrossRef]
175. Spirko, J.A.; Neiman, M.L.; Oelker, A.M.; Klier, K. Electronic structure and reactivity of defect MoS_2I. Relative stabilities of clusters and edges, and electronic surface states. *Surf. Sci.* **2003**, *542*, 192–204. [CrossRef]
176. Hung, A.; Muscat, J.; Yarovsky, I.; Russo, S.P. Density-functional theory studies of pyrite FeS_2 (111) and (210) surfaces. *Surf. Sci.* **2002**, *520*, 111–119. [CrossRef]
177. Wen, X.D.; Ren, J.; Li, Y.W.; Wang, J.G.; Jiao, H.J. NO adsorption on triangular $Mo_{28}S_{60}$ cluster. *Chem. Phys. Lett.* **2007**, *436*, 209–212. [CrossRef]
178. Wen, X.D.; Zeng, T.; Teng, B.T.; Zhang, F.Q.; Li, Y.W.; Wang, H.G.; Jiao, H.J. Hydrogen adsorption on a Mo(27)S(54)cluster: A density functional theory study. *J. Mol. Catal. A Chem.* **2006**, *249*, 191–200. [CrossRef]
179. Temel, B.; Tuxen, A.K.; Kibsgaard, J.; Topsoe, N.Y.; Hinnemann, B.; Knudsen, K.G.; Topsoe, H.; Lauritsen, J.V.; Besenbacher, F. Atomic-scale insight into the origin of pyridine inhibition of MoS_2-based hydrotreating catalysts. *J. Catal.* **2010**, *271*, 280–289. [CrossRef]
180. Tuxen, A.; Gobel, H.; Hinnemann, B.; Li, Z.S.; Knudsen, K.G.; Topsoe, H.; Lauritsen, J.V.; Besenbacher, F. An atomic-scale investigation of carbon in MoS_2 hydrotreating catalysts sulfided by organosulfur compounds. *J. Catal.* **2011**, *281*, 345–351. [CrossRef]
181. Topsoe, N.Y.; Tuxen, A.; Hinnemann, B.; Lauritsen, J.V.; Knudsen, K.G.; Besenbacher, F.; Topsoe, H. Spectroscopy, microscopy and theoretical study of NO adsorption on MoS_2 and Co-Mo-S hydrotreating catalysts. *J. Catal.* **2011**, *279*, 337–351. [CrossRef]
182. Joshi, H.M.; Lin, Y.P.; Aslam, M.; Prasad, P.V.; Schultz-Sikma, E.A.; Edelman, R.; Meade, T.; Dravid, V.P. Effects of Shape and Size of Cobalt Ferrite Nanostructures on Their MRI Contrast and Thermal Activation. *J. Phys. Chem. C* **2009**, *113*, 17761–17767. [CrossRef] [PubMed]
183. Moses, P.G.; Grabow, L.C.; Fernandez, E.M.; Hinnemann, B.; Topsoe, H.; Knudsen, K.G.; Norskov, J.K. Trends in Hydrodesulfurization Catalysis Based on Realistic Surface Models. *Catal. Lett.* **2014**, *144*, 1425–1432. [CrossRef]

184. Li, H.; Tsai, C.; Koh, A.L.; Cai, L.L.; Contryman, A.W.; Fragapane, A.H.; Zhao, J.H.; Han, H.S.; Manoharan, H.C.; Abild-Pedersen, F.; et al. Activating and optimizing MoS_2 basal planes for hydrogen evolution through the formation of strained sulphur vacancies. *Nat. Mater.* **2016**, *15*, 48. [CrossRef] [PubMed]
185. Tsyganenko, A.A.; Can, F.; Travert, A.; Mauge, F. FTIR study of unsupported molybdenum sulfide—In situ synthesis and surface properties characterization. *Appl. Catal. A Gen.* **2004**, *268*, 189–197. [CrossRef]
186. Mauge, F.; Lamotte, J.; Nesterenko, N.S.; Manoilova, O.; Tsyganenko, A.A. FT-IR study of surface properties of unsupported MoS_2. *Catal. Today* **2001**, *70*, 271–284. [CrossRef]
187. Siriwardane, R.V.; Woodruff, S. In Situ Fourier Transform Infrared Characterization of Sulfur Species Resulting from the Reaction of Water Vapor and Oxygen with Zinc Sulfide. *Ind. Eng. Chem. Res.* **1997**, *36*, 5277–5281. [CrossRef]
188. Kendelewicz, T.; Doyle, C.S.; Bostick, B.C.; Brown, G.E. Initial oxidation of fractured surfaces of FeS_2(100) by molecular oxygen, water vapor, and air. *Surf. Sci.* **2004**, *558*, 80–88. [CrossRef]
189. Guevremont, J.M.; Bebie, J.; Elsetinow, A.R.; Strongin, D.R.; Schoonen, M.A.A. Reactivity of the (100) plane of pyrite in oxidizing gaseous and aqueous environments: Effects of surface imperfections. *Environ. Sci. Technol.* **1998**, *32*, 3743–3748. [CrossRef]
190. Guevremont, J.M.; Elsetinow, A.R.; Strongin, D.R.; Bebie, J.; Schoonen, M.A.A. Structure sensitivity of pyrite oxidation: Comparison of the (100) and (111) planes. *Am. Mineral.* **1998**, *83*, 1353–1356. [CrossRef]
191. Guevremont, J.M.; Strongin, D.R.; Schoonen, M.A.A. Thermal chemistry of H_2S and H_2O on the (100) plane of pyrite: Unique reactivity of defect sites. *Am. Mineral.* **1998**, *83*, 1246–1255. [CrossRef]
192. Blanchard, M.; Wright, K.; Gale, J.D.; Catlow, C.R.A. Adsorption of As(OH)(3) on the (001) surface of FeS_2 pyrite: A quantum-mechanical DFT study. *J. Phys. Chem. C* **2007**, *111*, 11390–11396. [CrossRef]
193. Zezza, F.; Comparelli, R.; Striccoli, M.; Curri, M.L.; Tommasi, R.; Agostiano, A.; Della Monica, M. High quality CdS nanocrystals: Surface effects. *Synth. Met.* **2003**, *139*, 597–600. [CrossRef]
194. Fini, P.; Depalo, N.; Comparelli, R.; Curri, M.L.; Striccoli, M.; Castagnolo, M.; Agostiano, A. Interactions between surfactant capped CdS nanocrystals and organic solvent. *J. Therm. Anal. Calorim.* **2008**, *92*, 271–277. [CrossRef]
195. Ingrosso, C.; Panniello, A.; Comparelli, R.; Curri, M.L.; Striccoli, M. Colloidal Inorganic Nanocrystal Based Nanocomposites: Functional Materials for Micro and Nanofabrication. *Materials* **2010**, *3*, 1316–1352. [CrossRef]
196. Curri, M.L.; Comparelli, R.; Striccoli, M.; Agostiano, A. Emerging methods for fabricating functional structures by patterning and assembling engineered nanocrystals. *Phys. Chem. Chem. Phys.* **2010**, *12*, 11197–11207. [CrossRef] [PubMed]
197. Altomare, M.; Fanizza, E.; Corricelli, M.; Comparelli, R.; Striccoli, M.; Curri, M.L. Patterned assembly of luminescent nanocrystals: Role of the molecular chemistry at the interface. *J. Nanoparticle Res.* **2014**, *16*, 2468. [CrossRef]
198. Corricelli, M.; Comparelli, R.; Depalo, N.; Fanizza, E.; Sadhu, V.B.; Huskens, J.; Agostiano, A.; Striccoli, M.; Curri, M.L. Surface Functionalized Luminescent Nanocrystals Electrostatically Assembled onto a Patterned Substrate. *Curr. Nanosci.* **2016**, *12*, 386–395. [CrossRef]
199. Buonsanti, R.; Grillo, V.; Carlino, E.; Giannini, C.; Curri, M.L.; Innocenti, C.; Sangregorio, C.; Achterhold, K.; Parak, F.G.; Agostiano, A.; et al. Seeded growth of asymmetric binary nanocrystals made of a semiconductor TiO_2 rodlike section and a magnetic gamma-Fe_2O_3 spherical domain. *J. Am. Chem. Soc.* **2006**, *128*, 16953–16970. [CrossRef] [PubMed]
200. Cozzoli, P.D. *Advanced Wet-Chemical Synthetic Approaches to Inorganic Nanostructures*; Transworld Research Network: Kerala, India, 2008; p. 453.
201. Cozzoli, P.D.; Kornowski, A.; Weller, H. Colloidal synthesis of organic-capped ZnO nanocrystals via a sequential reduction-oxidation reaction. *J. Phys. Chem. B* **2005**, *109*, 2638–2644. [CrossRef] [PubMed]
202. Cozzoli, P.D.; Manna, L. Synthetic strategies to size and shape controlled nanocrystals and nanocrystal heterostructures. In *Bio-Applications of Nanoparticles*; Chan, W.C.W., Ed.; Springer: New York, NY, USA, 2007; Volume 620, pp. 1–17.
203. Cozzoli, P.D.; Manna, L.; Curri, M.L.; Kudera, S.; Giannini, C.; Striccoli, M.; Agostiano, A. Shape and phase control of colloidal ZnSe nanocrystals. *Chem. Mater.* **2005**, *17*, 1296–1306. [CrossRef]

204. Cozzoli, P.D.; Snoeck, E.; Garcia, M.A.; Giannini, C.; Guagliardi, A.; Cervellino, A.; Gozzo, F.; Hernando, A.; Achterhold, K.; Ciobanu, N.; et al. Colloidal synthesis and characterization of tetrapod-shaped magnetic nanocrystals. *Nano Lett.* **2006**, *6*, 1966–1972. [CrossRef] [PubMed]
205. Pileni, M.P.; Cozzoli, P.D.; Pinna, N. Self-assembled supracrystals and hetero-structures made from colloidal nanocrystals. *CrystEngComm* **2014**, *16*, 9365–9367. [CrossRef]
206. Kolny-Olesiak, J.; Weller, H. Synthesis and Application of Colloidal $CuInS_2$ Semiconductor Nanocrystals. *ACS Appl. Mater. Interfaces* **2013**, *5*, 12221–12237. [CrossRef] [PubMed]
207. Weller, H. Synthesis and self-assembly of colloidal nanoparticles. *Philos. Trans. R. Soc. Lond. Ser. A* **2003**, *361*, 229–240. [CrossRef] [PubMed]
208. Weller, H. Quantum size colloids: From size-dependent properties of discrete particles to self-organized superstructures. *Curr. Opin. Colloid Interface Sci.* **1998**, *3*, 194–199. [CrossRef]
209. Weller, H. Colloidal semiconductor Q-particles: Chemistry in the transition region between solid and molecular states. *Angew. Chem. Int. Ed.* **1993**, *32*, 41–53. [CrossRef]
210. Alivisatos, A.P. Semiconductor Clusters, Nanocrystals, and Quantum Dots. *Science* **1996**, *271*, 933–937. [CrossRef]
211. Anderson, N.C.; Hendricks, M.P.; Choi, J.J.; Owen, J.S. Ligand Exchange and the Stoichiometry of Metal Chalcogenide Nanocrystals: Spectroscopic Observation of Facile Metal-Carboxylate Displacement and Binding. *J. Am. Chem. Soc.* **2013**, *135*, 18536–18548. [CrossRef] [PubMed]
212. Antonietti, M.; Niederberger, M.; Smarsly, B. Self-assembly in inorganic and hybrid systems: Beyond the molecular scale. *Dalton Trans.* **2008**, 18–24. [CrossRef]
213. Bai, F.; Wang, D.; Huo, Z.; Chen, W.; Liu, L.; Liang, X.; Chen, C.; Wang, X.; Peng, Q.; Li, Y. A Versatile Bottom-up Assembly Approach to Colloidal Spheres from Nanocrystals. *Angew. Chem. Int. Ed.* **2007**, *46*, 6650–6653. [CrossRef] [PubMed]
214. Bealing, C.R.; Baumgardner, W.J.; Choi, J.J.; Hanrath, T.; Hennig, R.G. Predicting Nanocrystal Shape through Consideration of Surface-Ligand Interactions. *ACS Nano* **2012**, *6*, 2118–2127. [CrossRef] [PubMed]
215. Bruchez, M., Jr. Semiconductor Nanocrystals as Fluorescent Biological Labels. *Science* **1998**, *281*, 2013–2016. [CrossRef] [PubMed]
216. Brus, L. Noble Metal Nanocrystals: Plasmon Electron Transfer Photochemistry and Single-Molecule Raman Spectroscopy. *Acc. Chem. Res.* **2008**, *41*, 1742–1749. [CrossRef] [PubMed]
217. Cademartiri, L.; Kitaev, V. On the nature and importance of the transition between molecules and nanocrystals: Towards a chemistry of "nanoscale perfection". *Nanoscale* **2011**, *3*, 3435–3446. [CrossRef] [PubMed]
218. Casavola, M.; Buonsanti, R.; Caputo, G.; Cozzoli, P.D. Colloidal strategies for preparing oxide-based hybrid nanocrystals. *Eur. J. Inorg. Chem.* **2008**, *2008*, 837–854. [CrossRef]
219. Comin, A.; Manna, L. New materials for tunable plasmonic colloidal nanocrystals. *Chem. Soc. Rev.* **2014**, *43*, 3957–3975. [CrossRef] [PubMed]
220. Conde, J.; Dias, J.T.; Grazú, V.; Moros, M.; Baptista, P.V.; De La Fuente, J.M. Revisiting 30 years of Biofunctionalization and Surface Chemistry of Inorganic Nanoparticles for Nanomedicine. *Front. Chem.* **2014**, *2*. [CrossRef] [PubMed]
221. Courty, A.; Fermon, C.; Pileni, M.P. "Supra crystals" made of nanocrystals. *Adv. Mater.* **2001**, *13*, 254–258. [CrossRef]
222. De Roo, J.; Baquero, E.A.; Coppel, Y.; De Keukeleere, K.; Van Driessche, I.; Nayral, C.; Hens, Z.; Delpech, F. Insights into the Ligand Shell, Coordination Mode, and Reactivity of Carboxylic Acid Capped Metal Oxide Nanocrystals. *Chempluschem* **2016**, *81*, 1216–1223. [CrossRef]
223. Fu, A.; Gu, W.; Larabell, C.; Alivisatos, A.P. Semiconductor nanocrystals for biological imaging. *Curr. Opin. Neurobiol.* **2005**, *15*, 568–575. [CrossRef] [PubMed]
224. Gaponik, N.; Eychmueller, A. Colloidal nanocrystals. On the way from synthesis to applications. *Proc. SPIE Int. Soc. Opt. Eng.* **2007**, *6785*, M7850.
225. Gomez, D.E.; Califano, M.; Mulvaney, P. Optical properties of single semiconductor nanocrystals. *Phys. Chem. Chem. Phys.* **2006**, *8*, 4989–5011. [CrossRef] [PubMed]
226. Leite, E.R. Nanocrystals assembled from the bottom up. In *Encyclopedia of Nanoscience and Nanotechnology*; Nalwa, H.S., Ed.; American Scientific Publishers: Stevenson Ranch, CA, USA, 2004; Volume 6, pp. 537–554.

227. Motte, L.; Courty, A.; Anh-Tu, N.; Lisiecki, I.; Pileni, M.-P. Self-Organization of Inorganic Nanocrystals. *Nanocryst. Form. Mesoscopic Struct.* **2006**, 1–47. [CrossRef]
228. Niu, W.X.; Xu, G.B. Crystallographic control of noble metal nanocrystals. *Nano Today* **2011**, *6*, 265–285. [CrossRef]
229. Parak, W.J.; Gerion, D.; Pellegrino, T.; Zanchet, D.; Micheel, C.; Williams, S.C.; Boudreau, R.; Le, G.M.A.; Larabell, C.A.; Alivisatos, A.P. Biological applications of colloidal nanocrystals. *Nanotechnology* **2003**, *14*, R15–R27. [CrossRef]
230. Pileni, M.P. Supracrystals of Inorganic Nanocrystals: An Open Challenge for New Physical Properties. *Acc. Chem. Res.* **2008**, *41*, 1799–1809. [CrossRef] [PubMed]
231. Pileni, M.P. Self-organization of inorganic nanocrystals. *J. Phys. Condens. Matter* **2006**, *18*, S67–S84. [CrossRef]
232. Pileni, M.P. Nanocrystals: Fabrication, organization and collective properties. *Comptes Rendus Chim.* **2003**, *6*, 965–978. [CrossRef]
233. Pileni, M.P. *Nanocrystals: Size and Shape Control*; IOS Press: Amsterdam, The Netherlands, 2003; pp. 25–31.
234. Pileni, M.P. Semiconductor Nanocrystals. In *Nanoscale Materials in Chemistry*; Klabunde, K.J., Ed.; Wiley VCH: Weinheim, Germany, 2001; pp. 61–84.
235. Pileni, M.P. Nanocrystals. In *The Chemistry of Nanostructured Material*; Yang, P., Ed.; World Scientific Publishing Co. Pte. Ltd.: Singapore, 2003; pp. 127–146.
236. Pileni, M.P. Self-assembly of inorganic nanocrystals: Fabrication and collective intrinsic properties. *Acc. Chem. Res.* **2007**, *40*, 685–693. [CrossRef] [PubMed]
237. Pileni, M.P. Self assembly of inorganic nanocrystals in 3D supra crystals: Intrinsic properties. *Surf. Sci.* **2009**, *603*, 1498–1505. [CrossRef]
238. Pileni, M.P.; Lalatonne, Y.; Ingert, D.; Lisiecki, I.; Courty, A. Self assemblies of nanocrystals: Preparation, collective properties and uses. *Faraday Discuss.* **2004**, *125*, 251–264. [CrossRef] [PubMed]
239. Polarz, S. Shape Matters: Anisotropy of the Morphology of Inorganic Colloidal Particles—Synthesis and Function. *Adv. Funct. Mater.* **2011**, *21*, 3214–3230. [CrossRef]
240. Pradhan, N.; Reifsnyder, D.; Xie, R.G.; Aldana, J.; Peng, X.G. Surface ligand dynamics in growth of nanocrystals. *J. Am. Chem. Soc.* **2007**, *129*, 9500–9509. [CrossRef] [PubMed]
241. Rogach, A.L.; Talapin, D.V.; Weller, H. *Semiconductor Nanoparticles*; Wiley-VCH Verlag GmbH & Co. KGaA: Weinheim, Germany, 2004; pp. 52–95.
242. Scher, E.C.; Manna, L.; Alivisatos, A.P. Shape control and applications of nanocrystals. *Philos. Trans. R. Soc. Lond. Ser. A* **2003**, *361*, 241–257. [CrossRef] [PubMed]
243. Shavel, A.; Gaponik, N.; Eychmueller, A. The assembling of semiconductor nanocrystals. *Eur. J. Inorg. Chem.* **2005**, 3613–3623. [CrossRef]
244. Van Embden, J.; Chesman, A.S.R.; Jasieniak, J.J. The Heat-Up Synthesis of Colloidal Nanocrystals. *Chem. Mater.* **2015**, *27*, 2246–2285. [CrossRef]
245. Wang, X.; Zhuang, J.; Peng, Q.; Li, Y. A general strategy for nanocrystal synthesis. *Nature* **2005**, *437*, 121–124. [CrossRef] [PubMed]
246. Yin, Y.; Alivisatos, A.P. Colloidal nanocrystal synthesis and the organic-inorganic interface. *Nature* **2005**, *437*, 664–670. [CrossRef] [PubMed]
247. Yuan, Q.; Wang, X. Aqueous-based route toward noble metal nanocrystals: Morphology-controlled synthesis and their applications. *Nanoscale* **2010**, *2*, 2328–2335. [CrossRef] [PubMed]
248. Weller, H. Quantized semiconductor particles: A novel state of matter for materials science. *Adv. Mater.* **1993**, *5*, 88–95. [CrossRef]
249. Weller, H. Colloidal semiconductor Q-particles: Chemistry in the transition between solid-state and molecules. *Angew. Chem.-Int. Ed. Engl.* **1993**, *32*, 41–53. [CrossRef]
250. De Roo, J.; De Keukeleere, K.; Hens, Z.; Van Driessche, I. From ligands to binding motifs and beyond; the enhanced versatility of nanocrystal surfaces. *Dalton Trans.* **2016**, *45*, 13277–13283. [CrossRef] [PubMed]
251. De Roo, J.; Van den Broeck, F.; De Keukeleere, K.; Martins, J.C.; Van Driessche, I.; Hens, Z. Unravelling the Surface Chemistry of Metal Oxide Nanocrystals, the Role of Acids and Bases. *J. Am. Chem. Soc.* **2014**, *136*, 9650–9657. [CrossRef] [PubMed]
252. Grisorio, R.; Debellis, D.; Suranna, G.P.; Gigli, G.; Giansante, C. The Dynamic Organic/Inorganic Interface of Colloidal PbS Quantum Dots. *Angew. Chem.-Int. Ed.* **2016**, *55*, 6626–6632.

253. Hens, Z.; Martins, J.C. A Solution NMR Toolbox for Characterizing the Surface Chemistry of Colloidal Nanocrystals. *Chem. Mater.* **2013**, *25*, 1211–1221. [CrossRef]
254. Hens, Z.; Van den Broeck, F.; De Roo, J.; Dierick, R.; Van Driessche, I.; Martins, J.C. Surface Chemistry of Colloidal Nanocrystals—From Semiconductors to Metal Oxides. In *Abstracts of Papers of the American Chemical Society. VOL. 248. 1155 16TH ST, NW*; Amer. Chemical Soc.: Washington, DC, USA, 2014.
255. Mews, A. Surface chemistry of semiconductor nanocrystals. *Z. Phys. Chem.* **2007**, *221*, 295–306. [CrossRef]
256. Wu, B.; Zheng, N. Surface and interface control of noble metal nanocrystals for catalytic and electrocatalytic applications. *Nano Today* **2013**, *8*, 168–197. [CrossRef]
257. Beaulac, R.; Ochsenbein, S.T.; Gamelin, D.R. Colloidal transition-metal-doped quantum dots. In *Nanocrystal Quantum Dots*; Klimov, V.I., Ed.; Taylor & Francis: New York, NY, USA, 2010; p. 397.
258. Clift, M.J.D.; Stone, V. Quantum Dots: An Insight and Perspective of Their Biological Interaction and How This Relates to Their Relevance for Clinical Use. *Theranostics* **2012**, *2*, 668–680. [CrossRef] [PubMed]
259. De Roo, J.; Van Driessche, I.; Martins, J.C.; Hens, Z. Colloidal metal oxide nanocrystal catalysis by sustained chemically driven ligand displacement. *Nat. Mater.* **2016**, *15*, 517–521. [CrossRef] [PubMed]
260. Maillard, M.; Motte, L.; Pileni, M.P. Rings and hexagons made of nanocrystals. *Adv. Mater.* **2001**, *13*, 200–204. [CrossRef]
261. Capetti, E.; Ferretti, A.M.; Dal Santo, V.; Ponti, A. Surfactant-controlled composition and crystal structure of manganese(II) sulfide nanocrystals prepared by solvothermal synthesis. *Beilstein J. Nanotechnol.* **2015**, *6*, 2319–2329. [CrossRef] [PubMed]
262. De Queiroz, A.A.A.; Martins, M.; Soares, D.A.W.; França, É.J. Modeling of ZnS quantum dots synthesis by DFT techniques. *J. Mol. Struct.* **2008**, *873*, 121–129. [CrossRef]
263. Garcia-Rodriguez, R.; Hendricks, M.P.; Cossairt, B.M.; Liu, H.T.; Owen, J.S. Conversion Reactions of Cadmium Chalcogenide Nanocrystal Precursors. *Chem. Mater.* **2013**, *25*, 1233–1249. [CrossRef]
264. Kolny-Olesiak, J. Synthesis of copper sulphide-based hybrid nanostructures and their application in shape control of colloidal semiconductor nanocrystals. *Crystengcomm* **2014**, *16*, 9381–9390. [CrossRef]
265. Sweeney, R.Y.; Mao, C.; Gao, X.; Burt, J.L.; Belcher, A.M.; Georgiou, G.; Iverson, B.L. Bacterial Biosynthesis of Cadmium Sulfide Nanocrystals. *Chem. Biol.* **2004**, *11*, 1553–1559. [CrossRef] [PubMed]
266. Armelao, L.; Bertagnolli, H.; Gross, S.; Krishnan, V.; Lavrencic-Stangar, U.; Mueller, K.; Orel, B.; Srinivasan, G.; Tondello, E.; Zattin, A. Zr and Hf oxoclusters as building blocks for the preparation of nanostructured hybrid materials and binary oxides MO_2-SiO_2 (M = Hf, Zr). *J. Mater. Chem.* **2005**, *15*, 1954–1965. [CrossRef]
267. Patel, J.D.; Mighri, F.; Ajji, A. Generalized chemical route to develop fatty acid capped highly dispersed semiconducting metal sulphide nanocrystals. *Mater. Res. Bull.* **2012**, *47*, 2016–2021. [CrossRef]
268. Bae, S.; Mannan, M.B.; Lee, W. Adsorption of cationic cetylpyridinium chloride on pyrite surface. *J. Ind. Eng. Chem.* **2012**, *18*, 1482–1488. [CrossRef]
269. Henglein, A. Colloidal silver nanoparticles: Photochemical preparation and interaction with O-2, CCl_4, and some metal ions. *Chem. Mater.* **1998**, *10*, 444–450. [CrossRef]
270. Henglein, A.; Fojtik, A.; Weller, H. Reactions on colloidal semiconductor particles. *Ber. Bunsen-Ges. Phys. Chem.* **1987**, *91*, 441–446. [CrossRef]
271. Wang, M.; Zhang, Q.; Hao, W.; Sun, Z.-X. Surface stoichiometry of zinc sulfide and its effect on the adsorption behaviors of xanthate. *Chem. Cent. J.* **2011**, *5*, 73. [CrossRef] [PubMed]
272. Wang, X.; Shi, J.; Feng, Z.; Li, M.; Li, C. Visible emission characteristics from different defects of ZnS nanocrystals. *Phys. Chem. Chem. Phys. PCCP* **2011**, *13*, 4715–4723. [CrossRef] [PubMed]
273. Zhang, H.; Huang, F.; Gilbert, B.; Banfield, J.F. Molecular Dynamics Simulations, Thermodynamic Analysis, and Experimental Study of Phase Stability of Zinc Sulfide Nanoparticles. *J. Phys. Chem. B* **2003**, *107*, 13051–13060. [CrossRef]
274. Moreels, I.; Justo, Y.; De Geyter, B.; Haustraete, K.; Martins, J.C.; Hens, Z. Size-Tunable, Bright, and Stable PbS Quantum Dots: A Surface Chemistry Study. *ACS Nano* **2011**, *5*, 2004–2012. [CrossRef] [PubMed]
275. De Roo, J.; Justo, Y.; De Keukeleere, K.; Van den Broeck, F.; Martins, J.C.; Van Driessche, I.; Hens, Z. Carboxylic-Acid-Passivated Metal Oxide Nanocrystals: Ligand Exchange Characteristics of a New Binding Motif. *Angew. Chem. Int. Ed.* **2015**, *54*, 6488–6491. [CrossRef] [PubMed]
276. Erathodiyil, N.; Ying, J.Y. Functionalization of Inorganic Nanoparticles for Bioimaging Applications. *Acc. Chem. Res.* **2011**, *44*, 925–935. [CrossRef] [PubMed]

277. Ling, D.S.; Hackett, M.J.; Hyeon, T. Surface ligands in synthesis, modification, assembly and biomedical applications of nanoparticles. *Nano Today* **2014**, *9*, 457–477. [CrossRef]
278. Lü, C.; Gao, J.; Fu, Y.; Du, Y.; Shi, Y.; Su, Z. A Ligand Exchange Route to Highly Luminescent Surface-Functionalized ZnS Nanoparticles and Their Transparent Polymer Nanocomposites. *Adv. Funct. Mater.* **2008**, *18*, 3070–3079. [CrossRef]
279. Nag, A.; Zhang, H.; Janke, E.; Talapin, D.V. Inorganic Surface Ligands for Colloidal Nanomaterials. *Z. Phys. Chem.* **2015**, *229*, 85–107. [CrossRef]
280. Smolensky, E.D.; Park, H.Y.E.; Berquó, T.S.; Pierre, V.C. Surface functionalization of magnetic iron oxide nanoparticles for MRI applications—Effect of anchoring group and ligand exchange protocol. *Contrast Media Mol. Imaging* **2011**, *6*, 189–199. [CrossRef] [PubMed]
281. Wang, X.Y.; Tilley, R.D.; Watkins, J.J. Simple Ligand Exchange Reactions Enabling Excellent Dispersibility and Stability of Magnetic Nanoparticles in Polar Organic, Aromatic, and Protic Solvents. *Langmuir* **2014**, *30*, 1514–1521. [CrossRef] [PubMed]
282. Du, Y.Y.; Yang, P.; Matras-Postolek, K.; Wang, J.P.; Che, Q.D.; Cao, Y.Q.; Ma, Q. Low toxic and highly luminescent CdSe/CdxZn1-xS quantum dots with thin organic SiO_2 coating for application in cell imaging. *J. Nanopart. Res.* **2016**, *18*, 37. [CrossRef]
283. Morgese, G.; Causin, V.; Maggini, M.; Corra, S.; Gross, S.; Benetti, E.M. Ultrastable Suspensions of Polyoxazoline-Functionalized ZnO Single Nanocrystals. *Chem. Mater.* **2015**, *27*, 2957–2964. [CrossRef]
284. Amiens, C.; Ciuculescu-Pradines, D.; Philippot, K. Controlled metal nanostructures: Fertile ground for coordination chemists. *Coord. Chem. Rev.* **2016**, *308*, 409–432. [CrossRef]
285. Ma, M.-G.; Cölfen, H. Mesocrystals—Applications and potential. *Curr. Opin. Colloid Interface Sci.* **2014**, *19*, 56–65. [CrossRef]
286. Choi, J.J.; Bealing, C.R.; Bian, K.F.; Hughes, K.J.; Zhang, W.Y.; Smilgies, D.M.; Hennig, R.G.; Engstrom, J.R.; Hanrath, T. Controlling Nanocrystal Superlattice Symmetry and Shape-Anisotropic Interactions through Variable Ligand Surface Coverage. *J. Am. Chem. Soc.* **2011**, *133*, 3131–3138. [CrossRef] [PubMed]
287. Green, M.L.H. A new approach to the formal classification of covalent compounds of the elements. *J. Organomet. Chem.* **1995**, *500*, 127–148. [CrossRef]
288. Douglas, R.N.; Williamson, C.B.; Hanrath, T.; Robinson, R.D. Surface chemistry of cadmium sulfide magic-sized clusters: A window into ligand-nanoparticle interactions. *Chem. Commun.* **2017**. [CrossRef]
289. Cölfen, H. Double-hydrophilic block copolymers: Synthesis and application as novel surfactants and crystal growth modifiers. *Macromol. Rapid Commun.* **2001**, *22*, 219–252. [CrossRef]
290. Cölfen, H. Polymer-Mediated Growth of Crystals and Mesocrystals. In *Research Methods in Biomineralization Science*; Yoreo, J.J.D., Ed.; Elsevier Science Publishing Co., Inc.: New York, NY, USA, 2013; Volume 532, pp. 277–304.
291. Cölfen, H.; Antonietti, M. Mesocrystals: Inorganic superstructures made by highly parallel crystallization and controlled alignment. *Angew. Chem. Int. Edit.* **2005**, *44*, 5576–5591. [CrossRef] [PubMed]
292. Niederberger, M.; Garnweitner, G.; Krumeich, F.; Nesper, R.; Cölfen, H.; Antonietti, M. Tailoring the Surface and Solubility Properties of Nanocrystalline Titania by a Nonaqueous In Situ Functionalization Process. *Chem. Mater.* **2004**, *16*, 1202–1208. [CrossRef]
293. Boncher, W.; Dalafu, H.; Rosa, N.; Stoll, S. Europium chalcogenide magnetic semiconductor nanostructures. *Coord. Chem. Rev.* **2015**, *289*, 279–288. [CrossRef]
294. Abbad, A.; Bentata, S.; Bentounes, H.A.; Benstaali, W.; Bouadjemi, B. Study of electronic and magnetic properties of binary zinc sulfide and ternary manganese- and iron-substituted alloys. *Mater. Sci. Semicond. Process.* **2013**, *16*, 576–581. [CrossRef]
295. Owens, F.J.; Gladczuk, L.; Szymczak, R.; Dluzewski, P.; Wisniewski, A.; Szymczak, H.; Golnik, A.; Bernhard, C.; Niedermayer, C. High temperature magnetic order in zinc sulfide doped with copper. *J. Phys. Chem. Solids* **2011**, *72*, 648–652. [CrossRef]
296. Cardinali, M.; Valentini, L.; Fabbri, P.; Kenny, J.M. Radiofrequency plasma assisted exfoliation and reduction of large-area graphene oxide platelets produced by a mechanical transfer process. *Chem. Phys. Lett.* **2011**, *508*, 285–288. [CrossRef]
297. Baruah, S.; Ortinero, C.; Shipin, O.V.; Dutta, J. Manganese Doped Zinc Sulfide Quantum Dots for Detection of Escherichia coli. *J. Fluoresc.* **2012**, *22*, 403–408. [CrossRef] [PubMed]

298. Sluydts, M.; De Nolf, K.; Van Speybroeck, V.; Cottenier, S.; Hens, Z. Ligand Addition Energies and the Stoichiometry of Colloidal Nanocrystals. *ACS Nano* **2016**, *10*, 1462–1474. [CrossRef] [PubMed]
299. Manzoor, K.; Johny, S.; Thomas, D.; Setua, S.; Menon, D.; Nair, S. Bio-conjugated luminescent quantum dots of doped ZnS: A cyto-friendly system for targeted cancer imaging. *Nanotechnology* **2009**, *20*, 065102. [CrossRef] [PubMed]
300. Mathew, M.E.; Mohan, J.C.; Manzoor, K.; Nair, S.V.; Tamura, H.; Jayakumar, R. Folate conjugated carboxymethyl chitosan—Manganese doped zinc sulphide nanoparticles for targeted drug delivery and imaging of cancer cells. *Carbohydr. Polym.* **2010**, *80*, 442–448. [CrossRef]
301. Armelao, L.; Camozzo, D.; Gross, S.; Tondello, E. Embedding of electroluminescent ZnS:Cu phosphors in PMMA matrix by polymerization of particle suspension in MMA monomer. *J. Non-Cryst. Solids* **2004**, *345–346*, 402–406. [CrossRef]
302. Hu, H.; Zhang, W. Synthesis and properties of transition metals and rare-earth metals doped ZnS nanoparticles. *Opt. Mater.* **2006**, *28*, 536–550. [CrossRef]
303. Da Silva, A.R.; Aucelio, R.Q.; Rodriguez-Cotto, R.I.; Ortiz-Martinez, M.G.; Rivera-Ramirez, E.; Frias, D.P.; Macchione, M.; Jimenez-Velez, B.; Gioda, A. Physicochemical properties and toxicological assessment of modified CdS nanoparticles. *J. Nanopart. Res.* **2014**, *16*, 2655. [CrossRef]
304. Derfus, A.M.; Chan, W.C.W.; Bhatia, S.N. Probing the Cytotoxicity of Semiconductor Quantum Dots. *Nano Lett.* **2004**, *4*, 11–18. [CrossRef]
305. Hossain, S.T.; Das, P.; Mukherjee, S.K. Toxicity of cadmium nanoparticles to Bacillus subtilis. *Toxicol. Environ. Chem.* **2013**, *95*, 1748–1756. [CrossRef]
306. Li, H.; Li, M.Y.; Shih, W.Y.; Lelkes, P.I.; Shih, W.H. Cytotoxicity Tests of Water Soluble ZnS and CdS Quantum Dots. *J. Nanosci. Nanotechnol.* **2011**, *11*, 3543–3551. [CrossRef] [PubMed]
307. Li, Z.B.; Cai, W.; Chen, X.Y. Semiconductor quantum dots for in vivo imaging. *J. Nanosci. Nanotechnol.* **2007**, *7*, 2567–2581. [CrossRef] [PubMed]
308. Murray, C.B.; Norris, D.J.; Bawendi, M.G. Synthesis and characterization of nearly monodisperse CdE (E = sulfur, selenium, tellurium) semiconductor nanocrystallites. *J. Am. Chem. Soc.* **1993**, *115*, 8706–8715. [CrossRef]
309. Su, Y.; Peng, F.; Jiang, Z.; Zhong, Y.; Lu, Y.; Jiang, X.; Huang, Q.; Fan, C.; Lee, S.-T.; He, Y. In vivo distribution, pharmacokinetics, and toxicity of aqueous synthesized cadmium-containing quantum dots. *Biomaterials* **2011**, *32*, 5855–5862. [CrossRef] [PubMed]
310. Zhang, L.S.W.; Baumer, W.; Monteiro-Riviere, N.A. Cellular uptake mechanisms and toxicity of quantum dots in dendritic cells. *Nanomedicine* **2011**, *6*, 777–791. [CrossRef] [PubMed]
311. Zhang, L.W.; Monteiro-Riviere, N.A. Mechanisms of Quantum Dot Nanoparticle Cellular Uptake. *Toxicol. Sci.* **2009**, *110*, 138–155. [CrossRef] [PubMed]
312. Feng, W.; Nie, W.; Cheng, Y.H.; Zhou, X.J.; Chen, L.; Qiu, K.X.; Chen, Z.G.; Zhu, M.F.; He, C.L. In vitro and in vivo toxicity studies of copper sulfide nanoplates for potential photothermal applications. *Nanomed. Nanotechnol. Biol. Med.* **2015**, *11*, 901–912. [CrossRef] [PubMed]
313. Tan, X.X.; Pang, X.J.; Lei, M.Z.; Ma, M.; Guo, F.; Wang, J.P.; Yu, M.; Tan, F.P.; Li, N. An efficient dual-loaded multifunctional nanocarrier for combined photothermal and photodynamic therapy based on copper sulfide and chlorin e6. *Int. J. Pharm.* **2016**, *503*, 220–228. [CrossRef] [PubMed]
314. Grozdanov, I.; Najdoski, M. Optical and Electrical Properties of Copper Sulfide Films of Variable Composition. *J. Solid State Chem.* **1995**, *114*, 469–475. [CrossRef]
315. Öztaş, M.; Bedir, M.; Necmeddin Yazici, A.; Vural Kafadar, E.; Toktamış, H. Characterization of copper-doped sprayed ZnS thin films. *Phys. B* **2006**, *381*, 40–46. [CrossRef]
316. Sperling, R.A.; Parak, W.J. Surface modification, functionalization and bioconjugation of colloidal inorganic nanoparticles. *Ther. Innov. Regul. Sci.* **2013**, *47*, 1333–1383. [CrossRef] [PubMed]
317. Kim, K.-S. Functionalization of magnetic nanoparticles for biomedical applications. *Korean J. Chem. Eng.* **2014**, *31*, 1289–1305.
318. Sapsford, K.E.; Algar, W.R.; Berti, L.; Gemmill, K.B.; Casey, B.J.; Oh, E.; Stewart, M.H.; Medintz, I.L. Functionalizing Nanoparticles with Biological Molecules: Developing Chemistries that Facilitate Nanotechnology. *Chem. Rev.* **2013**, *113*, 1904–2074. [CrossRef] [PubMed]
319. Feldgitscher, C.; Peterlik, H.; Puchberger, M.; Kickelbick, G. Structural Investigations on Hybrid Polymers Suitable as a Nanoparticle Precipitation Environment. *Chem. Mater.* **2009**, *21*, 695–705. [CrossRef]

320. Otsuka, H.; Nagasaki, Y.; Kataoka, K. PEGylated nanoparticles for biological and pharmaceutical applications. *Adv. Drug Deliv. Rev.* **2012**, *64*, 246–255. [CrossRef]
321. Thiry, M.; Boldt, K.; Nikolic, M.S.; Schulz, F.; Ijeh, M.; Panicker, A.; Vossmeyer, T.; Weller, H. Fluorescence Properties of Hydrophilic Semiconductor Nanoparticles with Tridentate Polyethylene Oxide Ligands. *ACS Nano* **2011**, *5*, 4965–4973. [CrossRef] [PubMed]
322. Stenzel, M.H. Bioconjugation Using Thiols: Old Chemistry Rediscovered to Connect Polymers with Nature's Building Blocks. *ACS Macro Lett.* **2013**, *2*, 14–18. [CrossRef]
323. Ulman, A.; Kang, J.F.; Shnidman, Y.; Liao, S.; Jordan, R.; Choi, G.Y.; Zaccaro, J.; Myerson, A.S.; Rafailovich, M.; Sokolov, J.; et al. Self-assembled monolayers of rigid thiols. *J. Biotechnol.* **2000**, *74*, 175–188. [CrossRef]
324. Guarise, C.; Pasquato, L.; De Filippis, V.; Scrimin, P. Gold nanoparticles-based protease assay. *Proc. Natl. Acad. Sci. USA* **2006**, *103*, 3978–3982. [CrossRef] [PubMed]
325. Guarise, C.; Pasquato, L.; Scrimin, P. Reversible aggregation/deaggregation of gold nanoparticles induced by a cleavable dithiol linker. *Langmuir* **2005**, *21*, 5537–5541. [CrossRef] [PubMed]
326. Mancin, F.; Prins, L.J.; Scrimin, P. Catalysis on gold-nanoparticle-passivating monolayers. *Curr. Opin. Colloid Interface Sci.* **2013**, *18*, 61–69. [CrossRef]
327. Pasquato, L.; Pengo, P.; Scrimin, P. Nanozymes: Functional nanoparticle-based catalysts. *Supramol. Chem.* **2005**, *17*, 163–171. [CrossRef]
328. Di Pietro, P.; Strano, G.; Zuccarello, L.; Satriano, C. Gold and Silver Nanoparticles for Applications in Theranostics. *Curr. Top. Med. Chem.* **2016**, *16*, 3069–3102. [CrossRef]
329. Amstad, E.; Gillich, T.; Bilecka, I.; Textor, M.; Reimhult, E. Ultrastable iron oxide nanoparticle colloidal suspensions using dispersants with catechol-derived anchor groups. *Nano Lett.* **2009**, *9*, 4042–4048. [CrossRef] [PubMed]
330. Franzmann, E.; Khalil, F.; Weidmann, C.; Schröder, M.; Rohnke, M.; Janek, J.; Smarsly, B.M.; Maison, W. A biomimetic principle for the chemical modification of metal surfaces: Synthesis of tripodal catecholates as analogues of siderophores and mussel adhesion proteins. *Chem. Eur. J.* **2011**, *17*, 8596–8603. [CrossRef] [PubMed]
331. Maison, W.; Khalil, F.; Franzmann, E. New tripodal catechol derivatives having adamantyl skeleton, useful in a method for the functionalization of surfaces. 2012.
332. Huang, X.H.; Neretina, S.; El-Sayed, M.A. Gold Nanorods: From Synthesis and Properties to Biological and Biomedical Applications. *Adv. Mater.* **2009**, *21*, 4880–4910. [CrossRef] [PubMed]
333. Jain, P.K.; Huang, X.; El-Sayed, I.H.; El-Sayed, M.A. Noble Metals on the Nanoscale: Optical and Photothermal Properties and Some Applications in Imaging, Sensing, Biology, and Medicine. *Acc. Chem. Res.* **2008**, *41*, 1578–1586. [CrossRef] [PubMed]
334. Alexandridis, P. Gold Nanoparticle Synthesis, Morphology Control, and Stabilization Facilitated by Functional Polymers. *Chem. Eng. Technol.* **2011**, *34*, 15–28. [CrossRef]
335. Alkilany, A.M.; Lohse, S.E.; Murphy, C.J. The Gold Standard: Gold Nanoparticle Libraries to Understand the Nano-Bio Interface. *Acc. Chem. Res.* **2013**, *46*, 650–661. [CrossRef] [PubMed]
336. Barnard, A.S.; Young, N.P.; Kirkland, A.I.; Van Huis, M.A.; Xu, H. Nanogold: A quantitative phase map. *ACS Nano* **2009**, *3*, 1431–1436. [CrossRef] [PubMed]
337. Boisselier, E.; Astruc, D. Gold nanoparticles in nanomedicine: Preparations, imaging, diagnostics, therapies and toxicity. *Chem. Soc. Rev.* **2009**, *38*, 1759–1782. [CrossRef] [PubMed]
338. Thanh, N.T.K.; Green, L.A.W. Functionalisation of nanoparticles for biomedical applications. *Nano Today* **2010**, *5*, 213–230. [CrossRef]
339. Cao-Milan, R.; Liz-Marzan, L.M. Gold nanoparticle conjugates: Recent advances toward clinical applications. *Expert Opin. Drug Del.* **2014**, *11*, 741–752. [CrossRef] [PubMed]
340. Daniel, M.C.; Astruc, D. Gold Nanoparticles: Assembly, Supramolecular Chemistry, Quantum-Size-Related Properties, and Applications toward Biology, Catalysis, and Nanotechnology. *Chem. Rev.* **2004**, *104*, 293–346. [CrossRef] [PubMed]
341. Gross, S. Colloidal Dispersions of Gold Nanoparticles (Invited Chapter). In *Materials Syntheses*; Springer Verlag: Wien, Austria, 2008; Volume 1.
342. Grzelczak, M.; Perez-Juste, J.; Mulvaney, P.; Liz-Marzan, L.M. Shape control in gold nanoparticle synthesis. *Chem. Soc. Rev.* **2008**, *37*, 1783–1791. [CrossRef] [PubMed]

343. Li, N.; Zhao, P.; Astruc, D. Anisotropic Gold Nanoparticles: Synthesis, Properties, Applications, and Toxicity. *Angew. Chem. Int. Ed.* **2014**, *53*, 1756–1789. [CrossRef] [PubMed]
344. Narayanan, K.B.; Sakthivel, N. Biological synthesis of metal nanoparticles by microbes. *Adv. Colloid Interface Sci.* **2010**, *156*, 1–13. [CrossRef] [PubMed]
345. Pasquato, L.; Pengo, P.; Scrimin, P. Functional gold nanoparticles for recognition and catalysis. *J. Mater. Chem.* **2004**, *14*, 3481–3487. [CrossRef]
346. Sharma, P.; Brown, S.; Walter, G.; Santra, S.; Moudgil, B. Nanoparticles for bioimaging. *Adv. Colloid Interface Sci.* **2006**, *123–126*, 471–485. [CrossRef] [PubMed]
347. Ayyad, O.; Munoz-Rojas, D.; Oro-Sole, J.; Gomez-Romero, P. From silver nanoparticles to nanostructures through matrix chemistry. *J. Nanoparticle Res.* **2010**, *12*, 337–345. [CrossRef]
348. Colomban, P. The Use of Metal Nanoparticles to Produce Yellow, Red and Iridescent Colour, from Bronze Age to Present Times in Lustre Pottery and Glass: Solid State Chemistry, Spectroscopy and Nanostructure. *J. Nano Res.* **2009**, *8*, 109–132. [CrossRef]
349. Ghaffari-Moghaddam, M.; Hadi-Dabanlou, R.; Khajeh, M.; Rakhshanipour, M.; Shameli, K. Green synthesis of silver nanoparticles using plant extracts. *Korean J. Chem. Eng.* **2014**, *31*, 548–557. [CrossRef]
350. Grancaric, A.M.; Rybicki, E.; Tarbuk, A.; Pavlovic, G.; Botteri, L. Nanoparticles of silver in antimicrobial treatment of textiles. *Tekstil* **2011**, *60*, 629–639.
351. Henglein, A. Chemisorption effects on colloidal lead nanoparticles. *J. Phys. Chem. B* **1999**, *103*, 9302–9305. [CrossRef]
352. Henglein, A.; Giersig, M. Formation of colloidal silver nanoparticles: Capping action of citrate. *J. Phys. Chem. B* **1999**, *103*, 9533–9539. [CrossRef]
353. Le Ouay, B.; Stellacci, F. Antibacterial activity of silver nanoparticles: A surface science insight. *Nano Today* **2015**, *10*, 339–354. [CrossRef]
354. Liz-Marzan, L.M. Tailoring surface plasmons through the morphology and assembly of metal nanoparticles. *Langmuir* **2006**, *22*, 32–41. [CrossRef] [PubMed]
355. Mittal, A.K.; Chisti, Y.; Banerjee, U.C. Synthesis of metallic nanoparticles using plant extracts. *Biotechnol. Adv.* **2013**, *31*, 346–356. [CrossRef] [PubMed]
356. Narayanan, K.B.; Sakthivel, N. Green synthesis of biogenic metal nanoparticles by terrestrial and aquatic phototrophic and heterotrophic eukaryotes and biocompatible agents. *Adv. Colloid Interface Sci.* **2011**, *169*, 59–79. [CrossRef] [PubMed]
357. Padmos, J.D.; Zhang, P. Surface Structure of Organosulfur Stabilized Silver Nanoparticles Studied with X-ray Absorption Spectroscopy. *J. Phys. Chem. C* **2012**, *116*, 23094–23101. [CrossRef]
358. Pastoriza-Santos, I.; Liz-Marzan, L.M. Formation and stabilization of silver nanoparticles through reduction by *N*,*N*-dimethylformamide. *Langmuir* **1999**, *15*, 948–951. [CrossRef]
359. Pastoriza-Santos, I.; Liz-Marzan, L.M. Colloidal silver nanoplates. State of the art and future challenges. *J. Mater. Chem.* **2008**, *18*, 1724–1737. [CrossRef]
360. Pileni, M.P. Fabrication and physical properties of self-organized silver nanocrystals. *Pure Appl. Chem.* **2000**, *72*, 53–65. [CrossRef]
361. Pileni, M.P. Colloidal self-assemblies used as templates to control size, shape and self-organization of nanoparticles. *Supramol. Sci.* **1998**, *5*, 321–329. [CrossRef]
362. Pileni, M.P.; Taleb, A.; Petit, C. Silver metal nanosized particles: Control of particle size, self assemblies in 2D and 3D superlattices and optical properties. *J Dispers. Sci. Technol.* **1998**, *19*, 185–206. [CrossRef]
363. Quester, K.; Avalos-Borja, M.; Castro-Longoria, E. Biosynthesis and microscopic study of metallic nanoparticles. *Micron* **2013**, *54–55*, 1–27. [CrossRef] [PubMed]
364. Rai, M.; Deshmukh, S.D.; Ingle, A.P.; Gupta, I.R.; Galdiero, M.; Galdiero, S. Metal nanoparticles: The protective nanoshield against virus infection. *Crit. Rev. Microbiol.* **2016**, *42*, 46–56. [CrossRef] [PubMed]
365. Sarkar, A.; Kapoor, S.; Mukherjee, T. Synthesis and characterisation of silver nanoparticles in viscous solvents and its transfer into non-polar solvents. *Res. Chem. Intermed.* **2010**, *36*, 411–421. [CrossRef]
366. Stamplecoskie, K.G.; Scaiano, J.C. Silver as an Example of the Applications of Photochemistry to the Synthesis and Uses of Nanomaterials. *Photochem. Photobiol.* **2012**, *88*, 762–768. [CrossRef] [PubMed]
367. Sweet, M.J.; Chesser, A.; Singleton, I. Review: Metal-Based Nanoparticles; Size, Function, and Areas for Advancement in Applied Microbiology. In *Advances in Applied Microbiology*; Sariaslani, S., Gadd, G.M., Eds.; Elsevier Science Publishing Co., Inc.: New York, NY, USA, 2012; Volume 80, pp. 113–142.

368. Zhang, C.Q.; Hu, Z.Q.; Deng, B.L. Silver nanoparticles in aquatic environments: Physiochemical behavior and antimicrobial mechanisms. *Water Res.* **2016**, *88*, 403–427. [CrossRef] [PubMed]
369. Stewart, M.H.; Susumu, K.; Mei, B.C.; Medintz, I.L.; Delehanty, J.B.; Blanco-Canosa, J.B.; Dawson, P.E.; Mattoussi, H. Multidentate poly(ethylene glycol) ligands provide colloidal stability to semiconductor and metallic nanocrystals in extreme conditions. *J. Am. Chem. Soc.* **2010**, *132*, 9804–9813. [CrossRef] [PubMed]
370. Wu, P.; Yan, X.-P. Doped quantum dots for chemo/biosensing and bioimaging. *Chem. Soc. Rev.* **2013**, *42*, 5489–5521. [CrossRef] [PubMed]
371. Yao, J.; Yang, M.; Duan, Y.X. Chemistry, Biology, and Medicine of Fluorescent Nanomaterials and Related Systems: New Insights into Biosensing, Bioimaging, Genomics, Diagnostics, and Therapy. *Chem. Rev.* **2014**, *114*, 6130–6178. [CrossRef] [PubMed]
372. Deng, Z.; Tong, L.; Flores, M.; Lin, S.; Cheng, J.X.; Yan, H.; Liu, Y. High-quality manganese-doped zinc sulfide quantum rods with tunable dual-color and multiphoton emissions. *J. Am. Chem. Soc.* **2011**, *133*, 5389–5396. [CrossRef] [PubMed]
373. Kershaw, S.V.; Susha, A.S.; Rogach, A.L. Narrow bandgap colloidal metal chalcogenide quantum dots: Synthetic methods, heterostructures, assemblies, electronic and infrared optical properties. *Chem. Soc. Rev.* **2013**, *42*, 3033–3087. [CrossRef] [PubMed]
374. Kilina, S.V.; Tamukong, P.K.; Kilin, D.S. Surface Chemistry of Semiconducting Quantum Dots: Theoretical Perspectives. *Acc. Chem. Res.* **2016**, *49*, 2127–2135. [CrossRef] [PubMed]
375. Kloepfer, J.; Mielke, R. Quantum dots as strain-and metabolism-specific microbiological labels. *Appl. Environ. Environ. Microbiol.* **2003**, *69*, 4205–4213. [CrossRef]
376. Sk, M.A.; Ananthanarayanan, A.; Huang, L.; Lim, K.H.; Chen, P. Revealing the tunable photoluminescence properties of graphene quantum dots. *J. Mater. Chem. C* **2014**, *2*, 6954–6960. [CrossRef]
377. Xie, B.; Hu, R.; Luo, X.B. Quantum Dots-Converted Light-Emitting Diodes Packaging for Lighting and Display: Status and Perspectives. *J. Electron. Packag.* **2016**, *138*, 020803. [CrossRef]
378. Weissleder, R.; Mahmood, U. Molecular Imaging. *Radiology* **2001**, *291*, 316–333. [CrossRef] [PubMed]
379. Du, Z.N.; Xu, Z.Y.; Zhang, Y.C.; Zhang, M. Solvothermal Synthesis of Mn-doped CdS Nanorods Using Single-source Molecular Precursors. In *Materials and Design, Pts 1–3*; Sang, X.M., Wang, P.C., Ai, L., Li, Y.G., Bu, J.L., Eds.; Elsevier Publishing: New York, NY, USA, 2011; Volume 284–286, pp. 667–670.
380. Joswig, J.O.; Springborg, M.; Seifert, G. Structural and electronic properties of cadmium sulfide clusters. *J. Phys. Chem. B* **2000**, *104*, 2617–2622. [CrossRef]
381. Kozhevnikova, N.S.; Vorokh, A.S.; Uritskaya, A.A. Cadmium sulfide nanoparticles prepared by chemical bath deposition. *Russ. Chem. Rev.* **2015**, *84*, 225–250. [CrossRef]
382. Ni, T.; Nagesha, D.K.; Robles, J.; Materer, N.F.; Mussig, S.; Kotov, N.A. CdS nanoparticles modified to chalcogen sites: New supramolecular complexes, butterfly bridging, and related optical effects. *J. Am. Chem. Soc.* **2002**, *124*, 3980–3992. [CrossRef] [PubMed]
383. Sharma, R. Optical studies of CdS:Mn nanoparticles. *Luminescence* **2012**, *27*, 501–504. [CrossRef] [PubMed]
384. Singh, S.; Garg, S.; Chahal, J.; Raheja, K.; Singh, D.; Singla, M.L. Luminescent behavior of cadmium sulfide quantum dots for gallic acid estimation. *Nanotechnology* **2013**, *24*, 115602. [CrossRef] [PubMed]
385. Xu, Y.L.; Xia, J.R.; Hu, B.H. Controlled growth of CdS nanoparticles in polyurushiol matrices. *Prog. Org. Coat.* **2009**, *65*, 25–29. [CrossRef]
386. Klein, C.A.; Donadio, R.N. Infrared-active phonons in cubic zinc sulfide. *J. Appl. Phys.* **1980**, *51*, 797–800. [CrossRef]
387. Gross, S.; Camozzo, D.; Di Noto, V.; Armelao, L.; Tondello, E. PMMA: A key macromolecular component for dielectric low-kappa hybrid inorganic-organic polymer films (Invited review). *Eur. Polym. J.* **2007**, *43*, 673–696. [CrossRef]
388. Sharma, R.C.; Chang, Y.A. The S-Zn (Sulfur-Zinc) System. *Phase Diagr. Eval. Sect. II* **1996**, *17*, 261–266. [CrossRef]
389. Desgreniers, S.; Beaulieu, L.; Lepage, I. Pressure-induced structural changes in ZnS. *Phys. Rev. B* **2000**, *61*, 8726–8733. [CrossRef]
390. Gilbert, B.; Huang, F.; Zhang, H.; Waychunas, G.A.; Banfield, J.F. Nanoparticles: Strained and Stiff. *Science* **2004**, *305*, 651–654. [CrossRef] [PubMed]
391. Schrage, C.; Althues, H.; Klausch, A.; Adam, D.; Kaskel, S. ZnS:Cu Polymer Nanocomposites for Thin Film Electroluminescent Devices. *J. Nanosci. Nanotechnol.* **2010**, *10*, 4335–4340. [CrossRef] [PubMed]

392. Guo, L.; Chen, S.; Chen, L. Controllable synthesis of ZnS/PMMA nanocomposite hybrids generated from functionalized ZnS quantum dots nanocrystals. *Colloid Polym. Sci.* **2007**, *285*, 1593–1600. [CrossRef]
393. Song, H.; Lee, S. Photoluminescent (CdSe) ZnS quantum dot-polymethylmethacrylate polymer composite thin films in the visible spectral range. *Nanotechnology* **2007**, *18*, 055402. [CrossRef]
394. Yuan, Y.; Krueger, M. Polymer-nanocrystal hybrid materials for light conversion applications. *Polymers* **2012**, *4*, 1–19. [CrossRef]
395. Anand, K.V.; Chinnu, M.K.; Kumar, R.M.; Mohan, R.; Jayavel, R. Thermal stability and optical properties of HMTA capped zinc sulfide nanoparticles. *J. Alloy. Compd.* **2010**, *496*, 665–668. [CrossRef]
396. Taherian, M.; Sabbagh Alvani, A.A.; Shokrgozar, M.A.; Salimi, R.; Moosakhani, S.; Sameie, H.; Tabatabaee, F. Surface-treated biocompatible ZnS quantum dots: Synthesis, photo-physical and microstructural properties. *Electron. Mater. Lett.* **2014**, *10*, 393–400. [CrossRef]
397. Yu, Z.; Ma, X.; Yu, B.; Pan, Y.; Liu, Z. Synthesis and characterization of ZnS:Mn/ZnS core/shell nanoparticles for tumor targeting and imaging in vivo. *J. Biomater. Appl.* **2013**, *28*, 232–240. [CrossRef] [PubMed]
398. Hermanson, G.T. *Bioconjugate Techniques*; Academic Press: New York, NY, USA, 2008.
399. Parfitt, G.D.; Patsis, A.V. *Organic Coatings: Science and Technology*; Marcel Dekker: New York, NY, USA, 1984.
400. Aswathy, J.; Jahnavi, S.; Krishna, R.; Manzoor, K.; Nair, S.; Menon, D. Targeted Labeling of Cancer Cells Using Biotin Tagged Avidin Functionalized Biocompatible Fluorescent Nanocrystals. *J. Nanosci. Nanotechnol.* **2011**, *11*, 7611–7620. [CrossRef] [PubMed]
401. Koneswaran, M.; Narayanaswamy, R. L-Cysteine-capped ZnS quantum dots based fluorescence sensor for Cu^{2+} ion. *Sens. Actuators B Chem.* **2009**, *139*, 104–109. [CrossRef]
402. Zhang, Y.; Peng, Q.; Wang, X.; Li, Y. Synthesis and Characterization of Monodisperse ZnS Nanospheres. *Chem. Lett.* **2004**, *33*, 1320–1321. [CrossRef]
403. Stöber, W.; Fink, A.; Bohn, E.J. Controlled growth of monodisperse silica spheres in the micron size range. *J. Colloid Interface Sci.* **1968**, *26*, 62–69. [CrossRef]
404. Li, Y.B.; Lu, W.; Huang, Q.A.; Huang, M.A.; Li, C.; Chen, W. Copper sulfide nanoparticles for photothermal ablation of tumor cells. *Nanomedicine* **2010**, *5*, 1161–1171. [CrossRef] [PubMed]
405. Kundu, J.; Pradhan, D. Controlled Synthesis and Catalytic Activity of Copper Sulfide Nanostructured Assemblies with Different Morphologies. *ACS Appl. Mater. Interfaces* **2014**, *6*, 1823–1834. [CrossRef] [PubMed]
406. Ohmasa, M.; Suzuki, M.; Takeuchi, Y. A refinement of the crystal structure of covellite, CuS. *Miner. J.* **1977**, *8*, 311–319. [CrossRef]
407. Thongtem, T.; Phuruangrat, A.; Thongtem, S. Synthesis and analysis of CuS with different morphologies using cyclic microwave irradiation. *J. Mater. Sci.* **2007**, *42*, 9316–9323. [CrossRef]
408. Chaki, S.H.; Tailor, J.P.; Deshpande, M.P. Synthesis and Characterizations of Undoped and Mn Doped CuS Nanoparticles. *Adv. Sci. Lett.* **2014**, *20*, 959–965. [CrossRef]
409. Biswas, S.; Hait, S.K.; Bhattacharya, S.C.; Moulik, S.P. Synthesis of Nanoparticles of CuI, $CuCrO_4$, and CuS in Water/AOT/Cyclohexanone and Water/TX-100 + i-Propanol/Cyclohexanone Reverse Microemulsions. *J. Dispers. Sci. Technol.* **2005**, *25*, 801–816. [CrossRef]
410. Sugimoto, T.; Chen, S.; Muramatsu, A. Synthesis of uniform particles of CdS, ZnS, PbS and CuS from concentrated solutions of the metal chelates. *Colloid Surf. A* **1998**, *135*, 207–226. [CrossRef]
411. Raevskaya, A.E.; Stroyuk, A.L.; Kuchmii, S.Y.; Kryukov, A.I. Catalytic activity of CuS nanoparticles in hydrosulfide ions air oxidation. *J. Mol. Catal. A Chem.* **2004**, *212*, 259–265. [CrossRef]
412. Lin, L.; Li, X.; Yang, Y.; Jing, L.; Yue, X.; Chen, X.; Dai, Z. Chitosan Functionalized CuS Nanoparticles Boots Gene Transfection via Photothermal Effect. *Curr. Drug. Deliv.* **2016**, *13*, 1. [CrossRef]
413. Liu, R.F.; Jing, L.J.; Peng, D.; Li, Y.; Tian, J.; Dai, Z.F. Manganese (II) Chelate Functionalized Copper Sulfide Nanoparticles for Efficient Magnetic Resonance/Photoacoustic Dual-Modal Imaging Guided Photothermal Therapy. *Theranostics* **2015**, *5*, 1144–1153. [CrossRef] [PubMed]
414. Gong, Y.Y.; Liu, Y.Y.; Xiong, Z.; Kaback, D.; Zhao, D.Y. Immobilization of mercury in field soil and sediment using carboxymethyl cellulose stabilized iron sulfide nanoparticles. *Nanotechnology* **2012**, *23*, 294007. [CrossRef] [PubMed]
415. Van Koetsem, F.; Van Havere, L.; Du Laing, G. Impact of carboxymethyl cellulose coating on iron sulphide nanoparticles stability, transport, and mobilization potential of trace metals present in soils and sediment. *J. Environ. Manag.* **2016**, *168*, 210–218. [CrossRef] [PubMed]

416. Xiong, Z.; He, F.; Zhao, D.Y.; Barnett, M.O. Immobilization of mercury in sediment using stabilized iron sulfide nanoparticles. *Water Res.* **2009**, *43*, 5171–5179. [CrossRef] [PubMed]
417. Dickinson, R.G.; Pauling, L. The crystal structure of molybdenite. *J. Am. Chem. Soc.* **1923**, *45*, 1466–1471. [CrossRef]
418. Bakunin, V.N.; Suslov, A.Y.; Kuzmina, G.N.; Parenago, O.P. Synthesis and application of inorganic nanoparticles as lubricant components—A review. *J. Nanoparticle Res.* **2004**, *6*, 273–284. [CrossRef]
419. Kumar, N.; Seminario, J.M. Computational Chemistry Analysis of Hydrodesulfurization Reactions Catalyzed by Molybdenum Disulfide Nanoparticles. *J. Phys. Chem. C* **2015**, *119*, 29157–29170. [CrossRef]
420. Yan, Y.; Xia, B.Y.; Xu, Z.C.; Wang, X. Recent Development of Molybdenum Sulfides as Advanced Electrocatalysts for Hydrogen Evolution Reaction. *ACS Catal.* **2014**, *4*, 1693–1705. [CrossRef]
421. Sun, C.; Berg, J.C. Effect of moisture on the surface free energy and acid–base properties of mineral oxides. *J. Chromatogr. A* **2002**, *969*, 59–72. [CrossRef]
422. Ferretto, L.; Glisenti, A. Study of the surface acidity of an hematite powder. *J. Mol. Catal. A Chem.* **2002**, *187*, 119–128. [CrossRef]
423. Godocikova, E.; Balaz, P.; Bastl, Z.; Brabec, L. Spectroscopic study of the surface oxidation of mechanically activated sulphides. *Appl. Surf. Sci.* **2002**, *200*, 36–47. [CrossRef]
424. Mitchell, M.B. *Fundamentals and Applications of Diffuse Reflectance Infrared Fourier Transform (DRIFT) Spectroscopy*; American Chemical Society: Washington, DC, USA, 1993; Volume 236, pp. 351–375.
425. Noei, H.; Qiu, H.; Wang, Y.; Löffler, E.; Wöll, C.; Muhler, M. The identification of hydroxyl groups on ZnO nanoparticles by infrared spectroscopy. *Phys. Chem. Chem. Phys. PCCP* **2008**, *10*, 7092–7097. [CrossRef] [PubMed]

Chapter 2.

Low temperature batch synthesis and characterization of uncapped ZnS NPs

In his comprehensive review of synthesis of nanostructured semiconductors from water solution, Jing *et al.*[36] refers to the presence of ligands as stabilizing agents as indispensable, due to their influence on particles growth and to their role in providing colloidal stability to the NPs. In the same review, however, the door is left slightly open to alternatives by suggesting that these species could be, in some examples, not needed. However, in the same comprehensive work, these examples are not reported and the literature in general lacks recent investigations on the topic. The synthesis of uncapped NPs allows to prepare samples where the surface is left exposed, possibly allowing fundamental studies on their surface chemistry, which is still vastly unexplored. Since the surface properties may be size-dependent, a method that simultaneously leaves the surface exposed and allows the size control over the final product is particularly desirable. This, of course, represents a challenge, as the capping agents are one of the major tools to control the synthesis.

Following these guiding principles, an easy water-based synthesis approach was employed for the precipitation of ZnS. Common and inexpensive salts were used as precursors, namely $Zn(NO_3)_2$ for the metal and Na_2S (sample ZnS1) and NaHS (sample ZnS2) for sulfur. In the most common approaches for the synthesis of metal sulfides NPs, the sulfur precursor solution is quickly added to the metal precursor one. This allows the sudden increase of the concentration, necessary to separate nucleation and growth. Here, this approach was inverted, as both the zinc and the sulfide solutions were cooled down with an ice bath, and the metal precursor was added dropwise to the stirred sulfide solution. This was chosen for several reasons. ZnS is known to precipitate quantitatively very quickly (< 10 μs),[58] therefore, instead of focusing on achieving a single sudden supersaturation event in the solution (which is quite difficult to achieve with such high reaction rates), a multi-step addition was preferred, while maintaining the reaction mixture conditions as stable as possible. A 2:1 S:Zn molar excess was chosen, in order to maintain a sulfur-rich environment and limit the change of pH over the course of the metal precursor addition. The low temperature was instead chosen as a simple thermostat for the reactions, in order to avoid the formation of temperature gradients. Low temperature might also play a role in limiting the oxidation of the growing material, as temperature promotes the oxidation of ZnS (see Chapter 6).

2.1 Size, structure and morphology

The presence of crystalline ZnS was firstly assessed by XRD (Figure 2.1). The patterns showed broad reflections compatible with the cubic ZnS phase sphalerite (ICSD N. 98-065-1457, space group F-34m). No other phases or contaminants were detected, excluding the possible formation during the reaction of crystalline ZnO, $Zn(OH)_2$ or other crystalline contaminants, which was reported to sometimes occur in the water synthesis of zinc chalcogenides.[40,41]

For both ZnS1 and ZnS2 samples, the collected TEM micrographs (Figure 2.1) shoed rounded aggregated NPs having low polydispersity. The formation of aggregates was expected, since in the absence of capping ligands or surfactants NPs can get in close contact. To disperse the NPs for the TEM analysis, a 1 mM solution of oleylamine in hexane was used (see Chapter 8.2) to obtain a better separation of single NPs and allowing an easier segmentation procedure for the execution of the statistical analysis on the images. This preparative technique was observed to result in the encapsulation of NPs in nano- or micro- droplets directly seen on the TEM-grid, that allowed a partial disaggregation of the aggregates. In the case of ZnS1, smaller particles were obtained, having an average diameter $D_{0,1}$ of 7.8 nm, while the ZnS2 NPs showed an average $D_{0,1}$ diameter of 18 nm. The obtained size distributions were fitted employing a log-normal distribution, that normally allows a satisfactory fit of distributions displaying a tailing towards larger dimensional values, like the ones herein reported. Relevant statistical descriptors for both raw and fitted size distributions are reported in Table 2.1.

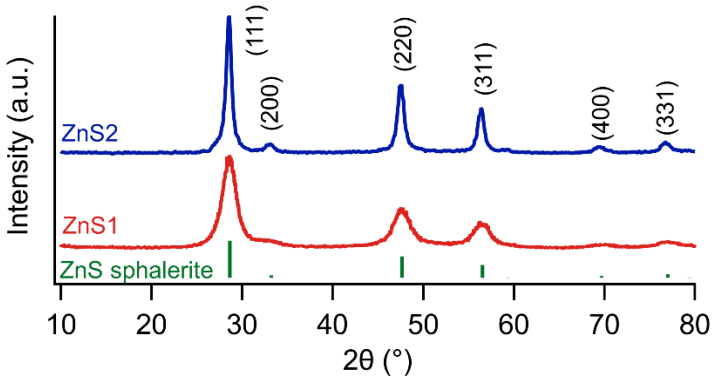

Figure 2.1 XRD diffraction pattern of samples ZnS1 and ZnS2 with indication of the reflection ZnS sphalerite (stick plot)

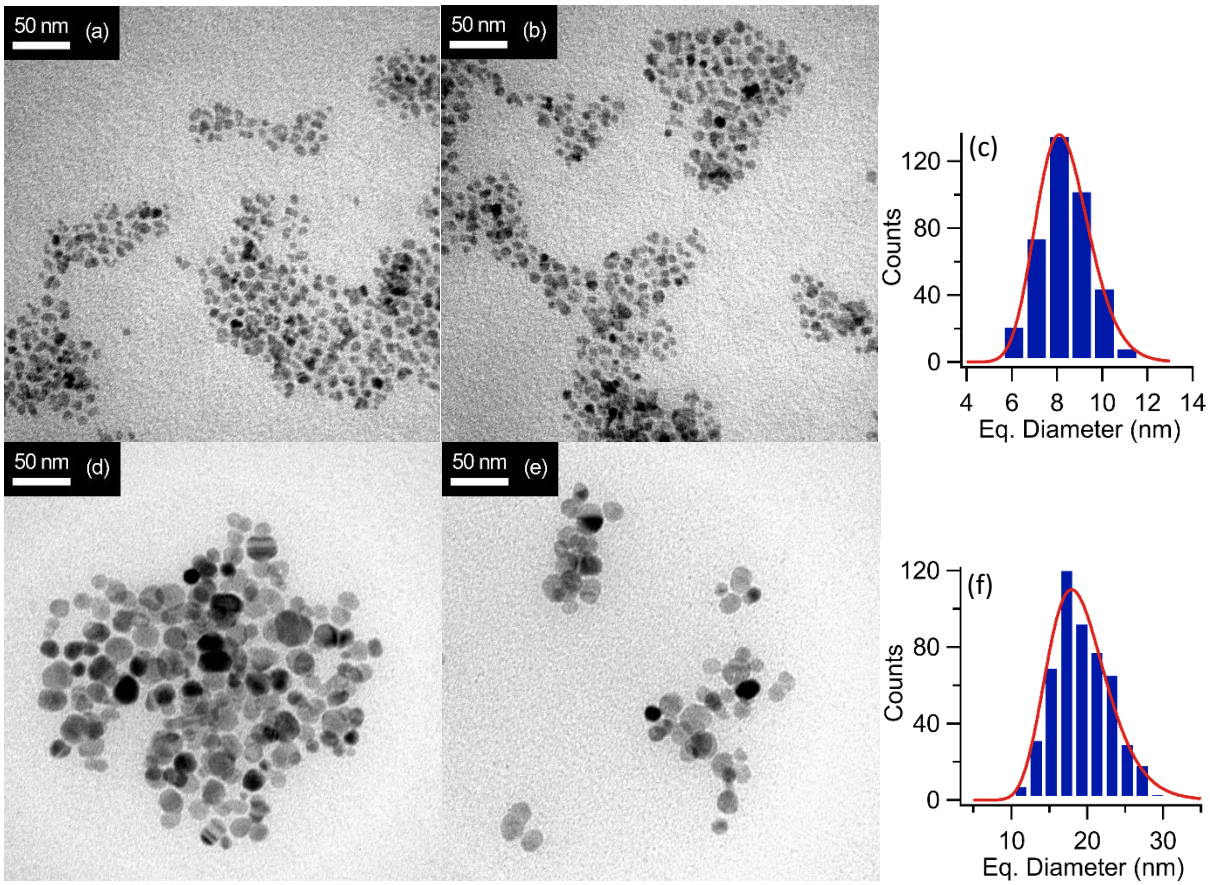

Figure 2.2 TEM micrographs of NPs retrieved in the samples ZnS1 (a, b) and ZnS2 (d, e). Fitted equivalent spherical diameter distributions obtained from the statistical analysis of the micrographs for sample ZnS1 (c) and ZnS2 (f).

Table 2.1 size distribution descriptors obtained from TEM population of sampled particles, from TEM distribution fitting and from the refinement on XRD data. The result obtained applying the Scherrer formula on the (111) reflection is reported for comparison with the indication of the variation with respect to the value obtained from the TEM analysis. GoF = goodness of fit; SF = stacking faults.

	ZnS1				ZnS2			
	TEM	TEM-fitted	Refined	Scherrer	TEM	TEM-fitted	Refined	Scherrer
$D_{1,0}$ (nm)[b]	7.8	8.4	8.1		18	19	17.9	
Std. dev. (nm)	1.2 (16%)	1.2 (14%)	0.7 (9%)		4 (22%)	4 (21%)	2.7 (15%)	
$D_{3,2}$ (nm)[b]	8.1	8.7	8.2		20	21	18.7	
$D_{4,3}$ (nm)[b]	8.3	8.9	8.2	4.7 (-42%)	21	22	19.1	12 (-33%)
Skewness	0.1	0.4	0.3		0.4	0.7	0.5	
Kurtosis	0.5	0.3	0.1		0.2	0.8	0.4	
GoF			1.6				1.7	
SF probability			0.04				0.01	

[b] Average diameter values are referred as $D_{n,m}$, being the ratio of the n^{th} over the m^{th} moments about zero of the considered distribution. $D_{1,0}$ = numeric average; $D_{2,3}$ = surface-weighted average, $D_{4,3}$ = volume-weighted average.

The analysis of the size distribution was extended with the calculation of several descriptors not only as a more detailed analysis of the retrieve size distribution, but also to allow the comparison with other techniques (like microstructural information obtained from the XRD analysis), that provides different averages in respect to the number-weighted one $D_{1,0}$. The difference between different averages is increased as the size distribution get wider, thus it is generally important to compare the correct values unless the size distribution is particularly sharp.

Noteworthy, despite the absence of any added capping ligand to control the final size and polydispersity, small NPs were straightforwardly obtained with only a relative standard deviation of 16% (ZnS1) and 22% (ZnS2) for the distribution of diameters. Even though these particles cannot be referred as monodisperse, for which a relative standard deviation below 5% is generally required,[10] the obtained size distribution with no influence of capping ligands still indicates a good degree of control over the size dispersion. In the framework of the growth theory described by Talapin *et al.*,[51] this can be interpreted as a prevalence of the diffusion-controlled growth regime. The two samples also clearly displayed two different average sizes. Since the only difference between the two samples was the sulfur precursor (Na_2S for ZnS1 and NaHS for ZnS2), the reason of this effect can be attributed to the different pH of the 0.2 M sulfide solutions employed in the synthesis (13.0 to 11.3 respectively). This indicates a pH-dependent growth of the particles, that was also previously reported in ligand-aided synthesis of the same material.[83] This result suggests the opportunity to control the final average NPs size in the range from 18 to 8 nm by simply tuning the relative concentration of the two precursors in the sulfide precursor solution. Moreover, adjusting the pH to values higher than 11.3 by adding an acid could allow to obtain even larger NPs.

Since the TEM analysis implicitly offers a limited view of the samples, being the micrographs typically limited to few hundreds of particles, microstructural information was also assessed by the refinement of the obtained XRD patterns, using the software MAUD.[84] In this approach, the whole pattern is fitted, allowing the extraction of microstructural data mainly from reflections broadening, and therefore assessing the properties of the whole bulk of the samples. In particular, the line profile fitting developed by Popa and Balzar was employed.[85] The structural model employed in the fitting was provided from data available in the literature for bulk ZnS.[86] More details on the fitting procedure is available in Chapter 8.1. Like many II-VI and III-V semiconductors, ZnS has a remarkable tendency to from planar defects like stacking faults.[87,88] This is likely due to the presence of two polymorphs, a cubic one (sphalerite) and a hexagonal one (wurtzite). These structures shares the same tetrahedral unit ZnS_4, but having staggered or eclipsed configuration respectively, that have a minimal energy difference.[88]

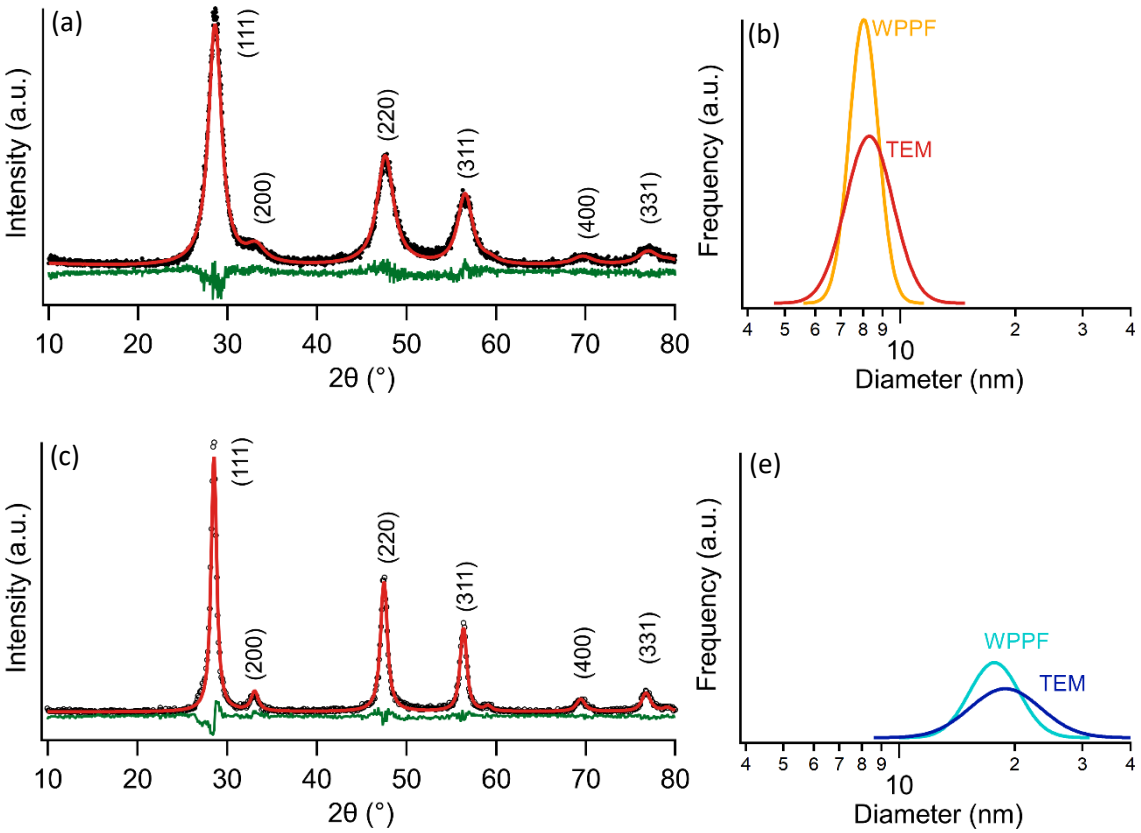

Figure 2.3 Refined XRD profiles of samples (a) ZnS1 and (b) ZnS2. Comparison on a same frequency scale of the log-normal diameter distributions obtained from TEM and XRD fitting (ZnS1: b. ZnS2: e).

The presence of such defects in these samples can also be qualitatively inferred by the marked asymmetry of the (111) reflection and from the anomalous broadening of the (200) reflection, that became almost a shoulder of the (111) reflection in the case of the ZnS1 sample (Figure 2.3a). Since the presence of planar defect alters both the profile and position of XRD reflections non-monotonically, their presence was included in the model employing the Warren model.[89] The obtained fittings reported in Figure 2.3 visually shows the good quality of the model, as also indicated by the GoF (goodness of fit) values of 1.6 and 1.7 for ZnS1 and ZnS2, respectively. Being the GoF close to unity, very little room for improvement of the model is left, as introducing new parameters may result in the overparameterization of the problem if the data quality is not improved by using more advanced equipment for the diffraction experiment.[90] From both the distributions reported in Figure 2.3b,e, and the relative descriptors reported in Table 2.1, a very good agreement between the results obtained by TEM and XRD analysis was evident. To better show the quality improvement of such analysis in comparison with the routinely employed[91–95] Scherrer formula, the results (to be compared with the $D_{4,3}$ average) obtained from the latter is also reported in Table 2.1. By neglecting the implicit limitations of using the just Scherrer formula, a strong underestimation of the crystallite size (here likely equivalent to the NP geometrical size) of -42% and -33% was obtained. In other words, limiting the

analysis to the application of the Scherrer formula, the true average size could be almost double the estimated size, possibly providing misleading result, and compromising also further analyses (e.g. the interpretation of size-dependent properties). This limitation can be especially dangerous for samples like the ones here analyzed, since aggregation phenomena may prevent a reliable dimensional analysis from TEM micrographs. The stacking faults probability obtained from the Warren model was 0.04 for ZnS1 and 0.01 for ZnS2. This is of course coherent with the larger error obtained from the Scherrer formula in the case of ZnS1, as the larger presence of stacking faults contributes more to the broadening of reflections with respect to ZnS2. Significantly different unit cell length was also obtained for the two samples. The value a = 5.4157 Å was retrieved for ZnS1, while for ZnS2 a = 5.3962 Å. The size-dependent shrinkage of the unit cell of ZnS NPs was explained by Khalkhali *et al.*[96], that described the NPs structure with a 3-phase model, where the external layers of materials are deformed as consequence of the under-coordination of atoms exposed to the surface. As a consequence, a macrostrain (i.e. a variation of the size of all the unit cells in the material) is induced on the internal crystalline core. Being surface-dependent, this macrostrain is also size-dependent and its magnitude is expected to increase with the specific surface area (SSA) of the particles. Therefore, for NPs having a size smaller than roughly 10 nm, the size-induced macrostrain effect is expected to be found.

The performed analysis indicated that the pH of the employed solution did not only resulted in different NPs average size, but also played a role in the regularity of the crystal structure, as an increased probability of stacking faults was retrieved in the case of the smaller ZnS1 NPs. The presence of these planar defects also strongly influences the broadening of XRD reflections, making the assessment of the crystallite size by the employment of the Scherrer formula inherently inaccurate. Interestingly, the higher stacking faults probability was retrieved in the sample having the smaller size. This may be related to the decreasing difference in energy between the cubic and the hexagonal polymorph of ZnS as NPs size decreases.[97]

2.2 Surface analysis

An important step in the characterization of ZnS, and of metal sulfides in general, deals with the surface of the material. Metal sulfides are known to be easily oxidized (see Chapter 6), so it is important to check if the synthetic approach employed is suitable to obtain the pure unoxidized material. This is especially important in view of applications that rely on the interaction of the material with the surrounding environment, like catalysis of for the development of functionalization strategies for biomedical applications[98] (see Chapter 1.3). Since the NPs here synthetized were free of capping

ligands, these samples also offer the opportunity to study the surface composition without interference.

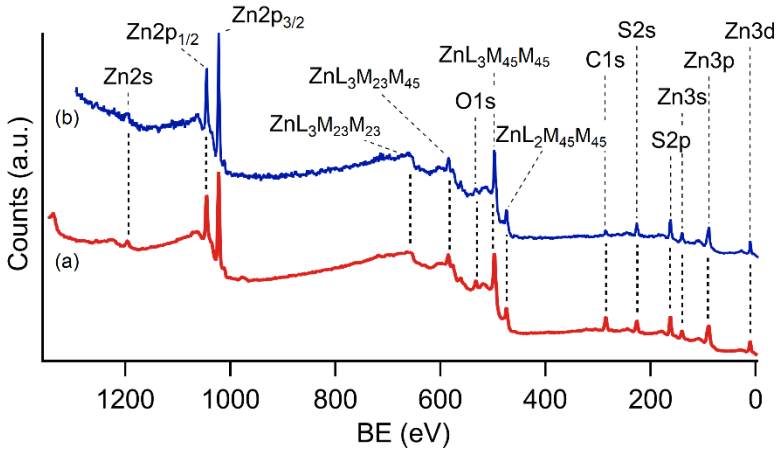

Figure 2.4 XPS survey spectra of samples ZnS1 (a) and ZnS2 (b).

Table 2.2 Observed peaks position in the XPS spectra of ZnS samples.

Peak	ZnS1 (eV)	ZnS2 (eV)	Reference[99]
Zn2s	1196.6	1197.4	1196
Zn2p3/2	1021.7	1021.9	1021.7 - 1022.0
Zn3s	139.8	139.8	141.5 - 139.9
Zn3p	86.6	88.6	88.4
Zn3d	10.2	10.2	9.8 -10.7
S2s	226.2	226.2	225.6 - 226.3
S2p	161.5	161.5	161.9 - 162.2
ZnAP-2p3/2,L3M45M45(1G)	2011.4	2011.4	2011.3 - 2011.9

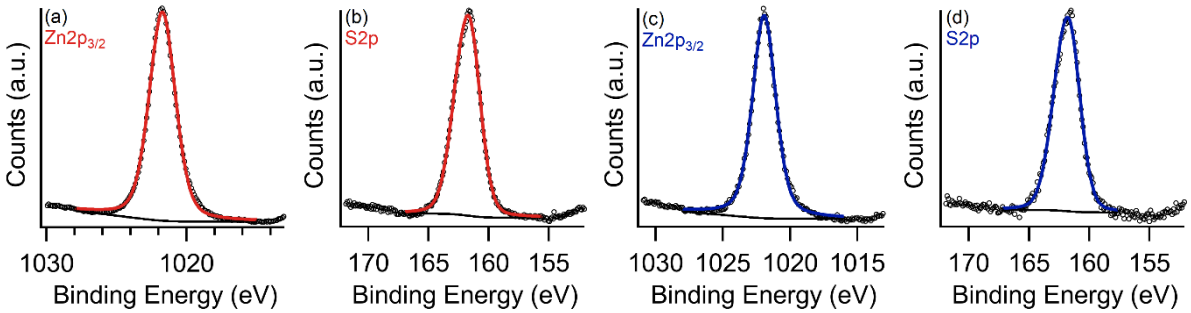

Figure 2.5 Fitting of the XPS $Zn2p_{3/2}$ (a) and S2p (b) peaks of the ZnS1 sample. Fitting of the XPS $Zn2p_{3/2}$ (c) and S2p (d) peaks of the ZnS2 sample.

XPS was chosen as a surface-sensitive technique, to analyze the surface composition of the samples. It is worth to mention that, due to the small size of the NPs, in the case of sample ZnS1 XPS also gives information on the bulk composition. From the survey spectra (Figure 2.4), only the presence of Zn, S,

C and O was evident. The presence of peaks of C and O resulting from adventitious surface contamination is commonly observed for samples that were not synthetized and stored under special high vacuum conditions.[100] The presence of the C1s signal was used to correct XPS spectra for charging effects on the calculated BE by assigning to the peak the value of 284.6 eV.[98] The position of the O1s peak, found at 532.0 eV for ZnS1 and 532.2 eV for ZnS2, cannot be attributed to surface ZnO (found at 530 eV, see Chapter 6) but is likely to arise from surface-adsorbed water molecules. The semi-quantitative analysis based on the $Zn2p_{3/2}$ and S2p peaks provided a Zn:S atomic ratio of 1:0.9 for both samples, that lies close to the stoichiometric expected value of 1:1. This slight deviation from the stochiometric ratio could be related to presence of sulfur vacancies, as previously reported for ZnS.[101] The presence of a cation-rich layer on the surface was also reported as a common feature for many small semiconductor NPs synthetized in water.[36] The modified Auger parameter (AP) was also calculated to further confirm the proposed interpretation of the spectra, using the $Zn2p_{3/2}$ and the $ZnL_3M_{45}M_{45}$ peaks. The resulting value of 2011.4 eV is compatible with literature values for ZnS.[99] The presence of Zn^{2+} was confirmed by the presence of the $Zn2p_{3/2}$ peak at 1021.7 eV for the ZnS1 sample and 1021.9 eV for the ZnS2 sample (Figure 2.5a,c), while the peak at 161.5 (Figure 2.5b,d) is typical of the S2p signal of S^{2-}.[102] Noteworthy, no further components in the S2p region were observed, ruling out the presence of a relevant surface oxidation for both samples, despite the synthesis were carried out in water, and without employing special degassing procedure other than the simple use of milliQ-quality water.

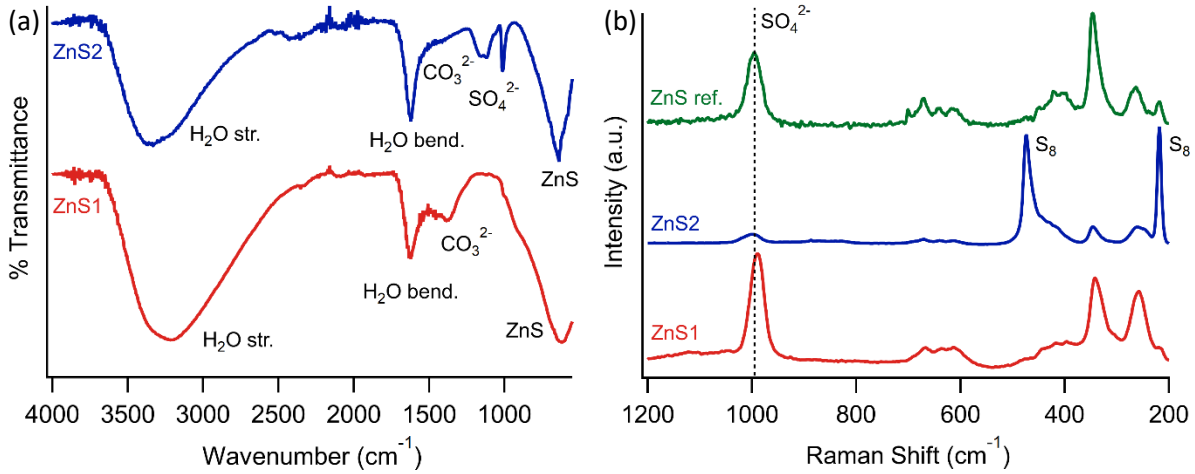

Figure 2.6 (a) FTIR spectra of samples ZnS1 and ZnS2. (b) Raman spectra of samples ZnS1 and ZnS2 compared to a reference spectra of 21 nm ZnS NPs.

The identification of surface moieties or adsorbed species on ZnS NPs was carried out by employing FTIR spectroscopy (Figure 2.6a). In both spectra the presence of adsorbed water was evident from the presence of the characteristic broad HOH stretching peak (ZnS1: 3219 cm^{-1}, ZnS2: 3348 cm^{-1}) and the

HOH bending peak (ZnS1: 1626 cm^{-1}, ZnS2: 1623 cm^{-1}). A shift towards lower wavenumbers of the maximum of the HOH stretching peak was observed for sample ZnS1 in comparison with sample ZnS2. Considering it was calculated that this peak shifts at lower wavenumber as the binding strength with the ZnS surface increases, a size-dependent binding strength of the adsorbed water can be inferred.[103] In particular, water appears to bind the surface more strongly as the NPs size decrease. Alternatively, the same effect can be explained as a reduced water coverage in sample ZnS1.[103] In the spectrum of ZnS2 two peaks at 1012 cm^{-1} and 1141 cm^{-1} were visible, that were possibly related to sulfates formed on the NPs surface. It was possible to rule out the presence of sulfites, as this moiety produces a set of peaks ranging from 1000 to 1100 cm^{-1} having a peculiar line shape.[104] From the position of the observable peaks, the geometry of interaction of sulfates can be inferred, thanks to the different point symmetry associated with different interaction modes.[105,106] In the ZnS1 spectra, the sharp peak at 1016 cm^{-1} can be attributed to the non-degenerate (single) symmetric stretching mode of the sulfate, while the broader signal at 1134 cm^{-1} can be attributed to the overlap of three non-degenerate (single) asymmetric stretching modes. Indeed, the presence of three overlapping components was observed from the line shape of the peak at roughly 1068, 1122 and 1157 cm^{-1}. This pattern can be attributed to sulfates having a C_{2v} symmetry, which is possible with two interaction modes: mononuclear or binuclear (bridging) bidentate. To distinguish between the two, a comparison with sulfate metal complexes was done, suggesting that the binuclear (bridging) bidentate coordination was preferred.[104] Since the presence of sulfates was not detected by XPS analysis, the concentration of this species on the surface was below the XPS detection limit of 0.1% at. Therefore, only traces of sulfates were found on ZnS2. On the contrary, ZnS1 sample showed the complete absence of sulfates by both XPS and FTIR analysis, confirming the complete lack of bulk and surface oxidation on the sample. In the ZnS1 sample, a peak at 1380 cm^{-1} was visible, that was also found in the spectra of the ZnS2 sample as shoulder of the HOH bending peak at around 1408 cm^{-1}. These signals may be attributed to carbonates interacting with the surface.[107] As it was established that CO_2 is not capable of a direct interaction with the ZnS surface, and no ZnO was retrieved by the analyses, the formation of carbonates was likely related to the interaction of atmospheric CO_2 with the adsorbed water molecules.[103] In both spectra no peaks belonging to -SH or -OH moieties was observed, in opposition to the infrared characterization carried out by Hertl on bulk ZnS samples.[108] The strong peak visible at low frequencies (ZnS1: 638 cm^{-1}, ZnS: 623 cm^{-1}) was identified as the overtone of the transversal optical mode TO at the X critical point of the Brillouin zone of the ZnS structure.[109]

To complement the FTIR analysis, Raman spectroscopy was performed on the samples (Figure 2.6b). For ZnS1, the expected first and second order Raman spectra of cubic ZnS were observed (Table 2.3). Additionally, a sharp peak at 989 cm^{-1} was also seen, which can be attributed to the Raman-active asymmetric stretching mode of surface sulfates.[104] However, the intensity of the peak was also

observed to increase during the analysis. Therefore, sulfates are likely to form during the analysis, because of the laser-induced sample heating. Indeed, ZnS was found to be susceptible to oxidation even after exposure to moderately high temperatures, as discussed in Chapter 6. Comparing the Raman spectrum of sample ZnS1 with the reference spectrum obtained from ZnS NPs of 21 nm obtained using an established hydrothermal approach,[103] an increase in the relative intensity of the TO mode at 258 cm^{-1} was observed. The first order LO and TO peaks also showed a shift towards lowers values, as reported in Table 2.3. This phenomenon was generally referred as phonons softening and was associated to quantum confinements effects arising from the small size of the NPs.[109,110] A shoulder to the LO mode was also visible, that might be generated by surface phonons (SO modes). Surface phonons are similar to their bulk counterparts, but they are generated by the peculiar vibrational properties of the sub-coordinated topmost surface atoms. As the intensity of SO modes depend on the specific surface area available, their presence was found in small ZnS NPs as an effect of the increase of surface to volume ratio.[110,111] Another visible size-related phenomenon was the broadening of the phononic peaks due to the relaxation of selection rules for the Raman scattering.[110]

Table 2.3 Peaks attribution of the Raman spectra of ZnS1 and ZnS2 samples compared with reference sample (ZnS 21 nm NPs) and values from the literature.

Peak	ZnS1 (cm^{-1})	ZnS2 (cm^{-1})	ZnS 21 nm (cm^{-1})	References[109,112] (cm^{-1})
TO	258	258	264	278, 275
LO	342	346	347	354, 350
2(0) on W	216	-	218	218, 219
TO+LA	396	-	399	401, 386
TO+LA	417	-	421	424, 422
2(0) on W	442	-	449	458, 448
2(TO)	611	612	612	618, 612
2(TO)	636	639	641	643, 636
2(TO)	667	671	671	677, 665

The Raman spectrum of the ZnS2 sample was dominated by the presence of orthorhombic sulfur S_8.[113] Its presence on the sample might be related to the excess of sulfur precursors employed in the synthesis, or it can be a result of photodegradation of the sample due to the laser irradiation. Sulfur peaks were found unaltered recording the Raman spectra either at low or high laser power. A similar phenomenon was observed for the MnS sample synthetized with the NaHS precursor (Chapter 3.3) and in some Raman spectra of ZnS NPs synthetized via CHFS (Chapter 5.1). The presence of ZnS was revealed by the TO peak at 346 cm^{-1} and the LO peak at 258 cm^{-1}, and by a group of second order signals ranging from 570 to 700 cm^{-1}.[109,112]

From the surface analysis, the complete absence of oxidation was retrieved for the ZnS1, while only minor traces of sulfates were observed for sample ZnS2, despite the syntheses were performed in water and without degassing the solvent. This indicates that the simple ligand-free method here used allowed a good control over both NPs size and composition. The complete lack of oxidation was remarkable, as it indicates a rather strong chemical resistance of the ZnS surface under conventional storage conditions, as samples were not stored under inert atmosphere. The observed stability against oxidation at room temperature might be related to the relatively abundant presence of water, that can significatively alter the surface reactivity of ZnS,[103] and may act as a passivating layer. Indeed, it was noticed as the sample showing a stronger bonding with water molecules, on the basis of the FTIR analysis, was also the one not showing any trace of oxidation. The surface of the NPs was found to be Zn-rich, as commonly reported for many metal chalcogenides synthetized by water-based approaches.[36]

2.3 Time resolved *in-situ* SAXS analysis

In-situ techniques offers many opportunities to study wet-chemistry approaches for the synthesis of NPs, as they allow to shed light on the time evolution of the studied system, overcoming many limitations of typical *ex-situ* characterization techniques. To study the evolution of the ZnS NPs synthesized with the proposed ligand-free approach, Small Angle X-Ray Scattering (SAXS) was chosen, as it allows to assess many relevant features of NPs like size and size distribution, shape and aggregation state.[114]

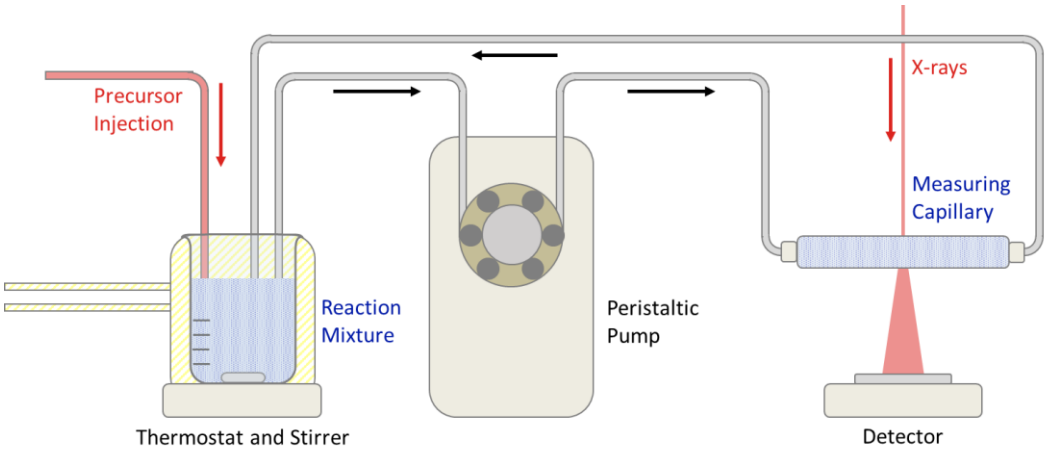

Figure 2.7 Schematic representation of the realized setup for the in-situ SAXS analysis.

The experiment was conducted at the SAXS beamline of Elettra Sincrotrone Trieste. The employed setup consisted in a thermostated reaction vessel equipped with a common magnetic stirring plate, a

syringe pump to allow a controlled introduction of the second precursor solution and a flow system that allowed the circulation of the reaction mixture through a measuring quartz capillary. The flow system was using a peristaltic pump capable and the total residence time was of 6 s. X-rays extracted from the synchrotron ring were monochromated at 16 eV and focused with a double toroidal mirror on the measuring quartz capillary. The final reciprocal space window available ranged from 0.1 to 6 nm^{-1}. SAXS profiles were collected with a 10 s time step with 8 s acquisition time. Water flowed through the measuring capillary was used as background. The zinc precursor was injected in the reaction vessel at a rate of 2 ml/min while keeping a vigorous stirring to simulate the procedure commonly employed during the synthesis of sample ZnS1.

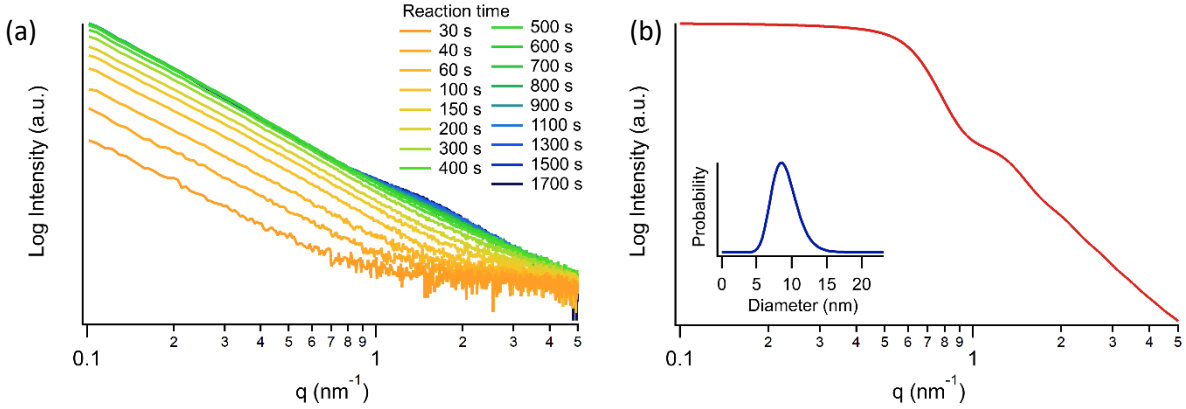

Figure 2.8 (a) Evolution of the SAXS profile followed in-situ during the ZnS batch synthesis. (b) Simulation of the SAXS profile of diluted spheres having an analogous size dispersion (inset) to the one retrieved for the ZnS1 sample.

The obtained SAXS profiles (Figure 2.8a) evidenced the increase of scattering intensity immediately after the injection of the zinc precursors. This was expected, as the formation of ZnS in water from Zn^{2+} and SH^- was previously observed to occur with virtually no induction time in a sub-10 µs time frame.[58] Therefore, it is safe to state that a 10 s time step allowed to consider a complete formation of NPs with the complete consumption of the zinc precursor. The obtained profile was remarkably linear in the range from 0.1 to approx. 0.5 nm^{-1}. Comparing these profiles with the one simulated for spherical NPs having an average $D_{1,0}$ diameter of 8.1 nm and a relative standard deviation of 20% (i.e. analogous of the size distribution obtained *ex-situ* by for the ZnS1 sample) reported in Figure 2.8b, it is evident how the plateau expected at low-q (the Guinier region) was missing. This feature was interpreted as the effect of aggregation on the primary NPs in the reaction mixture. The linearity observed towards low q values indicates the formation of fractal aggregates.[115] Fractals are irregular geometric structures originally introduced by Mandelbrot.[116,117] With his non-Euclidian geometry, Mandelbrot described fractals as defined by two fundamental concepts: self-similarity and fractal dimension *D*. The first reflects the absence of a characteristic length-scale associated with the structure, while the second

can be interpreted as the space-filling capability of the structure. This approach was applied to the description of irregular aggregates since they are commonly found in many colloidal systems, to characterize aggregation phenomena.[115,117] Depending from the nature of the system, and consequently from the observed scattering behavior, two different types of fractals can be distinguished: mass and surface fractals. While the second is typical of a dense object having a rough surface, the first can be described as irregular 3D networks originated from linked repeating building blocks. In this case, ZnS NPs can be interpreted as the building block that were assembled into disordered superstructures (the aggregates), therefore the system was correctly described as mass fractals. The fractal dimensions *D* assumes the value $D = 3$ for a homogeneous object completely filling the space, while for a mass fractals a value $D < 3$ is found, as the structure leaves some empty regions.[118] The *D* value is obtainable from the slope of the linear fractal region in the log-log plot of the SAXS profile. The time evolution of the fractal dimension *D* is showed in Figure 2.9c.

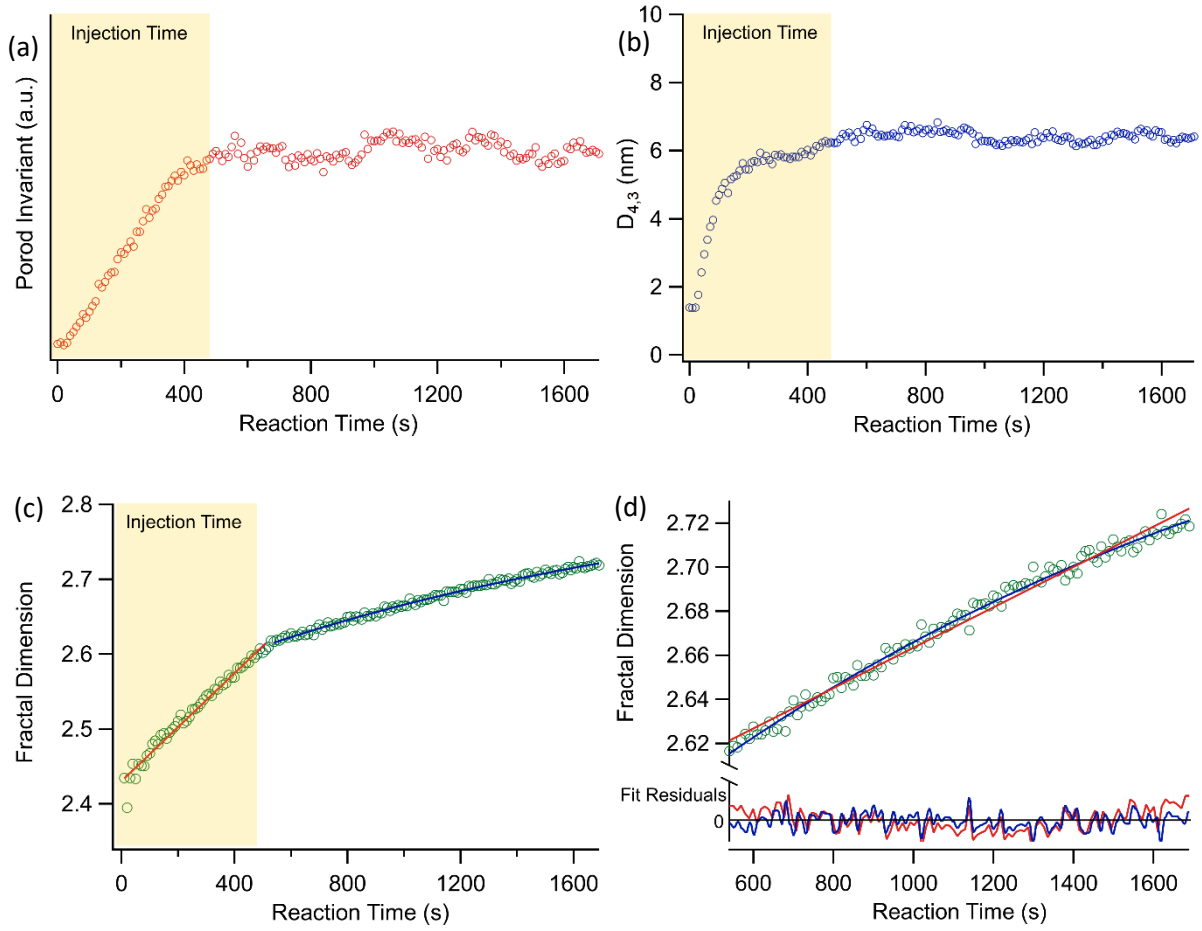

Figure 2.9 Time evolution of (a) Porod invariant, (b) estimated average $D_{4,3}$ diameter from the correlation length and (c) fitted fractal dimension *D* during the *in-situ* SAXS experiment. (d) comparison of the linear fit (red line) and the exponential fit (blu line) of *D* against the reaction time in the post-injection regime.

To evaluate variations in concentration and size of nanoparticles, an approach based on integral quantities was employed. Integrated intensity was calculated together with the Porod invariant[119] (Figure 2.9). From the ratio of the integrated intensity of the scattering profile and the Porod invariant, the correlation length was obtained. This last quantity is related to the $D_{4,3}$ average of the underlying NPs distribution.[120] The whole SAXS profile of the system is required to accurately calculate the $D_{4,3}$ value, but the presence of large aggregates made of small NPs led to a diffraction profile that exceeds the available q-range. Therefore, a precise determination of $D_{4,3}$ was not achievable, but rather an indication of the size of NPs and its variation as function of time was obtained.

Table 2.4 fitting parameters for the time evolution of the fractal dimension D during the reaction (10 s – 500 s) and after the reaction (540 s – 1690 s).

Time window	Fitting parameters		
	A	B	C
	Linear fit: $y = A + Bx$		
10 s – 500 s	2.4302 (0.0024)	$3.62 \cdot 10^{-4}$ ($0.08 \cdot 10^{-4}$)	
	Exponential fit: $y = A + Bexp(-Cx)$		
540 s – 1690 s	2.840 (0.018)	-0.323 (0.014)	$5.6 \cdot 10^{-5}$ ($0.6 \cdot 10^{-5}$)

The particle concentration is proportional to the Porod invariant (Figure 2.9a), as the latter depends only on the electron density contrast factor of the scatterers with respect to the continuous media (in this case the solution), and their volume fraction, but not on the geometrical configuration of the particles. During the injection time, the concentration of particle increased as expected. After the injection, the values of the Porod invariants stabilized as no more particles are expected to be formed. The absence of relevant particle growth with increasing reaction time was expected because of the aforementioned fast kinetics of ZnS formation. A different profile of the estimated $D_{4,3}$ value was instead obtained (Figure 2.9b), showing that particles grown to their final size rapidly after the initial part of the injection, and no relevant variations occurred afterwards. However, in the first part of the curve, after the first acquisitions during the injection, a slight increase in size was evidenced. This suggests that, in the first steps of the synthesis, smaller NPs were formed, while the addition of more zinc precursor led to a size increase until a certain equilibrium average size was reached. Despite the proposed primary nanoparticle size provided only an estimation, the obtained value lies close to the one expected based on the TEM and XRD analysis, suggesting that the final equilibrium average size corresponds to the one retrieved for the sample after the post reaction work-up. In other words, the obtained particles did not display a tendency to indefinitely grow after the reaction was concluded, right after the full injection of the precursors. The time evolution of the formed aggregates was also obtainable from the fractal dimension values (Figure 2.9c). The value of the fractal dimension *D* for

each SAXS profile was obtained from the corresponding slope of the linear fractal regime. The slope was obtained performing a linear fit of the region. On the available timescale, aggregates were formed simultaneously with primary particles, in agreement with the observation of Schmidt *et al,*[58] as the SAXS profiles immediately showed a clear linear fractal regime at the log-log plot (Figure 2.8a). Aggregates were determined to have an initial fractal dimension of 2.57. During the injection of the precursor, a linear increase of the fractal dimensions was observed, indicating that NPs in the aggregate were gradually assuming a more compact configuration. A second increase in the fractal dimension was also observed after the injection was completed. In the latter case, the observed rate was abruptly reduced after the end of the injection, and the resulting time evolution deviated from linearity (Figure 2.9c). Assuming the system evolved towards a final fractal dimension value, an exponential behavior was assumed. A comparison of the performed exponential fit with a linear one is proposed in Figure 2.9d, showing a better adherence to the observed trend of the first. The coefficients obtained from the linear fit and the exponential fit of the two regions are resumed in Table 2.4. From the exponential fit, the predicted final value for the fractal dimension of the aggregates was 2.84. The system is expected to reach the value of 2.80 after roughly one hour the reaction began. The two different behaviors observed may be associated to changes in the reaction media while the precursors are being added, and in particular to the decrease in concentration of HS^- ions from 0.20 M to 0.05 M due to the combined effect of the increase in the total volume of reaction (doubled at the end of the injection) and the reaction with Zn^{2+}. Related to this concentration change, the pH also decreased from 13.0 to 12.6. Since both pH and presence of SH^- ions showed to be relevant to determine the stability of ZnS NPs colloids (see Chapter 2.4 and Chapter 4.1), their variations during the reaction, together with the simple numerical increase of ZnS NPs in the reaction mixture are likely to destabilize the initially formed colloid aiding the aggregation phenomena that ultimately leads to the coagulation of the product.

Overall, the in-situ SAXS analysis confirmed that the precipitation of ZnS NPs was much faster than the injection time, as no relevant increase in scatteres concentration from the Porod invariant was observed after the zinc precursor was entirely added to the reaction mixture. The estimated size of the NPs during the reaction was close to the one obtained *ex-situ*, but a small size increase was observed in the initial part of the reaction. This suggested that smaller ZnS NPs were formed initially, possibly opening new opportunities for modified approaches to obtain even smaller ZnS NPs with respect to the one here synthesized. The NPs were not found to be individually separated in the suspension, as expectable from the absence of surfactants or ligands, but they were forming fractal aggregates. The aggregates got denser over the course of time, but without reaching the limit of a continuous big solid particle (D = 3), as a final fractal dimension of 2.84 was estimated.

2.4 NPs behavior in water suspension

The formation of a stable colloid is a mandatory condition for numerous applications, ranging from catalysis (e.g. hydrogen evolution reaction from ZnS suspensions) to the manufacturing of thin film (e.s. spin-coating or spray-coating). To pursue colloidal stability, the surface functionalization or the inclusion of a surfactant is often required (see Chapter 1.4).

In the case of ZnS samples obtained using the described batch synthesis, during the workup of the product, the formation of a stable suspensions was observed. After one or two washing cycles of the product (as described in Chapter 7), an incomplete sedimentation of the product was observed even after centrifugation time and speed up to 30 min and 12500 rpm. The formation of a clear opalescent water suspension was observed instead. By including a ultrasonication step, the obtainment of more concentrated colloids was possible, reaching values up to 3.4 mg/ml. The obtained colloids were stable for several days, or even weeks, without noticeable changes to a visual inspection, leaving a wide time window of stability for further use. Once the product was dried, the NPs were not dispersible in water again.

The pH of a water (milli-Q quality) suspension obtained from the dried samples was determined to be a slightly acidic, having a typical pH range of 4 – 6. The latter suspension was not stable and rapidly coagulate. On the contrary, suspension obtained during the workup had a pH typically varying in the range 12 – 10. Since the sulfide precursor was used in excess (S:Zn molar ratio of 2:1), the stabilization and the effect on pH was ascribed to the adsorption of excess SH^- on the surface, thus providing electrostatic stabilization. A similar phenomena was described by Tienmann *et al.*, who described as the increase of the S/Zn molar ratio led to a gradually increase of negative charge on the particles surface.[121] This behavior was also in line with the Zn excess retrieved by the XPS analysis, possibly leading to the formation of a positive charge on the surface that needs to be balanced by the adsorption of negative ions. In this framework, the non-dispersibility of dried NPs may be explained as the loss excess SH^- simply by volatilization as hydrogen sulfide. Similar dispersibility issues were observed also for suspension after repeated ultrasonication cycles, after dilution or upon exposure to open air. Indeed, all these conditions leads to dilution or loss of SH^- due to the existing equilibria involving SH^- (either its binding with the ZnS surface or the equilibria with gaseous H_2S).

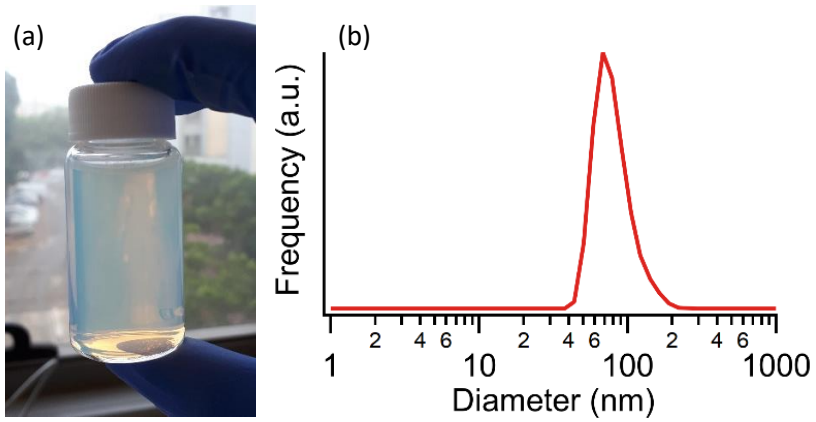

Figure 2.10 (a) Picture of a stable colloid obtained from the ZnS1 sample. (b) Number distribution obtained by DLS analysis on a diluted stable suspension formed during the workup of sample ZnS1.

The presence of an excess negative charge adsorbed on the NPs was confirmed by ζ potential measurements on the suspension at autogenous pH. In the case of the stable suspension, a ζ potential value of -41 mV was found, while for NPs re-suspended after being dried the valued of -20 mV was obtained. Since -30 mV is the commonly accepted ζ potential value to achieve electrostatic stabilization in low ionic strength conditions, its increase up to -40 mV for the as-synthetized suspension explains the observed stability.[122] To evaluate the size of the dispersed particles, a DLS characterization was performed on clear ultrasonicated suspension diluted from 10 to 100 times with milliQ water (Figure 2.10). The obtained number-weighted dimensional distributions were typically centered on 100 nm, with a tendency of shifting towards larger values overtime. The latter value was incompatible with the primary NPs size but confirmed the presence of aggregates obtained from the *in-situ* SAXS analysis.

All together, these results underlined that this synthetic approach was not only useful for the synthesis of small ZnS NPs, but it also led to the formation of stable colloids without the addition of surfactants. The adsorbed SH^- ions were easily removed by drying the product, as indicated by XPS measurements (*vide supra*), since the surface analysis pointed out a slightly Zn-rich surface. The absence of residual excess sulfide was also indicated by the non-dispersibility of dried NPs. Both SAXS and DLS results indicate that in the obtained stable suspension NPs were not individually separated, but it was rather composed of aggregates of roughly 100 nm.

2.5 ITC characterization of the liquid/solid interface

The binding affinity of NPs surface towards different moieties plays a fundamental role for a wide number of applications and is of special importance for the development of functionalization strategies (see Chapter 1.3). Interaction occurring at gas/solid or vacuum/solid interfaces with different species are already accessible with different techniques (e.g. in-situ FTIR spectroscopy), that were already applied to study the properties of ZnS NPs.[103] However, many applications rely on colloidal systems rather than dried nanomaterials. Despite the importance of the liquid/solid interface for many applications, a quantitative approach to the problem of its study is still unestablished. To probe the interaction of nanostructures with the colloidal environment using a quantitative method, a titration can be employed. Titrations are widely employed in fields like supramolecular chemistry or biochemistry,[123] but were rarely applied to the study of dispersed nanocrystalline inorganic compound. All these techniques rely on successive addition of a titrant solution (i.e. a ligand or the molecular species) in a second solution containing the analyte (normally another molecular or macromolecular species). The interaction is followed through the variation of a suitable and accessible physical quantity which has a known relation with either the amount of free titrant, the amount of interacting titrant or both. The binding constant is then determined fitting the obtained binding isotherm by mathematically modelling the interaction.[123] In principle, the same approach can be applied to study colloids where, however, the definition of a the analyte concentration (ideally the molar concentration of the available surface binding sites) is far less straightforward. A few examples of this kind of approaches can be found in the literature.[124–130] Among all the possible techniques that can be applied to follow this type of titrations (e.g. UV-Vis spectroscopy, NRM spectroscopy, fluorimetry),[123] the isothermal titration calorimetry (ITC) offers some unique advantages. Since it is a calorimetry-based method, no special properties of the titrants are necessary (i.e. luminescence or spin active nuclei), noticeably extending its applicability to many molecular probes. Moreover, it also allows the simultaneous determination of the binding constant and of the enthalpy of the binding process, in principle unlocking the access to a complete picture of binding phenomena thermodynamics.[123]

To prepare a sample suitable for an ITC measurement, a stable colloid with a known composition must be obtained. The isotherm resulting from the titration must be properly modelled and fitted to retrieve the thermodynamic parameters on the underlying process occurring during the measurement. All the relevant contributions to the detected heat transfer must be considered. The ideal sample should be made only of the dispersed analyte material and the dispersing solvent, since any other substance in the sample media in a relevant concentration level is in principle source of interference. Therefore,

the absence of any surfactant or surface functionalization is beneficial. Since this was obtained with the batch method described, the opportunity to study the fundamental surface chemistry of ZnS NPs at the liquid/solid interface emerged. The optimized ZnS1 synthetic approach was employed to probe the interaction of ammonia, methylamine, pyridine, methanol, and furan, used as probe molecules characterized by different interacting moieties. The probe molecules were used as titrants for ITC experiments on the water-based suspension of ZnS NPs obtained. ZnS1 was preferred instead of ZnS2 due to the larger available surface area, related to the smaller dimension of the NPs.

From the titrations, a clear adsorption isotherm was only obtained for pyridine, while excessively poor interaction (ammonia, methylamine, methanol) or the interference of unidentified side phenomena disturbing the thermogram (furan) were observed for the other molecules.

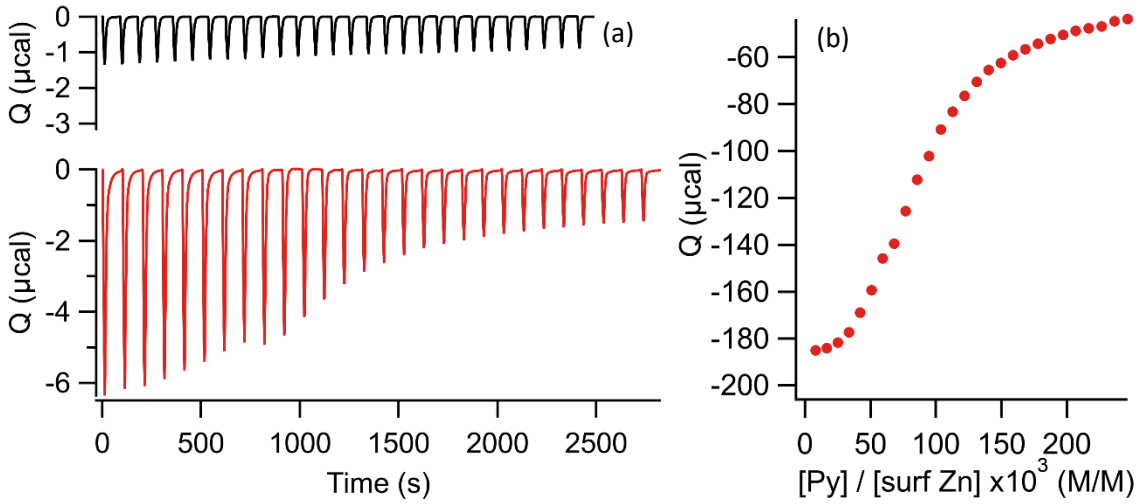

Figure 2.11 (a) ITC thermograms. Up: pyridine 100 mM in water. Down: pyridine 100 mM in 0.87 mg/ml bare ZnS suspension in water. (b) Binding isotherm obtained from the thermogram.

In figure 2.11a the ITC thermogram obtained from the titration of a 0.87 mg/ml ZnS NPs suspension with a 100 mM water solution of pyridine is reported. From the thermogram, the isotherm of Figure 2.11b was obtained. The isotherm is reported against the ratio between the pyridine concentration and the total available concentration of exposed surface Zn cations. The latter quantity was estimated considering spherical NPs of 7.8 nm assuming that the NPs surface only exposed the (110) facet.[103] The simplest and most used approach to fit isotherms for the liquid/solid interface is the employment of the Langmuir isotherm.[128,131] This approach is based on the following assumptions: *i.* no multilayer adsorption; *ii.* homogeneous surface with identical binding sites; *iii.* no interaction between adsorbed molecules.[131,132] To now, however, no satisfactory fit of the data could be obtained with such model, and the development of alternative approaches has yet to be completed. Similar limitations were also encountered by other authors.[125,126] However, from the shape of the isotherm, it is still possible to obtain insights on the observed adsorption phenomena. In particular, the shape of the isotherm was

readily recognizable as an S-type isotherm of the Giles classification.[133] This isotherm is typical of adsorption phenomena having a high activation energy in the exchange equilibrium with solvent molecules adsorbed to a surface, thus resulting in a cooperative adsorption mechanism. In this case, the adsorbate tends to pack in rows or clusters on the surface, rather that forming individual molecule-surface interactions. This adsorption mechanism is known to be typical of monofunctional solutes competing with a strongly adsorbed solvent. Interestingly, the last description matches the nature of pyridine as a ligand and the description of the ZnS surface capabilities previously elaborated using a hybrid experimental and theoretical approach for the gas/solid interface.[103] The high affinity of pyridine with respect to other moieties was also previously observed experimentally, as ZnS was proposed as pyridine-sensitive material for the development of dedicated sensors.[134]

Overall, despite the limitations arising from a still weak theoretical development of the field, using the ITC technique it was possible to obtain a confirmation of the pyridine binding capabilities on the ZnS surface. From the isotherm shape, it was also possible to obtain qualitative evidence of high impact of the water desorption in the pyridine interaction mechanism, as the first constitutes a high-energy-step that needs to be overcome before establishing the interaction, that is supposedly obtained via a cooperative interaction of the pyridine molecules.

Chapter 3.

Uncapped metal sulfides: a simplified wet-chemistry approach to CuS, PbS, MnS and Ag_2S

The simple batch precipitation method employed to the synthesis proposed in Chapter 2 was found to be successful to control the size of ZnS NPs despite the complete absence of surfactants or stabilizing agents. This stimulated a wider assessment on other metal sulfides, to evaluate the potentialities of the approach. On one hand, it is generally known that mixing a sulfide solution and with a transition metal solution generally leads to the precipitation of a solid due to the more than established very low solubility product of these compound.[45] On the other hand, little information can be retrieved on the actual features of such reaction products when crystallinity, size and morphology of the obtained particulate are regarded. Therefore, the method employed for ZnS was used as a reference approach to a more systematic study of the reactivity of different metal ions and to the synthesis of different organics-free NPs with a very simple and echo-friendly approach. This study was also extended to the surface chemistry of the obtained materials, as a interestin chance to assess their surface composition and behavior toward oxidation phenomena without the influence of other species. Overall, the studied metal ions were Cu^{2+}, Pb^{2+}, Mn^{2+}, Ag^{+}, Ni^{2+}, Co^{2+}, Cr^{3+}, Fe^{2+}, Sn^{2+}, Ti^{4+}, Nd^{3+}, Yb^{3+}, Gd^{3+}, Eu^{3+}. From these, pure crystalline compounds were obtained for Cu^{2+}, Pb^{2+}, Mn^{2+} and Ag^{+}. For the other ions, secondary compounds, or amorphous and/or highly oxidized materials were generally obtained. Different ionic sulfur precursors were considered to explore the effect of a different reaction pH, as reported in Table 3.1. In all the syntheses a double fold excess of SH^{-} was employed, while keeping the sulfur precursor solution at 0.2 M and adjusting the concentration of the metal precursor depending on the expected stoichiometry of the corresponding target meal sulfide.

Table 3.1 Metal ions tested for the water synthesis of metal sulfides and the sulfur precursors employed.

Sulfur precursor	pH (0.2 - 0.05 M)	Tested metal ions
Na_2S	13.0 - 12.6	Cu^{2+}, Pb^{2+}, Mn^{2+}, Ni^{2+}, Sn^{2+}, Ag^{+}
NaHS	11.3 - 10.6	Cu^{2+}, Pb^{2+}, Mn^{2+}, Ni^{2+}, Cr^{3+}, Fe^{2+}, Sn^{2+}, Ti^{4+}, Nd^{3+}, Yb^{3+}, Gd^{3+}, Eu^{3+}
$(NH_4)_2S$	9.2 - 9.2	Ti^{4+}, Gd^{3+}, Nd^{3+}

The obtained samples are referred as CuS1, PbS1, MnS1 when Na_2S was used, while CuS2, PbS2 and MnS2 indicates the employment of NaHS. AgS was synthetized using Na_2S.

3.1 Copper sulfide - CuS

Copper sulfides $Cu_{2-x}S$ ($0 < x < 1$) is a class of materials characterized by a wide variety of possible stoichiometries and crystal structures.[135] They had attracted scientists' attention for their peculiar p-type semiconducting properties and for wide possibilities of technological applications ranging from the development of sensors and photovoltaic devices to theranostics[136] and bioimaging applications.[135,137,138] The diversified structural and compositional properties on $Cu_{2-x}S$ NPs allowed a wide tunability of the optical properties, that combined with the known nontoxic nature of the material and the NIR absorption properties in the 800- 1400 range due to the formation of free charge carriers, made this material the ideal choice for many *in-vitro* and *in-vivo* biomedical applications.[137,139] Indeed, nanostructured copper sulfides were used as contrast agent in photoacoustic tomography (PAT) of deep tissues[140] and for the thermal ablation of tumor cells.[138] Copper sulfides are also used in applications such as cathode material for lithium batteries,[141] as infrared sensors[142] and as catalyst for the colorimetric estimation of human blood glucose level as substitute to the enzyme peroxidase.[143] Many synthetic routes were proposed for $Cu_{2-x}S$ NPs, such as solvothermal[144], hot injection[145,146], microwave-assisted,[145,146] sonochemical,[147] microemulsion[148–150] and miniemulsion[151] methods. In this work the synthesis of CuS covellite was pursued, which is a semiconductor having a 1.2 – 2.0 eV bandgap[152] that also displays an anisotropic metallic electrical conductivity (resistivity 10^{-6} Ωm).[152,153] Covellite NPs were obtained using the simplified ligand-free method, allowing a more in depth study of the surface composition and susceptibility toward oxidation phenomena.

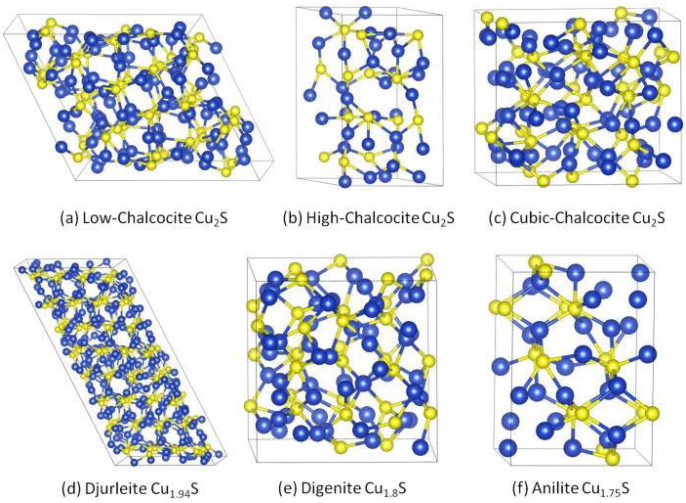

Figure 3.1 Examples of crystal structured for $Cu_{2-x}S$: (a) the low-chalcocite (monoclinic), (b) highchalcocite (hexagonal), (c) cubic-chalcocite (cubic), (d) djurleite, (e) digenite, and (f) Anilite. Reprinted from Xu *et al.*[151]

3.1.1 Crystal structure, size and morphology

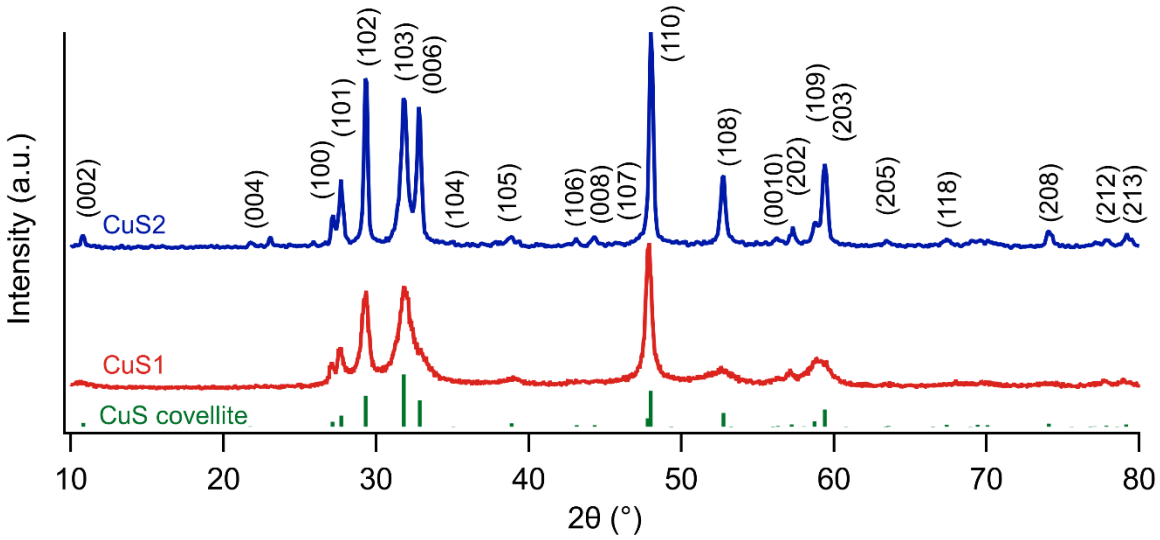

Figure 3.2 XRD diffraction pattern of CuS1 and CuS2 samples with indication of the reflection CuS covellite (stick plot).

The precipitation method employed led to the formation of a dark green powder. The XRD patterns acquired (Figure 3.2) was compatible with the CuS covellite (ICSD 98-004-1911, space group P 63/m m c), despite strong variations in the relative intensities of reflections were evident. Anisotropic broadening was also evident especially in sample CuS1 (see the (103) and (006) reflections) suggesting the presence of anisotropic crystallites. No further crystalline phases were detected, ruling out the presence of possible crystalline oxides or other spurious phases.

The TEM analysis showed the presence of nanosized platelets-like particles. By employing an oleylamine-aided dispersion on the TEM grid, particles tended to acquire a radial orientation with respect to the obtained nano/micro-sized oleylamine droplet. This caused a coffee-stain effect, and NPs were typically found to decorate the inner border of the droplets (Figure 3.3). NPs also displayed a tendency to stack along the short direction (Figure 3.3a, inset). Due to the NPs' plate-like shape, at least two parameters were necessary to describe their dimensional features. A cylindrical geometrical description was used, thus requiring one diameter and one height value. The latter was not accessible from the micrographs, as no indication about the tilt of the displayed 2D projection was obtainable. On the other side, assuming a circular cylindrical, the base diameter was accessible as the maximum Feret diameter (or caliper diameter), being the maximum distance measured between two points inside a single projection. A $D_{1,0}$ average diameter of 17 nm was measured for the CuS1 sample, with a standard deviation of 4 nm (21%).

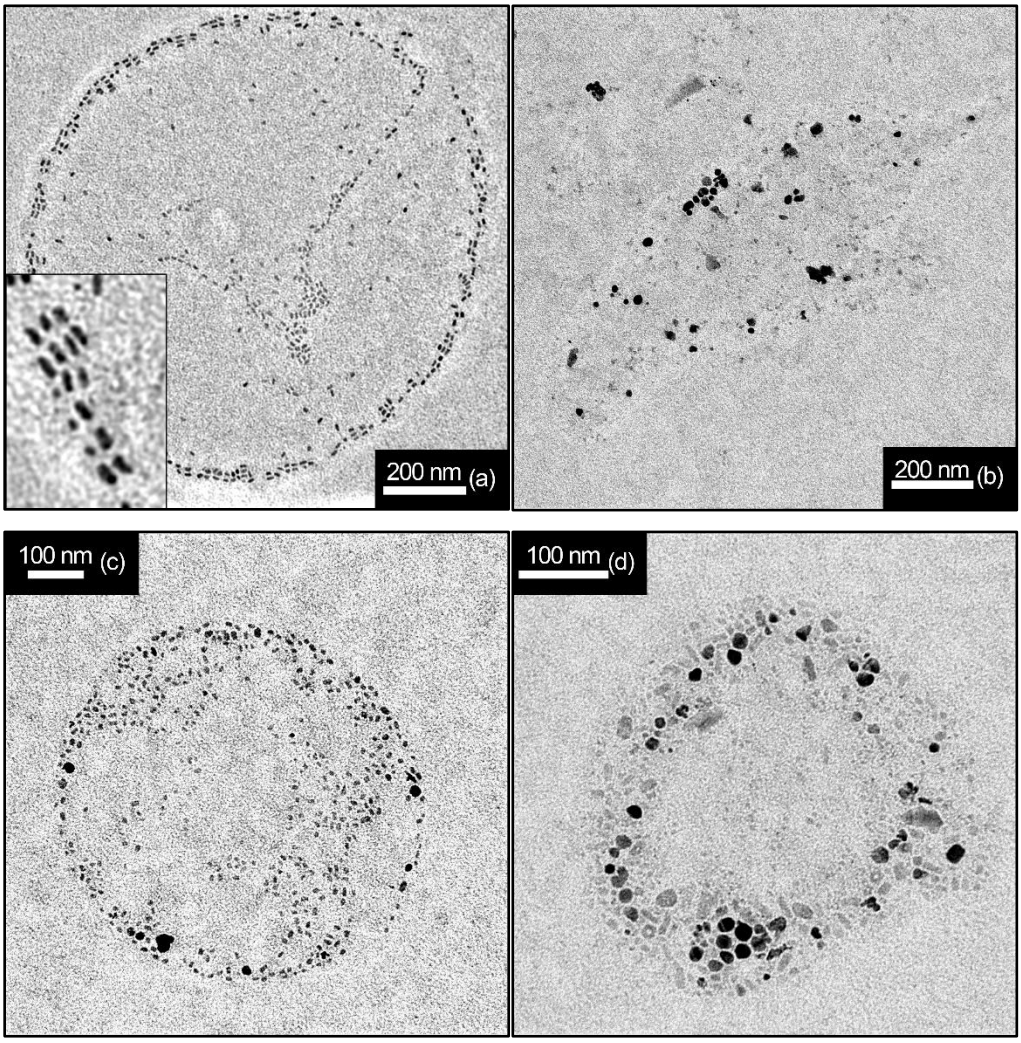

Figure 3.3 TEM micrographs of Cus1 (a,b) and CuS2 (c,d) samples. In the inset of picture (a) a magnification was provided to show the stacking effects on the NPs. The images were background-subtracted to remove the contribution of the oleylamine bubble-like structure.

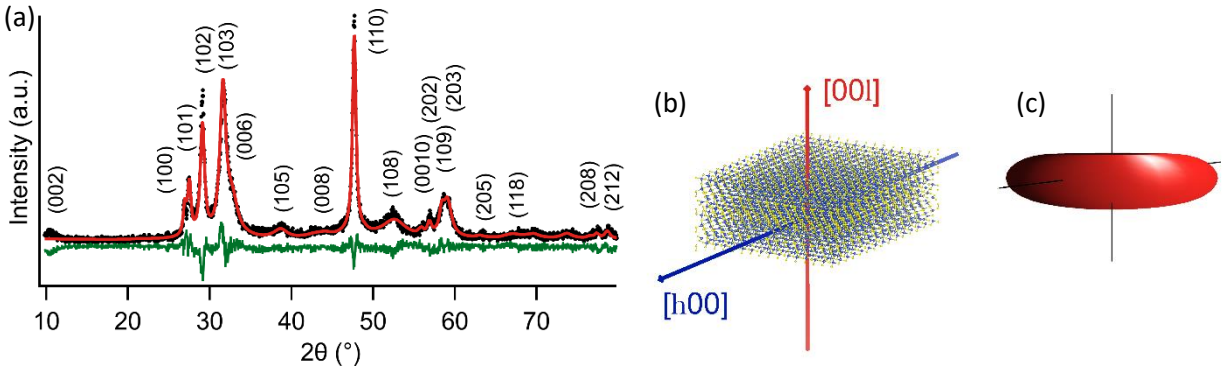

Figure 3.4 (a) Refined XRD CuS1 profile. (b) Crystallographic direction employed to evaluate the anisotropic crystallite dimension. (b) Equivalent crystallite shape obtained employing the Popa model for anisotropic crystallites.

For CuS2, a $D_{1,0}$ average diameter of 19 nm with a standard deviation of 6 nm (31%) was retrieved. In the case of CuS2, the presence of larger platelets was also evident, suggesting a relevant polydispersion. Overall, while a comparable morphology was obtained in the two cases, for CuS1 smaller and less polydispersed particles were obtained.

Starting from the information obtained with the TEM analysis, the CuS1 XRD pattern was refined. To account for particle anisotropy, the model developed by Popa *et al*. was employed for the size broadening of the reflections.[154] As platelets often assumes a stacked configuration, the presence of texture (i.e. preferred crystallographic orientation) was considered by using a spherical harmonic model. From the fitting procedure on CuS1 (Figure 3.4a), a plate-like crystallite was obtained. Thickness and diameter of the average nano-platelet was estimated as the obtained $D_{4,3}$ average size along [h k 0] directions, while the thickness was estimated along the [0 0 l] direction. A $D_{4,3}$[h k 0] value of 27 nm was obtained, together with a $D_{4,3}$[0 0 l] value of 6 nm. The obtained equivalent average crystallite matched the TEM observation of a plate-like structure, as depicted in Figure 3.4c from the reconstructed symmetrized shape obtained from the spherical harmonics employed in the Popa model.[154] From these two descriptors, an aspect ratio (the ratio of the diameter over the height) of 4.5 was obtained. The average spherical crystallite diameter obtained (i.e. the size of the spherical crystallite having the same volume of the anisotropic one) was 14 nm. A direct comparison of the $D_{4,3}$ [h k 0] value with the Feret diameter obtained from the TEM micrographs indicates an asymmetric size distribution having an extended tail towards larger values. In other words, the size distribution is influenced by the presence of a relatively small number of larger particles.

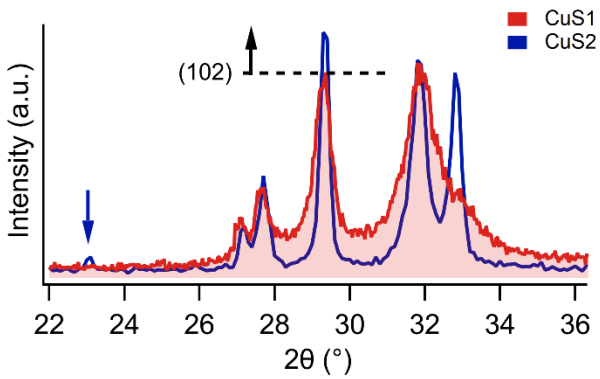

Figure 3.5 Detail of the anomalous reflection intensities observed in the sample CuS2, with reference of the intensity of the (102) reflection. The blue arrow indicates the unknown reflection at 23°.

In the case of sample CuS2, peak intensities could not be properly fitted accounting for crystallite anisotropy and texturing, or even refining the atoms positions and the possible deviations from the stoichiometry (i.e. the presence of vacancies). In particular, the (102) reflection appears to be anomalously intense. An unknown weak reflection was also visible at 23° (Figure 3.5), which could be

related to the observed variations of the crystal structure, or it could be attributed to an instrumental artefact. A more fundamental refinement of the unit cell would be necessary, possibly performed on high quality data obtained from a synchrotron source, to clarify these observed features. Since the observed pattern is very close to the one expected for covellite, the actual crystal structure is likely to be closely related to it as well. The presence of structural variability in copper sulfide is not surprising, since many crystalline phases are known for this class of compounds.[135]

3.1.2 Surface composition

To assess the surface composition of the samples, XPS analysis was carried out. To distinguish between spectral features arising from crystalline covellite and signals originated from surface oxidation or contaminations, a consolidated ionic model for the crystal structure is helpful, if not strictly necessary.

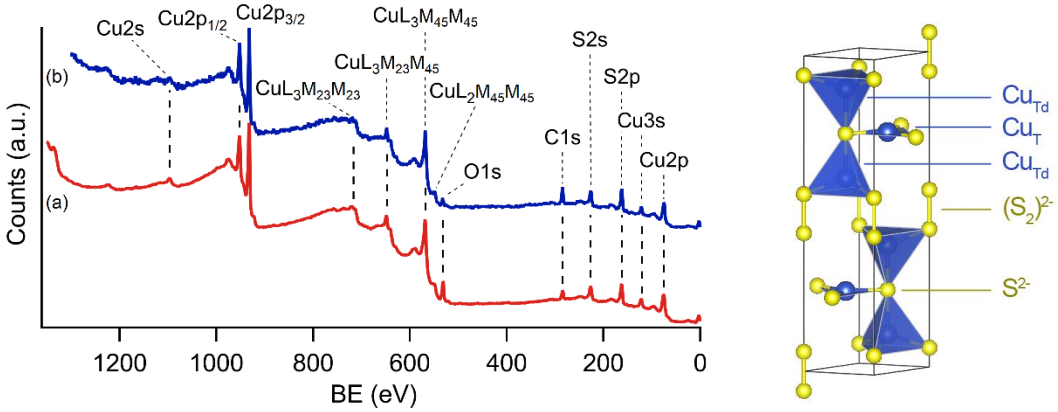

Figure 3.6 (left) XPS survey spectra of the CuS1 (a) and CuS2 (b) samples. (right) Unit cell of the covellite crystal structure showing the tetrahedral (Td) and trigonal (T) sites of Cu atoms, and the presence of $(S_2)^{2-}$ and S^{2-}.

Table 3.2 Observed peaks position in the XPS spectra of CuS1 and CuS2 samples.

Peak	CuS1 (eV)	CuS2 (eV)	Reference[99] (eV)
Cu2s	1096.4	1096.6	-
$Cu2p_{1/2}$	932.1*	932.0*	932.2 - 932.2
Cu2p3/2	951.9*	952.0*	952.3
Cu3s	122.0	121.4	121.4
Cu3p	75.6	75.0	74.6
S2p	161.7	161.7	161.0
S2s	226.0	226.2	225.5

(*) referred to the asymmetric peak position of the Cu(I) component using the asymmetric profile approach. See Table 3.3.

To assess the surface composition of the samples, XPS analysis was carried out. To distinguish between spectral features arising from crystalline covellite and signals originated from surface oxidation or contaminations, a consolidated ionic model for the crystal structure is helpful, if not strictly necessary. However, such unambiguous description of covellite is not available yet, as the appropriate ionic model to describe CuS covellite is still a matter of debate in the scientific community. While the stoichiometry suggests a simple Cu^{2+} S^{2-} model, and covellite is sometimes regarded as the copper(II) sulfide,[155] the crystal structure alone clearly shows a very different situation. Cu is found in two sites having a different coordination: one trigonal site and two tetrahedral sites (Figure 3.6 right). In a trigonal site, Cu is only binding S^{2-} ions, while in a tetrahedral sites Cu is bonded to three $(S_2)^{2-}$ ions and one S^{2-} ion. This led to the use of a $Cu_2S \cdot CuS_2$ model that reflected the two different coordination environment of Cu.[156] To explore the valence state of the metal in the different sites, many physico-chemical assessment have been performed, often resulting in non-resolutive or even contradictory results. EPR[157] and XPS[158,159] generally pointed to the presence of only Cu(I) in the structure with no Cu(II) character at all, indicating either a $(Cu^{+})_3(S_2^{2-})(S^{-})$[153] or a $(Cu^{+})_3(S^{2-})(S_2^{-})$[160] formula. The presence of a Cu(II) was instead pointed out by in XAS and XES experiments[161] and further supported by theoretical calculations on electron density topology of the covellite structure.[162] Therefore, the presence of Cu(II) suggested a ionic model having the formula $(Cu_{Td})^{+}(Cu_{T})^{+}(Cu_{Td})^{2+}(S_2)^{2-}(S)^{2-}$ (Td = tetrahedral site, T = trigonal site). In the latter case, the evidence of identical Td sites from crystallographic evidence may be justified with the presence of static disorder. Alternatively, assuming charge delocalization between the Td sites, an alternative description was employed: $[(Cu_{Td})_2]^{3+}(Cu_{T})^{+}(S_2)^{2-}(S)^{2-}$. In this case two identical Cu_{Td} having a fractional 1+1/2 oxidation state each was obtained.[161,162] Alternatively, a ionic model $(Cu^{1.3+})_3(S_2^{2-})(S^{-})$[153] with all three Cu atoms sharing the same 1+1/3 oxidation state was proposed on the basis of XPS and nuclear quadrupole resonance (NQR) analysis.[163] Recently, Cabrera-German *at al.* performed an in-depth quantitative XPS analysis on amorphous and crystalline covellite.[164] From the analysis a Cu(I)/Cu(II) ratio of 1:1 for the crystalline compound was obtained. The XPS fitting was however complicated by oxidation phenomena occurring after a calcination step employed to promote the crystallization of the sample. The analysis here performed started from the one proposed by Cabrera-German *et al.*, who adopted the traditional peak-fitting based approach to the analysis of the Cu2p region. It is worth to mention that the available literature rarely refers to the possibly relevant contribution of the phenomena of the multiplet splitting.[165] In the common interpretation of XPS spectra, a single electron excitation is generally considered. However, this approximation often breaks down for 2p electrons in atoms having partially filled 3d orbitals. Therefore, as the presence of copper having an oxidation state higher that Cu(I) is suspected, a rigorous approach to the description of this region should be performed according to more advanced approaches like the charge transfer multiplet (CMT) theory.[166]

The obtained XPS survey spectra (Figure 3.6 left) pointed out only the presence of Cu, S, C and O, confirming the high purity of the samples. The complete list of the retrieved peak positions for Cu and S is reported in Table 3.2. As no organic compounds were employed in any stage of the synthesis, the presence of C resulted from common adventitious contamination.[100] No charge effect was observed, likely thanks to the metallic conduction properties of CuS.[153] From the semi-quantitative analysis performed on the spectra, a Cu:S atomic ratio of 1:0.8 was found for CuS1, while 1:0.9 was found for CuS2, both close to the expected 1:1 Cu:S stoichiometry.

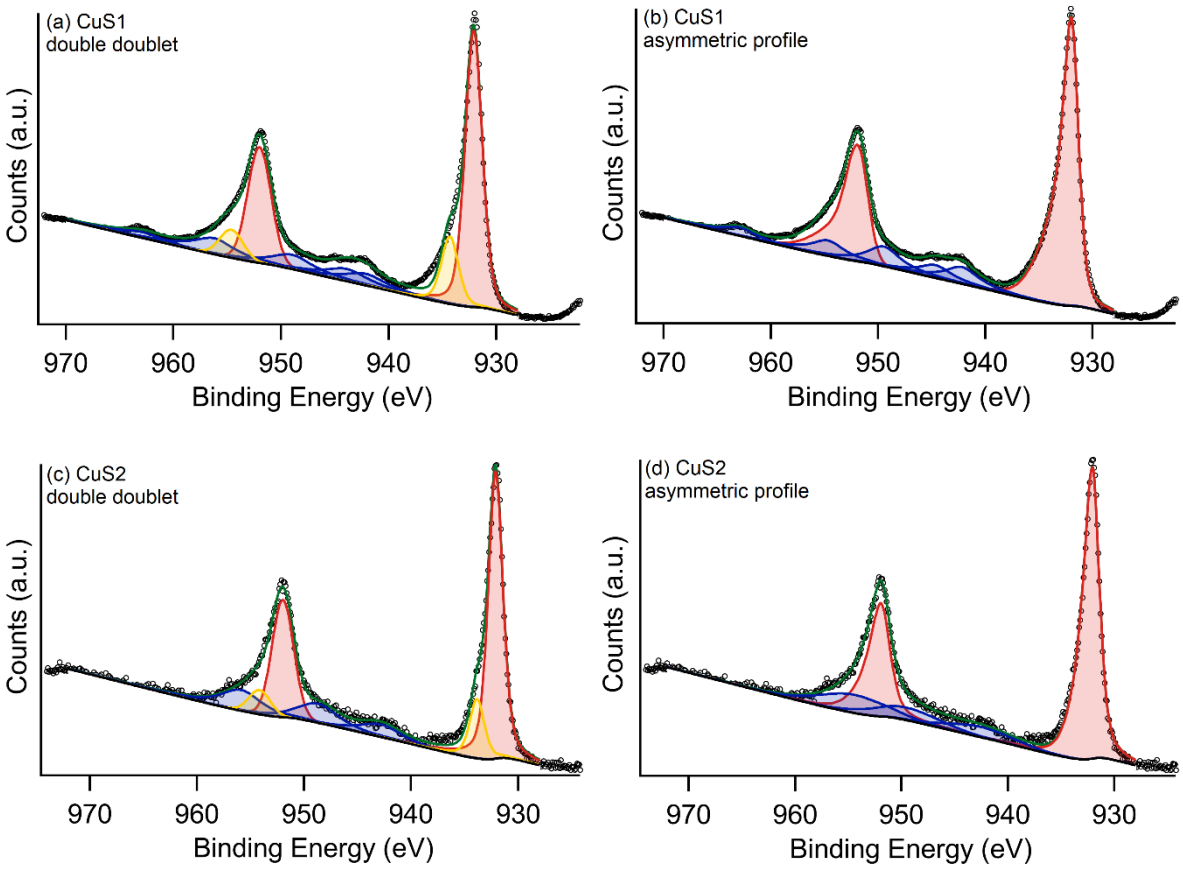

Figure 3.7 Comparison of the asymmetric-profile approach with the double-doublet approach for samples CuS1 (a,b) and CuS2 (c,d). Color scheme: red = main Cu(I) peak, yellow = possible Cu(I+) peak, blue = energy loss peak.

The interpretation of the Cu2p region was made difficult by the possible presence of oxidation phenomena together with the still undetermined ionic model. Moreover, the asymmetric profile of the main photoelectron peaks may arise not only from the presence of smaller peaks at higher binding energy (such as Cu(II), either as part of the covellite structure or as a result of oxidation phenomena), but may also be explained as the excitation of electron near the Fermi level typical of conductors[158,167] or from the presence of surface contaminations and interfacial bonding.[168] It may also noticed that the presence of asymmetry does not automatically exclude the presence of components at higher binding

energy, as the two might occur simultaneously. To account for both possibilities, the Cu2p photoelectron peaks was fitted by using two doublets or by a single asymmetric doublet, as two limit situations (Figure 3.7).

Table 3.3 Fitting parameters emplyed from the application of the asymmetric-profile approach and the double-doublet approach to samples CuS1 and CuS2. Cu(I+) indicates an oxidation state higher than Cu(I). GL (%) refers to the mixing of Gaussian and Lorentzian contributions in the pseudo-Voigt profile.

Peak		Position (eV)	Area	FWHM (eV)%	GL (%)	Position (eV)	Area	FWHM (eV)%	GL(%)
CuS1 - double doublet						*CuS1 - asymmetric profile*			
Cu(I)	2s 3/2	932.1	60871	1.9	32	932.0	98553	1.6	36
	2s 1/2	952.0	30436	2.6	3	951.9	49276	2.2	1
Cu(I+)	2s 3/2	934.3	15235	1.9	36				
	2s 1/2	954.6	7617	2.6	1				
Energy-loss		962.9	4088	4.7	100	944.6	7080	3.7	100
		942.2	8176	4.7	100	949.4	10898	3.7	100
		943.9	8650	4.7	100	954.7	8573	3.7	100
		942.2	8176	4.7	100	942.2	9327	3.7	100
		962.9	4088	4.7	100	962.9	4663	3.7	100
CuS2 - double doublet						*CuS2 - asymmetric profile*			
Cu(I)	2s 3/2	932.1	4558	1.6	45	932.1	6305	1.6	50
	2s 1/2	952.0	2279	2.4	3	951.9	3152	2.1	50
Cu(I+)	2s 3/2	933.8	945	1.6	45				
	2s 1/2	954.1	473	2.4	3				
Energy-loss		942.8	598	4.5	64	942.5	637	7.3	13
		948.7	906	4.5	64	949.6	775	7.3	13
		955.9	987	4.5	64	954.5	1117	7.3	13

The presence of multiple energy-loss peaks was needed to be included in order to correctly obtain the 1:2 area ratio for $p_{1/2}$ and $p_{3/2}$ photoelectron peaks. As starting guess for these components, the same secondary peaks used by Cabrera-German *at al.*[164] were considered, while minimizing the total number of peaks in the fitting. Five energy-loss peaks were necessary for the CuS1 sample, that indeed showed a more complex structure between the two photoelectron components, while only three were used for the CuS2. The fitting parameters obtained are reported in Table 3.3. The $2p_{3/2}$ photoelectron peaks were found around 932 eV, as typical of Cu(I), while in the case of the double-doublet approach, the secondary components were found at around 934 eV, that is a value compatible with Cu(II).[165] In the CuS1 sample, the photoelectron lines displayed a more asymmetric profile in comparison with the same components of the CuS2 sample. Moreover, the satellite components were more intense in the CuS1 sample. Indeed, the two additional peaks added in the CuS1 were found at higher binding energy to the $2p_{1/2}$ and $2p_{3/2}$ photoelectron lines respectively, and this might be related with the expected

presence of satellites for Cu(II). Since the presence of the shack up peaks is a typical feature of Cu(II),[165] from a qualitative point of view is possible to assume that a Cu(II) character may exist in CuS1. For CuS2, energy-loss components were barely visible from the spectra profile alone. Comparing the quality of the two fitting approaches, using an asymmetric line-shape allowed to obtain better results, with particular reference of the high binding energy side of the $2p_{3/2}$ peak. Therefore, it is possible to hypothesize that the correct line shape for the $2p_{3/2}$ components was the asymmetrical one. The more pronounced Cu(II) character in the CuS1 spectrum (more asymmetric profile of the $2p_{3/2}$ peaks and the increased intensity of satellites between them) might, at this point, be related to the presence of surface oxidation instead of being related to an intrinsic feature of the material surface.

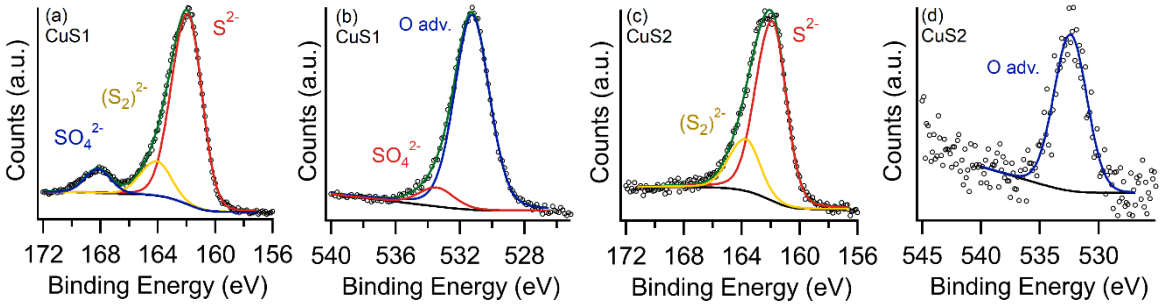

Figure 3.8 Fitted S2p (a) and O1s (b) XPS regions of sample CuS1, and S2p (c) and O1s (d) XPS regions of sample CuS1.

The fittings of the S2p region were entirely performed using the expected doublets for p photoelectron lines. Three sets were employed for CuS1, while two sets were used for CuS2. Both S^{2-} and $(S_2)^{2-}$ were obtained,[169] as expected from the crystal structure. In the case of CuS1, the additional doublet at 168.2 eV is compatible with the presence of sulfates.[169] Therefore, in the case of CuS1, a detectable surface oxidation was found, while no oxidation was visible for CuS2. This evidence supports the mentioned possible presence of Cu(II) in the CuS1 sample as results of surface oxidation. The presence of sulfates in CuS1 was also confirmed by the presence of a small peak at 533.5 eV in the O1s spectrum. Apart from this additional signal, only a single peak was found in the O1s regions, related to the common adventitious contamination. This also ruled out a detectable presence of oxide on the surface for both samples, as the O1s component for copper oxides was commonly reported to be around 529 eV.[164]

Overall, the XPS analysis revealed that the obtained samples were free of relevant surface contaminations, except for the presence of a small concentration of sulfates on CuS1. From the Cu2p analysis, it was not possible to confirm or disprove the presence of a Cu(II) character as related to the crystal structure alone. However, the best results were obtained assuming asymmetric peak shapes, suggesting that the formula $(Cu^{1.3+})_3(S_2^{2-})(S^-)$ could be best suited as a ionic model to describe the samples. A more advanced approach to the XPS analysis is advisable to achieve a better understanding

of the Cu2p region of the covellite, like the charge transfer multiplet (CMT) approach.[166] Meanwhile, from the obtained results, it is possible to hypothesize that a relevant intensity (more than what observed for sample CuS2) of the satellites' structure between the two Cu2p peaks could be used qualitatively as an indication of the presence of detectable surface oxidation on the CuS covellite surface.

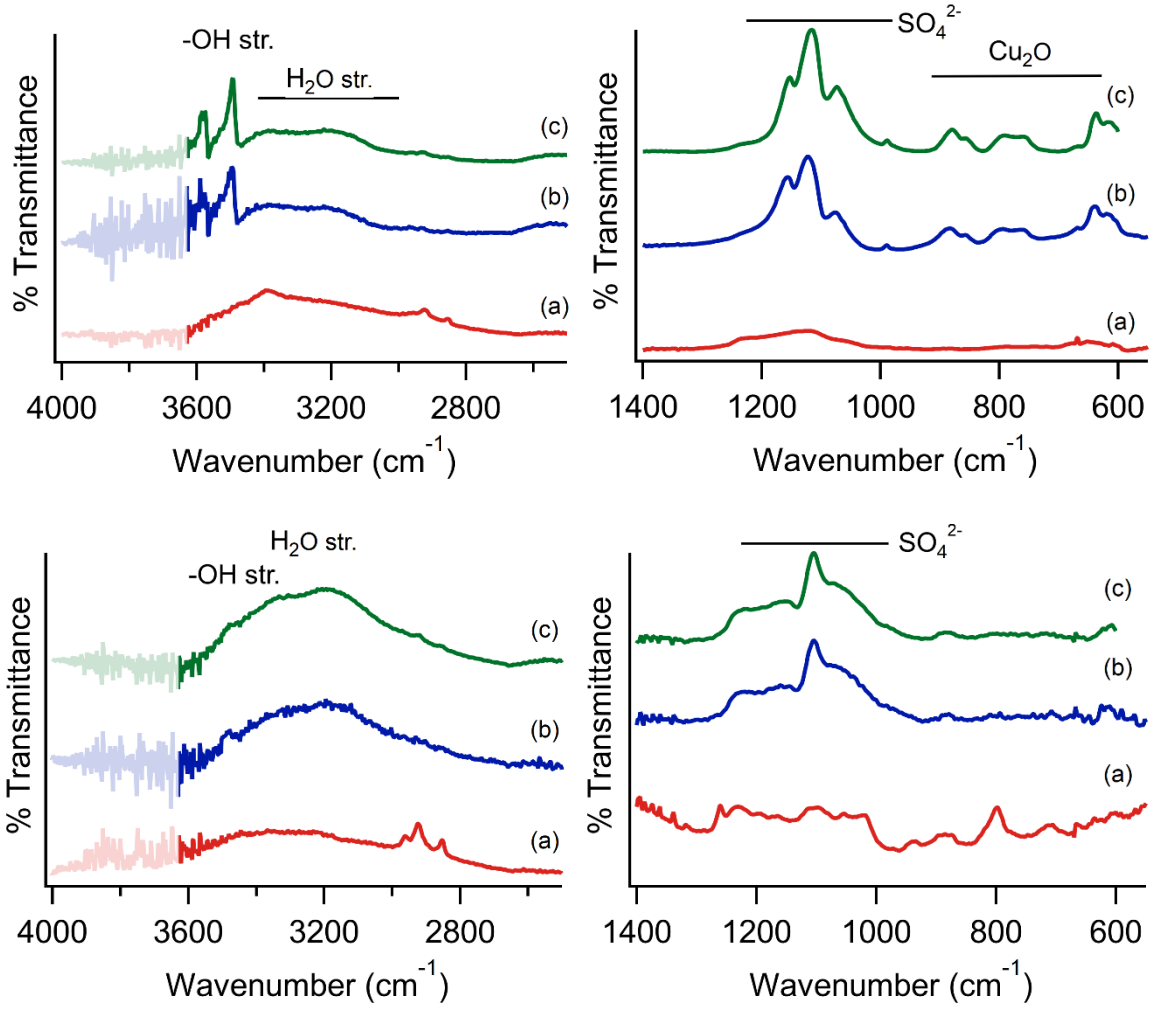

Figure 3.9 Relevant regions of the FTIR spectra of samples CuS1 (up) and CuS2 (down) recorded after different times: (a) freshly synthesized, (b) one month, (c) two months.

The assessment of the surface properties of the samples was complemented by FTIR spectroscopy, to detect possible adsorbed moieties or functional groups. The spectra were characterized by a strong background with weak IR peaks intensities in the analyzed range. The background was interpolated with a cubic spline function to reduce the possibility of generating artifacts. A first spectrum was obtained on the freshly synthetized samples, then they were analyzed again after one month and two months while normally storing them in closed vials with no special precautions. In all the obtained spectra, the sample-related signals showed negative intensities, i.e. they would correspond to wavelength where the sample were absorbing less radiation with respect to the background. Any

contribution from an erroneously subtracted background was excluded and observed line shapes and positions are compatible with the observation of Dunn and Muzenda.[170] The phenomenon was interpreted as a distortion related to the employment of the ATR setup equipped with a diamond crystal for the analysis of this material. Further investigations are ongoing. The interpretation was carried out as the peaks assumed the corresponding positive intensity, as this interpretation was confirmed by previous report on oxidation phenomena of CuS covellite.[170]

In the as-synthetized CuS2 sample, only a weak broad signal at 3317 cm^{-1} was observed, related to the presence of adsorbed water molecules on the surface. An analogous but more intense broad peak was observed in the CuS1 samples at 3394 cm^{-1}, indicating an increased presence of water molecules with respect to CuS2. Moreover, a peak at 1124 cm^{-1} was found, having two shoulder components at 1126 cm^{-1} and 1068 cm^{-1}. These peaks were compatible with the presence of sulfates, as also detected by XPS.[106,170] The presence of three visible components indicates the splitting of the v_3 triple degenerate asymmetric stretching mode, caused by a lowering in symmetry from the T_d point group. Such symmetry perturbation is likely to be small, as the v_1 symmetric stretching mode (that is not IR active in the T_d symmetry) is still not distinguishable. Therefore, sulfates are likely to only weakly bind the surface of the material. An alternative explanation would be the formation of a small amount of bulk sulfates that was not detectable with the XRD analysis. In CuS1, a weak signal centered at 652 cm^{-1} was also observed. This peak was described as diagnostic of the formation of Cu_2O.[170] On the fresh sample (red spectra, Figure 3.9) the presence of -CH_x stretching signals around 2900 cm^{-1} was attributed to the presence of traces of organic cleaning solvents on the ATR crystal.

Spectra acquired after one and two months showed an overall increase in the intensity of signals originating from oxidation phenomena, together with an increase of the signal arising from adsorbed water molecules. In CuS1 both the sulfate and the Cu_2O signals became more intense, while an increase in water absorption was also evident. Moreover, a peak at 3496 cm^{-1} appeared, that is likely related to the formation of isolated -OH moieties on the surface related to the oxide formation. In sample CuS2, a peak centered at 1105 cm^{-1} became visible, having two shoulders at 1059 cm^{-1} and 1689 cm^{-1}. This signal is compatible with the presence of sulfates also in the aged CuS2, however having a different geometry of interaction due to the different observed line shape. It is hypnotizable that the sharper central peak observed in this case was originated by a double degenerate v_3 degenerate asymmetric stretching mode of sulfates having the C_{3v} symmetry, and therefore interacting as monodentate.[106,170]

Overall, these results indicate that, with the exception of a minor amount of interacting water molecules, no functional groups were found on the pure surface (e.g. no native -OH or -SH groups). CuS NPs are however susceptible to oxidation at room temperature. Oxidation was found to produce sulfates and Cu_2O in accordance with previous reports of oxidation experiments on covellite.[170] Since

the oxidation proceeded to a faster rate on the smaller NPs of the CuS1 sample, it is likely that the phenomenon was size-dependent. This suggests that the reactivity of the material is altered as NPs size is lowered. Therefore, in the case of small NPs, it highly advisable to store the material under inter conditions and to use freshly made samples if a clean pristine surface is required or desirable.

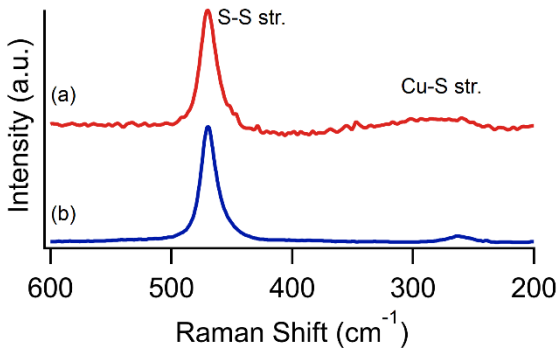

Figure 3.10 Raman spectra of the CuS1 (a) and CuS 2 (b) samples.

The FTIR analysis was complemented with Raman spectroscopy (Figure 3.10). In both spectra a strong peak was found at 470 cm^{-1} corresponding to the A_{1g} mode, referred as the S-S stretching in the crystal structure.[171] A second peak was found at 280 cm^{-1} for CuS1 and at 263 cm^{-1} for CuS2. This signal is commonly attributed to the Cu-S stretching in the structure.[171] While the S-S peak did not display a significant shift between the two samples, a relevant difference was found for the Cu-S signal. The position observed for CuS2 is indeed very close to the literature values,[171] while, in CuS1, the peak is significantly broadened and shifted toward higher frequencies.

From the surface assessment of the as-synthesizes samples, the absence of oxidation was retrieved for sample CuS2, while the formation of sulfates was observed for CuS1. The FTIR analysis indicated the appearance of sulfates for both samples and the formation of Cu_2O on the surface of the CuS1 after one month of air exposure. Therefore, CuS covellite showed to be sensitive to oxidation even at room temperature if not conserved under proper protected conditions. As smaller NPs sizes were retrieved in sample CuS1 in comparison to sample CuS2, it is plausible that the observed surface oxidation was size-dependent, indicating an increased reactivity of the smaller NPs.

3.2 Lead sulfide - PbS

Lead sulfide is a semiconductor having a band gap of 0.41 eV.[172] By reducing the size of the material down to the range of the nanostructures, the bandgap can be tuned from the NIR to the visible part of the spectrum, in the range 0.8 - 1.8 eV.[173] For this reason, PbS found many applications in photodevices that operated in the infrared range, like infrared detector, photoemitter, nonlinear element, and sensor.[174] Moreover, PbS is also a candidate light-harvesting additive in photovoltaic cells,[175–177] not only for the absorption properties in the visible spectrum, but also for the favorable conversion of the excess energy absorbed to extra hole-electron pairs (carrier multiplication phenomenon).[178,179] However, these attractive properties were also observed to be spoiled by the rapid oxidation of the NPs, that gradually reduces the size of the PbS phase, leading to the blue shift of the light adsorption.[180] Therefore, an increasing interest in the characterization of oxidation phenomena of PbS NPs is now emerging[181,182] as the protection of the PbS surface by employing passivating ligands was found to be not sufficient to protect the NPs.[182]

The most common synthetic methods of PbS nanoparticles relies on a colloidal organic-solvent based approaches and normally requires the employment of organometallic precursors for Pb,[183,184] while in the reports of syntheses carried out in water employed common salts as precursors and where aided by the addiction of stabilizing agents.[185,186] Here, the ligand-less batch approach was successfully applied to PbS, pursuing both the obtainment of NPs and the study of oxidation phenomena.

3.2.1 Crystal structure, size and morphology

The obtained crystal structure was assessed XRD. For both PbS1 and PbS2 samples only the pattern of PbS galena (ICSD 98-003-8293, space group F m -3 m) was retrieved, indicating the material was free of crystalline contaminations.

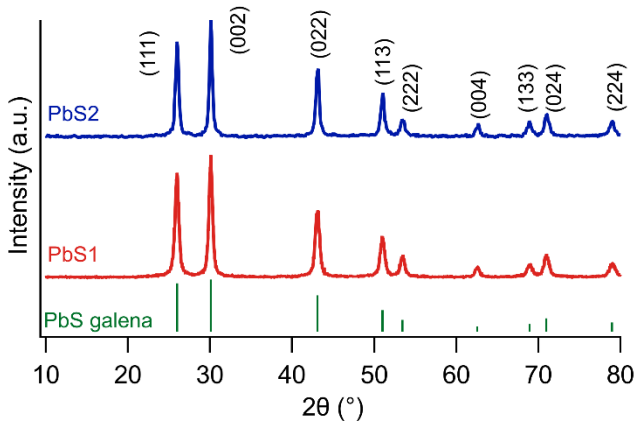

Figure 3.11 XRD patterns retrieved for the PbS1 and PbS2 samples.

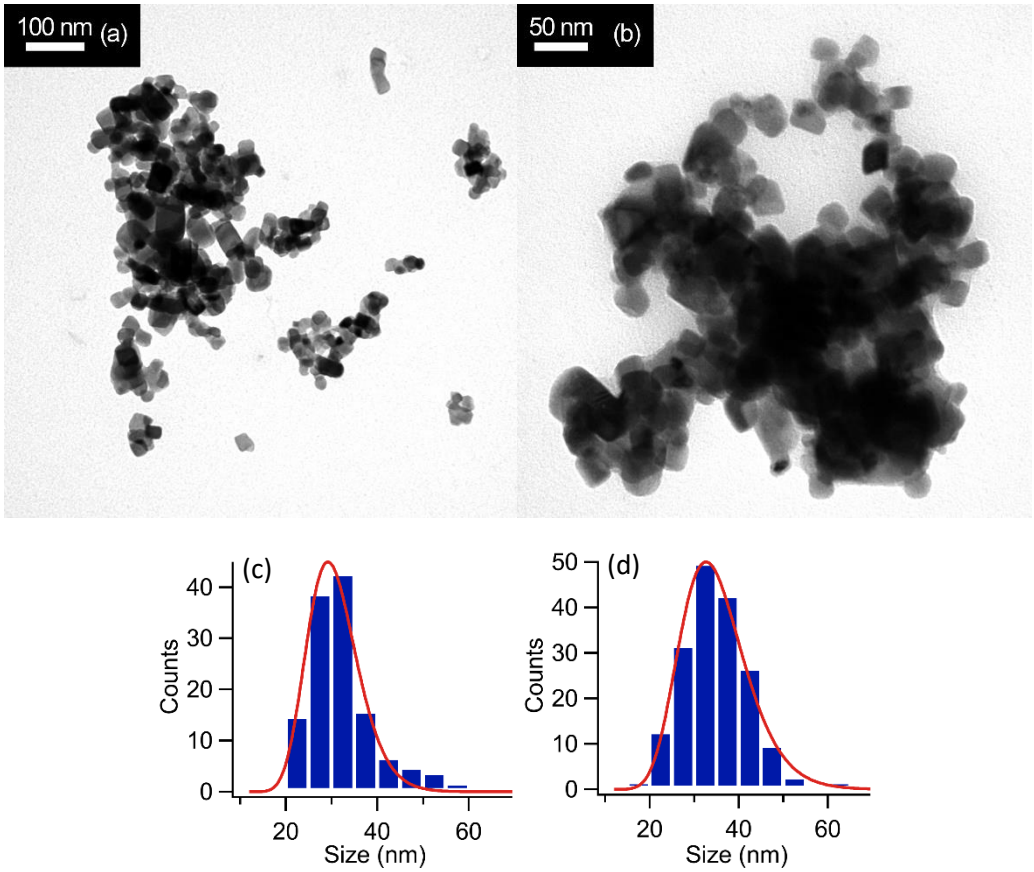

Figure 3.12 TEM micrographs from samples PbS1 (a) and PbS2 (b). Equivalent spherical diameter distribution obtained from the segmentation procedure for samples PbS1 (c) and PbS2 (d).

From the TEM micrographs (Figure 3.12), squared NPs were observed. As no capping ligands or surfactants were employed during the synthesis, particles displayed the tendency to aggregate on the TEM grid. Since a squared shape was observed, the dimensional analysis was performed by segmenting the individual particles with rectangles, obtaining a long a and a short dimension, along with the projected area. From the measured dimensions, aspect ratio and equivalent spherical diameter (i.e. the diameter of a sphere projecting the same area to a measured particle) were calculated.

Table 3.4 Size distribution descriptors obtained from TEM population of sampled particles, from TEM distribution fitting and from refined XRD data. AR = aspect ratio.

	TEM Major	Minor	Avg. AR	Eq. Diam	TEM-fitted Eq. Diam	Refined Eq. Diam
Sample PbS1						
$D_{1,0}$ (nm)	34	26	1.3	30	31	
Std. dev. (nm)	10 (30%)	7 (27%)		8 (27%)	5 (19%)	
$D_{3,2}$ (nm)				35	33	
$D_{4,3}$ (nm)				38	34	26
Skewness	1.5	1.3		1.4	0.6	
Kurtosis	2.3	2.9		2.9	0.6	
GoF						1.3
Sample PbS2						
$D_{1,0}$ (nm)	36	29	1.3	32	35	
Std. dev.	10 (27%)	7 (23%)		8 (23%)	8 (21%)	
$D_{3,2}$ (nm)				36	38	
$D_{4,3}$ (nm)				38	40	33
Skewness	0.8	1.0		0.6	0.7	
Kurtosis	2.3	1.0		1.3	0.8	
GoF						1.2

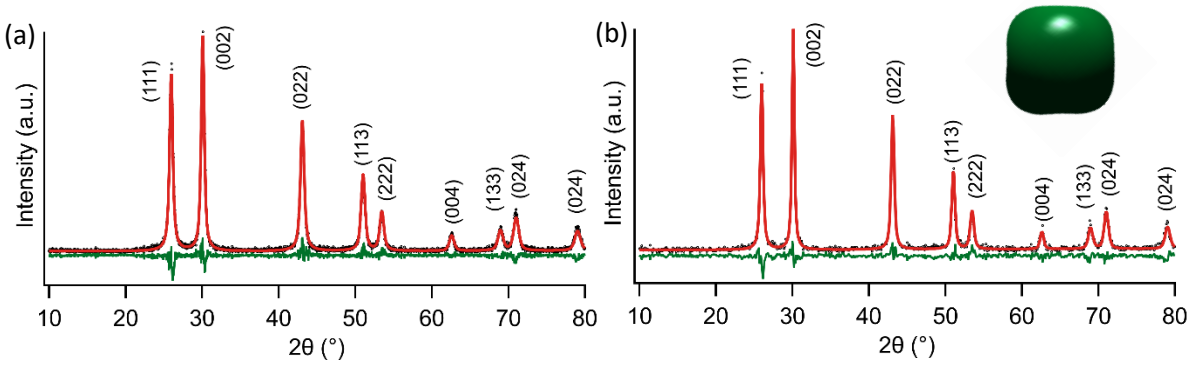

Figure 3.13 Refined XRD profile for samples PbS1 (a) and PbS2. (b) Inset: equivalent crystallite shape obtained employing the Popa model for anisotropic crystallites.

The equivalent spherical diameter was employed to obtain the relative diameter distribution to approximate a description based on a single dimensional descriptor. The obtained spherical diameter distribution was fitted using a lognormal distribution. The retrieved descriptors are reported in Table 3.4. Both PbS1 and PbS2 showed almost equal $D_{1,0}$ sizes of 31 nm and 32 nm. The polydispersion retrieved was limited, as the retrieved standard deviation was 8 nm in both cases, corresponding to a relative standard deviation of 27% and 23% respectively. In general, standard deviation values for the calculated parameters was comprised between 20% and 30%. The average aspect ratio of 1.3 for both samples indicates a similar average shape, being slightly deviated from the proportion expected for a

perfect cube. Overall, little difference was evident from the TEM analysis between the two samples with regards to size and morphology.

The dimensional and morphological analysis was complemented by refining the obtained XRD patterns.[84] The model developed by Popa *et al*.[154] was employed to model reflections broadening accounting for the observed anisotropy of the NPs. From the fits, the equivalent isotropic diameter $D_{4,3}$ (i.e the diameter of the spherical particle producing the analogous non-anisotropic pattern of the one recorded) obtained was 26 nm and 33 nm for the PbS1 and PbS2 respectively. Therefore, the analysis confirmed that, using Na_2S as precursor instead of NaHS, a sensibly smaller average particle size was achieved, similarly to ZnS and CuS. It can be assumed that the batch synthesis here employed allows to tune the final average NPs size by properly mixing the two sulfur precursors, even though the explorable NPs size range would be, in this case, minimal. By constructing the crystallite shape from the spherical harmonics used in the Popa model to account for crystallite anisotropy, a squared shape was obtained (Figure 3.13 inset), as expected from the NPs morphology observed with the TEM analysis. Comparing the estimated average values with the $D_{4,3}$ averages obtained from the TEM analysis, a relevant underestimation is evidenced. This is likely to be related to instrumental contributions in the reflections broadening, and a more accurate calibration of instrumental broadening effect might be required.

3.2.2 Surface composition

The surface composition of the samples was studied using XPS spectroscopy. From the survey spectra (Figure 3.14) only Pb and S were detected, apart from C and O originated from adventitious contamination.[100] From the semi-quantitative analysis, a Pb:S atomic ratio of 1:0.9 was retrieved, indicating that the surface shares the same stoichiometry of the bulk. A precise attribution of the higher energy binding component is matter of a long-lasting debate, and is connected to the oxidation mechanism of PbS galena.[181,187–190] Analogous peaks were attributed to the possible formation of lead oxide, hydroxide, carbonate and hydroxycarbonate in dedicated studies.[181,188,189] In the case of the region O1s of the sample PbS1, the presence of a component at 528.8 eV was observed, along with the adventitious peak at 531.3 eV, that confirmed the presence Pb-O bonds. In the PbS2 sample, only one peak attributed to adventitious contamination was found at 532.0. The interpretation of the S2p region is complicated by the presence of an irregular background caused by energy-loss components of the Pb4f peaks with the possible presence of contributions also arising from the Pb5s peak.

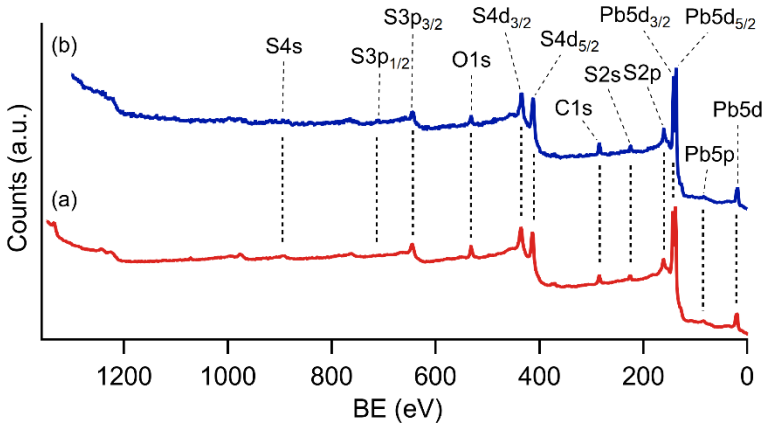

Figure 3.14 XPS survey spectra of samples PbS1 (a) and PbS2 (b).

Table 3.5 Observed peaks position in the XPS spectra of PbS samples.

Peak	PbS1 (eV)	PbS2 (eV)	Reference[99]
Pb4s	893.4	-	-
$Pb4p_{1/2}$	763.8	764.6	-
$Pb4p_{3/2}$	645.4	645.4	-
$Pb4d_{3/2}$	435.8	435.0	-
$Pb4d_{5/2}$	412.6	411.8	-
$Pb4f_{5/2}$	142.4	142.4	-
$Pb4f_{7/2}$	137.5	137.5	137.8 - 137.5
Pb5p	83.8	83.0	-
$5d_{3/2}$	19.0*	19.0*	21.6
$5d_{5/2}$	19.0*	19.0*	18.5 - 19.1
S2s	225.4	224.6	225.3
S2p	160.7	160.7	160.4 - 161.9

(*) spin-orbit components not resolved.

The S1p doublet displayed an additional feature at lower binging energy, around 159 eV (Figure 3.15 b,e). Since the retrieved position of the main component was 160.7 eV for both samples, which is compatible with S^{2-} in PbS,[181,187] the additional feature cannot be attributed to S photoelectrons emission. Therefore, the additional component was considered arising from the energy-loss peak of Pb4f. From the obtained spectra, no visible contribution from oxidized sulfur compounds was evident. The absence of these features despite the prolongated exposure to air, and, despite the evidence of oxidation in the Pb4f region, was already reported.[189] Cryogenic-temperature XPS experiments reported the formation of weakly bound elemental sulfur as primary product of the sulfide oxidation, while only after extensive periods of exposure to air, sulfates and sulfites were clearly detected.[187,189] Therefore, the samples here analyzed appears to be in an early step of S oxidation, where surface SO_x may not be already formed and S(0) could not be detected due to its desorption in high-vacuum conditions.

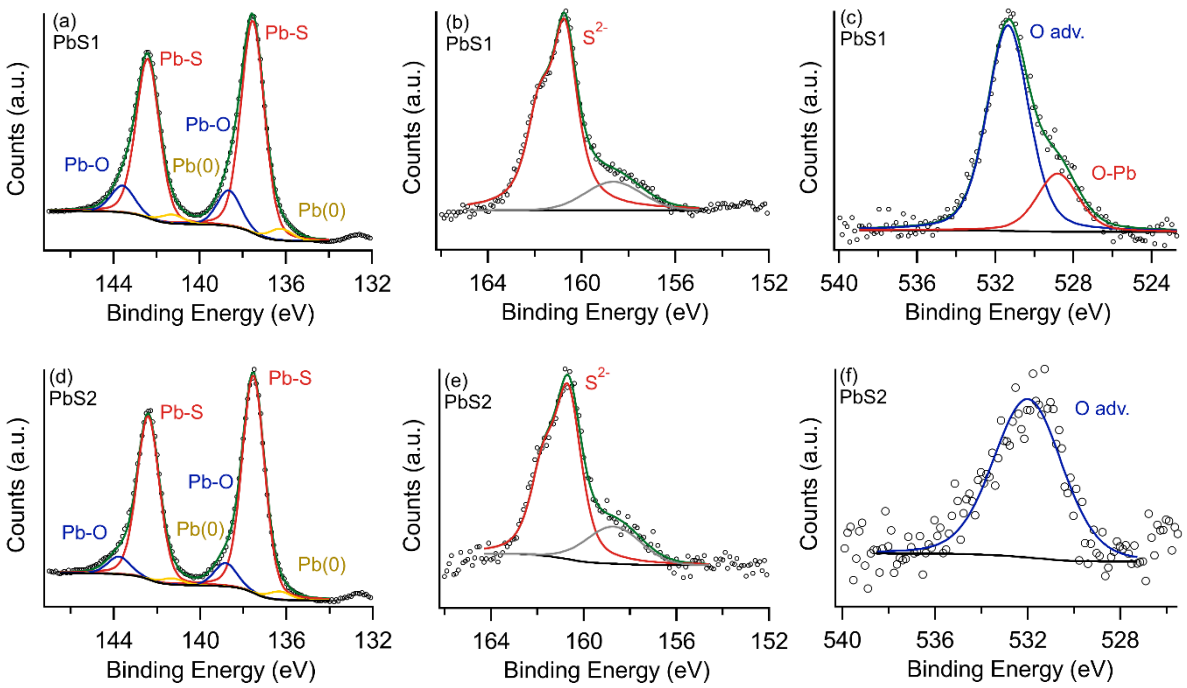

Figure 3.15 XPS fits of sample PbS1: Pb4f (a), S2p (b) and O1s (c); sample PbS2: Pb4f (d), S2p (e) and O1s (f).

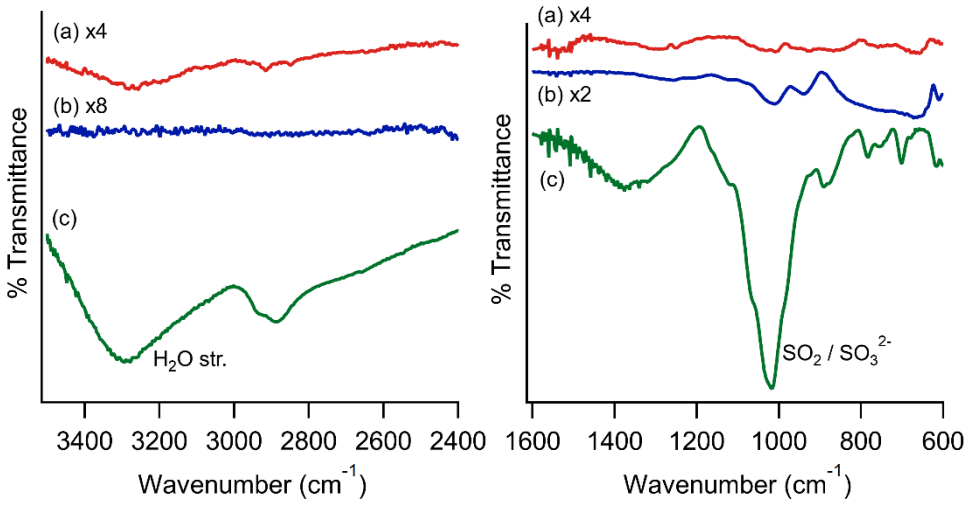

Figure 3.16 Relevant regions of the FTIR spectra obtained from as-synthetized PbS2 (a), two weeks aged PbS2 (b) and one year aged PbS1 (c). Spectra obtained from PbS2 were multiplied with the indicated factor to allow an easier visual comparison.

The analysis was extended using FTIR spectroscopy to detect the presence of adsorbed moieties or functional groups anchored to the surface. The interpretation of the spectra was complicated by an irregular background, that did not allow a reliable distinction of the weak peaks retrieved, especially for sample PbS2. PbS2 was analyzed shortly after the synthesis and after two weeks of normal (air-exposed) storage conditions. A group of weak signals in the range 1160 - 1450 cm^{-1} was observed in

both spectra. Similar signals were reported in the case of CO_2 interacting as a Lewis base to oxides surface,[191] but no complementary peaks around 2300 cm^{-1} were observed. An alternative explanation may consist in weakly adsorbed SO_2, as a weakly bound surface oxidation product.[192] In the low frequency region, the spectra background assumed a tightly bent shape, making difficult and prone to error the identification of peaks. Signals were retrieved in this region, especially at 1010 cm^{-1} and 937 cm^{-1}, that may be assigned to the presence of sulfites on the sample.[192,193] By considering the oxidation mechanism hypothesized by Cant *et al.*,[181] lead oxidation should proceed toward the formation of $Pb(OH)_2$, while the first step for the sulfur oxidation was predicted to be the protonation of sulfide to from -SH groups. Both these signals were not visible in the acquired spectra, as at high frequencies only a broad peak centered at 3267 cm^{-1} was visible in the as-synthetized sample. This signal was compatible with the stretching mode of adsorbed water molecules. The complete absence of adsorbed water was instead retrieved for the sample after two weeks. Therefore, it is possible that the obtained particles were in fact free of relevant surface oxidation, or that the currently proposed oxidation path is scarcely applicable to the analyzed system.

The PbS1 sample was analyzed after an extensive storage period of approximatively one year. The retrieved peaks were found to be substantially more intense, as expected from the gradual formation of oxidation products over time. In the spectra, the presence of adsorbed water was again retrieved from the HOH stretching band at 3288 cm^{-1}. A broad peak centered around 1363 cm^{-1} was also found, that may be again be interpreted weakly adsorbed SO_2.[192] The strong peak at 1018 cm^{-1}, having a weaker component at 889 cm^{-1} was again attributed to the formation of SO_x species, and likely attributed to sulfites.[192] A broad peak also appeared at 2885 cm^{-1}. The position of this signal would be typical of the stretching of aliphatic -CH_x groups, but, since no organic species were expected to be found on the surface, this attribution is unlikely. Comparing the retrieved line shape with the -SH stretching peak reported by Hertl[194] on commercial ZnS, a certain line shape similarity was noticed. Moreover, the broadening of this signal may be associated to the formation of hydrogen bonds (possibly with water molecules), similarly to the adsorbed water molecules, that do not occur with aliphatic -CH_x. This made possible to assume that the signal was related to the presence of -SH moieties having a peculiarly high stretching frequency, as they would normally appear around 2500 cm^{-1}. This observation would align with the predicted presence of such group on the PbS surface as effect of oxidation phenomena made by Cant *et al.*[181]

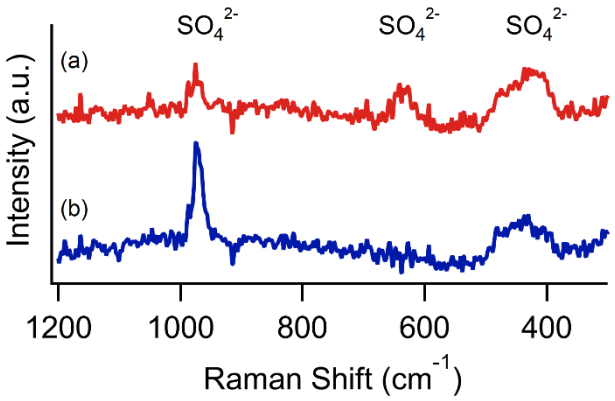

Figure 3.17 Raman spectra of samples PbS1 (a) and PbS2 (b).

The Raman spectra of the samples were also recorded to complement the characterization of the sample. Since CuS galena possess a rock-salt structure, none of the crystal vibrational modes are Raman active, and the spectra of a freshly cleaved galena surface was reported to be completely featureless.[195] The peaks found on air-exposed surfaces were therefore exclusively produced by oxidation products or other contaminations. In the case of PbS1, three weak peaks at 974, 635 and 439 cm^{-1} were visible, while only two peaks at 975 and 439 cm^{-1} were observed for PbS2. All these signal were consistent with heat-induced formation of sulfates caused from the laser irradiation during the Raman analysis.[195] Since no sulfates were visible at the FTIR analysis, the formation of sulfates is likely to be entirely caused by the local increase of temperature.

The characterization of the PbS NPs by XPS, FTIR and Raman spectroscopies showed for both samples a similar condition. The presence of oxidation was confirmed only by a minor component of the Pb4f XPS region, and from the presence of an additional component at low binding energy in the O1s region for PbS1, indicating the oxidation of Pb had occurred. In freshly made samples, a reliable identification of the formed surface compound was not achievable due to lack of other spectral components possibly arising from it. It was also not possible to clearly obtain evidence of the presence of sulfur oxidation. Overall, despite particles were synthetized in water and not conserved under inter atmosphere, only little oxidation was found, as typical of the very early stages of air-exposed PbS.[189] Therefore, employed synthetic method is suitable to obtain pure NPs. The presence of sulfur oxidation became more visible after approximatively two weeks of air exposure and gradually got relevant after a long period, remarking the importance of proper storage conditions for this material. This result contrasts with previous reports of the strong oxidation sensitivity for very small PbS NPs (about 4 mn), that where observed to be significantly oxidized even after few hours of air exposition.[180] This suggests a strong size-dependence for oxidation in PbS.

3.3 Manganese sulfide – MnS

Manganese sulfide is a p-type semiconductor having a wide band gap of ~3 eV,[196] that is also characterized by interesting magnetic properties, as it possess a Nèel temperature of 80 K (γ-MnS), 100 K (β-MnS) and 154 K (α-MnS), depending on the polymorph.[197] Indeed, MnS is known in three polymorphs. The most common and stable one is the cubic α-MnS, while other two metastable phases exists: cubic β-MnS and hexagonal γ-MnS. MnS properties were used to develop different applications in the fields of photocatalysis,[198] for bioimaging as contrasting agent in MRI,[199] as photoluminescent material[200] and in the field of short wavelength optoelectronics.[201] The different polymorphs were also applied in different fields. α-MnS found applications as microwave absorber and as electrode material in Li-ion batteries for its Li storage capabilities,[88,202,203] while γ-MnS was used for electroluminescent displays and light emitters.[204]

The first documented synthesis of MnS NPs was reported by Kan *et al.*[205] who employed a hydrothermal method to obtain pure α-MnS. The hydrothermal approach was than later developed, to allow the synthesis of either pure α-MnS or mixed β-MnS and γ-MnS in a organics-free approach.[206] Single-source precursors[207] and heat-up approaches[208] have also been used successfully.

3.3.1 Crystal structure, size and morphology

The crystalline phase of the obtained MnS1 and MnS2 samples was firstly checked by XRD. The diffractogram of sample MnS2 (Figure 3.18b) indicated the presence of β-MnS (browneite, ICSD 00-040-1288, space group F-43m) as major component, along with the presence of γ-MnS (rambergite, ICSD 00-040-1289, space group P63mc). Refining the obtained XRD pattern, it was determined that the sample was composed by 73% wt. of β-MnS, while γ-MnS constituted the remaining 27% wt. The reduced reflections broadening also indicated that the average crystallite size was > 100 nm. A very different situation was indeed detected for sample MnS1, where only a small bump was observed at 27.6°, suggesting the presence of poorly crystalline β-MnS, while the presence of $Mn(OH)_2$ (ICSD 98-002-3591, pyrochroite, space group P -3 m 1) was clearly visible. As the sample MnS1 displayed poor crystallinity and strong oxidation, it was not further characterized. Therefore, in the case of MnS, it appeared that the pH played an important role on the formation of MnS. In the case of MnS1, when Na_2S was employed as sulfur precursor (pH 13.0 – 12.6), a consistent formation of $Mn(OH)_2$ was observed. On the contrary, the employment of NaHS (pH 11.3 - 10.6) led to the formation of only MnS.

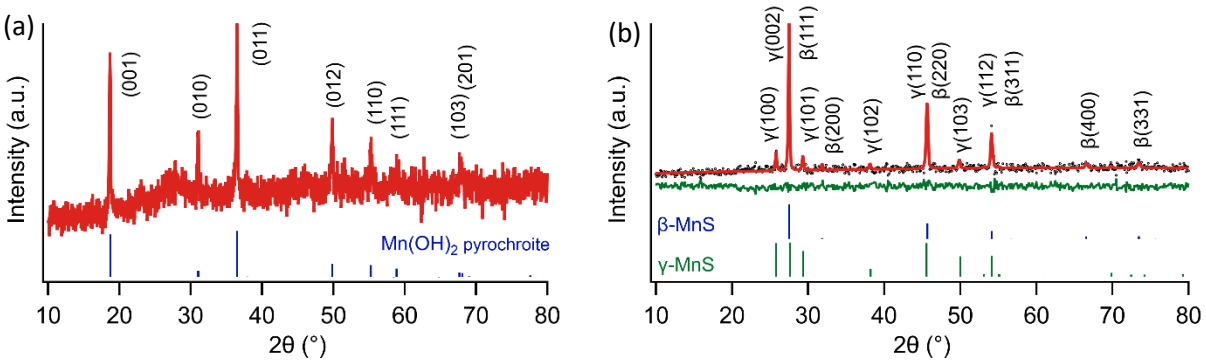

Figure 3.18 XRD pattern retrieved from samples MnS1 (a) and MnS2 (b), and refined profile of the MnS2.

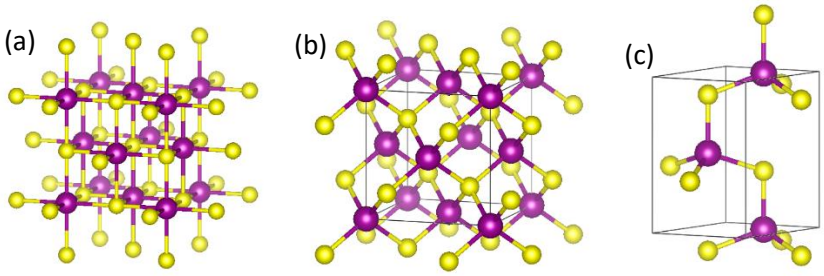

Figure 3.19 Crystal unit cells of α-MnS (a), β-MnS (b) and γ-MnS (g).

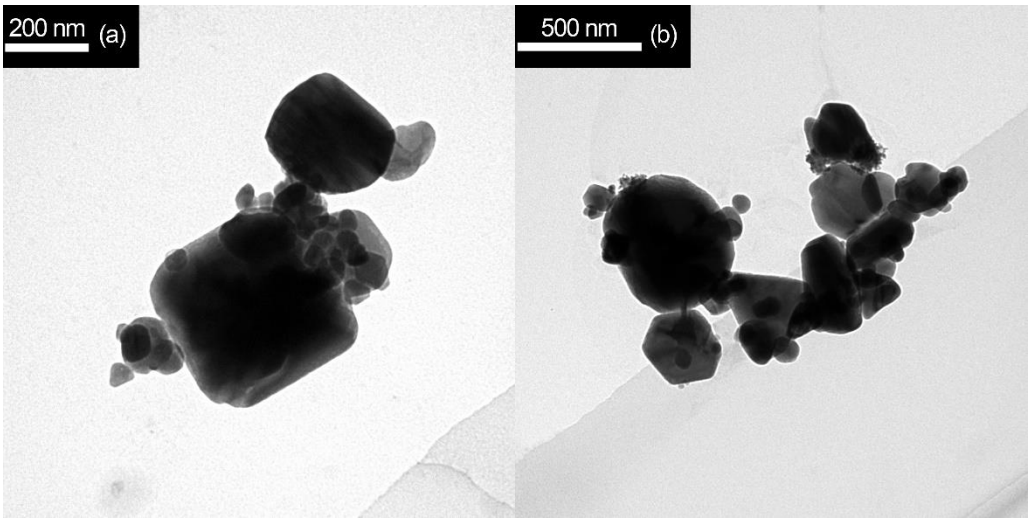

Figure 3.20 TEM micrographs of the MnS2 sample at different magnification.

From the TEM analysis, polygonal particles were obtained for sample MnS2, having a broad size polydispersion. Particles size were found to vary roughly from 40 nm to 200 nm, with additional smaller particles visible as small aggregates (Figure 3.20b). Noticeably, both β-MnS and γ-MnS are known to be metastable phases, since the thermodynamically stable phase is the cubic α-MnS phase, having a rock-salt type of structure.[206] An analogous synthetic approach was employed by Michel *at al.*,[206] who developed a hydrothermal method for the synthesis of pure α-MnS. In the same work, it was reported the precipitation of mixed β-MnS and γ-MnS by mixing a 0.2 M $ZnCl_2$ with 0.2 M Na_2S solution having low crystallinity and small particle dimension, being the first water-based and organics-free synthesis of these metastable phases. It was reported that particles were easily oxidized upon exposure to air, in perfect agreement with the presence of $Mn(OH)_2$ here reported for sample MnS1. The particles were described to convert entirely to α-MnS upon aging at high temperature. Veeramanikandasamy *et al.*[209] reported another water-based synthesis that allowed the obtainment of pure-phase crystalline microparticles of both β-MnS and γ-MnS at 65 °C. In this case, Veeramanikandasamy *at al.* employed thioacetamide as sulfur precursors, along with ammonium chloride, triethanolamine and trisodium citrate as additives. In that work, the importance of the Mn:S molar ratio to control the final obtained phase was pointed out. In the framework of these syntheses, the employment of NaHS allowed to obtain crystalline air-stable β-MnS / γ-MnS particles at low temperature without the need of additional aging steps. Moreover, as a strong influence of many reaction parameters (i.e. choice of precursors, employed molar ratios and reaction temperature) was reported before,[206,210] it is plausible that more room for further optimization exists for this water-based organics-free approach, possibly allowing a better control over the final product. Accounting for the these results and the work of Michel *at al.*,[206] by properly adjusting the precursor pH by using mixed Na_2S and NaHS solution, it is likely that a strong effect on crystalline phase, morphology and reactivity of the obtained particles may be pursued.

3.3.2 Surface composition

The surface composition of the air-stable MnS2 sample was assessed with XPS spectroscopy. From the survey spectra (Figure 3.21) only peaks originated from Mn, S, C and O were observed. The presence of the last two elements originated from the common adventitious contamination of the samples.[100] A semi-quantitative analysis was performed, resulting on a S:Mn ratio of 1:1, that perfectly matched the stochiometric 1:1 ratio expected from the compound stoichiometry. This results was in agreement with the known low-defectivity of manganese sulfides.[211]

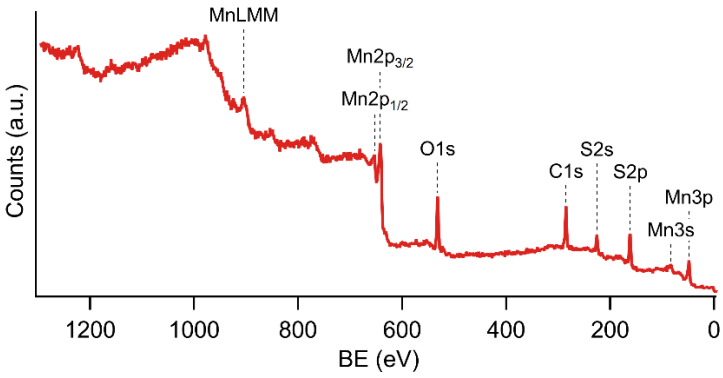

Figure 3.20 XPS survey spectrum of the MnS2 sample.

Table 3.6 Observed peaks position in the XPS spectra of the MnS2 sample.

Peak	MnS2 (eV)	Reference[99] (eV)
$2p_{1/2}$	652.6*	-
$2p_{3/2}$	641.2*	640.3 - 641.9
3s	83.0	82.6
3p	48.6	48.9 - 48.1
S2s	225.4	225.9
S2p	161.2	161.4 - 161.9

(*) maximum point of the multiplet.

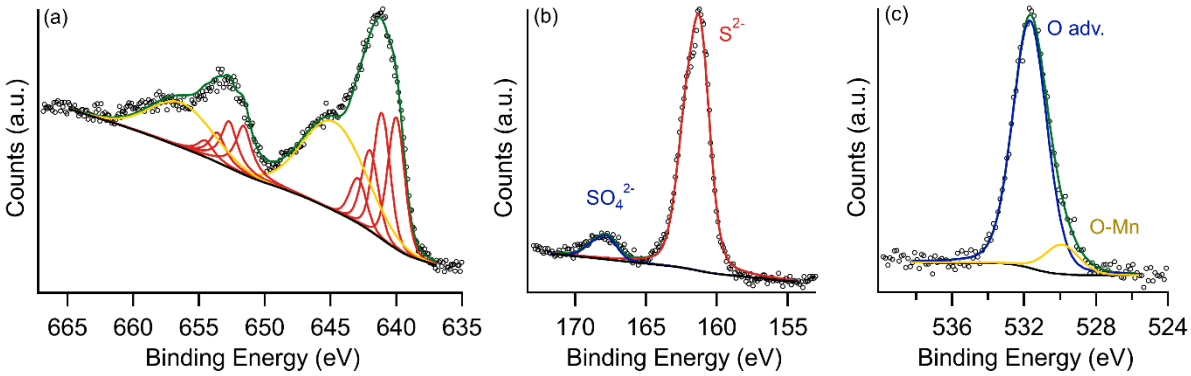

Figure 3.21 (a) XPS fitting of the Mn2p region employing the envelope approach developed for MnO (see text). XPS fitting of the S2p (b) and O1s (b) regions.

The interpretation of the Mn2p region was complicated by the known presence of relevant many-body effects.[212] The presence of unfilled 3d orbitals in Mn causes the single electron excitation approximation to break down, causing, in turn, the 2p signal to split in multiple overlapping components due to the coupling of the ionized core-level with the valence open shell. The total line shape is therefore highly asymmetric and complicated by the presence of satellites peaks.[166,212,213] For the interpretation of this region, different approaches can be found in the literature. Many authors based their analysis on a traditional single-body fitting, by employing the least number of peaks to

obtain a good reconstruction of the observed line shape. Normally, in this approach, components at different binding energy with respect to the main photoelectron line of Mn2p are ascribed to the presence of Mn in different oxidation states.[214–218] However, by using this method, serious concerns might be raised about the data interpretation, as the validity of the single electron excitation approximation is implied. Indeed, despite the Mn2p region has the highest photoionization cross section, the use of the 2s and 3p regions is generally best suited to retrieve information on the Mn oxidation state.[219–221] Alternatively, an improved empirical approach was developed to include multi-body effect. The single peaks employed for single-body excitation lines were substituted with envelopes of multiple narrow components.[222] These envelopes consists of peaks sharing a fixed relative width and were obtained for a reference compound having Mn in a known oxidation state. Starting from the reference fitting parameters, the analysis of a compound of unknown composition can be performed using the pre-determined fitting parameters for the envelopes on the experimental profile. However, these studies were mainly focused on Mn oxides, and no reference data to obtain peaks envelopes for manganese sulfides are currently available in the literature. As closest comparison, the envelope developed by Nessbit and Barnerjee[222] for MnO was employed to fit the MnS data in Figure 3.21.

Table 3.7 XPS fitting parameters employed for the application of the MnO envelope approach to the Mn2p region in MnS. GL (%) refers to the mixing of Gaussian and Lorentzian contributions in the pseudo-Voigt profile.

Peak	Position (eV)	Area	FWHM (eV)%	GL (%)
Envelope peak 1	640.0	454	1.5	19
Envelope peak 2	641.1	435	1.5	19
Envelope peak 3	642.0	277	1.5	19
Envelope peak 4	642.9	155	1.5	19
Satellite	644.7	1067	5.7	0
Envelope peak 1	651.6	227	1.5	100
Envelope peak 2	652.7	218	1.5	100
Envelope peak 3	653.6	139	1.5	100
Envelope peak 4	654.5	78	1.5	100
Satellite	656.3	534	5.7	0

In the model reported for MnO, five peaks were used with the addition of a sixth broader satellite peak. To allow a better evaluation of the background, both $2p_{3/2}$ and $2p_{1/2}$ peaks were fitted, by using for $2p_{1/2}$ an analogous envelope having a total area fixed to the half of the $2p_{3/2}$ area, as imposed from the spin-orbit coupling of 2p lines. The position of each $2p_{1/2}$ peak was fixed at 11.6 eV higher that the corresponding $2p_{3/2}$ component, to comply with the spin-orbit splitting of the region in MnS[223], with the exception of the satellite peaks position. The fitting parameters are reported in Table 3.7.

Comparing the obtained fit (Figure 3.21a) with the one reported by Nessbit and Barnerjee[222] for MnO, a much more intense contribution from the satellite peak was obtained, while the inclusion the fifth envelope component at the highest binding energy (originally employed for MnO) was observed to be unnecessary and was discharged. The fit performed poorly only in the $2p_{1/2}$ region not originally included by Nessbit and Barnerjee[222]. However, the increased intensity of the shoulder component at higher binding energy here fitted with the free satellites peaks resulted in a remarkably different line shape. Overall, the MnO envelope model did not appeared to be a good approximation to the observed MnS line shape, as different features were evidenced between the two spectra. Qualitatively, the position of the $2p_{3/2}$ maximum at 641.2 eV was compatible with other reports in the literature for MnS, and in general with Mn^{2+}.[222,224] Due to the lack of specific investigations on MnS, it was not possible to obtain reliable information on the presence of other oxidation states other than Mn^{2+} on the probed surface, or to assess the formation of Mn-O bonds from this spectral region. Since the line shape of the Mn2p region in pure MnS has not been established yet in the literature, it was not possible to distinguish possible additional components other the ones expected just for MnS alone.

The S2p region of the spectra showed a main peak located 161.2 eV, that can be associated to the S^{2-} oxidation state, while a weak additional signal was found at 167.7 eV. This second component can be associated either to sulfate or sulfite moieties as surface oxidation product of the material.[181] While the presence of sulfates or sulfites could not be confirmed by the O1s region, as no high energy components were found, a small contribution at 529.4 eV suggests the presence of MnO.[225] The main O1s peak at 531.6 was related to the adventitious contamination of the sample. Overall, despite the complexity and the lack of fundamental investigation on the Mn2p spectral region prevented an in-depth analysis of the contributions to the peaks, the purity of the surface could be assessed combining information from the S2p and O1s regions. The material surface was found to be mostly pure, with traces of Mn and S oxidation.

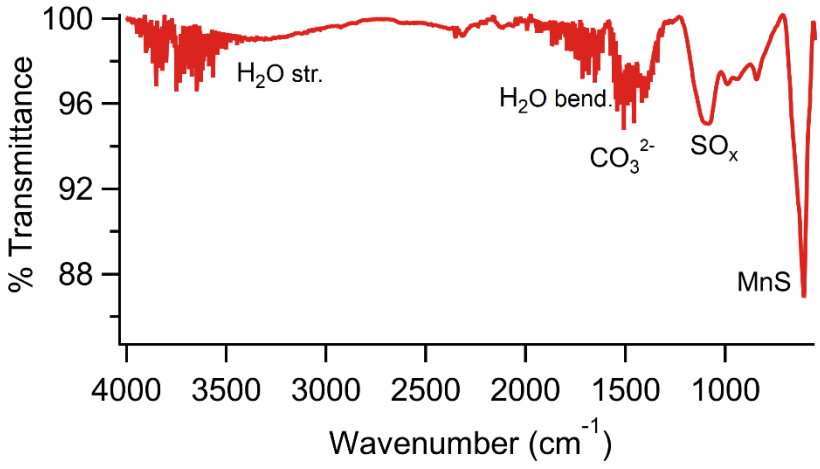

Figure 3.22 FTIR spectrum of the MnS2 sample.

The MnS2 sample was further analyzed by FTIR spectroscopy to probe the vibrational properties of possibly present moieties anchored to surface. The presence of the broad peak centered at 3332 cm^{-1} was commonly associated to the stretching modes of adsorbed water. The formation of carbonates was shown by the presence of the two peaks at 1512 cm^{-1} and 1400 cm^{-1} formed by the splitting of the double degenerate OCO stretching mode ν_3 upon adsorption. The retrieved positions suggest the formed carbonates were binding the surface in a monodentate mode.[107] A group of peaks was found a lower frequency, having the most intense contribution at 1094 cm^{-1}, and other distinguishable components at 987, 945 and 843 cm^{-1}. As XPS analysis indicated the formation of SO_x species, these signals may be related with the formation of sulfites.[192,193] Lastly, the strong peak at 604 cm^{-1} can be attributed to Mn-S lattice vibrational modes, as similar peaks were previously reported by other authors for α-MnS.[209]

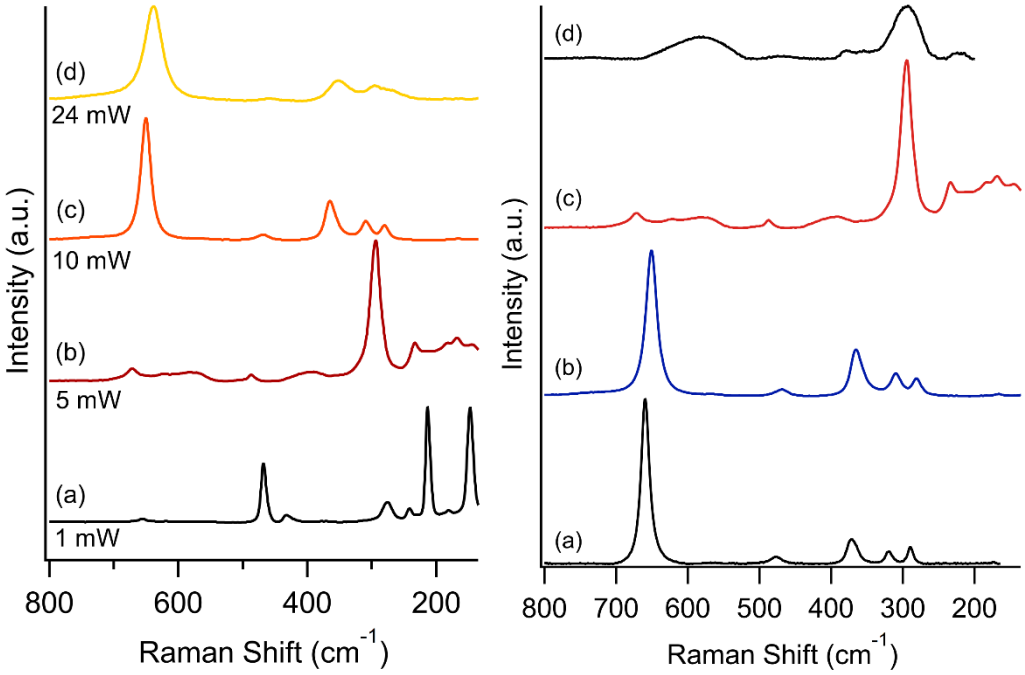

Figure 3.23 (left) Raman spectra of the MnS2 sample acquired with laser power at 1 (a), 5 (b), 10 (c) and (d) 24 mW. (right) Comparison of the spectra obtained at 5 (c) and 10 (b) mW with natural samples of α-MnS (d) and Mn_3O_4 (a).

The characterization of the obtained particles was complemented by Raman spectroscopy. In Figure 3.23 the spectra were acquired on the same spot using a laser power of 1, 5, 10 and 24 mW, resulting in very different patterns. The spectra acquired at 1 mW was dominated by the peaks of orthorhombic sulfur S_8.[113] The presence of sulfur was also observed in sample ZnS2 (Chapter 2.2, Figure 2.6b), and can be explained either as a product of photodegradation of the material, as no other characterization technique revealed its presence, or as a contamination caused from the employed excess of sulfur precursor in the synthesis. A peak at 276 cm^{-1} was also observed, that however is of unknown origin.

By increasing the laser power to 5 mW, any sulfur-related peak disappeared, possibly due to its evaporation in consequence of the local heating caused by the laser irradiation. The obtained pattern matches the one reported for natural α-MnS,[226] and the one predicted by Avril *et al.*[227] This indicates that the local heating produced from the laser irradiation has changed the crystal structure of the sample, causing the formation of the thermodynamically stable phase. It is interesting to notice that according to the group theory, α-MnS should not display any Raman-active mode. However, local symmetry breaking phenomena allows the obtainment of a diagnostic spectra for this phase.[227] By further increasing the laser power, a different pattern was again obtained. Four peaks were outlined at 281, 310, 365, 469, 650 cm^{-1}. The same pattern was also obtained by Zhang *et al.*,[228] and it was fully attributed to β-MnS. However, as also Avril *et al.*[227] reported for laser-heated α-MnS samples, this pattern almost perfectly matched the one of natural Mn_3O_4,[226] that was therefore formed as consequence of sample heating during the analysis. By further increasing the laser power to 24 mW, a general shift and broadening of the previous peaks was obtained, that likely indicates further oxidation or a loss of crystallinity of the sample. Overall, the obtainment of diagnostic peaks for the original β-MnS and γ-MnS phases was not possible due to the presence of sulfur and due to the sensitivity of this phases to the heat produced by the laser irradiation. Only the unknown peak 276 cm^{-1} observed at 1 mW may be related to the original MnS phases, but a reliable attribution was not possible due the lack of data found in the literature for metastable MnS phases and the possible presence of other contaminations.

Overall, the surface characterizations performed on MnS2 indicates the presence of detectable surface oxidation, especially from the S2p and O1s region of the XPS spectra and from the FTIR spectra. The main oxidation phenomena that was observed consisted in the formation of both sulfites and manganese oxide. The Raman analysis was unsuited for detecting such species, as the material displayed a remarkable sensitivity to heat-induced modifications, that altered completely the obtained pattern. This observation is coherent with the know metastability of the obtained β-MnS and γ-MnS, that easily converts to α-MnS when heated.

3.4 Silver sulfide - Ag_2S

Ag_2S is a semiconductor having a small bandgap of ~0.8 eV, that attracted attention for its ionic and electron conductivity at room temperature.[229] This material display a remarkable optical absorption in the 700 – 1000 nm range, thus in correspondence to the first biological window.[230] Indeed, in these frequencies the material strongly produces heat upon irradiation.[230] For this reason, one of the most appealing applications of Ag_2S resides in the development of biomedical nanosystems for phototermal therapy (PTT).[231,232] Other relevant application of Ag_2S are in the field of infrared detectors, electronic memories and sensors for the detection of hydrogen sulfide.[233]

Ag_2S is found in three polymorphs, that are stable at different temperatures. The low temperature polymorph is the monoclinic α-Ag_2S acanthite, which is stable at temperature below 450 K, while between 450 K and 852 K the stable phase is the cubic β-Ag_2S argentite. Over the temperature of 852 K the cubic γ-Ag_2S is obtained.[233] The α-Ag_2S to β-Ag_2S transition was also observed to be size-dependent, as for smaller particles the transition temperature is lowered.[233]

Many approaches have been applied for the synthesis of nanostructured Ag_2S, such as precipitation in water, template-based, sol–gel, microemulsions, sonochemical, hydrothermal, solvothermal, electrochemical, microwave-based methods.[234] In these approaches, stabilizing agents are normally used to prevent both aggregation and oxidation phenomena to occur.[234] Here, the ligand-free precipitation method presented was used to characterize the effect of the absence of such moieties on the properties of the material. For the synthesis, Na_2S was used as a sulfur precursor.

3.4.1 Crystal structure, size and morphology

The obtained crystal structure was firstly checked by XRD. From the diffractogram, only the presence of the monoclinic crystalline phase α-Ag_2S (ICSD 98-003-0445, acanthite, space group P 1 21/c 1) was retrieved. Along with the sharp reflections of α-Ag_2S, a broad diffuse scattering contribution was noticed.

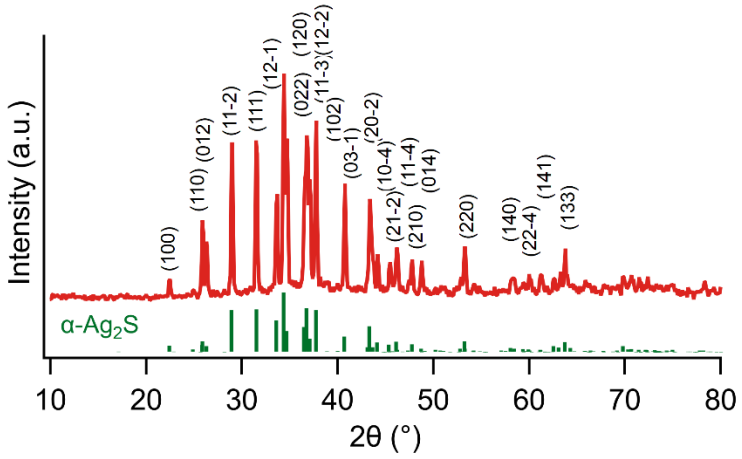

Figure 3.24 XRD pattern obtained from the synthetized Ag_2S sample.

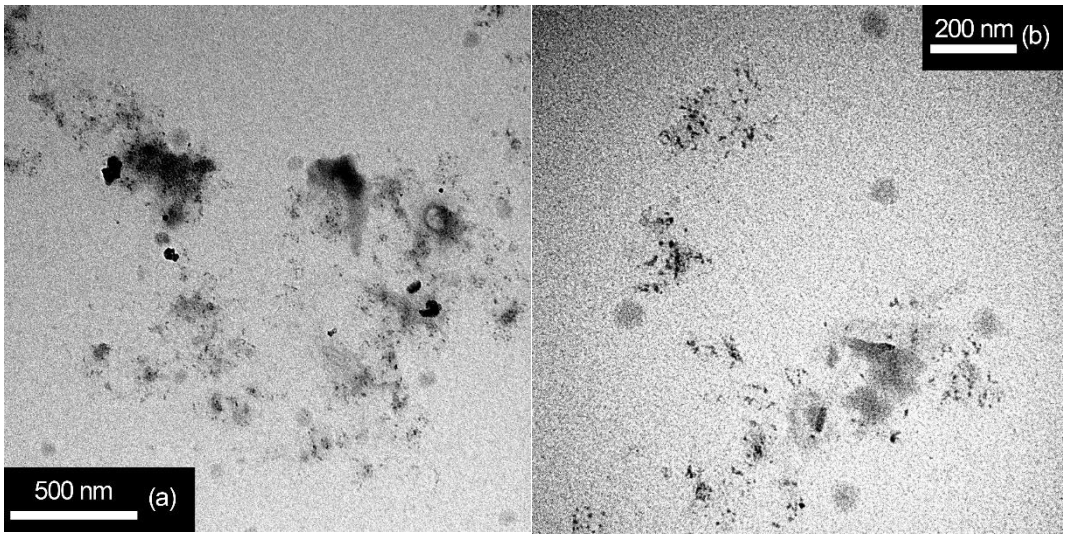

Figure 3.25 TEM micrographs obtained for the Ag_2S sample.

The TEM analysis was made difficult by the degradation of particles under the electron beam. Only zoomed-out micrographs could be obtained without incurring in a visible modification of the particles. From the obtained images (Figure 3.25), the presence of bigger particles (approx. 50 – 120 nm) along with smaller particle (approx. 10 – 20 nm) were visible, suggesting the presence of two sets of particles.

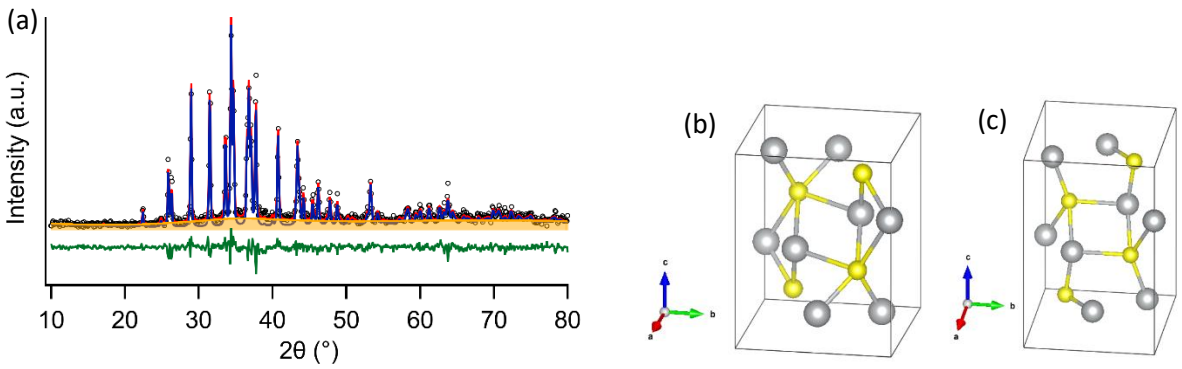

Figure 3.26 (a) Refined XRD profile of the Ag_2S sample, fitted using the approach by employing two sets of particles. Color scheme: blue = set of big particles; yellow = set of amorphous material / small particles; red = total intensity of the fit; green = fit residuals. Crystal structure retrieved from the refinement of the XRD pattern for the larger particles (b) compared with the crystal structure refined by Zamiri *et al* [235] (c).

Table 3.8 Retrieved crystal structure of larger particle fraction of the synthetized Ag_2S in comparison with the values reported by Zamiri *et al.*[235]

Cell parameters	a (Å)	b (Å)	c (Å)	α (°)	β (°)	γ (°)
This work	4.228(1)	6.929(2)	8.284(2)	90	110.577(9)	90
Zamiri *et al.*[235]	4.2278	6.9289	9.5323	90	125.58	90

Structure	Element	X	Y	Z	Occup.	Wyckoff site
This work	S	0.268(6)	0.233(4)	0.133(3)	1	4e
	Ag	0.047(2)	0.018(1)	0.309(1)	1	4e
	Ag	0.647(1)	0.318(1)	0.438(1)	1	4e
Zamiri *et al.*[235]	S	0.49293	0.23577	0.13261	1	4e
	Ag	0.07245	0.01478	0.30895	1	4e
	Ag	0.72498	0.32529	0.43819	1	4e

As the presence of small and/or poorly crystalline NPs produces a much weaker scattering intensity in comparison to large crystals, the presence of the diffuse scattering in the XRD pattern was attributed to the small NPs observed in the TEM micrographs. To estimate the relative amount of the two set of particles, the XRD profile was fitted. Initially, the unit cell and crystal structure parameters were adjusted starting from the structure retrieved in the literature for α -Ag_2S,[236] while treating the diffuse scattering contribution as background. From the obtained pre-optimized structure, two populations of particles sharing the same crystalline phase were used to fit again the experimental pattern. A first set was used to describe the contribution of the sharp reflections showed by the larger particles, therefore a crystallite size >100 nm was employed. The second set was used to model the diffuse scattering contribution, assuming a crystallite size smaller than 10 nm. After a pre-optimization of the relative

amount of the two models in the experimental pattern, the crystal structure of the large particles was finally optimized. The obtained parameters are reported in Table 3.8. The final goodness of fit (GoF) was 1.4, indicating a good convergence of the model. No crystal structure optimization was performed for the set of smaller particles, as no information on the reflection intensities could be obtained. From the final refinement, the sample composition was estimated to contain a 30(7)% mass fraction of smaller particles, and consequently a mass fraction of 70% for the larger ones. This result agreed with the results of the TEM analysis. Overall, the system may be described as composed of a large number fraction of small (approx. 10 – 20 nm) poorly crystalline particles and a smaller number fraction of number of large (> 100 nm) crystalline particles. This result can be directly compared with the analysis performed by Zamiri *et al.*,[235] who employed a very similar batch synthesis approach, where the synthesis was carried out at 80 °C. In his analysis, only one population of particles was retrieved, having an average crystallite size >200 nm. The refined crystal structure was also different, as different atomic positions in the unit cell were reported, especially for the sulfur atom. Moreover, in his work the unit cell displayed a wider β angle and a slightly more elongated shape. A comparison between the two structure is reported in Table 3.8, while a visual comparison between the refined unit cells is proposed in Figure 3.26b-c. By this comparison, it became evident that the choice of temperature affects both the crystal structure of the product as well as the size of the particles, as the formation of the smaller particles was not reported at 80 °C. Therefore, variable-temperature experiments may be extremely relevant to gain detailed information about the growth of the final large (> 100 nm) particles and the evolution of the crystal structure of the α -Ag_2S. As the population of small poorly crystalline was not retrieved at higher temperature, and the larger particles displays a crystallite size compatible with the observed particle size, it is possible to hypothesize that the larger particles may be formed from the coalescence of the smaller ones, or by the Ostwald ripening phenomenon. This also accounts for the importance of employing capping ligands in the water synthesis of Ag_2S to avoid further growth of the particles, that was previously reported in the literature.[234]

3.4.2 Surface composition

The surface composition was firstly studied using XPS spectroscopy. From the survey spectrum (Figure 3.27) the presence of Ag, S, O and C was retrieved, where the presence of C and O was expected due to adventitious contamination.[206]

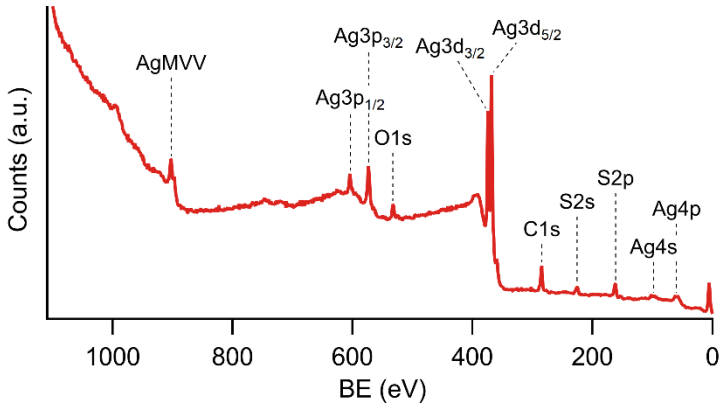

Figure 3.27 XPS survey spectra of the Ag_2S sample.

Table 3.9 Observed peaks in the Ag_2S XPS spectra.

Peak	Experimental (eV)	Reference[99] (eV)
$Ag3p_{1/2}$	603.8	-
$Ag3p_{3/2}$	573.4	-
$Ag3d_{3/2}$	374.2	-
$Ag3d_{5/2}$	368.2	368.0-368.8
Ag4s	98.2	-
Ag4p	59.8	-
S2s	225.4	-
S2p	161.2	161.0-160.8

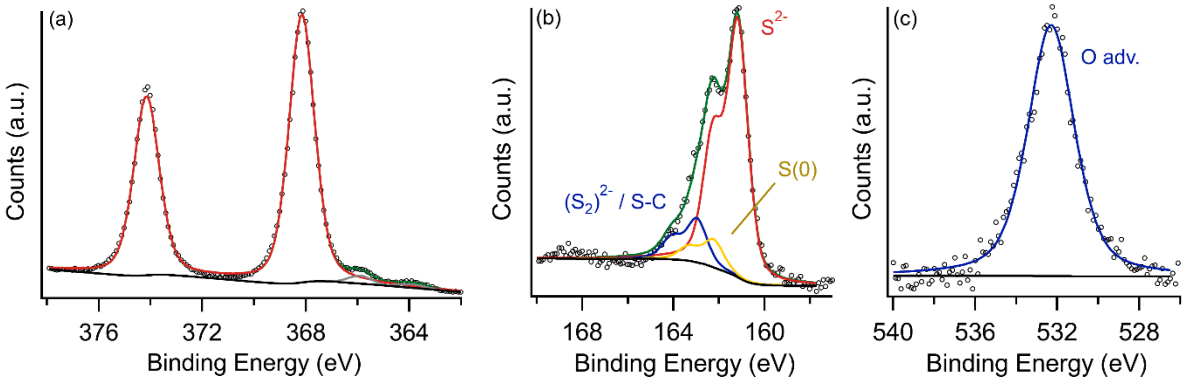

Figure 3.28 Fitted Ag3d (a), S2p (b) and O1s (c) XPS regions of the Ag_2S sample.

The semi-quantitative analysis performed on the Ag3d and S2p peaks resulted in an Ag:S atomic ratio of 1.9:1, that lies close to the expected 2:1 stoichiometric ratio. In the Ag3d region (Figure 3.28a), two additional components were visible at lower binding energy with respect to the $3d_{5/2}$ peak. Their positions, however, were inconsistent with any silver compound, so they were treated as spectral components unrelated to the Ag3d region and fitted independently.

The employment of only the d doublet expected for pure Ag_2S (other than the additional unrelated peaks at low binding energies) resulted in the fitting depicted in Figure 3.28a. The position of the $3d_{5/2}$ peak was at 368.2 eV compatible with the previously reported values.[237,238] Minor fitting inaccuracies were observed, therefore the inclusion of other components was also tested. The inclusion of Ag(0), Ag_2O and AgO starting from the fitting parameters reported by Ferraira *et al.*[239] did not allow any significant improvement to the obtained fit, while employing unconstrained additional d doublets sharing the same split-orbit coupling of 6 eV retrieved for the main 3d peaks resulted in large shifts that were only compatible with $AgNO_3$ and AgF_2.[99] The presence the latter two compounds was ruled out as no N1s nor F1s peaks were retrieved in the spectra. Since in the O1s region only a single component at 532.3 eV was pointed out, with no additional components al lower binding energy, the formation of surface Ag_2O or AgO was also ruled out. Therefore, little imperfections in the reported fits were finally attributed to an irregular background in the spectral region, or to a minor presence of Ag(0) having a undeterminable asymmetric profile. The S2p region was fitted with three components. The main peak was found at 161.2 eV, which is compatible with the commonly reported values of S^{2-} in Ag_2S.[99] A second component was retrieved at 162.2 eV, and was attributed to elemental S^0, while the third component at 163.0 eV was attributed to disulfides[240,241] $(S_2)^{2-}$ or to the formation of C-S bonds.[181,242] Overall, no relevant oxidation phenomena was retrieved from the XPS analysis. The minor components observed in the S2p region were attributed to early oxidation phenomena or to the presence of residuals from the synthesis.

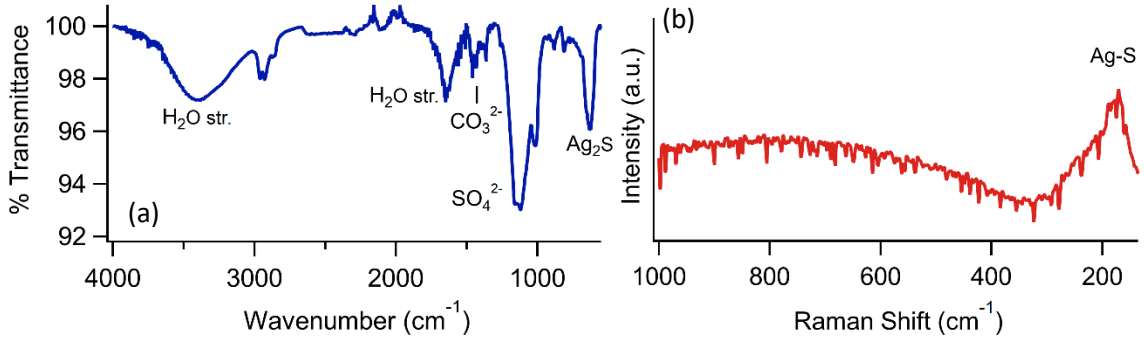

Figure 3.29 FTIR (a) and Raman (b) spectra of the Ag_2S sample.

The identification of adsorbed moieties on the Ag_2S surface and a further characterization of oxidation phenomena was performed using FTIR spectroscopy. From the spectra, the presence of adsorbed water molecules was evident from broad HOH stretching peak at 3398 cm^{-1} and the HOH bending peak at 1637 cm^{-1}. The peaks found at 1120 cm^{-1} to 1013 cm^{-1} were attributed to the asymmetric and symmetric stretching modes of sulfates respectively.[106] The presence of both these signals indicated that sulfates had a C_{2v} symmetry, suggesting a mononuclear or bridging coordination with the surface.[106] Since no sulfates were detected with the XPS analysis, and the intensity of the FTIR signal

suggests a rather clear presence of this species, the oxidation has likely occurred in the time between the two characterizations. In turn, this indicated that Ag_2S surface was subjected to oxidation during a limited timeframe of air-exposure and that inert atmosphere is required to preserve the material surface in its pristine condition. The formation of carbonates was evidenced by the presence of the two peaks at 1454 cm^{-1} and 1371 cm^{-1},[107] while the peak observed at 633 cm^{-1} was previously attributed to Ag-S lattice modes.[235,243] The group of peaks centered on 2922 cm^{-1} was attributed to the presence of residual acetone on the ATR crystal.

The particles characterization was complemented with Raman spectroscopy. Due to a strong photosensitivity[45] of the sample, the lowest power irradiation of 0.1 mW was needed to avoid photodegradation. From the spectra, only a weak broad peak was retrieved at 170 cm^{-1}. This large signal was associated with stretching Ag-S modes, and its low intensity was attributed to the low energy for defect formation in the β-Ag_2S structure and the consequent formation of Ag vacancies under illumination.[244,245] No other signal was retrieved at the Raman analysis.

The surface analysis indicated that in the as-synthesized material very little oxidation was formed, while, after a period of air-exposure, the presence of sulfates was clearly retrieved from the FTIR spectra. This indicates that the employed method was suitable to obtain the unoxidized material despite the lack of protective ligands on the surface.

3.5 Other metal sulfides

The employment of the ligand-free batch approach for the synthesis of ZnS, CuS, PbS, MnS and Ag_2S led to positive results, since for all these the formation of crystalline compounds could be pursued. The same approach was also applied to Ni^{2+}, Co^{2+}, Cr^{3+}, Fe^{2+}, Sn^{2+}, Ti^{4+}, Nd^{3+}, Yb^{3+}, Gd^{3+}, Eu^{3+} ions, as described in Table 3.1. However, in these cases, the crystallization was not achieved, as poorly crystalline or completely amorphous materials were obtained instead. Moreover, in many cases strong oxidation phenomena were also noticed.

The reaction of $Ni^{2+}$and Sn^{2} solutions with the Na_2S solution led to the formation of $Ni(OH)_2$ and SnO_2 respectively. For the latter, aggregates of very small SnO_2 particles were obtained, having an estimated size of approximatively 2 – 3 nm.

By using a 0.2 M NaHS in a double fold excess in respect to the stoichiometry of the corresponding metal sulfide, the synthesis was attempted with Ni^{2+}, Cr^{3+}, Fe^{2+} and Sn^{2+} solutions. For all these precursors, amorphous compounds were obtained. In the case of Fe^{2+}, a black amorphous powder was obtained, thus having the color expected for the formation of FeS pyrite.[45] The powder was observed to be very sensitive to oxidation, as after few hour of air exposure a complete conversion to orange FeO(OH) lepidocrocite was observed. The micro-Raman characterization on an oxidation-free spot (i.e. a part of the sample not showing orange spots) resulted in a pattern which was analogous to the one reported for rasvumite KFe_2S_3. Since no potassium was introduced in the reaction mixture, it is possible that the obtained solid had an analogous composition to rasvumite, but with sodium ions instead of the potassium ones.

For Ti^{4+} and the lanthanides (Nd^{3+}, Yb^{3+}, Gd^{3+}, Eu^{3+}) both NaHS and $(NH_4)_2S$ were used in order to avoid very high pH, like the case of the Na_2S 0.2 M solution (pH 13.0), as all these elements are well known hard ions in the HSAB theory (see Chapter 1.1). For these syntheses, the employed water was previously degassed, and the reactions were carried out under inert atmosphere. In all the syntheses, amorphous compounds were obtained. The XPS analysis pointed out a large presence of oxygen and only a minor presence of sulfur on the surface, while the Raman analyses excluded the formation the corresponding oxides, despite no identification of the retrieved patterns was possible. After a thermal treatment of 100 °C in vacuum, the appearance of Raman peak around 1000 cm^{-1} was generally observed, that was interpreted as the formation of sulfates in analogy to ZnS (see Chapter 2.2) or PbS (see Chapter 3.2.2).

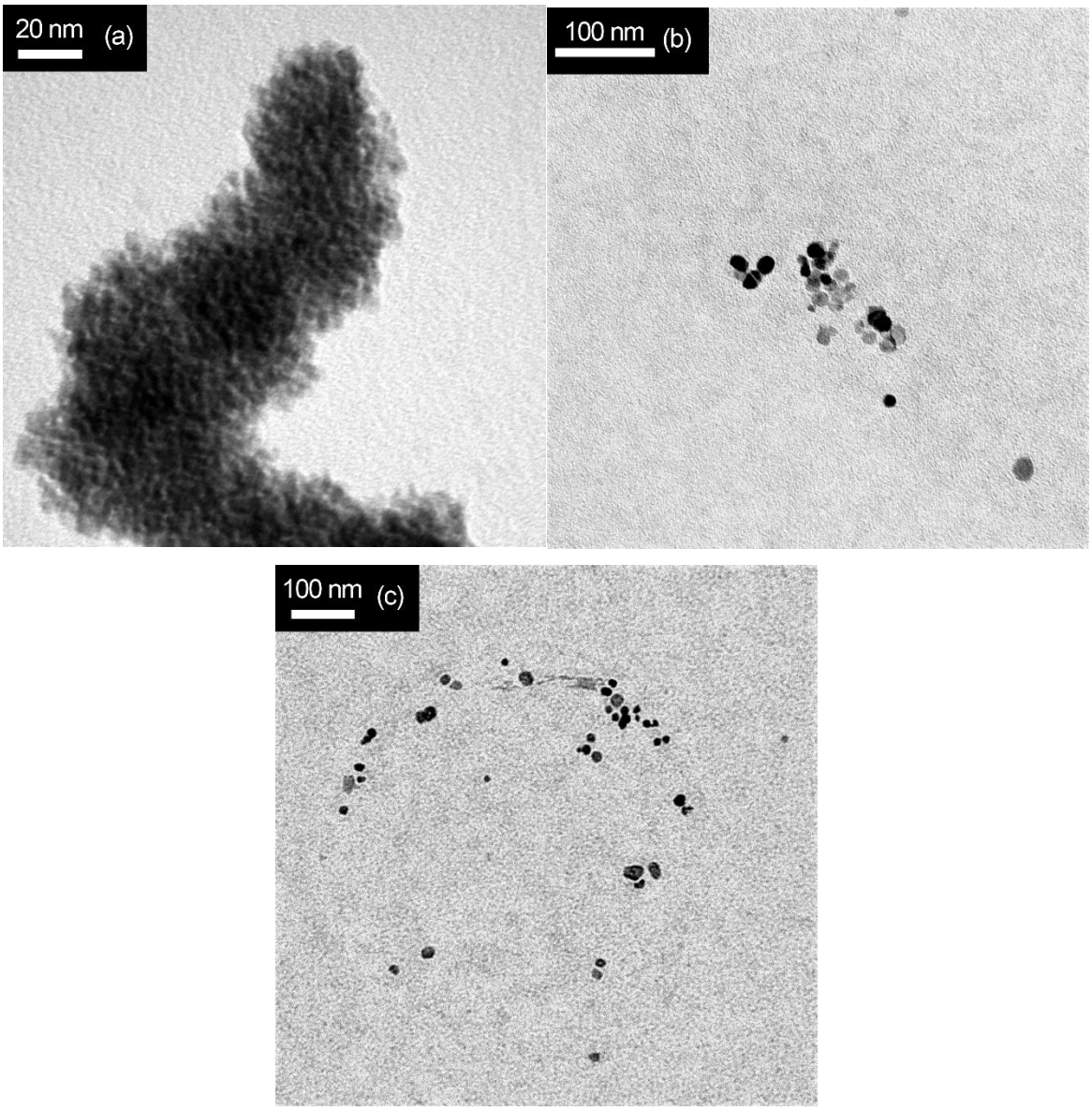

Figure 3.30 TEM micrographs of (a) an aggregate of small SnO_2 particles obtained from the reaction of Sn^{2+} and Na_2S solutions; particles obtained from the reaction of (b) Nd^{3+} and (b) Ti^{4+} solutions with the employment of the NaHS precursor.

TEM micrographs were acquired for Nd^{3+} and Ti^{4+} samples, showing the formation of NPs in the 10 – 40 nm length scale, together with the formation of larger aggregates. Overall, is was plausible that the syntheses led to the formation of amorphous and air sensitive metal sulfide particles, despite the oxophilicity of the employed ions. This hypothesis was supported by the observed color of the dried powders, which largely corresponded to the expected color for the corresponding metal sulfides.[246]

3.6 Conclusions

In this Thesis a simple low-temperature water-based ligand-free batch method was employed for the synthesis of ZnS (Chapter 2). The same method was successfully applied to the synthesis of crystalline CuS, PbS, MnS and Ag_2S. A brief summary of the structural features retrieved for these materials is reported in Table 3.10, along with the results obtained for the synthesis of ZnS NPs (Chapter 2).

Table 3.10 Summary of the morphological, dimensional and structural features obtained from the syntheses of metal sulfides in Chapters 2 and 3.

Material	Sulfur precursor					
	Na_2S			NaHS		
	Shape	Size [a] (nm)	Phase	Shape	Size [a] (nm)	Phase
ZnS	Rounded	7.8 (1.2)	Sphalerite	Rounded	19 (4)	Sphalerite
CuS	Platelets	17 (4)[b]	Covellite	Platelets	19 (6)[b]	Covellite
PbS	Squared	30 (8)	Galena	Squared	32 (8)	Galena
MnS				Polyhedral	*microsized*	β,γ-MnS
Ag_2S		50 - 120	Acanthite			

(a) Size determined from TEM analysis. (b) Maximum Feret diameter.

The syntheses led to the formation of nanostructured (< 100 nm) particles for ZnS, CuS and PbS, while in the case of MnS and Ag_2S larger particles (> 100 nm) were obtained. The synthesis of ZnS showed a remarkable pH dependence, as the employment of Na_2S resulted in smaller particles to the ones obtained using NaHS. In the case of CuS and PbS the final size was observed to be only slightly dependent on the reaction pH, as minor size variations were retrieved. Moreover, while the size reduction of ZnS was observed along with an increased presence of planar defect in the crystal structure, no indication of relevant amount of defects was obtained from the crystallographic assessment for CuS and PbS.

In the case of sample CuS2, synthetized with NaHS, a variation of the relative intensity of the XRD reflections suggested a deviation of the obtained crystal structure from the known covellite structure, hinting to the possibility to tune the structure by changing the experimental parameters.

For MnS and Ag_2S, relevant size dispersion was retrieved by the TEM analysis, possibly indicating an important role of growth phenomena, like Ostwald ripening or coalescence. In both cases, the employment of the low temperature route led to the formation of different crystal structures in comparison to the known stable and expected crystal phases. This was particularly evident in the case of MnS, where a mixture of β-MnS and γ-MnS metastable phases was retrieved instead of the

thermodynamically stable α-MnS. This suggests that an in-depth investigation of the synthesis of MnS could lead to the obtainment of a phase-selective synthesis, favoring the metastable polymorphs. Overall, the synthesis conditions displayed relevant effects on both structural and dimensional features of the samples. This, in turn, discloses the valuable opportunity of optimizing the synthesis of technologically relevant nano- or microstructured materials at low temperature, in water and without the addition of additional species to control the reaction, starting from cost-effective precursors.

The assessment of the surface composition of the synthetized materials indicated that little to no oxidation of the material generally occurred during the synthesis of the crystalline compounds, despite the employment of water as solvent. This very important result indicated that the syntheses may be suitable even for application that strongly rely on the surface properties of the prepared materials (e.g. heterogeneous catalysis or photocatalysis). However, the materials showed to be susceptible to oxidation if stored under ordinarily conditions (i.e. exposed to air). Moreover, the oxidation was generally observed to occur faster as the particles size were reduced. The materials oxidation consisted in the formation of SO_x moieties, along with the formation of the metal oxides in the case of PbS and MnS. FTIR was observed to be the most sensitive technique to identify the presence of moieties associated to oxidation phenomena. An important exception to the general increased susceptibility of smaller particles to these phenomena was observed in the case of ZnS, where no detectable traces of oxidation were found for the smaller ZnS particles. This was possibly related to a surface passivating effect caused by water molecules strongly bound to the surface.

For other metals sulfides (Section 3.5), the synthetic approach led to unsatisfactory results, as amorphous materials or the formation of secondary compounds (i.e. oxides or hydroxides) was retrieved. Interestingly, TEM investigations often results in the observation of nanosized particles being formed. Moreover, the presence of S^{2-} was observed in some exploratory XPS analyses. Thus, it was possible to hypothesize that, in some cases, amorphous sulfides might be obtained, that were however strongly susceptible to oxidation. Therefore, the obtainment of these metal sulfides using this approach might be fundamentally limited by the inability of the materials to crystallize using the employed conditions, and by the high susceptibility of the same compounds to oxidation.

Chapter 4.

Room temperature microfluidic synthesis and characterization of pure and doped uncapped ZnS NPs

4.1 Microfluidic synthesis of small ZnS NPs

In Chapter 2 encouraging results were obtained on the synthesis of pure organics-free uncapped ZnS NPs by a simple water based precipitation approach. To critically explore the possibility of further developments, the limitations intrinsically connected with the batch approach were reviewed. In the batch process, the mixing of the two precursors was achieved by dropwise addition of the Zn^{2+} solution into the stirred HS^- solution. This allow a mixing time that is typically in a much larger time scale with respect to the formation of ZnS NPs, as seen by *in-situ* SAXS measurements (Chapter 2.3) and as outlined by the literature.[58] Moreover, as the reaction proceeds, the chemical environment also changes due to the gradual consumption of HS^- and due to the progressive dilution originated by the increasing volume and the gradual variation of the pH in the reaction mixture. To overcome these limitations, turning to a microfluidic approach seemed a straightforward choice. The flow approach instead of a batch one allows stable reaction conditions overtime, as the mixing of precursors solution occurs always at the same concentrations. Moreover, in the case of microfluidic setup, significant improvements can be accomplished through a more controlled mixing and a more efficient heat transfer, leading to the abatement of concentration and temperature gradients.[65,247] In addition to this advantages, a flow setup also allowed a continuous production of material. This advantage is important when a larger production of material is concerned, as the scale-up of the synthesis can simply be obtained by numbering-up the reactor, i.e. running numerous identical parallel microfluidic reactors.[248,249]

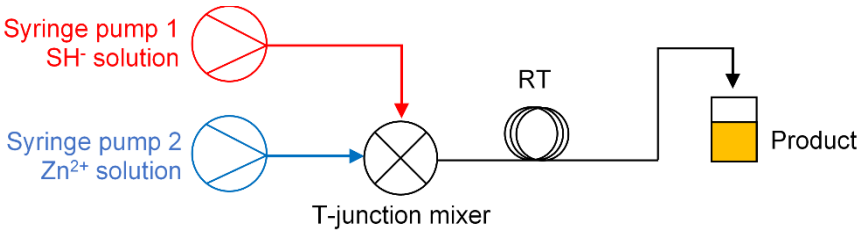

Figure 4.1 Microfluidic setup schematics.

For the microfluidic transposition of the batch synthesis of ZnS NPs, a simple setup was realized. Precursor solutions were pumped using reciprocating syringe pumps into a cross-flow T-jucntion mixer. After a short residence time, the obtained suspension was simply collected in a flask. Three different samples were synthetized to explore the effect of precursors concentration and flow rate. In analogy to sample ZnS1, only Na_2S and $Zn(NO_3)_2$ solutions were used as precursors.

Table 4.1 Experimental parameters varied in the samples obtained using the microfluidic approach.

Sample	Flow rate (ml/min)	Zn^{2+} conc. (M)	S:Zn ratio (mol/mol)
ZnS MF1	2.0	0.10	2:1
ZnS MF2	1.2	0.01	5:1
ZnS MF3	1.2	0.10	2:1

4.1.1 Crystal structure, size and morphology

Possible variations of the crystal structure of the obtained material was firstly checked by XRD. The retrieved patterns were compatible with ZnS sphalerite (ICSD N. 98-065-1457, space group F-34m), in analogy with the batch synthetizes samples (Chapter 2). The absence of other reflections indicates the absence of contaminations from other crystalline compounds like ZnO or $Zn(OH)_2$. Therefore, analogously to the batch synthetic route, a pure compound was obtained. From the qualitative comparison proposed in Figure 4.2, a significant broadening of the reflections was observed. Moreover, comparing the reflection (200) in samples ZnS1 and ZnS MF1, the reflection line shape was almost entirely undetectable, as it formed an uninterrupted tailing towards high angles with the (111) reflection. Since in batch-synthetized samples the presence of planar defects was retrieved, it was possible, from these observations, to presume that an increase in these defects may be obtained using these microfluidic conditions. In particular, the asymmetric broadening of the (111) reflection suggested that intrinsic stacking faults may be the dominating type of planar defects.[250]

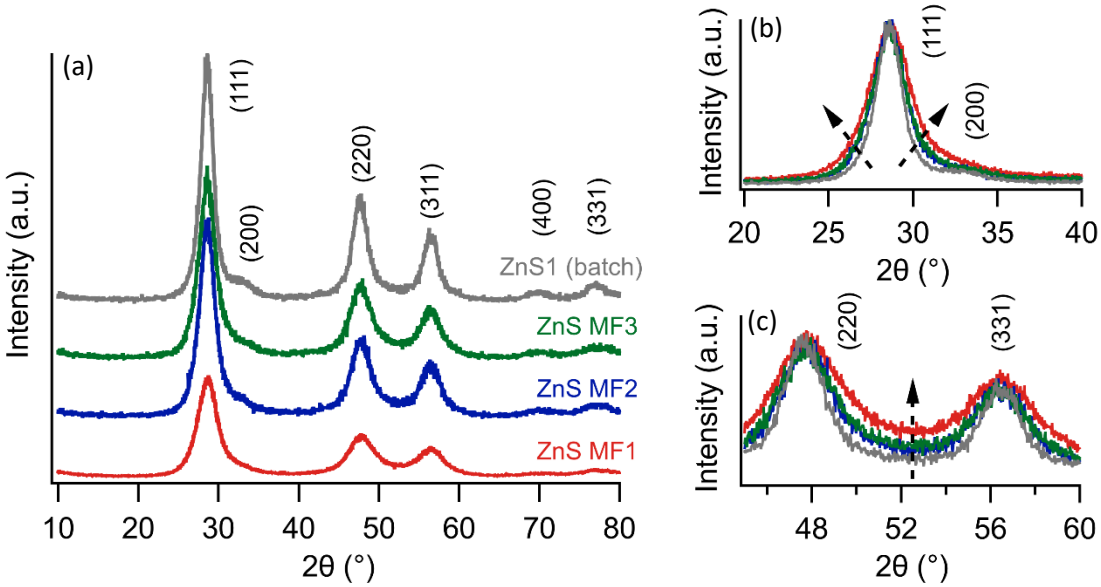

Figure 4.2 (a) Area-normalized XRD patterns of samples ZnS MF1-3 compared to sample ZnS1 (batch synthesis – Chapter 2). (b) Comparison of the broadening of the (111) and (200) ZnS sphalerite reflections between the patterns of samples ZnS MF1-3 and ZnS1 (batch synthesis – Chapter 2) normalized on the intensity of the (111) reflection. (c) Increase of the diffuse scattering intensity between the (220) and the (331) reflections.

A qualitative confirmation of an increased presence of planar defects may be obtained from the increased intensity between the (220) and (331) reflections, which was an evident anomalous feature in highly defective ZnS NPs reported by Zhang *et. al.*[87]

TEM micrographs where obtained for all three samples (Figure 4.3). The obtainment of accurate size and morphological information from the images was made especially difficult due to the small size of the NPs and for the occurrence of aggregation phenomena. Interestingly, sample ZnS MF1 was found in an unaggregated state, as TEM images showed well separated particles. For all three samples, rounded NPs were visible, which were morphologically compatible with NPs obtained using the batch synthetic route. The equivalent sphere diameter distributions were obtained by segmentation of individual particles observed in the images and fitted to a log-normal distribution. The latter was chosen as a general asymmetry of the distribution towards larger sizes was evident. The obtained statistical descriptors of the obtained distributions are reported in Table 4.2. The dimensional data indicates that a similar size distribution was obtained in the case of samples ZnS MF1 and MF3, having them an average $D_{1,0}$ diameter of 5.1 and 4.8 nm respectively. Comparing these values to the $D_{1,0}$ average of 7.8 nm obtained for the batch ZnS1 sample, it was evident how the different synthetic approach led to a 35% and 38% size reduction respectively for the batch-synthesized NPs.

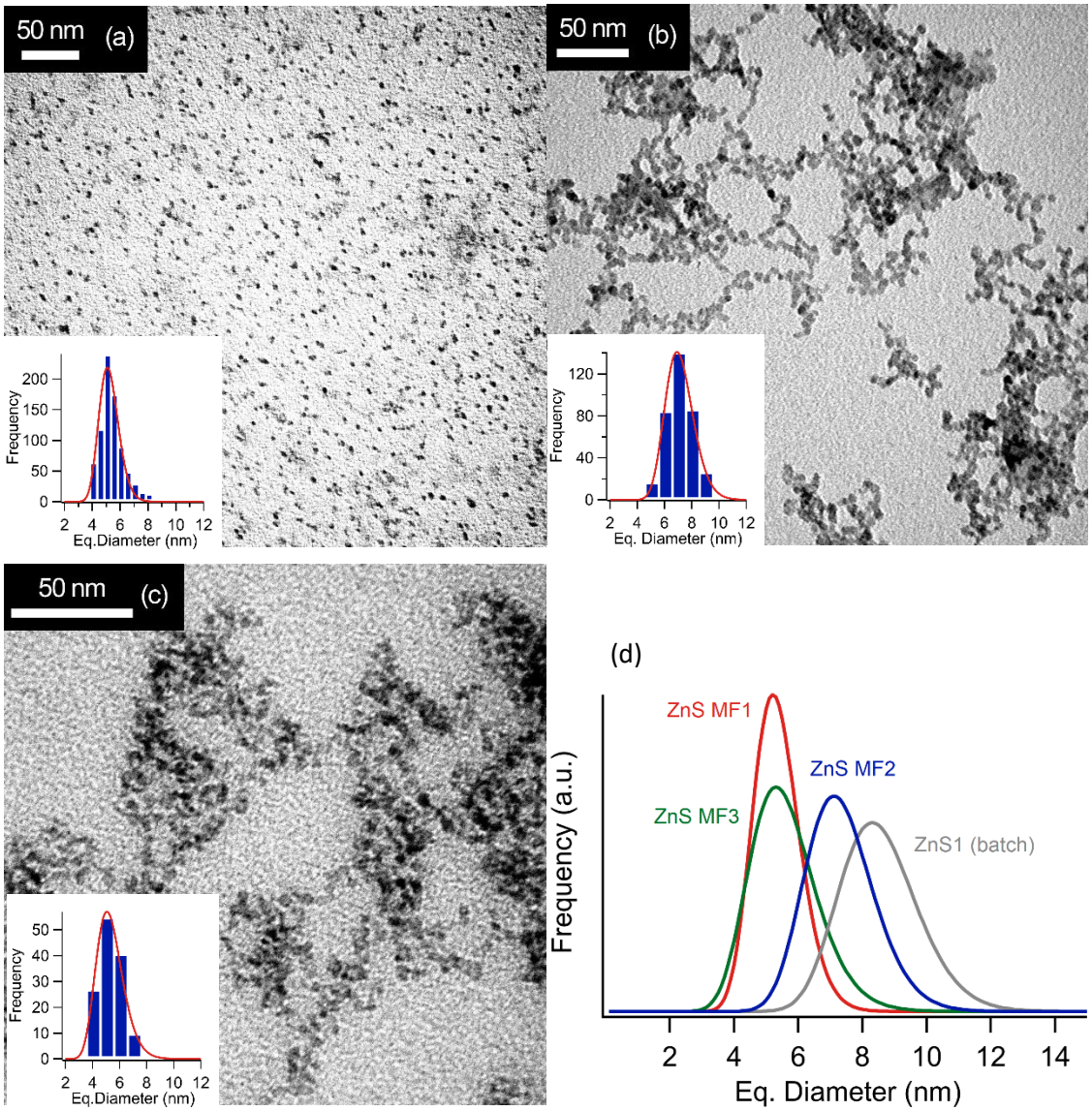

Figure 4.3 TEM micrographs of samples ZnS MF1 (a) ZnS MF2 (b) and ZnS MF3 (c) with the relative fitted equivalent diameter distributions (d). Comparison of the fitted distributions of samples ZnS MF1-3 with sample ZnS1 (batch synthesis, Chapter 2)

Table 4.2 Size distribution descriptors obtained from TEM population of sampled particles and from TEM distributions fitting.

	ZnS MF1		ZnS MF2		ZnS MF3		ZnS1 (batch)	
	TEM	fit	TEM	fit	TEM	fit	TEM	fit
$D_{1,0}$ (nm)	5.1	5.2	6.6	7.1	4.8	5.3	7.8	8.4
Std. dev. (nm)	0.9 (17%)	0.7 (14%)	1.0 (20%)	1.2 (14%)	0.8 (17%)	1.0 (19%)	1.2 (16%)	1.2 (14%)
$D_{3,2}$ (nm)	5.4	5.4	6.9	7.5	5.0	5.7	8.1	8.7
$D_{4,3}$ (nm)	5.6	5.5	7.0	7.6	5.1	5.9	8.3	8.9
Skewness	1.0	0.4	0.5	0.4	0.4	0.6	0.1	0.4
Kurtosis	1.3	0.3	-0.5	0.4	-0.8	0.6	0.5	0.3

Noteworthy, being the solvent and precursors employed the same, the only relevant difference in the synthetic protocol was indeed the flow microfluidic conditions. Therefore, it can be inferred that the mixing strategy alone of the two precursors may play a significant role in controlling the final average size of the obtained particles. This observation discloses the interesting opportunity of tuning ZnS NPs size without having to rely on different chemical strategies (i.e. by tuning the decomposition kinetics of the sulfur precursor[29]), but simply using different mixing conditions for the same precursor solutions. The effect of different flow rates on the NPs size was observable comparing ZnS MF1 and MF3 for which the average $D_{1,0}$ diameters of 5.1 and 4.8 respectively were obtained, while maintaining a reduced polydispersion, being the relative standard deviation 17% in both cases. This result suggests that the small difference in the flow rate explored only resulted in a minor variation of the NPs size. Thus, a more remarkable variation of the mixing parameters is required to significantly vary the size of the NPs, even though the flow rate might be employed to finely tune the NPs size. Considering the results obtained by the *in-situ* SAXS experiment on the batch synthesis method (Chapter 2.3), these results might be explained by the very first values of the $D_{3,2}$ average diameter estimated as function of the increasing reaction time (Chapter 2, Figure 2.9b). In the first tenths of seconds, a slight upward curve is visible, suggesting a relevant size increase of NPs in the very first stages of the synthesis. Since the timestep of the *in-situ* analysis was 10 s, thus much slower that the mixing time in a microfluidic reactor, the actual size of the just-mixed precursors is not observable. Since the microfluidic tests showed the formation of smaller particles, the observed small curvature may be interpreted as the tail of a fast and much more pounced growth phenomena. NPs are likely to increase in size in the first part of the reaction, where more and more zinc precursor is added to reaction mixture, on the suspension containing already formed NPs. In the case of a flow-reactor, precursors are instead constantly mixed in stable conditions (i.e. the reaction occurs always with the same conditions in any point in time, unlike to the batch approach), not allowing further growth of NPs. Alternatively, the formation of smaller NPs may also be considered in the framework of the LaMer homogeneous nucleation and growth theory[251] as further refined by Chu *et al.*[16] Being the sulfur precursor already available as SH^- in solution, it is possible to interpret the *monomer supply rate* term employed in the modelling of the NPs nucleation and growth kinetics (see Chapter 2.1) as a mass-transfer limited term responsible for the final average size on NPs, ultimately dependent on the mixing efficiency of the two precursors. In other words, considering the formation of ZnS starting from SH^- and Zn^{2+} in water was observed to occur under 10 µs,[58] the reaction is likely to occur at the interface when the two precursors solutions are mixed together. Therefore, the improved efficacy of the microfluidic mixer over a simple dropwise addition may be responsible to a faster supply rate of the precursors to the reaction, allowing a smaller final NPs average size according to the Chu theory.[16]

In the case of sample ZnS MF2, the concentration was lowered to 0.01 M for the zinc precursor solution, while the Zn:S molar ratio was set to 1:5. In this case larger particles having a $D_{1,0}$ average diameter of 6.6 nm were obtained. Comparing these results with the synthesis performed using the batch synthetic strategy, the dimensional increase may be due to the lowered pH value connected with a reduced concentration of SH^- in solution. This suggests that, combining the reagents mixing rate to a proper tuning of the chemical environment may disclose even broader possibilities to obtain a tight control over final NPs size. Another important aspect of the obtained result is the limited polydispersion of NPs sizes. Indeed, the relative standard deviation of the obtained distributions are between 15% and 20% despite no stabilizing agents or surfactants were used in the reaction. By turning to a flow setup, the limited size dispersion that the batch route showed was conserved, or even improved, despite the reduction in the average size (i.e. the standard deviation value is reduced as well by a similar magnitude). This allowed to obtain smaller particles without trading off the quality of the size control, while keeping the reaction protocol as simple as it gets, since no compound other than the solvent and the precursors were employed.

Since the size determination from TEM micrographs was made difficult by the small size of the obtained NPs, and a qualitative assessment of the XRD profiles suggested the presence of planar defects, a more quantitative and in-depth investigation based on the samples diffractograms was performed. The refinement of the XRD diffraction pattern was proven to be an effective tool estimate size distribution and concentration of stacking faults in the case of the bigger particles obtained using the batch route (Chapter 2.1). However, as particles got smaller, the complexity of the procedure increased. Three main modelling challenges needed to be faced: *i*. Bragg peaks got broader due to the smaller domain size, gradually making the distinction between the reflections and the background more difficult to obtain; *ii*. as dimension shrinks, the specific surface area increases making structural deformation coming from surface relaxation phenomena gradually more relevant, introducing a strong microstrain-related broadening of reflections;[252] *iii*. diffuse scattering (i.e. off-Bragg scattering) gradually gets more and more relevant, making a Bragg-based fitting approach more difficult to use.[253] The latter effect is tightly related to the nanocrystalline nature of the samples, as in small NPs the approximation of an infinite crystal gradually breaks down. Moreover, in the case of ZnS, the likely presence of stacking faults and their contributions to reflections broadening makes separating the domain-size contribution alone even more difficult. Overall, for small ZnS NPs, many effects got relevant obtaining smaller and possibly more faulted NPs, especially for reflections broadening. All these effects needed to be accounted to properly fit the recorded patterns, even though the information content of the diffractogram approached with the Bragg approximation remained the same and the analysis was further complicated by a more ambiguous determination of the background.

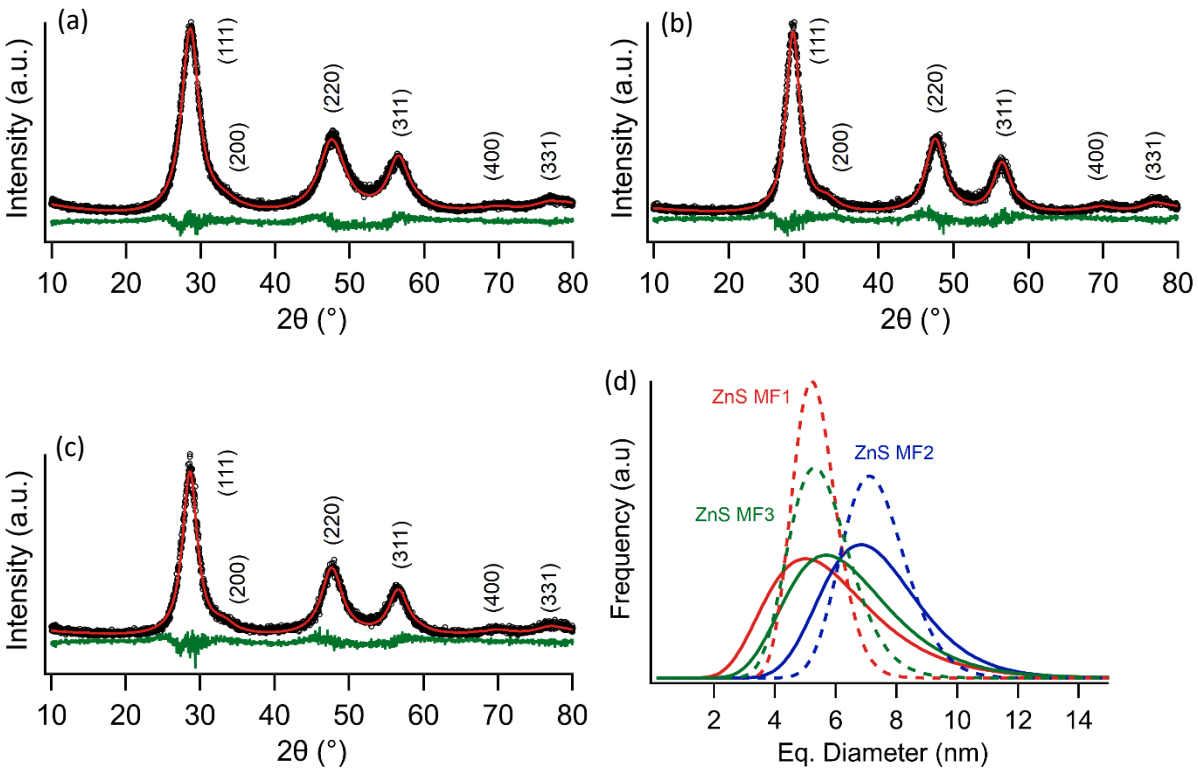

Figure 4.4 Refined XRD profiles of samples ZnS MF1 (a), MF2 (b) and MF3 (c). (d) Comparison of the log-normal diameter distributions obtained from TEM and XRD.

Table 4.3 Comparison between the size distribution descriptors obtained from the log-normal fits of the experimental size distribution obtained by TEM analysis and the distribution obtained by fitting the XRD patterns of ZnS MF1-3 samples.

	ZnS MF1		ZnS MF2		ZnS MF3	
	TEM-fit	Refined	TEM-fit	Refined	TEM-fit	Refined
$D_{1,0}$ (nm)	5.2	5.9	7.1	8.1	5.3	6.3
Std. dev.	0.7 (14%)	2.0 (34%)	1.1 (15%)	1.6 (20%)	1.0 (19%)	2.6 (41%)
$D_{3,2}$ (nm)	5.4	7.4	7.5	8.7	5.7	8.6
$D_{4,3}$ (nm)	5.5	8.3	7.6	9.1	5.9	10
Skewness	0.4	11	0.4	0.6	0.6	1.3
Kurtosis	0.3	2.1	0.4	0.7	0.6	3.1
GoF		2.0		1.7		1.6
SF probability		0.14		0.08		0.09

An analogous fitting approach to the one described in Chapter 2.1 was employed for the fits of Figure 4.4. Since the calculated average size was systematically underestimated, the size-dependent effect of microstrain was also added. The obtained distribution (Figure 4.4) lies close to the one obtained from TEM analysis, but the refined log-normal distribution indicates a larger size polydispersity. In general, it was evident during the fitting procedure that the many broadening contributions that needed to be modelled to estimate the size distribution of the samples made the fitting results more unstable.

As the GoF values reported in Table 4.3 are equal or less than 2, thus indicating an already good fit of the available data, it is possible that the parameters employed to obtain the fits exceeds the information content accessible from the available data, generating parameter correlations and making the quality of the obtained values less and less reliable. On the other side, all the considered parameters describe a precise physical phenomenon that was observed to be present and relevant in the samples. Therefore, more reliable information in unlikely to be obtain from this same fitting approach and XRD data. Still, relevant qualitative information can be obtained. Both the line profile and the fitting results indicates that the stacking fault probability is higher in all the samples obtained using the microfluidic approach in comparison to the ones obtained using the batch synthesis. This can be especially seen from the almost complete disappearance of the (200) reflection. Moreover, fitting artifacts were evident due to limitation of the Warren theory to model stacking faults in this samples, as the theory was developed only for low concentrations of planar defects.[89] Overall, it was evident as the microfluidic approach does not only lead to smaller NPs, but also to a noticeable increase of stacking faults in the crystal structure. Interestingly, both the flow approaches employed in this Thesis (microfluidic and CHFS) led to the formation of highly faulted ZnS NPs, suggesting a correlation between the employment of flow conditions and the perturbation of the crystallographic stacking in ZnS.

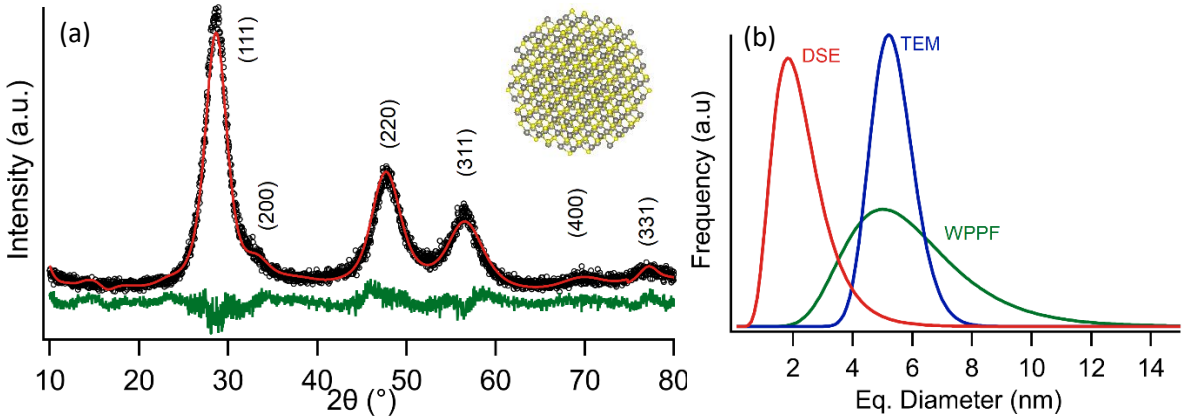

Figure 4.5 (a) DSE-based fit of the ZnS MF1 sample. Inset: example of a model 2.5 nm spherical ZnS NP used in the database built to perform the fit. (b) Comparison of the size distributions obtained via DSE with the results obtained with TEM analysis and the refined XRD profile.

The employment of a DSE-based fitting method would allow to completely overcome the limitations of separating the X-Ray scattering phenomenon into Bragg and diffuse contributions. However, to obtain the diffraction profile from a DSE approach, the knowledge of the distribution of interatomic distances in the systems is required. As the size of the particles shrinks, the obtainment of model particles for the systems and the calculation of interatomic distances becomes feasible, unlocking this powerful tool for the structural investigation of materials. This approach was attempted to further

investigate the structural features of the samples. A population of spherical model nanoparticles was built using the DebUsSy suite,[254] ranging from a single unit cell up to a 25 nm NP (60 layers). From these, a database of sampled interatomic distances was obtained. The total scattering profile of each particle was calculated through the DSE, while the final diffractogram of the sample was obtained by fitting the experimental data with the weighted sum of contributions from each modeled particle. Since the data were acquired using a common lab diffractometer working in Bragg-Brentano geometry, the total scattering of the sample was not obtainable. Therefore, a background was fitted using a linear combination of Chebyshev polynomials. It was however not possible to account for stacking faults contributions, as a specialized faulted-particle-modelling algorithm was only very recently obtained and successfully applied to cubic CdSe having a similar structure to the NP here considered.[254] Therefore, despite the relative good quality of the obtained fits in relation of the data quality, this approach without a proper description of the contribution for planar defects systematically and strongly underestimated the NPs average size (Figure 4.5b). This clearly showed that estimating the size of very small faulted ZnS NPs (like the one here considered or generally obtained from simple precipitation routes) from powder diffraction data by just accounting for the size broadening effects leads to misleading results.

4.1.2 Surface composition

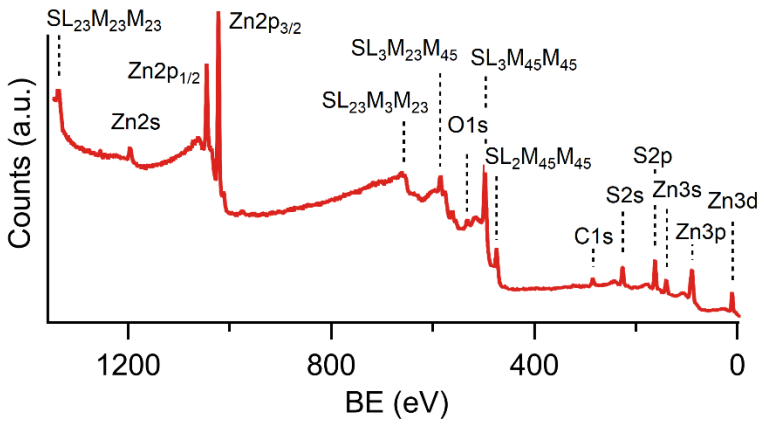

Figure 4.6 XPS survey spectra of sample ZnS MF3.

XPS analysis was performed on ZnS MF3 as reference sample. Commonly XPS is regarded as a surface sensitive technique but, accounting for the small size of the obtained NPs, the obtained composition can be related to bulk one. From the survey spectra, only the presence of Zn S was retrieved along with C and O from adventitious contamination.[100]

Table 4.4 Retrieved ZnS XPS peaks the ZnS MF3 sample.

Peak	ZnS MF3 (eV)	Reference[99]
Zn2s	1196.6	1196
$Zn2p_{3/2}$	1021.8	1021.7 - 1022.0
Zn3s	140.2	141.5 - 139.9
Zn3p	89.4	88.4
Zn3d	10.6	9.8 -10.7
S2s	226.6	225.6 - 226.3
S2p	161.6	161.9 - 162.2

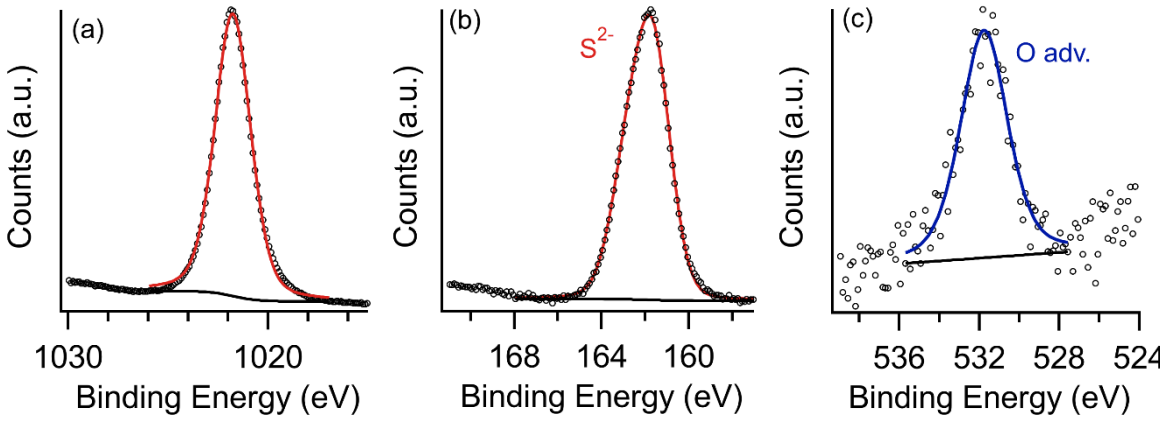

Figure 4.7 Fittings of the $Zn2p_{3/2}$ (a), S2p (b) and O1s (c) region of the XPS spectra of sample ZnS MF3.

The presence of the C1s signal was used to correct XPS spectra for charging effects on the calculated BE by assigning to the peak the value of 284.6 eV. From the semi-quantitative analysis a S:Zn at. ratio 0.7:1 was retrieved, which shows a remarkable deviation from the expected 1:1 ratio. The $Zn2p_{3/2}$ and S2p peaks were found at 1021.8 eV and 161.6 eV respectively, thus in a comparable position with respect to the batch synthetized samples (Chapter 2.2), that was attributed to the sole presence of Zn^{2+} and S^{2-} oxidation states. No indication of oxidized S (e.g. sulfates) was retrieved. Only a weak signal was observed in the O1s region at 531.7 eV, and it was attributed to adventitious contaminations, with no indications of signals arising from metal oxides. It could be therefore concluded that the sample was obtained in a pure form and free of oxidation, despite a remarkable variation of the measured composition with respect to the ZnS stoichiometry.

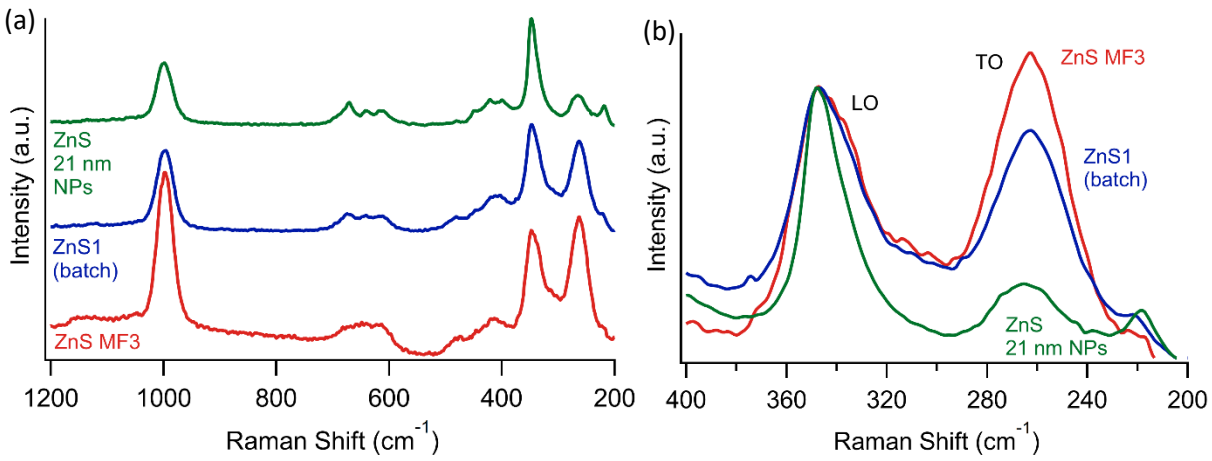

Figure 4.8 (a) Raman spectrum of sample ZnS MF3 compared with Raman spectra of samples ZnS1 (batch synthesis, Chapter 2.2) and with a reference sample of ZnS NPs of 21 nm. (b) Detail of the broadening effects on the LO mode and on the increased relative intensity of the TO mode. Intensities were normalized on the LO phonon.

The structural and compositional analysis on the obtained ZnS NPs was complemented using Raman spectroscopy. The Raman spectrum of sample ZnS MF3 showed the expected features for the single and two phonons processes of the ZnS cubic crystal structure. However, a general variation from the usual pattern was evident. In Figure 4.8 a comparison with the (batch) ZnS1 samples and a reference ZnS sample is proposed. The strong LO peak was found in all three patterns at 347 cm^{-1}. In comparison with the reference 21 nm ZnS NPs sample, the profile was noticeably asymmetrically broadened toward smaller wavenumbers. This effect was commonly found in small NPs and was attributed to the quantum confinement of phonons,[110] and is generally evident in the whole profile, as in ZnS MF3 the spectral features were less sharp and resolved. Another evident variation was the increase of the relative intensity of the TO mode, which was rather weak in the 21 nm reference NPs but got more intense in sample ZnS1 (batch), while in sample ZnS MF3 it became even more intense than the LO peak. Since this variation was likely to reflect the structural features of the samples, some hypothesis can be drawn on its origin. Its attribution to a specific feature arising from the presence of planar defects was discarded, since bigger but highly defective ZnS NPs described in Chapter 5 did not displayed this variation. A morphological effect was as well not considered, as XRD and TEM analysis indicated the presence of isotropic NPs. Therefore, the origin might be related to a size effect or to the presence of other unobserved defects in the structure, like the presence of specific point defects. Since the effect was quite strong, if reliably identified and explained, it might serve as a useful analytical tool. Other than the ZnS peaks, in the spectrum the presence of a signal at 999 cm^{-1} was also observed,

which was also ubiquitously retrieved for all the synthetized ZnS samples, and it was attributed to laser heating-induced formation of sulfates during the analysis.

4.1.3 NPs behavior in water suspension

From ZnS NPs synthetized employing the microfluidic method, the tendency to form stable suspensions during the purification procedure was observed, in analogy to the samples obtained using the batch approach. The phenomenon might be relevant to further simplify the uses of the material, as often a suspension having a suitable concentration of material is necessary (e.g. catalysis or preparation of films). From the batch synthesis approach, it was determined that the suspended NPs displayed relevant aggregation leading to the formation of self-assembled bigger objects, that however reached stability in suspension even for an extended period (several weeks upon visual inspection). Colloidal stability can originate by two different mechanisms: steric and electrostatic stabilization. The first is based on the repulsive interaction of long chain ligands or surfactants adsorbed on the NPs surface, and is entropy driven. The latter is based on the electrostatic repulsion between charges found on the surface.[255] As no ligand or surfactant was used in the syntheses performed in this work, the nature of the observed stabilization was likely electrostatic. To identify the origin of the stabilization, it is necessary to refer to the surface chemistry of ZnS. Similarly to other metal sulfides,[110] a sound description of the surface chemistry of ZnS has yet to be achieved. Hertl[110] reported the presence of -SH moieties on bulk commercial ZnS samples, that however was never observed in the case of NPs from FTIR measurements (e.g. Chapter 2.2), and is generally rarely observed on the surface of many metal sulfides (e.g. Chapter 3). A fundamental role was identified in the interaction toward exposed Zn atoms, that affects both the NPs structure and their capability to interact with their surroundings.[256,257] In particular, the adsorption of water was recognized as a main factor affecting the surface properties of the material.[103] The same interacting water molecules are affected from the pH of the solution, allowing protonation/deprotonation and therefore altering the charge found on the NPs surface. The stability of as-synthetized ZnS suspension (i.e. before being dried) was attributed to the presence of residual SH^- adsorbed on the surface. To further test the properties of ZnS NPs surface in water suspension, the ζ potential was measured at different pH values. The ζ potential is a measure of the electric potential at the shear surface, being the separation plane from the solvent layer that adheres to a particle through and the mobile solvent.[255] As a rule of thumb, electrostatic colloidal stability is generally achieved with a ζ potential over ±30 mV.

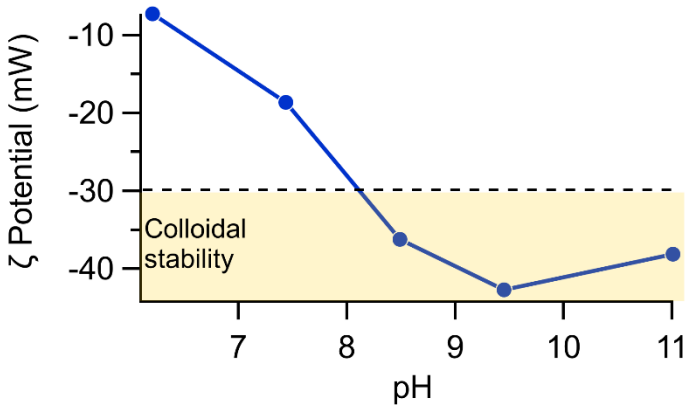

Figure 4.9 ζ potential measured as a function of the suspension pH for the re-dispersed MF ZnS 3 sample (after drying the NPs).

For the stable suspensions obtained directly from the synthetic procedure, having a pH typically in the range 12 – 10, a value of -41 mV was obtained. The ζ potential was also measured for the re-suspended NPs after drying the products as a function of pH. The autogenous pH of samples dispersed in pure (milliQ-quality) water was slightly acidic, ranging from 6.0 to 6.5. In this case, the measured ζ potential ranged from -5 mV to -20 mV. Indeed, once dried, the resuspended product was not stable in pure water and the complete coagulation was observed in few minutes. By lowering the pH with NaOH, a gradual decrease of the potential was observed (Figure 4.9), as the suspension crosses the threshold stability value around pH 8. Since no native -SH moieties were observed on the ZnS NPs surface, but a strong tendency to bind water molecules was instead retrieved, the reason of the increased stability was likely related to the adsorption of OH^- ions on the surface or to the deprotonation of adsorbed water molecules.

While the employment of a mildly basic solution to obtain a stable dispersion might be acceptable for some applications, it certainly is not adequate in the field of the biomedical applications. In the latter case, a colloidal stabilization needs to be achieved in the physiological range of pH 7.53-7.45,[255] making NPs functionalization a mandatory step. Post-synthesis modifications would also allow to exploit steric stabilization instead of the electrostatic one, which is generally best suited for environments having different electrolytes concentrations. Moreover, a properly designed ligand is not only capable to strongly bind the NPs surface, but it can be also engineered to selectively recognize specific target biological tissues.[255] It is worth to mention that a necessary functionalization step may also be added in-line with the microfluidic synthesis by adding a secondary mixer, resulting in a very efficient one-step approach to a final functional product.[258]

4.1.4 Photocatalytic activity for hydrogen evolution reaction

ZnS is a known photocatalyst for hydrogen evolution reaction (HER), and many different synthetic protocols were developed to obtain the pure, doped or defective material in order to enhance the its catalytic activity.[259] One of the main advantages of ZnS for this application is the remarkable resistance to oxidation in normal operating conditions, while other factors limit its activity. Pure and perfectly crystalline ZnS generally shows low radiation adsorption in the visible range, limiting the employability of visible or solar radiation, together with a high charge recombination rate.[259] Different type of defects are known to enhance ZnS activity in different ways. The introduction of sulfur vacancies was reported to extend the light absorption properties of ZnS in the visible range and enhance its activity using solar radiation,[260] while the introduction of planar defects was described to improve the charge carriers separation in the $Cd_{0.5}Zn_{0.5}S$ NPs.[261] The presence of planar defects was revealed by XRD analysis of ZnS NPs obtained with both batch and microfluidic approaches in this Thesis, while the presence of sulfur vacancies was suggested by the semi-quantitative XPS analysis. Moreover, the small NPs dimension could potentially increase the available surface area, which can be beneficial to increase the efficiency of the photocatalyst by increasing the concentration of active sites in the reaction mixture.[259] For these reasons, the activity as photocatalysts for the HER of samples ZnS MF1-3 were tested in comparison with sample ZnS1 (batch).

Table 4.5 Average $D_{1,0}$ diameter obtained by TEM analysis, SSA obtained by N_2 adsorption measurements and HER activity for both full spectrum (500 W Hg (Xe) lamp) and visible only ($\lambda > 420$ nm) of ZnS MF1-3 samples and ZnS1 sample.

Sample	TEM $D_{1,0}$ (nm)	BET SSA ($m^2\ g^{-1}$)	HER full spectrum (mmol $h^{-1}\ g^{-1}$)	HER visible only (mmol $h^{-1}\ g^{-1}$)
ZnS MF1	5.1	*	34	2
ZnS MF2	6.6	298 ± 4	37	1
ZnS MF3	4.8	265.5 ± 0.9	46	1
ZnS1 (batch)	7.8	225.0 ± 2.2	43	1

(*) to be measured.

The specific surface area (SSA) was firstly assessed in the dry powders of samples ZnS MF2 and ZnS MF3 via N_2 physisorption. The obtained adsorption isotherms were interpreted using the BET model.[262] The obtained values range from 200 $m^2\ g^{-1}$ to almost 300 $m^2\ g^{-1}$ greatly exceed the surface area of many previously employed ZnS photocatalysts, due to the small NPs size.[259] As reference, the surface

area was referred to be high when reaching the value of 100 m^2 g^{-1}.[260] By calculating the average $D_{3,2}$ diameter from SSA using a spherical shape approximation, the values 5.6, 5.0 and 6.6 nm were obtained for samples ZnS MF2, ZnS MF3 and ZnS1 (batch) respectively. Comparing this result with the one reported in Table 4.2, a slight underestimation of the NPs average size with respect to the values obtained by TEM micrographs was obtained for samples ZnS MF2 and ZnS1 (batch), while a good agreement was found for sample ZnS MF3. The underestimation may be related either to experimental errors or to surface roughness and/or particle anisotropy, that led to an increase of the available surface area in comparison to a flat sphere. In general, the obtained values were in good agreement with the retrieved NPs size distribution and the relative geometrical SSA.

The photocatalytic activity of the samples was evaluated for both the full spectrum of a 500 W Hg (Xe) lamp (including the UV fraction of the emitted spectrum) and the visible fraction only (radiation having $\lambda < 420$ nm filtered). In general, smaller NPs size or larger SSA did not result in a more active catalyst, as the highest values were obtained for ZnS1 (batch) and ZnS MF3 samples for the full spectrum irradiation. In the case of the filtered radiation ($\lambda > 420$ nm) the highest value was obtained from the ZnS MF1 sample, while comparable results were seen for the others. Overall, the relative activity did not show an obvious trend with the characterized features of the samples, and therefore the influence of multiple parameters was evidenced, requiring a much wider study to be rationalized. The error of the measurements was estimated to be ± 4 by the three repetition on the ZnS1 (batch) samples, and therefore results obtained using only the visible part of the spectrum were affected by a large error. The comparison of the retrieved values with literature values is complicated as no reference samples were available and the employed conditions were remarkably different from the one commonly reported in the literature (i.e. a 500 W Hg (Xe) lamp was employed, while a 300 W is much more common). As reference values, the best reported activities obtained using a Xe lamp 300 W ($\lambda > 420$ nm) for ZnS samples with an optimized concentration of sulfur vacancies was 0.47 mmol h^{-1} g^{-1},[260] while in case of nanotwinned $Cd_{(1-x)}Zn_xS$ nanorods the best activity was 2.0 mmol h^{-1} g^{-1}.[263] Introductory information on the current state-of-the-art in HER using ZnS and related photocatalysts can be found in the review by Wang *et al.*[264]

4.2 Microfluidic synthesis of TM and Ln doped ZnS NPs

Zinc sulfide have been vastly explored as host material for the inclusion of dopants, thanks to its wide band gap (E_g ~3.6 eV) and its good resistance to oxidation at room temperature.[265] To explore the obtainment of new functional materials, and especially to develop new photoluminescent (PL) NPs, many different ions were studied, including Cu^{2+}, Mn^{2+}, Pb^{2+}, Ni^{2+}, Cd^{2+}, Co^{2+}, Eu^{3+}, Sm^{3+}, Tb^{3+}, Er^{3+}.[265] Along with the presence of point defects, the dopants can be used to modulate the PL of ZnS by introducing new energy levels within the material bandgap. As the production of doped ZnS NPs typically relies on batch approaches, the simple but effective microfluidic method developed in this Thesis for pure ZnS NPs was further extended to evaluate the obtainment of doped NPs. This could in principle extend the discussed advantages of the microfluidic approach to the synthesis of NPs having interesting functional properties such as suitable luminescence emission in different ranges of the spectrum. The same setup described for the pure particles was employed, including the simple addition of the dopant precursor to the zinc precursor solution. The screened dopants were Mn^{2+}, Cu^{2+}, Ni^{2+}, Eu^{3+}, Sm^{3+}, Nd^{3+}, Yb^{3+}, while for each ion three dopants concentrations (intended as M^{n+} / (M^{n+} + Zn^{2+}) molar ratio) were considered: 0.1%, 1.0% and 5.0%. Mn^{2+}, Cu^{2+}, Ni^{2+} were chosen as transition metal dopants, as numerous reports exists in the literature for their successful employment to obtain PL in the visible range, while lanthanides were chosen to potentially obtain emission in the NIR range.[265] All the precursors where simple and widely available nitrate or chloride salts (see Chapter 7.1). The synthetic conditions of sample ZnS MF3 were employed for the synthesis of all the doped samples (see Table 4.1).

The microfluidic synthesis of doped ZnS samples and their characterization was performed in cooperation with the Master Student Francesca Tajoli.

4.2.1 Composition and structure

The presence of the doping elements in the samples was quantified by ICP-MS measurements. Both the experimental concentration of dopants and their uptake (i.e. the ratio between the retrieved dopants concentrations and to the one predicted from the precursors concentration employed) were determined. In the ICP -MS analysis, Zn, S and dopants concentration was determined.

Table 4.6 Composition of transition metal doped M:ZnS samples determined by ICP-MS on Zn, S, Mn, Cu, Ni elements. The nominal at. concentration refers to the one expected based on the concentration employed in the synthesis. Uptake is determined as the ratio between the experimental and the predicted concentration. Doping concentration are calculated as M^{2+} / (M^{2+} + Zn^{2+}) molar ratio.

	%at. doping			Stoichiometry $M_nZn_1S_m$	
Sample	Nominal	Experimental	%Uptake	n	m
Mn:ZnS	0.1	0.10	100	0.001	0.990
	1.0	1.06	106	0.011	1.095
	5.0	5.96	119	0.063	1.040
Cu:ZnS	0.1	0.10	100	0.001	1.158
	1.0	1.07	107	0.011	1.092
	5.0	5.84	117	0.062	1.255
Ni:ZnS	0.1	0.11	110	0.001	1.134
	1.0	0.87	87	0.009	1.010
	5.0	6.04	121	0.064	1.272

Table 4.7 Composition of lanthanides doped Ln:ZnS samples determined by ICP-MS on Zn, S, Eu, Sm, Nd and Yb elements. The nominal at. concentration refers to the one expected based on the concentration employed in the synthesis. Uptake is determined as the ratio between the experimental and the predicted concentration. Doping concentration are calculated as Ln^{3+} / (Ln^{3+} + Zn^{2+}) molar ratio.

	%at. doping			Stoichiometry $Ln_nZn_1S_m$	
Sample	Nominal	Experimental	%Uptake	n	m
Eu:ZnS	0.1	0.07	70	0.001	1.131
	1.0	0.90	90	0.009	1.080
	5.0	6.08	122	0.065	1.230
Sm:ZnS	0.1	0.09	90	0.001	1.081
	1.0	0.90	90	0.009	0.963
	5.0	5.44	109	0.058	1.212
Nd:ZnS	0.1	0.08	80	0.001	1.484
	1.0	0.48	48	0.005	1.284
	5.0	2.78	56	0.029	1.303
Yb:ZnS	0.1	0.08	80	0.001	1.306
	1.0	0.48	48	0.005	0.878
	5.0	2.65	53	0.027	1.141

From the obtained uptake values, the presence of doping elements in the samples was confirmed. Values around 100% were obtained for transition metal doped samples, while a diminished uptake was observed for the lanthanides, and especially for Nd and Yb. The presence of uptake percentages over 100% might be due to the formation of secondary compounds (compounds different from ZnS) in the samples that are more easily separated from the water suspension during the purification procedure. Indeed, ZnS NPs displayed the tendency of maintaining a certain colloidal stability even after prolonged high speed (12 500 rpm) centrifugations. Therefore, a fraction of ZnS NPs was easily lost due to incomplete separation from the liquid phase. If secondary compound were formed during the syntheses, that likely did not share the same colloidal stability of ZnS NPs, an enrichment in these secondary compounds in comparison to ZnS was likely obtained. In the case of lanthanides, the competing precipitation of the sulfides (i.e. Ln_2S_3) at highly basic pH was unlikely, as these oxophilic elements displays a marked tendency to form hydroxides in basic conditions. Therefore, the reduced uptake was likely related to the dissolution of these secondary compounds in the purification stage of the syntheses.

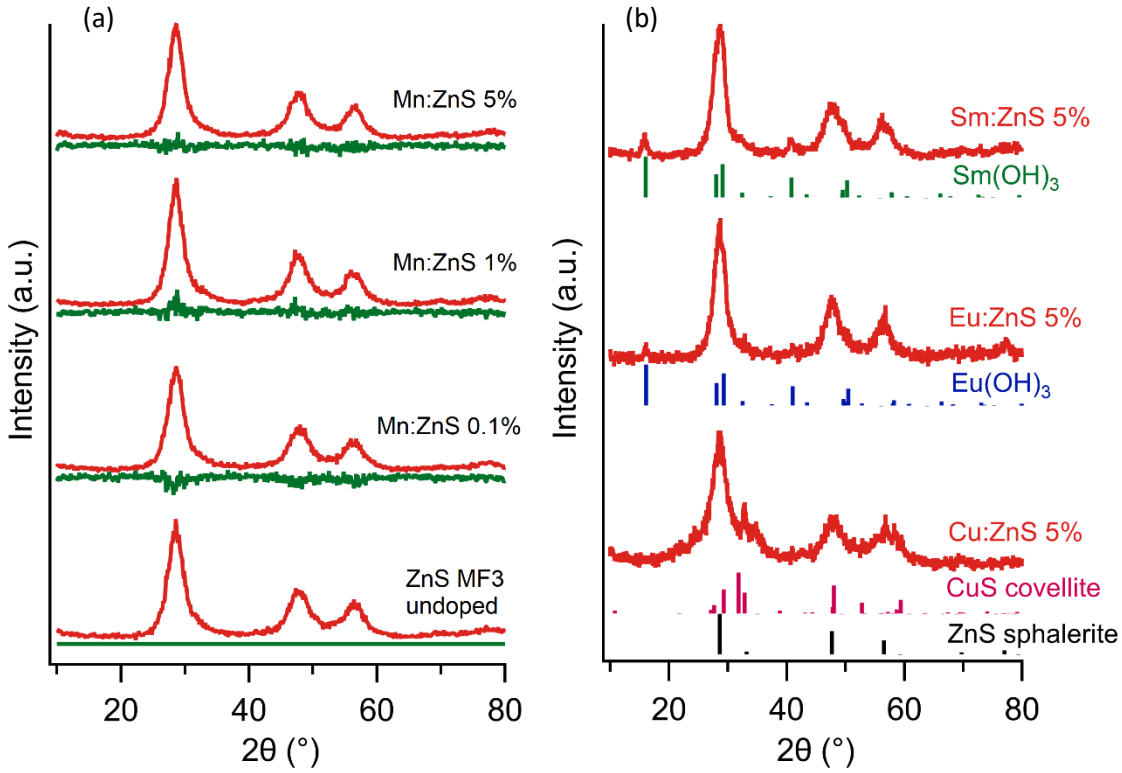

Figure 4.10 XRD diffractograms of (a) Mn:ZnS 0.1%, 1% and 5% compared with sample ZnS MF3 (undoped). (b) samples Cu:ZnS 5%, Eu:ZnS 5% and Sm:ZnS 5% with indication of the retrieved phases (stick plots).

Both possible variations of the ZnS NPs crystal structure and presence of crystalline contaminations were analyzed collecting the XRD patterns of the samples. In all samples, no variations on the profile of ZnS reflections were observed, indicating unvaried crystallographic features in comparison with the reference undoped sample ZnS MF3. In the case of Mn-doped NPs, no additional reflections were visible, while in the case of Cu and Ni-doped NPs, the presence small additional reflections were observed for samples at higher dopant concentration. The position of the additional features visible in sample Cu:ZnS 5% (Figure 4.10b) indicated the competing formation of CuS covellite (ICSD 98-004-1911, space group P 63/m m c), that was also observed as the main product of the analogous batch reaction of Chapter 3.1. In the case of Ni-doped NPs, an additional reflection at 23.1° was visible (not shown) but it was not possible to reliably assign it. In the case of lanthanides-doped samples, the presence of the relative hydroxides was retrieved for samples at 5% concentration ($Sm(OH)_3$ ICSD 01-083-2036, $Eu(OH)_3$ ICSD 01-083-2305, $Nd(OH)_3$ ICSD 01-075-1902, space group P63/m) with exception of the Yb:ZnS samples. In the obtained XRD patterns a shift of the ZnS reflections due to a variation of the unit cell size was not observed, possibly due to the large broadening effects caused by to small crystallite size and stacking faults. Moreover, in the case of the transition metal employed, a small difference on ionic radii exists,[266] leading to minor lattice variations in the case of dopants inclusion. The absence of additional reflections on the samples was not considered a safe indication of the absence of contaminations, as the formation of amorphous compound could be possible, together with the presence of compounds in concentrations below the XRD detection limit (approx. 1%).

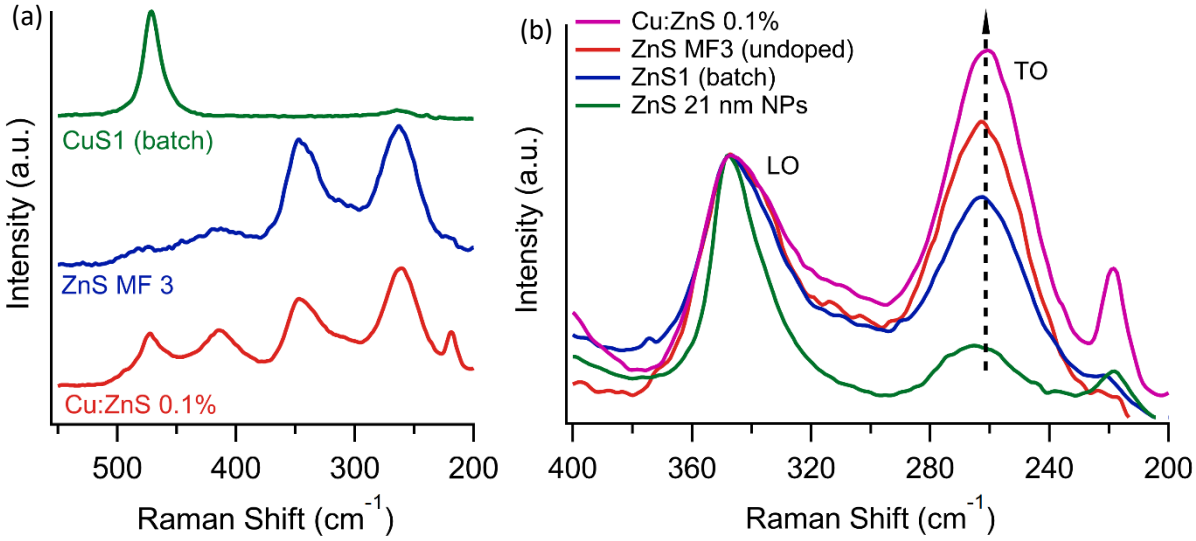

Figure 4.11 (a) Comparison between the Raman spectra of samples Cu:ZnS 0.1%, ZnS MF3 and CuS1 (batch, Chapter 3.1). (b) Detail of the increased relative intensity of TO mode in different samples.

The identification of secondary compounds was also attempted with the employment of Raman spectroscopy. The collected spectra showed a profile like the one of sample ZnS MF3, while the identification of other peaks was complicated due to the extended second order Raman spectra of the ZnS NPs. As visible in Figure 4.11, in the analyzed spectra the LO peak at 347 cm^{-1}, that would normally be the main peak of the ZnS spectra (see Figure 4.8), got even less intense in comparison with the TO mode and the other two-phonons peaks with respect to the undoped ZnS MF3 reference sample (e.g. peaks at 219, 261, 414, 473 cm^{-1}). Comparing the expected Raman spectra obtained for sample CuS1 obtained under analogous condition using a batch approach (Chapter 3.1), the diagnostic peaks would fall almost perfectly in correspondence of a second-order Raman component of ZnS. Since these contributions were determined to be varied from the undoped reference, the increased intensity of the contribution of the peak at 473 cm^{-1} could be related to both the presence of CuS in the sample and to the variation of the two phonon peaks in the ZnS spectra. Therefore, is not possible to safely identify the presence of CuS, and analogously other materials, employing this technique. Since no relevant size and morphological difference among doped and undoped samples was observed by TEM (see below) and XRD analysis, the increase in the relative intensity of the TO mode and the two-phonons modes was likely related to the presence of defects in the ZnS structure.

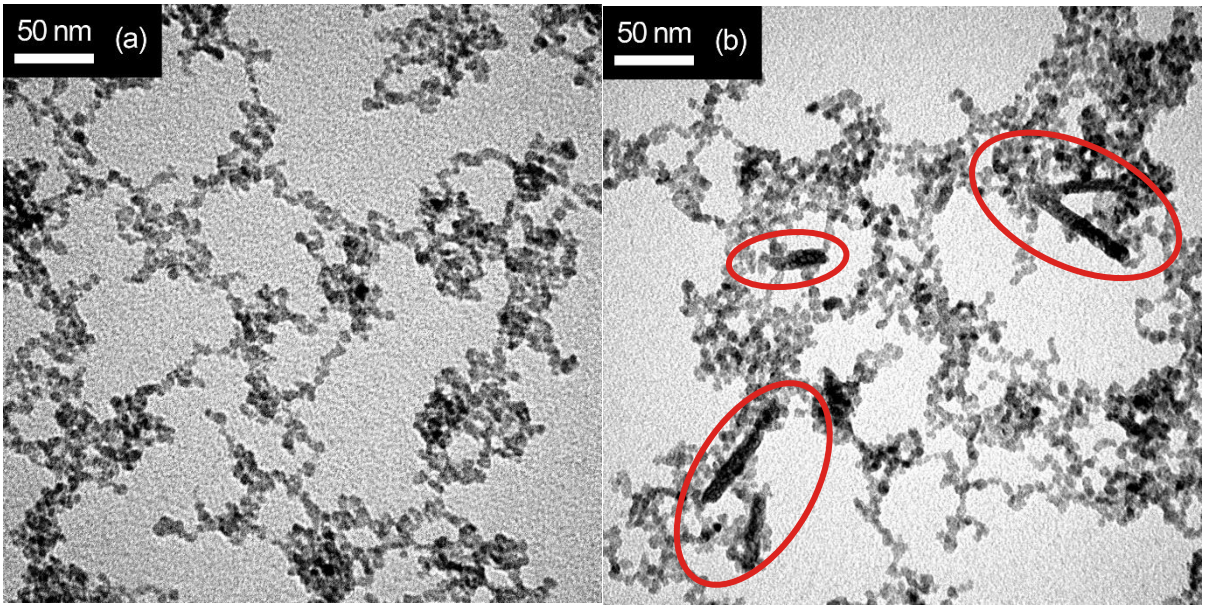

Figure 4.12 TEM micrographs of (a) Yb:ZnS 5% and (b) Sm:ZnS 5% samples.

TEM micrographs were acquired to confirm that no significant variations of the obtained NPs occurred. In all the collected micrographs (Figure 4.12) the observed NPs displayed analogous morphology and size to the undoped particles. The same tendency of the undoped samples to form aggregates of fractal appearance was also noticed (see Figure 4.3, with exception of the ZnS MF 1 sample). The presence of a secondary set of particles was only observed clearly for samples Cu:ZnS 5%, Sm:ZnS 5%, and only

possibly on sample Eu:ZnS 5%. An example of such particles in sample Sm:ZnS 5% is visible in Figure 4.12b, where the presence of rod-like particles having a variable length between 30 and 70 nm was retrieved along with the ZnS NPs. These rods were probably composed of $Sm(OH)_3$, which was identified by XRD analysis in the same sample.

To complete the compositional analysis, XPS spectra were also acquired for samples having 5% dopant concentration. Overall the analysis showed the presence of Zn, S, O and C analogously to the reference ZnS MF 3 reference sample. The retrieved $Zn2p_{3/2}$ and S2p positions were in the range 1021.5 – 1022.2 eV and 161.5 – 162.0 eV respectively, consistently with the attribution of Zn^{2+} and S^{2-} and with the value obtained for the undoped samples (see Table 4.4). The semi-quantitative analysis indicated a Zn-rich samples, having an atomic Zn:S ratio ranging from 1:0.9 to 1:0.5. This is in contrast with the ICP-MS measurements, that indicated the presence of an excess of S in the samples in respect to the ZnS stoichiometry. The reason might be related to a variable composition (i.e. the presence of different types of point defects) of the sample in the surface with respect to the core of the NPs, or to the presence of residual sulfur compounds on the surface of NPs that might be eliminated during the XPS degassing procedure (e.g. elemental sulfur like S_8). The presence of dopants was not observed in all samples with the exception of Cu:ZnS 5%. In the latter, a very weak Cu2p doublet was visible at approx. 932 and 953 eV, that however presented an insufficient signal to noise ratio to be fitted. In general, the presence of dopants could not be confirmed by XPS, possibly due to the insufficient concentration of the elements in the material.

Overall, the presence of doping elements in the samples was confirmed by ICP-MS measurements. It was not possible, however, to safely identify if the elements were successfully included in the ZnS matrix and to which extent. The presence of secondary compounds was observed in the case of samples Cu:ZnS 5%, Eu:ZnS 5%, Sm:ZnS 5% and Nd:ZnS 5% mainly via XRD analysis, and further confirmed by TEM analysis for samples Cu:ZnS 5% and Sm:ZnS 5%. These analyses also confirmed that ZnS NPs were substantially unaltered in their dimensional, morphological and structural features, as no relevant variation with respect to the undoped ZnS MF 3 were observed. No useful information was obtained via Raman spectroscopy about the presence of secondary compounds, while an additional increase of the relative intensity of second order ZnS Raman spectra and of the TO mode was observed in respect to the undoped sample. XPS measurements were also not useful to identify relevant contaminations due to the small concentrations these might be found. To prove or rule out the presence of dopants inside the ZnS, and to identify their chemical environment, the use of synchrotron-based x-ray absorption spectroscopies like EXAFS or XANES may be required.

The formation of secondary compounds instead of solid solutions can be rationalized considering the crystallographic features of cubic ZnS in comparison with coordination environment normally

preferred by the dopants. All the employed metals showed a different preferred coordination in their compounds obtained using by the same chemical environment of the microfluidic synthesis, as also directly observed for some of them Chapter 3. The most stable phase of MnS is the α-MnS (alabandite), that displays a rock-salt type of structure where Mn^{2+} ions possess an octahedral coordination.[201] However, two metastable polymorphs were obtained using the synthetic conditions here discussed, namely the β-MnS and γ-MnS. The first is characterized by a cubic unit cell where both Mn^{2+} and S^{2-} ions possess a tetrahedral coordination. Thus, considering Mn^{2+} possess the same charge and a similar ionic radius (as IV-coordinated: Mn^{2+} 0.66 Å, Zn^{2+} 0.6 Å),[266] and considering a MnS phase having an analogous coordination was also formed in the same chemical environment, the inclusion of Mn^{2+} in the lattice of sphalerite ZnS in substitutional position can be regarded as plausible. Indeed, Mn-doped ZnS was probably the most widely studied and reported doped ZnS compound, while its presence in substitutional position was also experimentally observed along with its presence as interstitial ion.[265] Despite this, surface segregation phenomena of Mn in Mn-doped ZnS NPs were also reported.[267–269] Similar considerations on charge and ionic radii can be done for Cu^{2+} and Ni^{2+} (as IV-coordinated: Cu^{2+} 0.57 Å, Ni^{2+} 0.55 Å),[266] but a less favorable situation emerges considering their chemistry. As reported in Chapter 3, using analogous batch conditions, the precipitation of CuS covellite was obtained. This material is characterized by a prevalent Cu^{+} character, while the mere presence of Cu^{2+} in its structure is matter of long-lasting debate.[161,270] Thus, a tendency of Cu^{2+} to reduce to Cu^{+} in the reductive environment of the SH^{-} solution was observed. Despite this, a certain favor towards a tetrahedral coordination may be evinced from the CuS covellite crystal structure, as in this structure Cu is found in both tetrahedral and trigonal coordination. In the case of Ni^{2+}, analogous batch conditions led to the formation of $Ni(OH)_2$ (Chapter 3.5), thus indicating the oxophilic behavior of this ion. Despite all this, the obtainment of both Cu^{2+} and Ni^{2+} doped ZnS was reported by using simple water-based coprecipitation routes.[271–274] Considering lanthanides, a radically less favorable situation for dopants inclusion emerges. Lanthanides are commonly found in the Ln^{3+} oxidation state, thus their inclusion in the ZnS necessarily results in a charge unbalance that needs to be compensated by the formation of point defects. Moreover, hexacoordination is generally observed as the minimum coordination for Ln^{3+} ions, which possess larger ionic radii than first-row M^{2+} transition metals (as VI-coordinated: Nd^{3+} 0.983 Å, Sm^{3+} 0.958 Å, Eu^{3+} 0.947 Å, Yb^{3+} 0.868 Å).[266] For this reasons, co-precipitation or other low temperature methods were often find unsuited for the preparation of Ln-doped ZnS, as high temperatures were needed to promote the inclusions in the ZnS matrix.[275]

4.2.2 Functional properties

The photoluminescence (PL) properties of the obtained doped samples were characterized to test if the synthesis approach led to the obtainment of functional doped ZnS NPs. Moreover, in the view of possible bioimaging applications, NPs cytotoxicity was also tested.

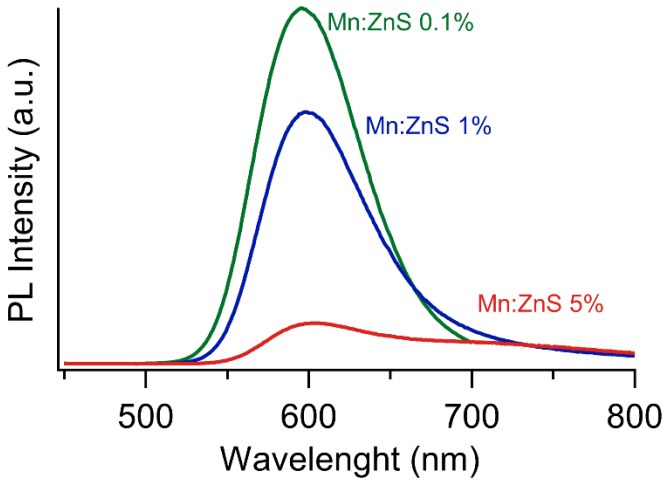

Figure 4.13 PL spectra of Mn:ZnS samples upon excitation at λ_{exc} = 293 nm (ZnS matrix).

In the Mn:ZnS samples, a PL band centered at 596 nm (orange emission) was observed upon excitation of ZnS matrix at 293 nm, connected to the $^4T_1 \rightarrow {}^6A_1$ transition of the Mn^{2+} 3d orbitals. This emission indicates an effective energy transfer from ZnS energy levels to the one of the Mn^{2+} ions, thus confirming the inclusion of Mn^{2+} in the ZnS matrix.[276] Noticeably, the PL intensity was stronger in the Mn:Zns 0.1% sample, while its intensity decreased as the concentration of dopant was increased. This effect might be related to clustering effects of Mn^{2+} ions, that gradually reduces the PL efficiency due to the concentration quenching phenomenon.[277,278] A similar effect was recently observed by Tuan *et al.*, who also described the quenching of orange PL from Mn-doped ZnS as the concentration of dopant increased, due to the non-radiative charge transfer between Mn^{2+} clusters.[279]

In the case of Ni-doped ZnS NPs, upon excitation of the ZnS matrix, a green emission at 520 nm was expected,[279] while for the Cu-doped ones the emission in the range 425 – 525 nm, or at 600 nm, was reported.[91,273] In the samples here synthetized no emission was observed for these samples upon excitation of the ZnS matrix. This agrees with the previous structural and compositional characterization, that indicated the presence of secondary products especially for the Cu:ZnS samples. Therefore, the inclusion of Cu^{2+} and Ni^{2+} was not achieved employing this method.

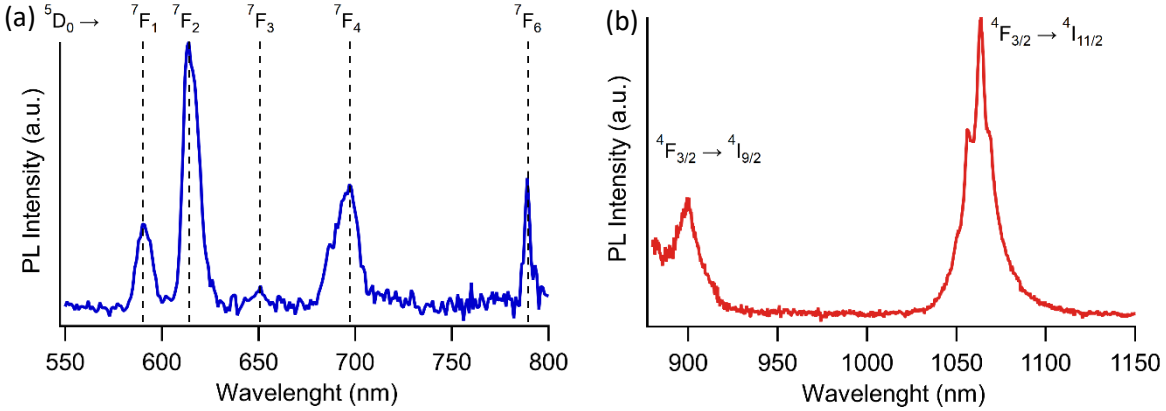

Figure 4.14 PL spectra of (a) sample Eu:ZnS 0.1% (λ_{exc} = 394 nm) and (b) sample Nd:ZnS 5% (λ_{exc} = 578 nm).

The emission from lanthanides levels of Ln-doped ZnS samples were obtained only employing excitation wavelengths centered on the typical frequencies of lanthanides f-f transitions, while no emission upon excitation of the ZnS matrix was observed. This indicated that, also for the case of lanthanides, the inclusion of dopants was not successful, as no charge transfer was observed between ZnS and the Ln^{3+} ions. PL spectra were acquired to confirm the presence of the lanthanides on the samples. For all the tested samples, the characteristic emission peaks were retrieved. Figure 14.4a shows the emission spectra from the Eu:ZnS 0.1% sample excited at λ_{exc} = 394 nm, corresponding to the $^7F_0 \rightarrow {}^5L_6$ transition.[275] On the spectra, five components were detected at 590, 614, 651, 697, 789 nm respectively, that can be attributed to the transition from the excited $^5D_0$ state to the states $^7F_1$, $^7F_2$, $^7F_3$, $^7F_4$, and $^7F_6$ respectively.[280] From the Sm:ZnS samples excited at λ_{exc} = 403 nm, the presence of two weak peaks at 595 and 648 nm for the transitions from the $^4G_{5/2}$ excited state to the $^6H_{7/2}$ and $^6H_{9/2}$ states respectively was observed.[281] In the Yb:ZnS samples excited at λ_{exc} = 375 nm a single very weak peak was observed at 976 nm, attributed to the $^2F_{5/2} \rightarrow {}^2F_{7/2}$ transition.[281] Lastly, for the Nd:ZnS samples (Figure 14b) excited at λ_{exc} = 578 nm, two components were observed for the $^4F_{3/2} \rightarrow {}^4I_{9/2}$ transition at 900 nm and the $^4F_{3/2} \rightarrow {}^4I_{11/2}$ transition at 1064 nm. Overall, the presence of the lanthanides on the synthetized samples was confirmed, but no energy transfer was observed from the ZnS. Thus, lanthanides were probably found on the samples as hydroxides, in accordance with the XRD results. In successfully included in the ZnS NPs, the most useful ions for the development of NPs for bioimaging applications would be Eu^{3+} and Nd^{3+}, that displayed emission lines in suitable ranges the NIR spectrum.[282]

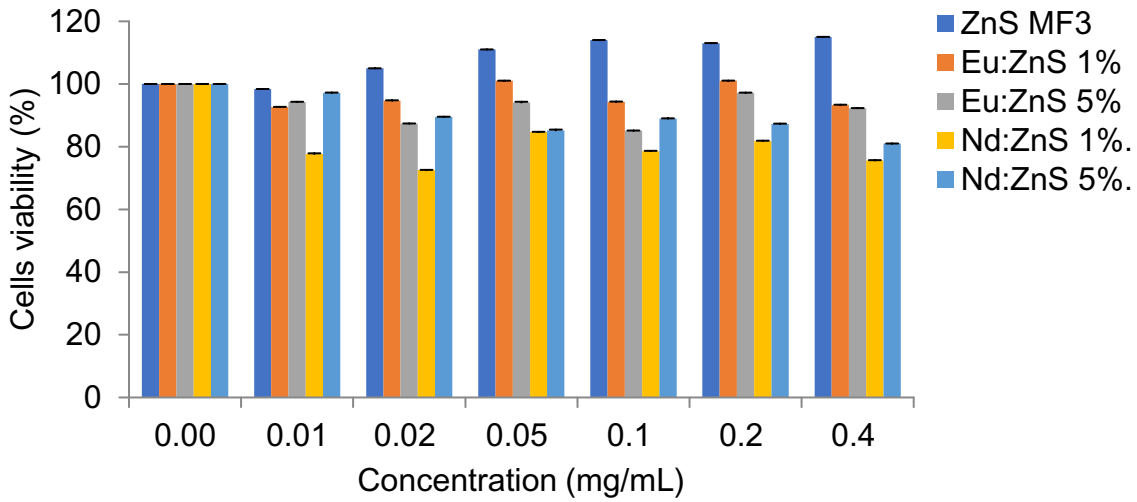

Figure 4.15 Results of the MTS assay on human lung adenocarcinoma A549 cells incubated for 24 h with ZnS MF3, Eu:ZnS 1-5% and Nd:ZnS 1-5% samples at different concentrations. Data reported with error bars.

In the view of possible bioimaging applications, a determination of NPs cytotoxicity is important to evaluate possible the cytotoxicity of the NPs, to assess it the material is harmful to living cells. This aspect was evaluated on sample ZnS MF3 as reference and on Eu:ZnS 1%, Eu:ZnS 5%, Nd:ZnS 1% and Nd:ZnS 5% samples. NPs were dispersed in at different concentrations ranging from 0.01 to 0.40 mg/ml and incubated for 24 h in human lung adenocarcinoma A549 cells. Cells viability was evaluated via MTS assay. The latter is a colorimetric assay based on the reduction of MTS tetrazolium compound to the colored formazan, detectable at 490 mn, caused by the activity NAD(P)H-dependent dehydrogenases enzymes in metabolic active cells. Thus, the viability of cells was simply evaluated comparing absorbance values recorded at 490 nm with the values obtained from the non-treated cells, used as reference for 100% viability. From the results reported in Figure 4.15, a scarce cytotoxicity was evidenced, with the exception of the Nd:ZnS 1% for which a decrease of 20% in cell viability was observed. For more reliable results, an extended analysis over longer incubation times would be required, along with the employment of a clonogenic assay. In the case of the undoped ZnS MF3 sample, the increase of the viability over the value of 100% indicates that the treatment favored either cells proliferation or the metabolism of the employed dye (MTS, 3-(4,5-diMethylthiazol-2-yl)-5-(3-carboxymethoxyphenyl)-2-(4-sulfophenyl)-2H).

Chapter 5.
Continuous hydrothermal synthesis and characterization of pure and Ln-doped defective ZnS NPs

5.1 Continuous hydrothermal synthesis of defective ZnS NPs

Continuous flow hydrothermal synthesis (CFHS) is a very versatile synthetic approach that represents an easily scalable water based approach for the synthesis of wide variety of different compounds,[61,77,283] including metal sulfides.[78] This method exploits water at high temperature (up to 500 °C) and pressures (up to 24 MPa), often in supercritical conditions. Applied to the synthesis of semiconductors, it allows the replication of many features of the hot-injection approach, such as the fast generation of a supersaturation of precursors in the reaction mixture. In the conditions employed in CHFS, the water physico-chemical properties, such as pK_w, dielectric constant, density and viscosity, are altered, allowing the crystallization to proceed through different pathways.[284] Dunne *at al.*[78] applied this technique to the synthesis of metal sulfides developing two single-mixer methods (Figure 5.1). The overall strategy consisted in the decomposition under supercritical conditions of thiourea to produce SH^- *in-situ*, that was allowed to react with a metal precursor and rapidly form the metal sulfide NPs. In the first of the two methods Dunne *at al.*[78] developed, a thiourea solution was firstly pre-heated to allow its decomposition, and afterwards it was mixed with a metal salt solution. In the second method, only water was preheated, while a solution of both the metal salt and the thiourea was later mixed to the supercritical water, causing the decomposition of thiourea to occur in direct presence of the metal precursor. Using this strategies, ZnS, CdS, PbS, CuS, $Fe_{(1-x)}S$ and Bi_2S_3 were obtained by properly tuning the synthesis conditions. The setup employed in this Thesis was developed as a variation of the methods optimized by Dunne *at al.*[78], that was especially realized to obtain a more flexible control over the decomposition of thiourea.

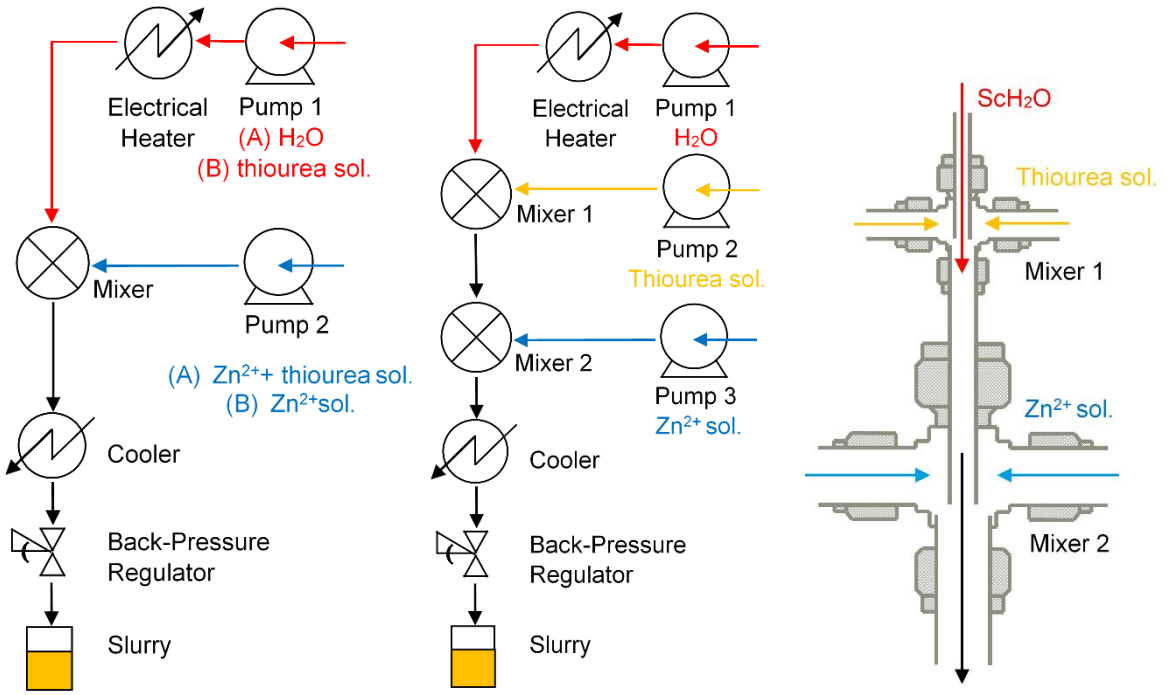

Figure 5.1 Comparison between the CHFS approach developed by Dunne *et al.*[78] (left) and the setup employed in this Thesis (center). Detail of the double mixer employed (right).

CHFS was used to synthetize ZnS NPs using a two-mixer approach (Figure 5.1). Pure milli-Q quality water was fed though a heater, allowing its temperature to raise to 450 °C, while the pressure was kept at 24 MPa. The obtained supercritical water was than mixed to a thiourea solution, causing the decomposition of the latter and formation of SH^-. This solution was secondly channeled through a second mixer to add a zinc nitrate solution, resulting in the precipitation of ZnS NPs. A S:Zn 2:1 molar ratio was kept in all reactions to allow an excess of SH^- to be produced to avoid the formation of ZnO. Since supercritical water was mixed to room-temperature solutions, the mixing temperature was simply tuned by adjusting the feeding rate of the precursors. The temperature at the first mixer was kept fixed at 380 °C, to allow the same thiourea decomposition conditions in all the obtained samples, while the second mixer temperature was varied between 241 °C and 335 °C to explore the effect of this parameter. In comparison to the setups developed by Dunne *at al.*[78], this double-mixer setup allowed an independent control of the temperature of decomposition of thiourea from the actual reaction temperature a the second mixer. Moreover, the thiourea decomposition and the ZnS precipitation were separated in two different stages, allowing a more independent control of the two processes.

Thiourea was chosen as precursor not only to allow a better comparison with the literature setups, but also due to its wide availability, its clean decomposition and its affordability. The decomposition of this molecule can be pursued either by basic catalysis[285] or thermal decomposition.[78,80,286–288] In the case of

the base-catalyzed decomposition, SH^- is firstly produced together with urea, that subsequently decomposes in ammonium fulminate, according to the following equations:

$$SC(NH_2)_2 + OH^- \rightarrow SH^- + OC(NH_2)_2 \quad (5.1)$$

$$OC(NH_2)_2 \rightarrow NH_4^+ + CNO^- \quad (5.2)$$

In the case of the thermal decomposition, different mechanisms were reported depending of the employed temperature.[80] Up to 180 °C the formation of carbodiimide was reported, along with the evolution of hydrogen sulfide. Over 220 °C the formation of thiocyanic acid occurs, together with the evolution of ammonia. The overall decomposition results in the formation of hydrogen sulfide, ammonia and carbon dioxide, making this precursor an ideal candidate to obtain a clean decomposition an prevent the deposition of organic residues on the final product.

$$SC(NH_2)_2 + 2H_2O \xrightarrow{\Delta} H_2S + 2NH_3 + CO_2 \quad (5.3)$$

The obtained ZnS samples were named in the text as indicated in Table 5.1, according to the reaction temperature at the second mixer as a relevant parameter.

Table 5.1 Specification of the sample name in correlation with the temperature at the second mixer of the CFHS setup.

ZnS sample	Reaction temperature (°C)
CH1	241
CH2	251
CH3	260
CH4	271
CH5	282
CH6	294
CH7	307
CH8	321
CH9	335

5.1.1 Size and morphology

Size and morphology of the obtained particles were firstly analyzed. TEM micrographs of samples CH1, CH5 and CH9 were acquired in order to identify a possible trend of the retrieved size with respect to the reaction temperature. In all samples, rounded particles were observed, sometimes assuming a slightly elongated shape. The tendency to aggregate of the particles was also noticed, similarly to ZnS samples described in Chapters 2 and 4.

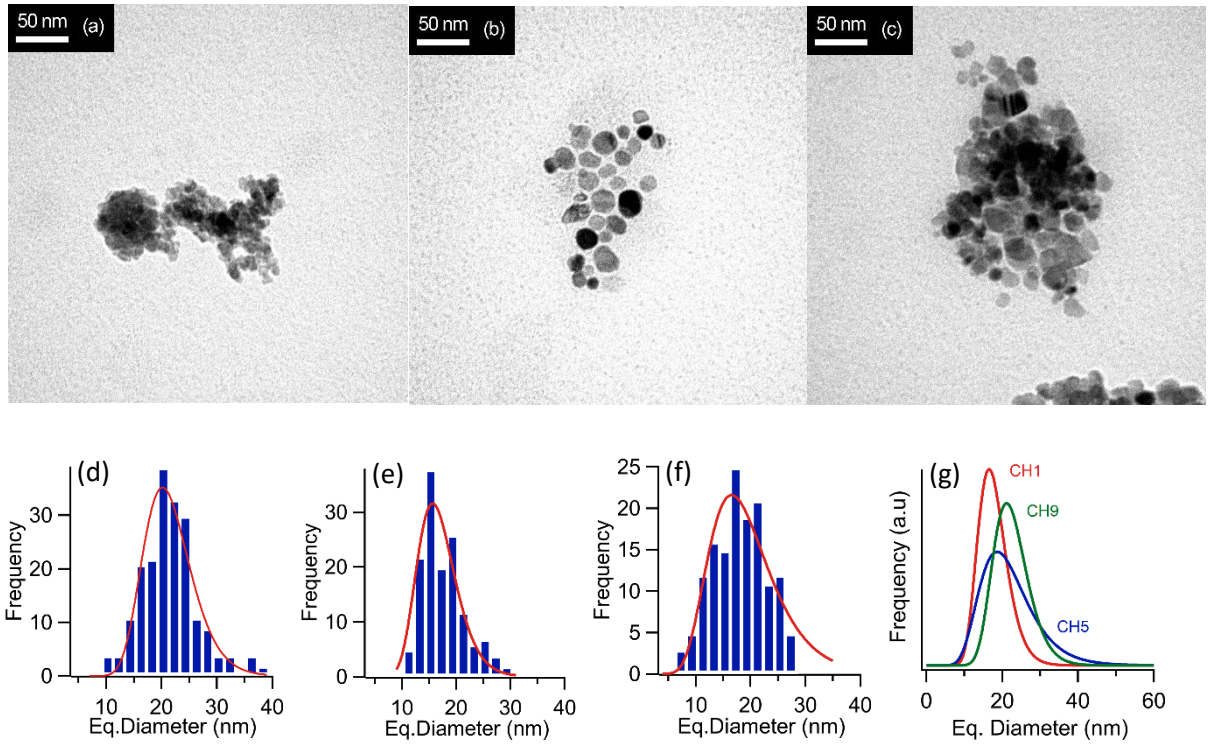

Figure 5.2 TEM micrographs of samples CH1 (a), CH5 (b) and CH9 (c), retrieved size distributions of samples CH1 (d), CH5 (e) and CH9 (f). Comparison of the fitted size distributions (g).

Table 5.2 Size distribution descriptors obtained from TEM population of sampled particles and their log-normal fits.

	CH1		CH5		CH9	
	TEM	Fit	TEM	Fit	TEM	Fit
$D_{1,0}$ (nm)	17	17	17	19	21	22
Std. dev. (nm)	4 (25%)	4 (22%)	5 (29%)	7 (34%)	6 (27%)	5 (34%)
$D_{3,2}$ (nm)	19	19	19	24	24	23
$D_{4,3}$ (nm)	20	19	20	27	25	25
Skewness	1.0	0.7	-0.1	1.1	0.8	0.6
Kurtosis	0.8	0.8	-0.5	2.0	1.4	0.7

The size distributions were measured by the segmentation of individual particles. The equivalent spherical diameter was calculated from the area of each measured nanoparticle and employed for the description of the size distributions. From the obtained descriptors (Table 5.2) and the relative distribution and log-normal fits (Figure 5.2), the particle size only showed minor variations using a different reaction temperature. An average $D_{1,0}$ diameter of 17, 17 and 21 nm was obtained for samples CH1, CH5 and CH9 respectively, thus an average size increase of +27% was observed comparing samples CH1 and CH9, with little effect on the polydispersity. In the case of sample CH5, the obtained size distribution curve was slightly left-screwed and flatter in comparison with the other two. Even though the log-normal distribution is intrinsically right-skewed and fundamentally unsuited to reconstruct a symmetrical curve, it was still chosen as this distribution shape was considered to more plausible on the basis of CH1 and CH9 samples. In the framework of the LaMer model,[16] the slight increase of the NPs size might be related to a sensibly faster growth rate of the particles as the reaction temperature increased. A similar but stronger size increase with the reaction temperature was instead reported by Dunne *at al.*[78] for the setup in which thiourea was decomposed prior to be mixed with the metal precursor solution. Using that approach, the reported average size varied from 3.5 to 10.6 nm as the reaction temperature was increased. As opposed to the method here employed, in the single mixer setup employed by Dunne a lower reaction temperature also corresponded to a slower decomposition rate. The comparison of the two results suggests that the final particles size might be connected to the decomposition rate of the sulfur precursor, more than to the reaction temperature.

5.1.2 Crystal structure and defectivity

From the XRD diffractogram obtained for the CH1 – CH9 samples, a mixed pattern of the cubic phase ZnS sphalerite (ICSD 98-065-1457, space group F-34m) and its hexagonal polymorph wurtzite (ICSD 98-006-7777, space group P 63 m c) was retrieved. Comparing the patterns as a function of the reaction temperature, an increase of the wurtzite content was observed (Figure 4.5), as visible in particular from the increasing contribution of the wurtzite (100) reflection in the profile. By carefully analyzing the diffractogram, the anomalous absence of the wurtzite (101) reflection at 46.5° was observed (Figure 5.3). This feature was described by Zhang *et al.*[87] as a specific indication that the material was consisting of a single phase having a mixed cubic-hexagonal stacking. Wurtzite and sphalerite are two polytypes of ZnS where both Zn and S atoms are tetrahedrally coordinated, having a free energy difference for the bulk of about 10 kJ mol^{-1}. For bulk materials, the transition temperature for the conversion from sphalerite to wurtzite is 1020 °C.[97]

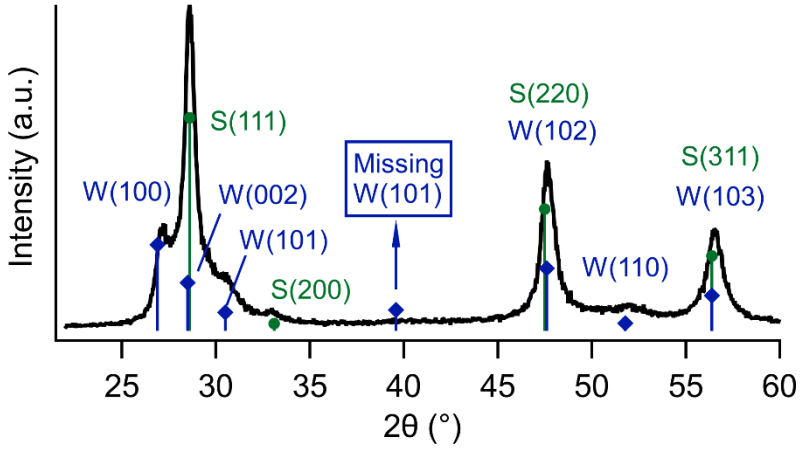

Figure 5.3 XRD pattern of the CH9 sample with reference of the expected reflections intensities and positions in the case of a physical mixture of ZnS sphalerite and ZnS wurtzite.

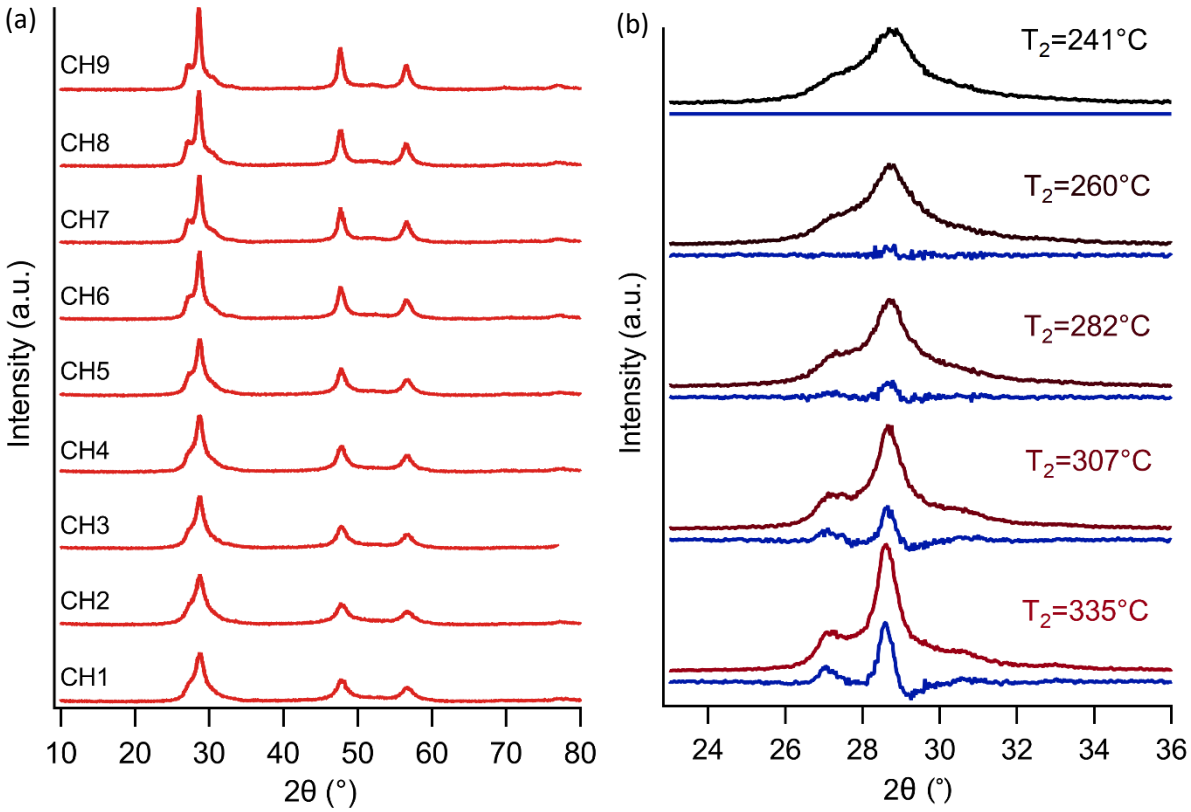

Figure 5.4 (a) XRD patterns of samples CH1 – CH9. (b) Detail of pattern around the main sphalerite (111) reflection showing the gradual increase of the wurtzite contribution to the pattern. The blue line is the difference diffractogram with respect to sample CH1. The reflections position are reported in Figure 5.3.

However, the energy difference between the two polymorphs decreases as the particle size is reduced, leading to a noticeably lower transition temperature in the case of nanostructures (see Chapter 6).[97] Moreover, ZnS has a low stacking faults energy[289] of 0.006 J m^{-2}. The tendency of ZnS to produce a relevant amount of planar defect was also observed by all the other syntheses methods employed in this Thesis, as stacking faults were always found to a different extent in the XRD patterns of the synthetized samples (see Chapters 2 and 4). As the particles dimension are reduced, the energy difference between the two polytypes are reduced as well,[97] and the influence of the external environment becomes more relevant.[290,291] All these aspects contributes to the possible formation of a high concentration of stacking faults. By increasing the amount of stacking faults, the approximation of a distorted cubic main phase breaks down, as the amount of the hexagonal polytype gets relevant and determines the occurrence of different features in the XRD pattern. In other words, in the crystal structure of a single nanocrystal both phases are found without discontinuity between the two, constituting a distinct entity with respect to a simple physical mixture of the two phases.

The patterns in Figure 5.4 shows the increase of the wurtzite content as the reaction temperature increased. A similar correlation was reported by Dunne e*t al.,*[78] who reported the formation of pure sphalerite a 250 °C and a gradual increase of the wurtzite content as temperature was raised to 400 °C. In that case, however, the combined analysis of XRD patterns and HRTEM micrographs indicated that the two phases were produced as physical mixture, where single nanocrystals assumed only one of the two polymorphs. Mixed stacking NPs were also obtained by Dunne *et al.* by the second CHFS method, but no study with variable reaction temperature was performed in that case. An explanation of the defective nanocrystals phenomenon was hypothesized by Zhang *et al.,*[87] who attributed the enhanced probability of hexagonal stacking at higher temperature as related to the higher entropy of wurtzite with respect to sphalerite. Additionally, the effect may also be explained as a combination of temperature and Zn:S ratio.[78] At lower temperature, it is possible to assume that the decomposition of thiourea may proceed slower, resulting in a reduced availability of SH^- at the second mixer in respect to the reaction preformed at higher temperature. Luther *et al*.[157] suggested that the formation of different polymorphs of ZnS reflects the formation of different molecular clusters that behave as monomers in the growth of the NPs. At higher Zn:S at. ratios, corresponding to a less complete thiourea decomposition in this synthetic approach, the formation of smaller $Zn_3S_3(H_2O)_6$ and $Zn_4S_6(H_2O)_4^{4-}$ clusters may be favored, that results in interaction between clusters that favors the attachment mechanism that leads to the cubic phase. With a faster thiourea decomposition, leading to a lower Zn:S at. ratio, the formation of a larger $Zn_6S_6(H_2O)_4$ might be favored, that instead leads to the formation of the hexagonal polymorph instead, as hypothesized by Luther *et al*.[157]

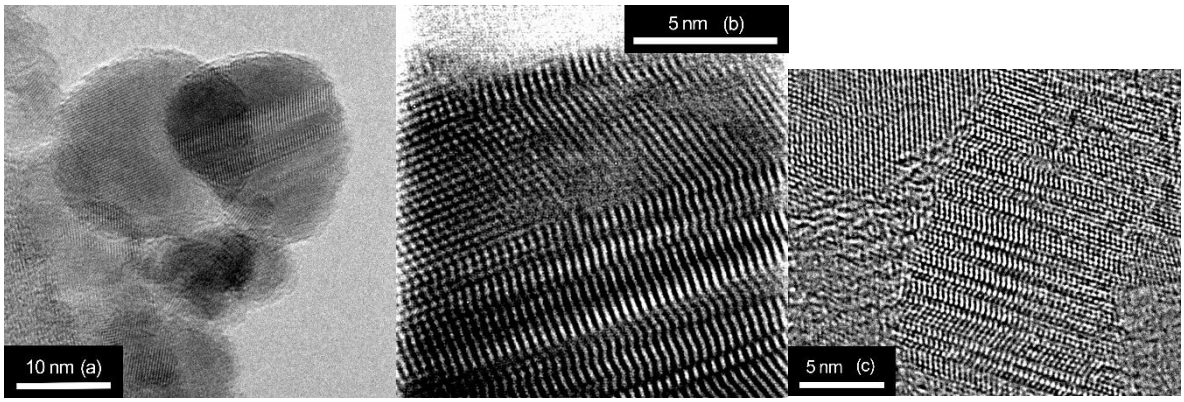

Figure 5.5 HRTEM micrographs of the CH7 sample.

To confirm the XRD analysis of the samples, HRTEM micrographs of the sample CH7 were acquired. Stacking disorder was evident in the particles, as seen in by the characteristic change in the crystallographic planes visible as striations that indicated the presence of stacking faults in NPs (Figure 5.5). The images also confirmed that the two phases were not forming unrelated domains but were constituting single nanocrystal with both stacking orders. This result confirmed that the different CHFS setup employed here allowed the production of nanocrystals having different wurtzite stacking probability as a function of the reaction temperature, rather than a physical mixture of the two phases that Dunne *et al.* reported in his work. Therefore, the precursor decomposition and mixing strategy alone appears to have a dramatic impact in the NPs crystallization mechanism.

The quantification of the wurtzite content represents a crystallographic challenge, as the structure cannot be formally described as a simple mixture of sphalerite and wurtzite, but rather as a distinct phase. The employment of the Warren model to estimate high twinning and stacking faults probability (i.e. considering the cubic phase as reference phase and altering the peak functions to fit the observed patterns) is not possible, as such a high concentration of defects greatly exceeds the limits of the Warren approach.[89] This limit was already evinced in the fitting procedure of by the visibly less defective NPs synthetized by the microfluidic approach in Chapter 4, where the XRD patters was still mainly corresponding to the one of the cubic phase. Two alternative empirical approaches were developed to estimate the relative content of the two phases. Smith *et al.*[292] proposed a correlation between the ratio of the two phases and the integrated intensity of their reflections at high scattering angles. However, for this approach, sharp and separated reflections are required. In the case of nano-sized crystalline domains, the overlap caused by the broadening effect does not allow the separation of isolated reflections, and possible multipeak fitting approaches are impaired by the low intensity of the reflections and their challenging distinction from the background.

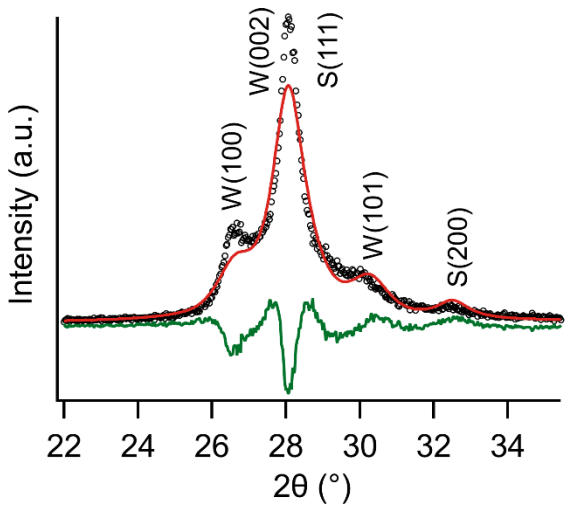

Figure 5.6 Refined partial fitting of sample CH9 using ZnS sphalerite and wurtzite crystal structures.

Another approach was initially developed by Zhang *et al.,*[87] who performed a numerical peak decomposition using Pearson VII functions to estimate the proportion of the two phases based on pre-determined intensities ratios between the reflections measured on the pure phases.[293] In the proposed fit, the pattern profile was reproduced removing the missing wurtzite (102) reflection and adding an additional Bragg peak around 62°.

A similar approach was here attempted by limiting the fit region from 20° to 36° with the fitting method implemented in MAUD,[84] thus employing pseudo-Voigt functions for the peak profile instead of the Pearson VII functions and using relative peak intensities extracted from sphalerite and wurtzite crystal structures. Using this strategy, a good fit was not achievable as intensities were not correctly reconstructed, as likely consequence of a fundamentally incorrect structural model. To improve the profile analysis of these samples, WPPM (Whole Pattern Profile Modelling) or a DSE (Debye Scattering Equation) approach may be used, as in these approaches the influence of microstructure and lattice defects are directly described using appropriate physical models instead of being treated empirically.[294] Zhang *et al.* indeed updated his analysis approach employing a complex DSE-based method, that required the modelling of a sizable populations of whole ZnS particles having variable cubic and hexagonal stacking probabilities. Moreover, to properly fit the experimental data, the model encompassed also the influence of NPs anisotropy and surface-related microstrain, making the analysis exceedingly demanding.[295] To strengthen the analysis of a similar problem, recently Moscheni *et al.*[294] relied in a combined high- and small-angle DSE-based total scattering analysis that included comprehensively all the relevant contributions to the pattern profile. Therefore, to obtain a good estimation of the cubic and hexagonal stacking probability in the samples, advanced XRD patterns analysis techniques are required.

Raman spectroscopy was employed as an alternative approach to XRD and HRTEM to obtain information about the temperature dependence of the presence of cubic and the hexagonal polymorphs. Firstly, the phonon dispersion and the DOS (density of states) was calculated *ab-initio.* The calculation was performed with the plane waves – pseudopotential implementation of the density functional theory (DFT) employed in the code package ABINIT.[296] The local density approximation (LDA) was used for the exchange correlation potential. Details on the computational method are available in Chapter 8.

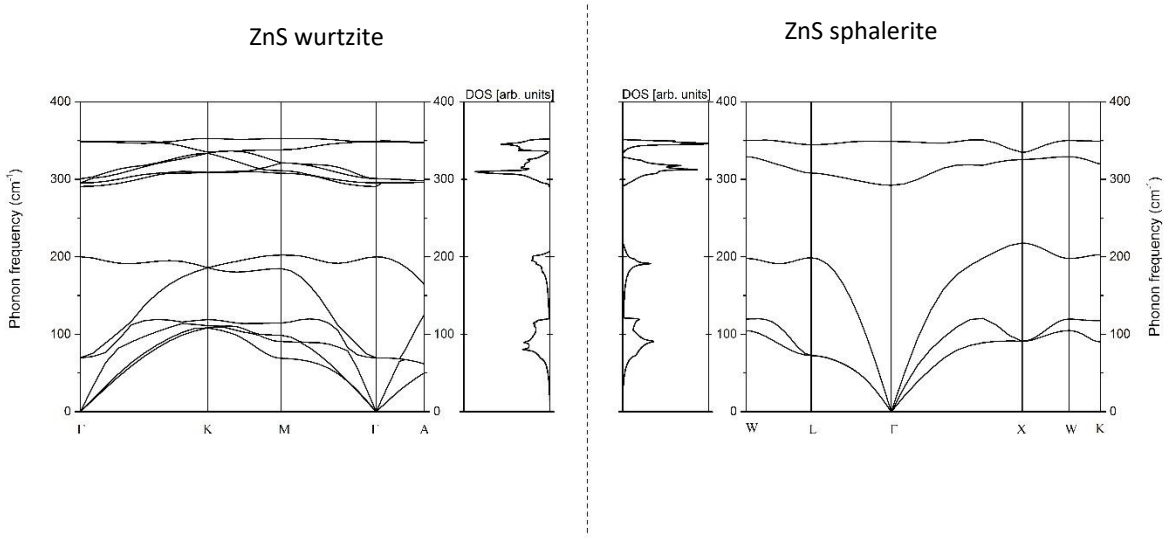

Figure 5.7 Phonon dispersion and DOS of (left) ZnS wurtzite and (right) ZnS sphalerite. Phonon energy is in wavenumber (cm^{-1}).

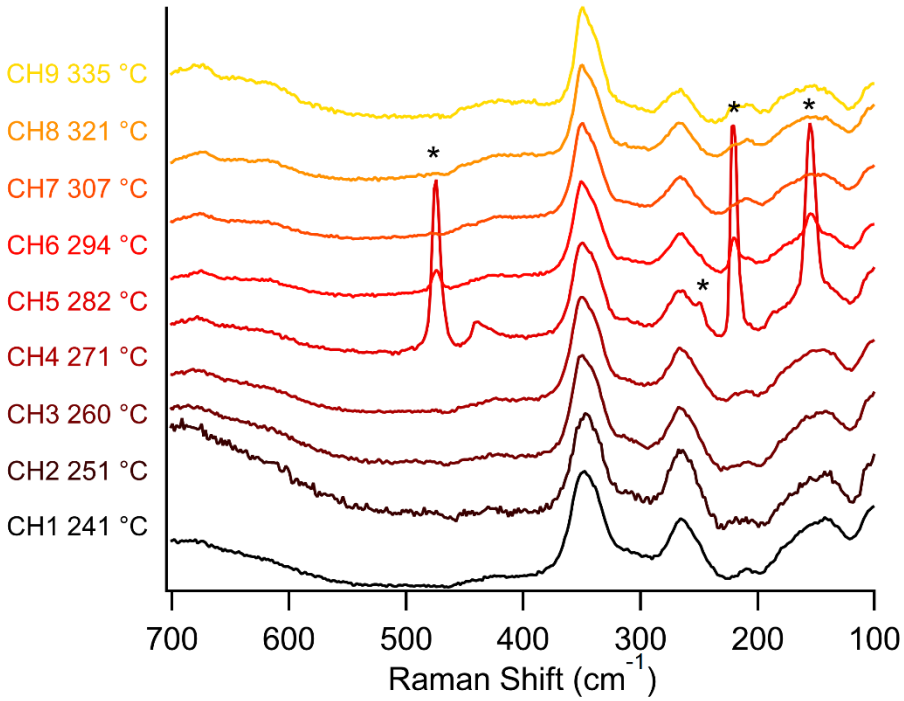

Figure 5.8 Raman spectra of the samples CH1 – CH9. (*) Raman peaks of orthorhombic sulfur S_8.

The computed phonon dispersion and DOS reported in Figure 5.7 were in good agreement with previous reports in the literature.[109] Since in both cubic and hexagonal phases of ZnS, the lattice consists of a network of ZnS_4 tetrahedra, distinguished only from a different stacking, the obtained phonon dispersions were similar (Figure 5.7). The transversal optical (TO) mode the longitudinal optical (LO) mode were found in the frequency range between 208 cm^{-1} and 360 cm^{-1}, whereas the transversal acoustic (TA) mode was located below 220 cm^{-1}.

Figure 5.8 shows the collected Raman spectra of the series of samples. The main peak at 349 cm^{-1} was attributed to the LO phonon at the Γ-point of the 1st Brillouin zone. As visible by the DOS plot in Figure 5.7, the position of this mode is the same within a few wavenumbers for both phases. The assignment holds also for the mixed phase NPs, as no relevant shifts were observed. Most of the Raman signals located at lower wavenumbers are due to second-order Raman scattering, that involves two phonons process. In this case, two phonons having an opposite wavevectors are created, generating a sum mode, or one phonon is created and one phonon that possess an opposite wavevector is annihilated, generating a difference mode.[109,297,298] Relevant contributions from difference modes were located only below 250 cm^{-1} (e.g., TO-TO up to LO-TA), while sum modes contributes more at higher wavenumbers. Acoustic modes contribute mainly between 180 and 300 cm^{-1} (e.g. 2TA, LA+TA), while sums of acoustic and optical modes (e.g. TO+TA, LO+LA) contributes at about 340 cm^{-1}. Sum of optical modes (i.e., 2TO, TO+LO, 2LO) are instead relevant between 580 and 700 cm^{-1}. Overall, the similarity of the DOS for the two phases resulted in similar Raman spectra, even if samples possessed different fractions of wurtzite-like and sphalerite-like sequences. Therefore, this made the estimation of the relative content more difficult to perform. The more, due to the nanosized dimension of the particles, the polarization selection rule for the activation of Raman modes does not strictly applies. Additionally, broadening of the Raman features occurs for phonon quantum confinement phenomena and for the effect of particles polydispersion. In the case of samples CH5 and CH6, the presence of peaks belonging to orthorhombic sulfur S_8 was also observed. Its presence may be related to unwashed reaction residuals or to a product of ZnS photodecomposition, as its presence was observed also in a batch-synthetized samples in Chapter 2.

Principal component analysis (PCA) was performed on the series of area normalized Raman spectra to reveal correlated changes in the spectra and shed more light on the structural changes underneath. The PCA method is based on the analysis of covariance matrix of the normalized Raman spectra. The eigenvalues of the covariance matrix and corresponding eigenvectors (principal components, PC) are labelled according to descending order of the positive eigenvalues. PCs had the form of Raman spectra, and were given as Raman intensities (loadings) against Raman shift values.

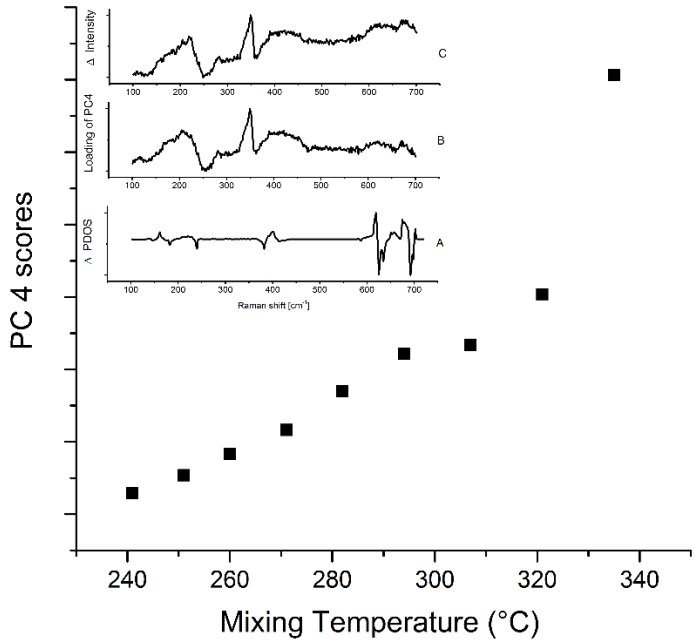

Figure 5.9 Plot of the PC 4 scores against the reaction temperature of the samples. (A) Difference calculated phonon DOS for cubic and hexagonal phases. (B) Loading of the PC 4. (C) Difference spectra between samples CH1 and CH9.

Each spectrum can be expanded as a series of principal components, where the corresponding scores are the coefficients of the expansion. The evolution of the Raman spectra was clear from the fourth PC against the reaction temperature, showed in Figure 5.9. Indeed, PC 4 was found to be the most sensitive to the variation of the Raman spectra and the best suited to describe the passage from a dominant sphalerite pattern to a dominant wurtzite one. To corroborate this finding, a simple comparison between PC 4 (inset B, Figure 5.9) and the difference spectra between sample CH1 and CH9 (inset C, Figure 5.9) is presented, showing that PC 4 reflects the variation between the two limit spectra. Moreover, a comparison with the difference DOS of cubic and hexagonal ZnS is showed in Figure 9 (inset A, Figure 5.9), which was plotted on a double Raman shift scale to indicate the position of second-order same-phonon sum modes (i.e., 2TA, 2LA, 2TO, and 2LO). From these comparisons, the PC 4 was found to reflect the difference spectra between CH1 and CH9, whereas the sharp feature in PC 4 reflects changes in the two-phonon Raman components. Additionally, the sharp feature in PC 4 around 350 cm^{-1} reflected the change of one-phonon LO mode, which was found at slightly lower energies for CH1 (sphalerite-dominated) in respect to CH9 (wurtzite-dominated). Overall, the Raman analysis supported the XRD interpretation, and showed a nearly linear increase of the hexagonal phase content from samples CH1 to CH8, and followed by an abrupt further increase at CH9, suggesting a threshold-effect at high temperature. Altogether, XRD, HRTEM and Raman analyses indicate that a linear increase of the presence of the hexagonal stacking on the ZnS NPs as function of the reaction

temperature was obtained, with only a limited size increase of the NPs with the temperature. Therefore, this approach could be potentially employed to finely tune the presence of the planar defects, that can affect the functional properties of the NPs (e.g. the photocatalytic activity, see Chapter 5.2).

5.1.3 Surface composition

The surface composition of the CH7 sample, chosen as reference, was analyzed using XPS spectroscopy. From the survey spectra (Figure 5.10) the presence of Zn, S was retrieved together with C and O, as expected from the common presence of adventitious contamination.[100] The presence of the C1s signal was used to correct XPS spectra for charging effects on the calculated BE by assigning to the peak the value of 284.6 eV. From the semi-quantitative analysis performed on the S2p and $Zn2p_{3/2}$ peaks, the retrieved Zn:S ratio was 1:1, which matches the 1:1 expected from the ZnS stoichiometry. Thus, this method did not lead to the formation of a Zn-rich surface, which was retrieved using the batch (Chapter 2) and the microfluidic (Chapter 4) synthesis methods. The $Zn2p_{3/2}$ was fitted with a single component (Figure 5.11a) at 1021.9 eV. Therefore, only the presence of Zn^{2+} was retrieved. The S2p region was fitted with a single p doublet at 161.8, as expected for the S^{2-} oxidation state (Figure 5.11b). No components at higher binding energy were observed, indicating the absence of oxidized sulfur moieties such as sulfates.

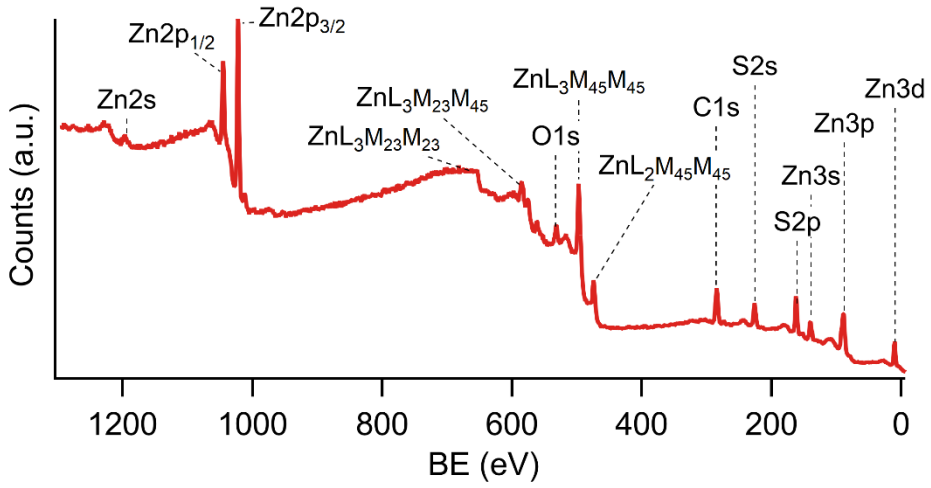

Figure 5.10 XPS survey spectra of sample CH5.

Table 5.3 Observed peaks position in the XPS spectra of the CH5 sample.

Peak	CH5 (eV)	Reference[99] (eV)
Zn2s	1195.8	1196
Zn2p3/2	1021.9	1021.7, 1022.0
Zn3s	139.8	139.9, 140.3, 141.5
Zn3p	89.4	88.4
Zn3d	10.2	9.8, 10.1, 10.7
S2s	226.2	225.6. 226.0, 226.3
S2p	161.8	162.2, 161.9

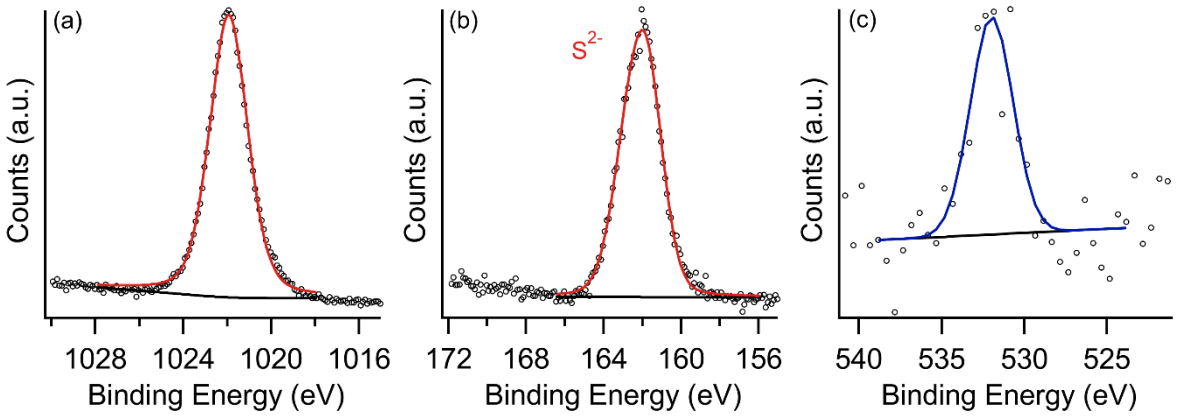

Figure 5.11 Fitting of the $Zn2p_{3/2}$ (a), S2p (b) and O1s (c) peaks of the sample CH5.

The O1s peak was found at 532.0 eV (Figure 5.11c), which was attributed to adventitious contamination or to the presence of adsorbed water (see Chapter 6). No contributions from ZnO were observed, since the relative O1s peak would appear at 532.2 eV (see Chapter 6). Overall, the analysis indicated that the surface of the obtained ZnS NPs was free of contaminants and unoxidized, despite the synthesis was conducted in water at high temperatures.

5.1.4 Photocatalytic activity for hydrogen evolution reaction

ZnS is an important photocatalyst for the hydrogen evolution reaction (HER).[259] Its light harvesting properties can be modulated, especially in the visible part of the spectrum, by introducing dopants or controlling the formation of defects.[259] Normally, the photocatalytic efficiency of ZnS is limited by a high charge recombination rate and by photocorrosion or oxidation phenomena.[34,299,300] To improve the photocatalytic performances, a key factor is the improvement of the charge separation lifetime.[34,259] Recently, the presence of stacking faults and the formation of twinned nanocrystals (i.e

NPs having a high concentration of twin planes as planar defects) was recognized as an useful tool to improve charge carriers separation.[263,301,302] Liu *et al.*[263] showed the superior performances of twinned $Cd_{0.5}Zn_{0.5}S$ nanorods with respect to the analogous un-twinned particles due to the formation of homojunctions at the twin boundaries. Such homojunctions were described to favor the transfer process of charges formed under irradiation, opposing the charge recombination and consequently enhancing the photocatalytic properties of the material. On the contrary, other authors reported that planar defects may also act as centers for nonradiative recombination of charge carriers, as highly twinned particles showed a relevant decrease in photocatalytic activity instead.[303] Since the CHFS approach led to formation of highly faulted ZnS nanocrystals, as showed by the XRD and HRTEM analysis, and the ratio between the two phases was also tunable as function of the reaction temperature, the photocatalytic properties of the samples were tested.

ZnS was used as a heterogeneous catalyst, therefore an important step of the characterization was the determination of the specific surface area (SSA, i.e. the mass-normalized surface area). As only a small difference between the particle size distribution was observed by TEM, and particles displayed similar morphologies regardless the reaction temperature employed, the SSA was determined only for sample CH7 as reference sample. The measure was performed via N_2 physisorption on the dry product, and the obtained adsorption isotherm was interpreted using the BET model,[262] resulting in an SSA value of 51.46 ± 0.25 $m^2 g^{-1}$. Considering a spherical model, the corresponding average diameter $D_{4,3}$ calculated from the SSA was 29 nm. This indicates that the probed surface area was close to the geometrically available surface area expected from the dimensional assessment of the samples.

Since the NPs synthetized were not specifically engineered to improve the light harvesting properties of the material in the visible range of the spectrum, the activity of the samples for the hydrogen evolution reaction (HER) was tested using the full spectrum of 500 W Hg (Xe) lamp, thus including the UV fraction. Details on the experimental procedure for the photocatalytic test are reported in Chapter 8.

The obtained HER activity values (displayed in Figure 5.12) showed an irregular behavior on top of a general trend that indicated an increased activity with the reaction temperature employed at the second mixer for the synthesis of the NPs. The Pearson's correlation coefficient of 0.64 for the proposed linear fit indicated a moderate linear correlation, therefore is possible to assume that an underlying linear trend may exist, even though other parameters here not considered were contributing as well (e.g. quality of the NPs dispersion). Reviewing the proposed characterizations, two trends were observed by raising the reaction temperature: a slight tendency of particles to growth and the increase in wurtzite content. Since the obtained size distributions were highly overlapping, it was assumed the influence of size variation was minimal.

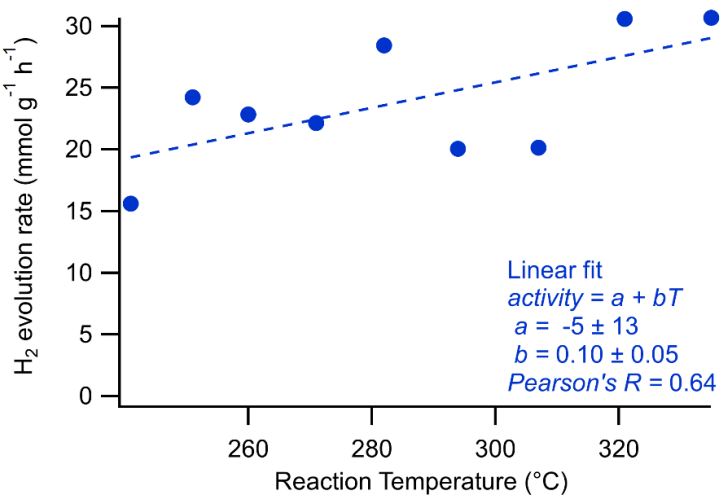

Figure 5.12 HER activity of the synthetized samples as function of the reaction temperature used for the synthesis of the NPs. The dashed line is the linear fit of the observed trend.

Therefore, it is more likely the observed trend can be ascribed to the crystallographic features of the particles, indicating a positive effect of the planar defects on the photocatalytic performances. The scattering of the obtained datapoints in Figure 5.12 indicates that other factors were also playing an important role. Since ZnS was observed to form fractal aggregates in the SAXS analysis of the suspensions obtained using the simple precipitation batch approach in Chapter 2, it is likely that the NPs here considered were also forming aggregates during HER tests. Therefore, the surface area accessible to reactants may be affected, as well as the illumination of inner particles.[304] The characterization of the aggregation state in the suspension used for the HER tests may be highly beneficial to assess this possible correlations. Lastly, oscillating values may also be caused by experimental errors. A more solid assessment of casual error may be necessary to improve the correlation analysis. Overall, a positive effect of the presence of planar defects was retrieved together with the influence of other still undetermined factors, that indicated the necessity of developing of a sounder description of the tested suspensions.

5.2 Continuous hydrothermal synthesis of Ln-doped ZnS NPs

ZnS is a wide band gap (E_g ~3.6 eV) II-VI semiconductor widely recognized as a good host material for doping.[265] The inclusion of selected elements in ZnS NPs can alter significantly the properties of the material, with particular reference to the photoluminescence ones. Therefore, many opportunities for the development of new functional materials were created and are still being explored.[265] Many transition metal and rare earths ions were used for the doping and the co-doping of ZnS NPs, including Cu^{2+}, Mn^{2+}, Pb^{2+}, Ni^{2+}, Cd^{2+}, Co^{2+}, Eu^{3+}, Sm^{3+}, Tb^{3+}, Er^{3+}.[265] In this work, the focus was the obtainment of doped Nd:ZnS, Yb:ZnS and Gd:ZnS NPs, as well as co-doped Nd,Yb:ZnS NPs. Multiple elements and opportunities were considered in the choice. Lanthanides ions may be used for the inclusion of new luminescence centers in the NIR range.[281] Emission properties in this part of the spectrum are of special interest in biological and bio-medical fields, as living tissues displays partial transparency in two different regions of the spectrum, called biological windows. The first biological window is located in the 650–950 nm range, while the second one is found in the range 1000–1350 nm.[282] Nanosystems with engineered luminescence properties in these ranges are being studied to develop *in-vivo* non-invasive imaging techniques.[282,305] Moreover, lanthanides also possess interesting magnetic properties due to the presence of a large number of unpaired electrons in the f orbitals. In particular, Gd^{3+} was employed for the development of different diluted magnetic semiconductors (DMS), where favorable magnetic properties were introduced using this element as a dopant in semiconducting matrixes.[306,307] The combination of magnetic and luminescence properties can also be exploited to develop combined imaging techniques.[306] Lastly, co-doping can also be employed to develop energy-transfer based nanosystems, that exploits the transfer of excitation between two luminescent ions. Being energy-transfer an activated process, the relative intensity of two emission bands depends on the temperature and may be used to develop fluorescence-based ratiometric nano-thermometers.[308,309]

The choice of ZnS as matrix to develop material for bioimaging applications was justified by different relevant advantages. ZnS showed a remarkable resistance to oxidation,[265] unlike many other semiconductors (or even other metal sulfides, as seen in Chapter 6). Moreover, ZnS is also known for its low cytotoxicity, which is a mandatory requirement for *in-vivo* applications.[310] Lastly, promising robust functionalization strategies for ZnS NPs for in-vivo applications have already been developed and are currently a matter of further developments.[310] In our workgroup, doped ZnS has been already developed specifically for bioimaging applications.[102]

In this work, the following ranges of dopant atomic concentrations (expressed as Ln/Zn) were considered: Nd:ZnS 0.05% - 10%; Gd:ZnS 0.05% - 10%, Yb:ZnS 0.5% - 3%. In the co-doped samples, Yb and Nd individual atomic concentrations were ranged from 0.5% to 2%, while considering a maximum total atomic concentration of dopants of 3%. The synthesis was carried out using the same experimental conditions employed for sample CH7 (second mixer temperature 307 °C), by adding to the Zn^{2+} solution a proper amount of Ln precursors (nitrate salts) to realize a targeted Ln/Zn molar ratio. The inclusion of lanthanides within the ZnS matrix was already attempted using the microfluidic approach presented in Chapter 3, with doubtful results. Since in the literature the obtainment of Ln-doped ZnS NPs required the employment of high temperatures, CHFS was tested as a possible approach to achieve the inclusion of these elements.[275]

The CHFS synthesis of Nd,Yb co-doped ZnS samples and their PL characterization was performed in cooperation with the Master Student Francesca Tajoli.

5.2.1 Composition and structure

The sample composition was firstly checked by ICP-MS measurements, to determine both the experimental dopant concentration and the uptake efficiency (i.e. the ratio between the retrieved dopants concentrations and to the one predicted from the precursors concentration employed).

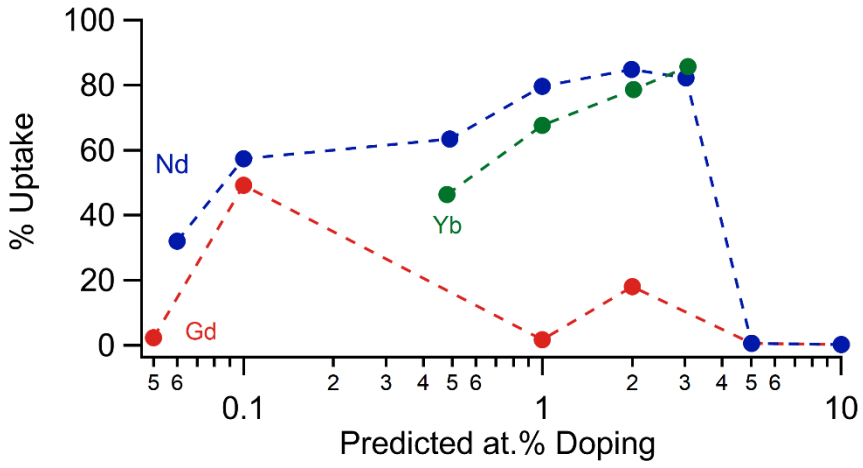

Figure 5.13 Dopants experimental uptake as function of the predicted nominal doping level. The horizonal axis is displayed in logarithmic scale.

Table 5.4 Composition of Ln:ZnS samples determined by ICP-MS on Zn, Nd, Gd, Yb elements. The nominal at. concentration refers to the one expected on the base of the concentration employed in the synthesis. Uptake is determined as the ratio between the experimental and the predicted concentration. Doping concentration are calculated as Ln/Zn at.

Sample	Dopant	%at. doping		%Uptake	Stoichiometry $Ln_nZ_n1S_m$	
		Nominal	Experimental		n	m
Nd:ZnS1	Nd	0.06	0.02	32.0	0.0002	0.7885
Nd:ZnS2	Nd	0.10	0.06	57.3	0.0006	0.7750
Nd:ZnS3	Nd	0.49	0.31	63.4	0.0031	1.2167
Nd:ZnS4	Nd	1.00	0.79	79.6	0.0079	0.7576
Nd:ZnS5	Nd	1.99	1.68	84.8	0.0168	0.7333
Nd:ZnS6	Nd	3.03	2.49	82.2	0.0249	1.2079
Nd:ZnS7	Nd	5.02	0.03	0.6	0.0003	0.7685
Nd:ZnS8	Nd	10.02	0.03	0.3	0.0003	0.7380
Gd:ZnS1	Gd	0.05	0.00	2.4	0.0000	0.6982
Gd:ZnS2	Gd	0.10	0.05	49.2	0.0005	0.4637
Gd:ZnS3	Gd	1.00	0.02	1.7	0.0002	2.2268
Gd:ZnS4	Gd	2.00	0.36	18.0	0.0036	0.8236
Gd:ZnS5	Gd	5.02	0.03	0.6	0.0003	0.6784
Gd:ZnS6	Gd	10.02	0.02	0.2	0.0002	0.7804
Yb:ZnS1	Yb	0.48	0.22	46.4	0.0022	1.1506
Yb:ZnS2	Yb	1.00	0.68	67.6	0.0068	1.0223
Yb:ZnS3	Yb	2.02	1.58	78.6	0.0158	1.1734
Yb:ZnS4	Yb	3.07	2.63	85.7	0.0263	1.1537

From the ICP-MS analysis (Table 5.4), the retrieved lanthanides uptake was observed to be dependent of both the element chosen and the concentration employed. Nd and Yb showed the best results, reaching values around 80% for predicted doping levels from 3% to 4%. As reported in Figure 5.13, Nd and Yb showed a similar behavior in their incorporation in the ZnS matrix. In the case of Gd a different behavior was observed, as low uptake values were generally retrieved instead, with exception of the 0.1% predicted doping, where the uptake reached almost 50%. The highest experimental doping concentrations achieved were 2.49% for Nd, 2.63% for Yb and 0.36% for Gd. A threshold effect was observed for Nd and Gd, as employing 5% and 10% concentrations with respect to Zn resulted in uptake values close to zero, despite the highest concentration of lanthanides were introduced in the precursor solutions. Therefore, high concentration of lanthanides displayed an inhibitory effect for the inclusion of dopants in the ZnS NPs. The origin of this effect was not clear. For this reason, the maximum total nominal at. concentration employed for the Nd, Yb co-doped samples was chosen as 3%. From the determined stoichiometries, an excess of sulfur was determined, suggesting the presence of relevant metal vacancies in the structure or the presence of oxidized sulfur moieties (e.g. S(0)) in the samples.

Table 5.5 Composition of Nd,Yb:ZnS samples determined by ICP-MS on Zn, Nd, Yb elements. The predicted at. concentration refers to the one expected based on the concentration employed in the synthesis. Uptake is determined as the ratio between the experimental and the predicted concentration. Doping concentration are calculated as Ln/Zn at.

Sample	Nominal %at. doping			Exp %at. doping			%Uptake			Stoichiometry $Nd_nYb_mZn_1S_f$		
	Nd	Yb	Tot	Nd	Yb	Tot	Nd	Yb	Tot	n	m	f
Nd,Yb:ZnS1	1.01	0.97	1.98	0.72	0.69	1.42	71.3	71.4	71.4	0.0072	0.0069	0.9917
Nd,Yb:ZnS2	0.50	0.99	1.49	0.42	0.78	1.20	82.9	79.4	80.6	0.0042	0.0078	1.1396
Nd,Yb:ZnS3	1.04	0.51	1.55	0.02	0.04	0.06	2.3	7.1	3.9	0.0002	0.0004	1.0039
Nd,Yb:ZnS4	2.07	0.51	2.59	0.40	0.11	0.51	19.4	21.5	19.8	0.0040	0.0011	1.1005
Nd,Yb:ZnS5	0.50	1.98	2.48	0.44	1.47	1.91	88.9	74.0	77.0	0.0044	0.0147	1.1748
Nd,Yb:ZnS6	0.56	0.49	1.05	0.24	0.23	0.47	43.3	46.4	44.7	0.0024	0.0023	1.1417
Nd,Yb:ZnS7	1.00	1.96	2.96	0.73	0.32	1.05	73.1	16.4	35.6	0.0073	0.0032	1.1053
Nd,Yb:ZnS8	2.03	0.95	2.97	0.45	0.84	1.29	22.2	88.5	43.3	0.0045	0.0084	1.1972

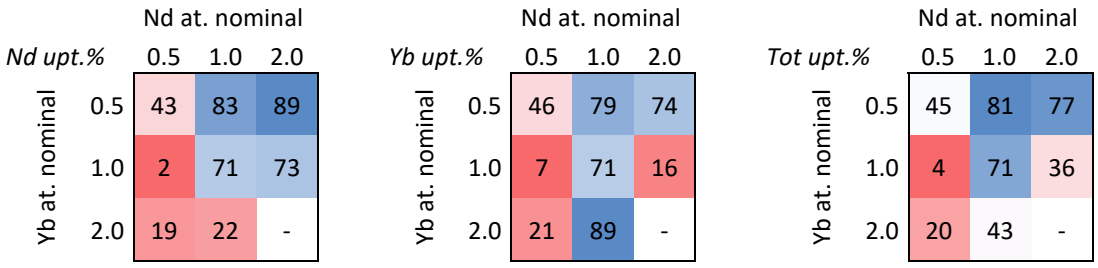

Figure 5.14 Matrix representation of the retrieved Nd, Yb and total (Nd+Yb) uptakes as function of the predicted doping level of both Nd and Yb. In the matrixes, every cell represents the uptake obtained by using the sum of the concentrations readable in horizonal (Nd at. nominal concentrations) and vertical (Yb at. nominal concentration) directions. The three matrixes refers to the uptake of Nd, Yb and Nd+Yb, respectively.

For the co-doped Nd, Yb samples, the best results in terms of uptakes were obtained at higher concentrations of Nd, and especially for Nd (1%,2%),Yb 0.5% samples, as visible for the presence of the highest uptake values toward the up-right corner of the matrixes in Figure 4.14. In general, the uptake of both elements was higher as the concentration of dopants increased, confirming the trend observed for nominal doping levels in the 0.5 % - 3 % range, visible in Figure 5.13.

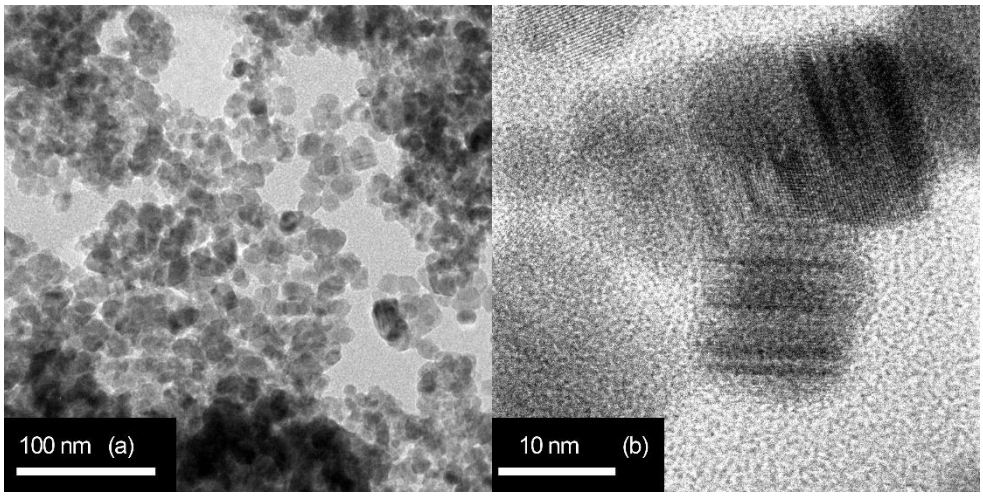

Figure 5.15 HRTEM micrographs of sample Nd:ZnS5 (1.68% at).

To check if the presence of the dopants induced relevant variation on the host ZnS NPs, HRTEM, XRD and XPS analyses were performed. For both doped and co-doped samples, no relevant variations were observed with respect to the reference undoped sample CH7, with exception of detectable variations of the ZnS unit cell. Both the HRTEM micrographs and the XRD pattern indicated the presence of NPs with staking disorder to an extent comparable to the undoped sample. No additional crystalline phases or particles sets were observed. Commonly, in doped materials, the presence of the elements in the crystal structure having a different ionic radius causes a variation of the unit cell, resulting in the shift of reflection position.[311]

In this case, being the ionic radius of the lanthanides larger than the one of Zn^{2+}, an expansion of the unit cell and a consequent shift of reflections towards smaller angles would be expected in the case the dopants ions were found in substitutional position inside the ZnS lattice. From the observed position of the sphalerite (111) - wurtzite (002) reflections (overlapped) in Figure 5.16 with respect with the undoped sample CH7, irregular shifts toward both higher and lower angles were observed along with changes in the line shape. This indicates that lanthanides may have been included in the ZnS matrix, as variations of the unit cell dimension of ZnS were observed, but not exclusively in a substitutional position to the Zn atoms, resulting in different structural alterations of the unit cell. This was likely related to the bigger ionic radii of lanthanides (as VI-coordinated: Nd^{3+} 0.983 Å, Yb^{3+} 0.868 Å)[266] in respect to Zn^{2+} (as IV-coordinated: Zn^{2+} 0.6 Å).[266] Moreover, lanthanides generally assumes a minimum coordination number of six, while in the ZnS crystal structure the zinc atoms possess a tetrahedral coordination, thus not favorable for a substitutional doping.

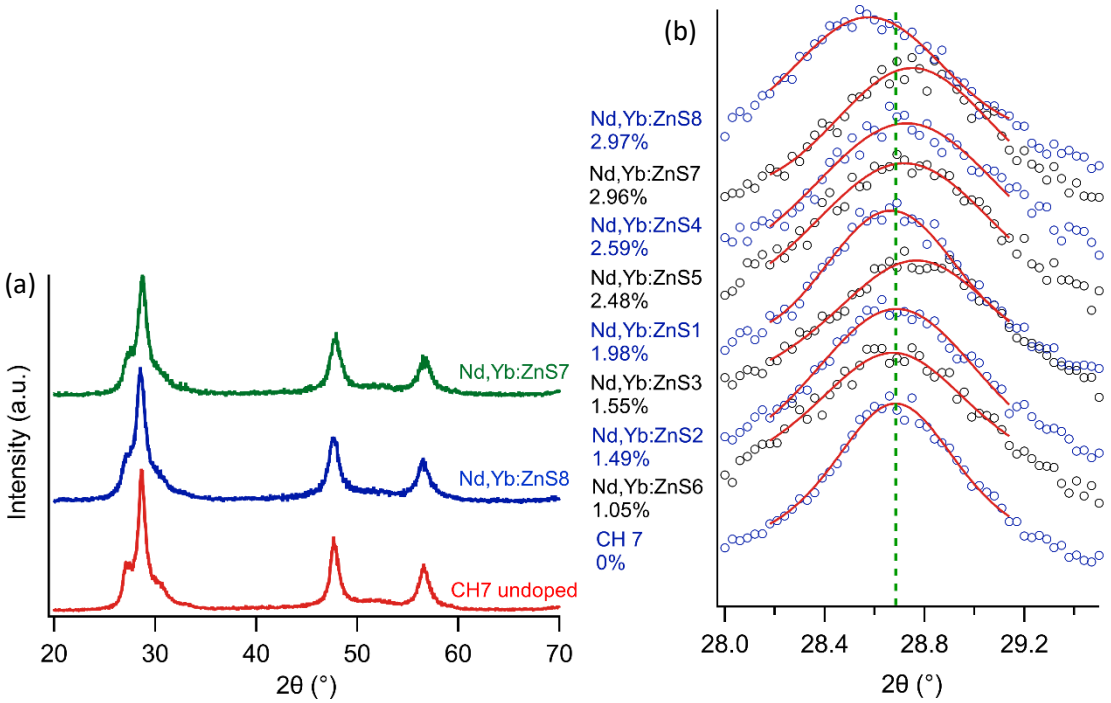

Figure 5.16 (a) Comparison of XRD patterns obtained from the Nd,Yb:ZnS7 and Nd,Yb:ZnS8 sample with the undoped sample CH7. (b) Sphalerite (111) - wurtzite (002) reflections for Nd, Yb co-doped samples compared with the undoped CH7 sample. Traces are ordered by the total dopant concentration. The red lines are pseudo-Voigt fitting of the experimental patterns, performed in a limited angular range. The green vertical dashed line represents the maximum position for the CH7 sample.

XPS spectra were also acquired to analyze the surface composition of selected samples. From the XPS analysis, only S, Zn, C and O were retrieved, while no signal was observed for Gd, Nd, and Yb even at the highest doping concentrations. This ruled out the presence of a relevant amount of other secondary compound (e.g. the lanthanides oxides) and indicated the absence of surface segregation phenomena of the dopants. All the retrieved peaks were substantially unchanged with respect to the undoped CH7 sample. The indication of the possible absence of surface segregation was particularly relevant, as it was previously reported to occur in previous attempt to synthetized lanthanides-doped ZnS.[265]

5.2.2 Photoluminescence properties of Ln-doped ZnS NPs

The obtainment of Nd and Yb-doped ZnS NPs is potentially of high technological interest, as the resulting NPs may be good candidate for the bioimaging applications, since it would allow the combination of the non-toxicity of ZnS[312] with the optical emission of the lanthanides in the NIR range.[281] For this reason, and to further confirm the presence of Nd and Yb in the samples, the PL properties of selected samples were analyzed. Moreover, for Nd,Yb:ZnS co-doped samples, the occurrence of energy transfer was checked, as this phenomenon may be used for the development of thermometric devices based on the ratio of the fluorescence intensity of the two ions.[308,309]

In Nd:ZnS samples the presence of the Nd PL peaks around 1057 nm (radiative transition $^4F_{3/2} \rightarrow {}^4I_{3/2}$)[311] and 880 nm (radiative transition $^4F_{3/2} \rightarrow {}^4I_{11/2}$)[311] were observed upon excitation at 582 nm (Nd excitation), while no PL from Nd ions was observed by exciting the ZnS matrix (e.g. 370 nm). Therefore, no energy transfer between the host material and the Nd ions was observed. Interestingly, PL peaks were obtained respectively on the first (650–950 nm) and second (1000–1350 nm) biological window,[282] suggesting potentiality for the Nd-doped NPs for bioimaging applications, even though the antenna effect granted by the energy transfer from the ZnS matrix to Nd is not employable. From the Yb:ZnS, only a very weak emission on 980 nm (radiative transition $^2F_{5/2} \rightarrow {}^2F_{7/2}$)[311] was observed upon excitation at 375 nm (Yb excitation).

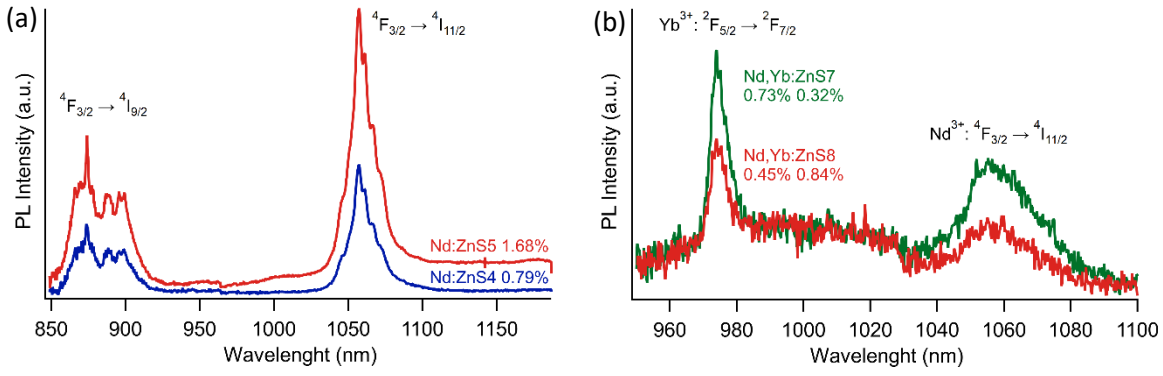

Figure 5.17 PL spectra of Nd:ZnS5 and Nd:ZnS4 samples (λ_{exc} = 582 nm, Nd). PL spectra of Nd,Yb:ZnS7 and Nd,Yb:ZnS8 samples (λ_{exc} = 578 nm, Nd). Percentages indicates the experimental doping level as Ln/(Zn + Ln).

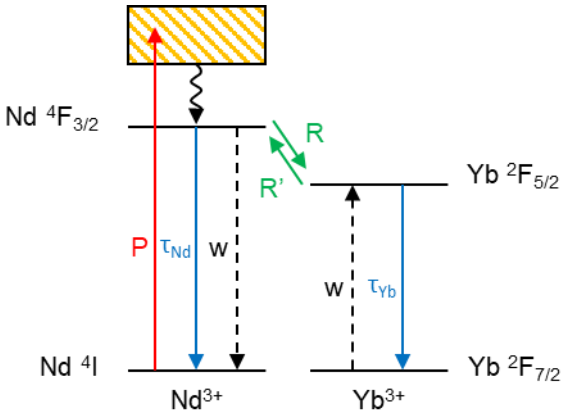

Figure 5.18 Simplified representation of energy levels and transitions involved in the co-doped Nd,Yb:ZnS samples. P = optical pumping rate for Nd^{3+}. τ_{Nd}, τ_{Yb} = intrinsic lifetimes of excited Nd^{3+} and Yb^{3+} ions. w = transfer probability coefficient for $^4F_{3/2} \rightarrow {}^4I_{3/2}$ of $Nd^{3+}$and $^2F_{7/2} \rightarrow {}^2F_{5/2}$ of Yb^{3+} exchange. R, R' = direct and inverse energy transfer rate from Nd^{3+} $^4F_{3/2}$ to Yb^{3+} $^2F_{5/2}$.

In the case of co-doped Nd, Yb samples, no PL was observed upon excitation at 375 nm (Yb excitation), but both emissions of Nd and Yb ions were obtained upon excitation at 578 nm (Nd excitation). In the latter case, a stronger peak at 975 nm (radiative transition $^2F_{5/2} \rightarrow {}^2F_{7/2}$ of Yb^{3+})[281] and a weaker signal at 1055 nm (radiative transition $^4F_{3/2} \rightarrow {}^4I_{3/2}$ of Nb^{3+})[281] were observed. This result indicates the existence of non-radiative energy transfer from Nd ions to the Yb ions. The phenomenon was already reported for other systems in the literature.[309,313,314] Therefore, in the case of co-doped Nd,Yb:ZnS samples, PL from both ions was obtained, each falling in a biological window. This suggests the potential use of the system for bioimaging applications, which adds up to the possible presence of temperature dependent PL derived from the energy transfer between the ions. The latter phenomenon may be studied to evaluate possible ratiometric thermometry applications.[308,309] To the best of our knowledge, no other reports of Nd,Yb co-doped ZnS NPs were found in the literature.

Magnetic properties of Gd:ZnS samples were tested by SQUID magnetometry, in the view of possible applications in MRI, but the retrieved doping level of was excessively low to allow the measurements, and therefore they were not suitable for the further magnetic properties-based developments.

Overall, the obtained doped and co-doped NPs showed analogous dimensional, morphological and crystallographic features of the undoped counterparts. The doping uptake was observed to be higher when the total employed molar concentration of lanthanides was in the 3% to 4% range with respect to the zinc precursor concentration. Only low uptake levels were instead observed for Gd. Suitable PL was obtained for Nd:ZnS and Yb,Nd:ZnS samples upon excitation at Nd energetic levels, while both showing emissions peaks in the first and second biological window. In the case of the co-doped Yb,Nd:ZnS samples, energy transfer from Nd towards Yb was obtained, allowing resulting in PL from

both dopants. As the excitation on ZnS levels in the case of Nd:ZnS samples did not resulted in energy transfer towards the Nd ions, the actual inclusion of lanthanides inside the ZnS matrix remains doubtful[275] despite the absence of indications of secondary compounds from all the characterization techniques employed and the evidence of (irregular) unit cell size variations from the XRD patterns. Thus, to prove or disprove the inclusion of dopants, dedicated analysis such as EXAFS or XANES may be required, other than more extensive PL assessments to the obtained samples.

Chapter 6.

Thermal evolution of ZnS nanostructures: effect of oxidation phenomena on structural features and photocatalytic performances

Optical and electronic properties of ZnS can be easily modulated altering its size, morphology, composition and defectivity.[264,315] The relatively easy optimization of its functional properties led to the employment of ZnS to many applications, ranging from optical devices[316–319] to photocatalysis.[264] Indeed, when photoexcited, the material shows a fast electron-hole generation,[320] that was largely exploited to develop photocatalyst for the production of hydrogen[260,321,322] and the reduction of carbon dioxide.[323,324]

Despite ZnS is commonly regarded as very stable towards oxidation phenomena at room temperature, upon heating the material is also known to be easily oxidized, eventually leading to the formation of ZnO and the evolution of SO_2.[325] Therefore, since many of the applications of the material are closely related to its structural, morphological and compositional properties, it became crucial to understand how these were altered from the exposure of the material to different temperatures, thus leading to possible alterations of these properties and exposing the material to oxidation. This task was complicated by the size-dependent properties of ZnS, especially related to the different relative stability of its two main polymorphs (sphalerite and wurtzite)[97] and the likely variations of its reactivity at a different NPs size. Moreover, recently, the peculiar opto-electronic properties that partially oxidized ZnS possess were indicated as potential tool to further improve its activity as photocatalysts, due to the formation of ZnS-ZnO heterojunctions that may favor the charge carrier separation.[326–330]

Despite the importance of oxidation phenomena on ZnS and the possible implications of oxidation to the technological application of the material, no in-depth study on this topic was carried out and the available information on the topic were fragmentary. Therefore, in this work, the thermal evolution of ZnS was studied as a function of the NPs size, comparing the effect of oxidation on structure, size, morphology, bulk and surface composition, and photocatalytic activity on ZnS NPs of 7 and 21 nm. To

probe the variations in the ZnS NPs activity as photocatalyst, the hydrogen production was chosen, as one of the prevalent applications of this material.[259]

Inorganic Chemistry
Cite This: Inorg. Chem. 2018, 57, 13104−13114
Article
pubs.acs.org/IC

Thermal Evolution of ZnS Nanostructures: Effect of Oxidation Phenomena on Structural Features and Photocatalytical Performances

Nicola Dengo,[†,‡] Angela F. De Fazio,[†,§] Morten Weiss,[∥] Roland Marschall,*[,∥] Paolo Dolcet,[†,‡,#] Mattia Fanetti,[⊥] and Silvia Gross*[,†,‡]

[†]Dipartimento di Scienze Chimiche, Università degli Studi di Padova and INSTM UdR, via Marzolo, 1, 35131, Padova, Italy
[‡]Istituto di Chimica della Materia Condensata e di Tecnologie per l'Energia, ICMATE-CNR, via Marzolo, 1, 35131, Padova, Italy
[§]Physics and Astronomy, Faculty of Physical Sciences and Engineering, University of Southampton, Southampton, SO17 1BJ, U.K.
[∥]Institute of Physical Chemistry, Justus-Liebig-University Giessen, 35392 Giessen, Germany
[⊥]Materials Research Laboratory, University of Nova Gorica, Vipavska 11c, SI-5270 Ajdovščina, Slovenia

Supporting Information

ABSTRACT: ZnS nanosystems are being extensively studied for their possible use in a wide range of technological applications. Recently, the gradual oxidation of ZnS to ZnO was exploited to tune their structural, electronic, and functional properties. However, the inherent complexity and size dependence of the ZnS oxidation phenomena resulted in a very fragmented description of the process. In this work, different-sized nanosystems were obtained through two different low temperature wet chemistry routes, namely, hydrothermal and inverse miniemulsion approaches. These protocols were used to obtain ZnS samples consisting of 21 and 7 nm crystallites, respectively, to be used as reference material. The obtained samples were then calcinated at different temperatures, ranging from 400 to 800 °C toward the complete oxidation of ZnO, passing through the coexistence of the two phases (ZnS/ZnO). A thorough comparison of the effects of thermal handling on ZnS structural, chemical, and functional evolution was carried out by TEM, XRD, XAS, XPS, Raman, FT-IR, and UV−Vis. Finally, the photocatalytic activity in the H_2 evolution reaction was also compared for selected ZnS and ZnS/ZnO samples. A correlation between size and the oxidation process was observed, as the smaller nanosystems showed the formation of ZnO at lower temperature, or in a larger amount in the case of the ZnS and ZnO co-presence. A difference in the underlying mechanism of the reaction was also evidenced. Despite the ZnS/ZnO mixed samples being characterized by an increased light absorption in the visible range, their photocatalytic activity was found to be much lower.

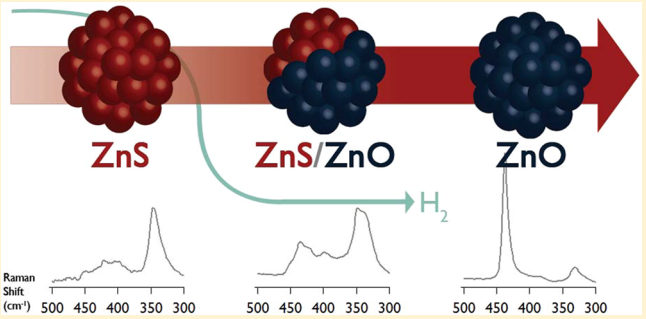

INTRODUCTION

Nanostructured ZnS is a large band semiconductor extensively studied because of its particular and easily tunable optoelectronic properties.[1−3] It is suitable for a wide range of applications, including catalysis, photonic, nonlinear optical devices, light-emitting diodes, flat panel displays, infrared windows, field emitters, sensors, and lasers.[4−8] ZnS exists in two main polymorphs, namely, sphalerite and wurtzite.[9] At room temperature, the most stable phase is the cubic sphalerite (spatial group $F\bar{4}3m$), while, above 1023 °C, the most stable phase is the hexagonal wurtzite (spatial group $P6_3mc$).[9] ZnS can also be obtained as high-pressure polymorphs having rocksalt type (spatial group $Fm\bar{3}m$) or orthorhombic type (spatial group $Cmcm$) structures.[10,11] The existence of a low-pressure BCT (body-centered tetragonal). polymorph was also predicted[12] and lately proven through a wet chemistry coprecipitation method.[13] ZnS can be prepared in a great variety of sizes and shapes, and it can host a large variety of dopants, allowing a wide tunability of its properties, as reviewed by Fang et al.[8]

ZnS is easily oxidized upon heating in open air, leading to the formation of the wurtzitic hexagonal polymorph of ZnO, with the evolution of gaseous SO_2.[14,15] This reaction was historically employed for the development of regenerative high temperature sulfur adsorption beds based on ZnO.[14] Detailed studies on the reaction kinetics and mechanism were also performed.[16,17] Moreover, it could be shown as the oxidation reaction does lead not only to the formation of ZnO but also to the formation of surface sulfates and sulfites species.[18]

ZnS is also a widely investigated photocatalyst for H_2 production[19−21] and CO_2 reduction,[22,23] characterized by a remarkably fast generation of electron−hole pairs under photoexcitation.[24]

Received: April 21, 2018
Published: October 10, 2018

DOI: 10.1021/acs.inorgchem.8b01101
Inorg. Chem. 2018, 57, 13104−13114

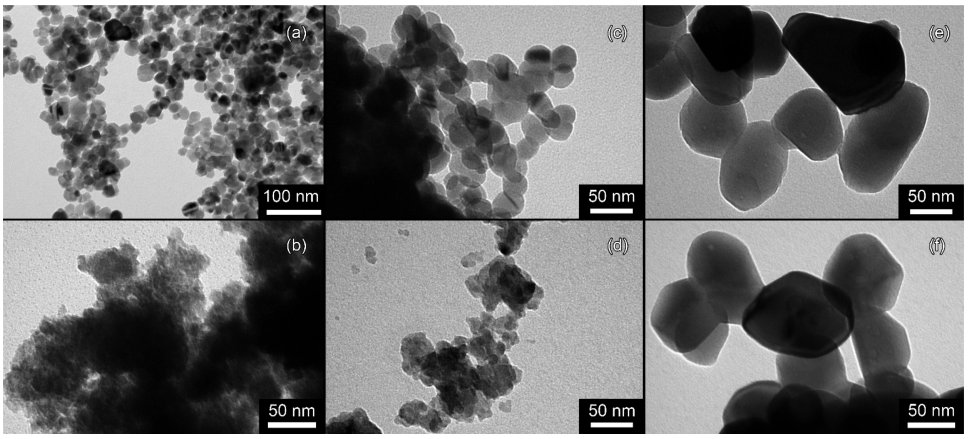

Figure 1. TEM micrographs of the HY (top) and ME (bottom) samples. HY samples: as-synthesized (a), treated at 450 °C (c), treated at 800 °C (e). ME samples: as-synthesized (b), treated at 450 °C (d), treated at 800 °C (f).

The oxidation of ZnS also occurs whenever a nanostructured material is considered. In this case, the phenomenon can become more complicated considering reactivity alterations that can occur upon downsizing the material at the nanoscale level. Moreover, it is known that the relative stability of the two different ZnS phases becomes comparable as the dimensions are reduced, leading also to the lowering of the polymorphs transition temperature.[23,25−28] Considering that all these phenomena can occur simultaneously and to different extents, also depending on the size of the nanostructures, a simple and common procedure like annealing the material can lead to a very complex situation. Moreover, oxidation in the sample could promote substantial changes in the (photo)catalytic properties of the material, by altering the surface catalytic sites or even forming a ZnS−ZnO heterojunction that could lead to different charge carriers dynamics in the photoexcited material.[29−34] In fact, the formation of ZnS−ZnO heterostructures and the connected changes in the electronic structure are known to affect the optical properties of the material, extending its light absorption range toward the visible light[30−32,34] and affecting the nonlinear optical behavior.[35] The strategy of coupling ZnS with other materials was also extended to other materials, such as ZnSe[36] or carbon composites.[37]

Despite the importance of nanosystems' crystal structure and composition (of both the surface and bulk material) in affecting their functional properties, the ZnS thermal evolution is still poorly investigated. Different reports are available in the literature, describing the oxidation of different ZnS nanostructures in air. The formation of the oxide is reported to occur at 400 °C,[34] 500 °C,[30−32] or 600 °C[38] for nanoporous platelets obtained calcining $ZnS(en)_{0.5}$, coherently with the temperature of 500 °C[39,40] observed for porous ZnS microspheres made of nanosized particles. Similarly, 450 × 20 × 20 nm nanobelts where found to be fully oxidized at 600 °C,[41] while a noticeably lower temperature of 300 °C was reported in the case of particles as small as 3−5 nm.[42]

In this framework, the aim of this work was to shed light on the complex effect of thermally treating ZnS nanostructures in open air, as well as to get insight into the different structural and compositional properties of different ZnS samples. Two different wet chemistry routes were used, namely, hydrothermal synthesis and miniemulsion. In this latter case, the precipitation of the targeted compound was achieved by exploiting the confined space of the droplets generated in the miniemulsion process. To draw a connection between the described oxidation phenomena and the related change in the functional properties, we also assessed the effect of a partial oxidation of ZnS to ZnO in the photocatalytic H_2 evolution, a process chosen both as a widely studied application of these materials[43] and as a phenomenon which was less systematically evaluated by other authors.[31,32,44,45]

RESULTS AND DISCUSSION

Size and Morphological Evolution. Zinc sulfide nanostructures were prepared via two different wet chemistry routes, namely, miniemulsion (ME) and hydrothermal (HY) synthesis, both well-known for affording high reproducibility and size control on the final products, and enabling the crystallization of the targeted product at low (in the case of HY) or even room temperature (for ME). Starting with the as-prepared materials, the thermal evolution of the samples was followed through different techniques, while keeping the same treatment conditions equal (i.e., time, atmosphere, and annealing temperature) to consistently compare the obtained data. We aimed also at relating observed differences to the properties of the samples, without the potentially confusing influence of external factors. Sample morphology was first assessed via electronic microscopy. The TEM micrographs (Figure 1a) collected from the HY as-synthesized sample show well-defined polyhedral nanoparticles with an average size of 21 nm. Notably, the observed morphology appears to be compatible with the theoretically predicted shape for ZnS sphalerite-phase crystals (a rhombic dodecahedron).[46] For the ME as-synthesized sample (Figure 1b), the nanoparticles do not appear to be as easily outlined, though it can be certainly stated that the particle sizes are in the nanometric range. The formation of agglomerates is clearly visible and is likely to be favored by the presence of residual surfactant (PGPR) tightly adsorbed on the nanoparticles' surface. The primary individual particles that constitute the agglomerates can be estimated to have an average size below 10 nm. This estimation is confirmed by the average crystallite size of 7 nm determined by the size−strain analysis performed on the corresponding XRD pattern (*vide infra*). After treating the samples at 450 °C, the particles average diameters (Table 1) increased for both HY (Figure 1c) and ME (Figure 1d) samples to 31 and 11.8 nm, respectively. Moreover, the particles appear also to acquire a slightly more rounded shape. Interestingly, despite the detected occurrence

DOI: 10.1021/acs.inorgchem.8b01101
Inorg. Chem. 2018, 57, 13104−13114

Table 1. Calculated Parameters for the Obtained Numerical Equivalent Diameters Distributions and Their Log-Normal Fit from TEM Data

	ME			HY		
	as-syn.	450	800	as-syn.	450	800
measured						
average		11.8	79	21	31	106
std. dev.		2.4	18	5	7	37
skewness		1.2	1.1	0.9	0.7	1.4
kurtosis		3.2	1.6	1.0	1.3	2.1
log-norm fit						
average	7[a]	12.0	78	21	32	101
std. dev.	1[a]	1.8	14	4	8	25

[a]Values chosen to visualize a placeholder distribution for the as-synthesized ME sample (see text).

of one or more partial phase transitions at 450 °C (*vide infra*), both samples could be described with a single set of nanoparticles, indicating a gradual conversion of the particle structure, rather than the formation of separate objects. This in turn implies that, during the phase transition or the oxidation process, the phases are likely to be structurally related within the same particles. Treating both HY (Figure 1e) and ME (Figure 1f) samples at 800 °C led in both cases to the formation of similar sets of particles having an average size of 106 and 79 nm, respectively. The relevant growth observed can be ascribed to temperature-induced coalescence phenomena. The particles appear also to be more elongated and rounded in comparison with the one treated at 450 °C.

HRTEM images of both the HY (Figure 2a,b) and ME (Figure 2c,d) as-synthesized samples were also performed to obtain a clear confirmation of crystalline nature of the nanoparticles. The direct analysis of the visible fringes and the FFT (Fast Fourier Transform) analysis shows interplanar distances compatible with the ZnS sphalerite phase. For this structure, the first calculated spacings are 3.12 (*hkl* = 111), 2.70 (200), 1.91 (220), 1.63 (311).[47] The Selected Area Electron Diffraction (SAED) patterns obtained from particles ensembles in the two samples are displayed in Figure 2e,f. For both samples, the inner and brightest ring can be assessed as the (111) plane of the cubic ZnS phase, and the two outer rims correspond to the (220) and (310) planes of the same phase, indicating the absence of spurious crystalline contaminations such as oxides. This result supports the very relevant absence of oxidation phenomena in the pristine material, which were ruled out with XRD and XPS analysis (*vide infra*). The SAED rings for the ME sample appear noticeably broadened, as a consequence of the small dimension of the crystallites.

The equivalent diameter numerical distribution was obtained for all the samples (Figure 3), with the sole exception of the as-synthesized ME sample, which appeared to be too thoroughly aggregated to reliably perform the segmentation of the primary particles. All the retrieved distributions are right-screwed (skewness > 0) and leptokurtic (kurtosis > 0), as reported in Table 1. The plotted distribution was also fitted using the log-normal distribution. The obtained area-normalized curves are plotted in Figure 3, together with an analogous synthetic distribution designed for the ME as-synthesized sample, inserted to better allow a complete visual comparison of the samples evolution. This placeholder distribution was obtained using a log-normal distribution having an average equivalent diameter imposed at 7 nm, being this the calculated average crystallite size of the sample, and a standard deviation of the equivalent diameter imposed at 1. This second value was chosen purely for the sake of visualization as an educated guess based on the observed trends of the standard deviations with respect to the temperature of synthesis or the temperature of treatment.

The evolution of the equivalent diameter size distribution confirms the gradual growth of the nanoparticles with the treatment temperature. Moreover, the final size also depends on the initial size of the ZnS nanoparticles used, being the treated ME samples dimensional distributions consistently found at smaller values with respect to the analogous HY distributions. It is worth to mention that the observed size distributions reflect both the dimensional dispersion of the samples and their shape transformation. In fact, treated nanoparticles appear to be noticeably more anisometric with respect to the untreated ones, thus possibly generating a larger variety of possibly observed bidimensional projections even for particles sharing the same size and shape.

Structural and Chemical Conversion. The crystalline phase of the as-synthesized nanostructures was assessed by XRD. For both HY and ME routes, only the sphalerite polymorph (ICSD No. 98-065-1457) was detected in the as-prepared samples. Both diffractograms show wide reflections, as expected in the case of nanosized material. The average size of

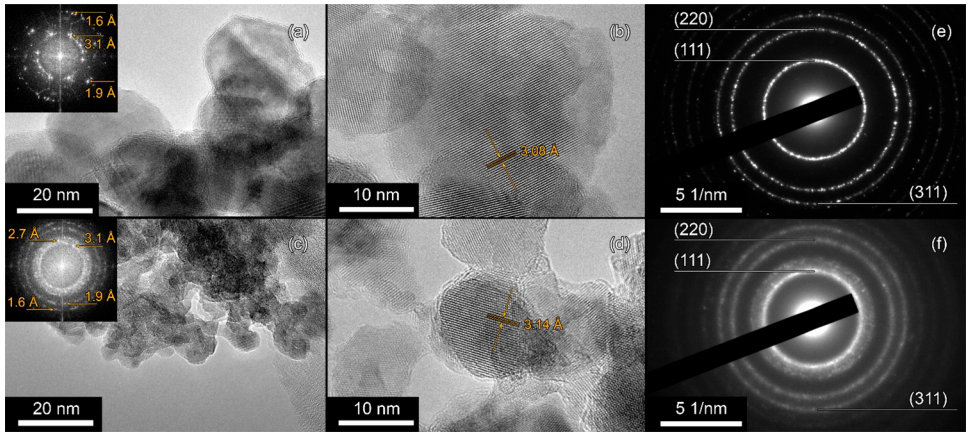

Figure 2. HRTEM images of the as-synthesized HY (a, b) and ME (c, d) samples. Images (a) and (c) include the corresponding FFT image. SAED pattern obtained for the as-synthesized HY (e) and ME (f) samples. Indexes are referring to ZnS sphalerite phase.

DOI: 10.1021/acs.inorgchem.8b01101
Inorg. Chem. 2018, 57, 13104−13114

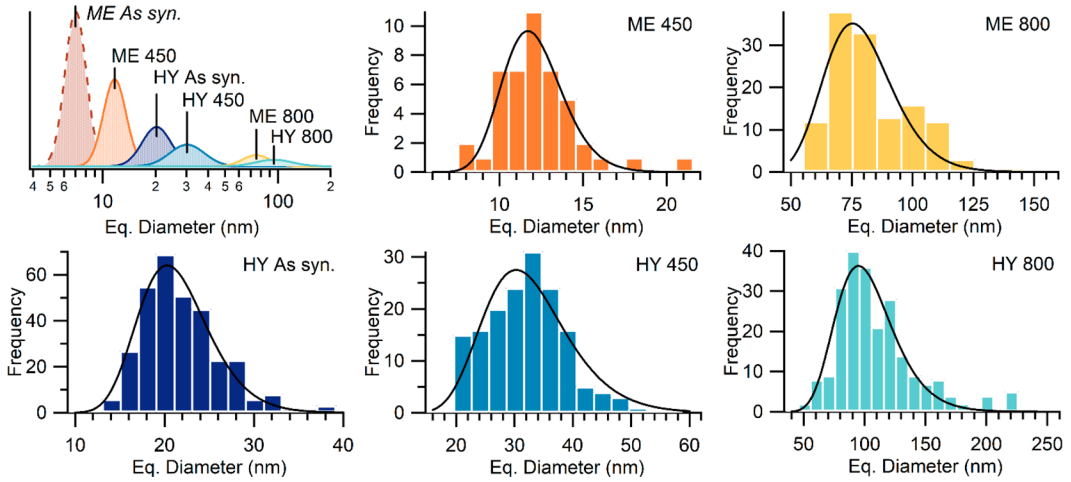

Figure 3. Log-normal fitted equivalent diameter numerical distribution obtained from the TEM images and the comparison of the area-normalized fitted log-normal distribution. The ME as-synthesized displayed curve was synthetically made (see text).

the crystallite was estimated to be 21 nm for HY and 7 nm for ME by whole-pattern fitting (Rietveld method, MAUD[48]). These values are in a good agreement with the particle sizes observed in the TEM micrographs (*vide supra*), indicating the conformity between crystallites and particles in the samples. Both synthetic methods were shown to be capable of yielding pure sphalerite-phase ZnS, but with substantially smaller crystallites in the case of ME. This latter finding can be ascribed to the space confinement effect provided by the droplets, limiting the growth of the formed ZnS precipitate. To follow the structural evolution as a function of the treating temperature, we chose analytical methods providing information referred to different length scales, from atomic to macroscopic range.

Indeed, XRD was chosen to investigate the material structure on a macroscopic scale, while XAS focused on determining the local structure around the metal (i.e., Zn) absorbing atom. XAS also provided information on the coordination number, on the chemical nature of the scattering atoms surrounding an absorbing atom, on the interatomic distance between the absorbing atom and the backscattering atoms, and on the structural disorder of the different shells.

By comparing the *ex situ* XRD patterns of the different samples annealed at different temperatures in the range displayed in Figure 4, a gradual conversion from sphalerite ZnS, visible as the (111) reflection, to wurtzite ZnO (ICSD No. 98-006-5122), visible as the (100), (002), and (101) reflections, could be pointed out. Together with the (111), the (200) reflection of ZnS sphalerite is also found as a small bump located at 33.16°, but it is too weak to be clearly visible in Figure 4.

The coexistence of the two compounds in a narrow range of temperatures could also be evidenced. The relative amount of the detected crystalline phases (quantified by whole-pattern fitting - Rietveld method, MAUD)[48] is reported in Table 2. For samples prepared with both procedures, the conversion to ZnO became visible at 450 °C with the appearance of the (100), (002), and (101) reflections, and is complete at 550 °C, while the relative amount of oxide is higher in the case of ME for both 450 and 500 °C treated samples. Interestingly, the characteristic pattern of the wurtzitic ZnS phase (ICSD No. 98-015-7133) is also observed in the ME 450 and 500 °C treated samples. Therefore, the phase transition from the cubic to the hexagonal ZnS phase appears to occur at a much lower temperature in comparison with bulk ZnS, where it is reported

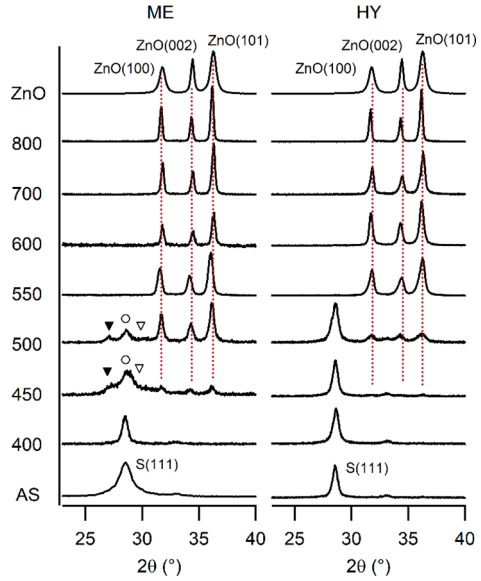

Figure 4. Evolution of the XRD diffractograms at different calcination temperatures. The S(111) index is referred to sphalerite-phase ZnS. The dotted lines emphasize the presence of the three main reflections of ZnO. Markers show the presence of the wurtzitic ZnS reflections: (▼) = (100), (○) = (100), (▽) = (100). AS = as-synthesized. Temperatures are indicated in Celsius degrees.

Table 2. Crystalline Phase Composition of the Samples from Rietveld Refinement Performed on the XRD Data as Weight Percentages

	ME			HY	
T (°C)	%sph	%wur	%ZnO	%sph	%ZnO
as-syn.	100	0	0	100	0
400	100	0	0	100	0
450	60	28	12	96	4
500	31	3	66	65	35
550	0	0	100	0	100
600	0	0	100	0	100
700	0	0	100	0	100
800	0	0	100	0	100

to occur at 1023 °C.[9] This observation agrees with the studies of Qadri et al.,[25] who showed the formation of the ZnS

DOI: 10.1021/acs.inorgchem.8b01101
Inorg. Chem. 2018, 57, 13104−13114

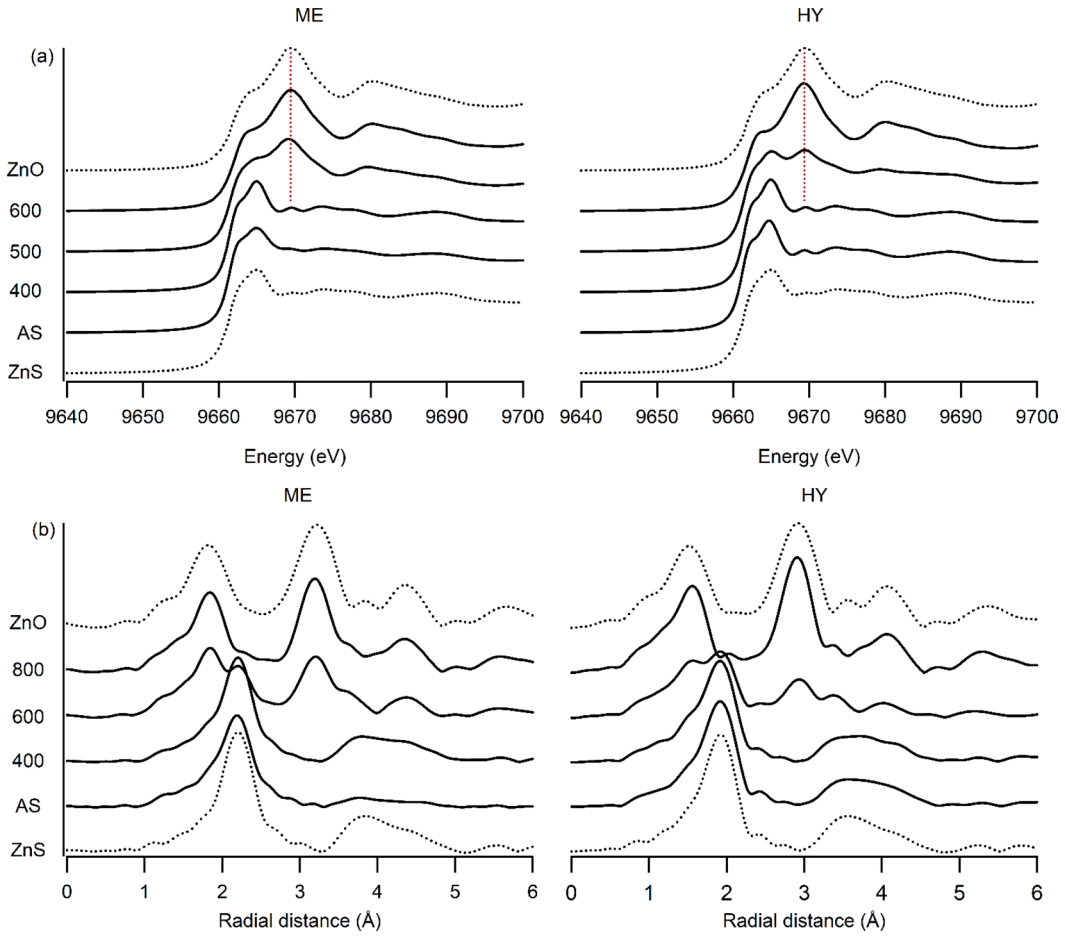

Figure 5. (a) Zn K-edges XANES spectra of the samples in comparison with ZnS and ZnO reference spectra. The dotted lines are emphasizing the main spectral feature of ZnO. (b) Fourier transforms of the same EXAFS curves. AS = as-synthesized. Temperatures are indicated in Celsius degrees.

hexagonal phase at a temperature as low as 400 °C from 2.7 nm cubic-phase ZnS nanocrystals. The same behavior was also observed by Balantseva et al.,[49] while calcining cubic phase ZnS nanoparticles in vacuum, where the formation of hexagonal phase ZnS was also detected by treating the samples in vacuum at 700 °C. In our work, the crystallites obtained by ME are small enough to show this ZnS cubic-to-wurtzitic phase transition before reaching the complete oxidation to ZnO, while, for the bigger HY particles, such transition is not observed due to the increased stability of the cubic phase in comparison with the hexagonal one.[9,25] Moreover, the higher amount of ZnS wurtzite observed for the 450 °C sample (28% wt.) in comparison with the 500 °C sample (3%) indicates that the hexagonal phase is oxidized first. These could be interpreted as an increased reactivity against oxidation of the latter, or even as a hint to the existence of a preferential oxidation path where the structural evolution to the hexagonal crystal structure is occurring before the chemical conversion.[50] Comparing the ZnO XRD patterns with a bulk reference, a slight shift in the reflections angular positions can be observed. This could be related to lattice distortion arising from the presence of contiguous ZnS and ZnO phases, or from point defects in the structure itself. The latter hypothesis is further supported by the light absorption properties found in these samples (*vide infra*). The inherently poor extrapolation of the angular position due to the broadening arising from the small crystallites size prevents a more refined analysis.

The structural conversion from sulfide to oxide was also followed on a short-range order by performing X-ray absorption measurements at Zn K-edge (9659 eV). The X-ray absorption near edge (XANES) spectra are depicted in Figure 5a, including a comparison with those of reference sphalerite ZnS and wurtzite ZnO. The sulfide reference is characterized by a peak centered at 9665 eV, while, for the oxide, the maximum absorption is found at 9669 eV, with a second band at 9680 eV.

Both as-prepared ZnS samples show spectral features typical of sphalerite, in agreement with XRD data. At 400 °C, a small bump due to incipient formation of ZnO starts appearing at about 9669 eV. This feature indicates that the oxidation of the sulfide begins already at this temperature, which is lower in comparison to the one evidenced by the XRD and Raman (*vide infra*) data analysis. This apparent inconsistency could be ascribed to the fact that, in the early stages of their growth, the crystallites are too small to originate well-defined diffraction patterns, and are, though present, not detectable by XRD. The feature is slightly more evident in the ME sample, and this trend is confirmed in the samples treated at higher temperatures, in agreement with XRD findings. At 600 °C, both XANES spectra are comparable with that of ZnO.

The data were analyzed by linear combination fitting (LCF) to estimate the relative abundance of the two phases, expressed as atomic percentages of zinc in the two different species.

DOI: 10.1021/acs.inorgchem.8b01101
Inorg. Chem. 2018, 57, 13104−13114

By comparing these results with the XRD data, the formation of ZnO is detected already in the 400 °C treated samples. In the case of the samples treated at 500 °C, the percentage of ZnO estimated by XAS is larger than the same value obtained from the XRD data.

The Fourier transforms of the EXAFS curves, taken at the ZnK$_\alpha$ edge, show a similar behavior (Figure 5b). The sulfide curve is characterized by a first shell signal at 2.3 Å (Zn−S distance; see also Table S2 in the Supporting Information), with a second band ranging from 3.5 to 5 Å, comprising Zn−Zn and a further and longer Zn−S distance. Conversely, the oxide shows shorter first (2.0 Å, representing the Zn−O distance) and second (2.8−3.8 Å, with Zn−Zn and Zn−O contributions) shell distances. The as-prepared samples both resemble the sulfide curve, as expected. In the case of the ME sample, the second shell signal is low, likely due to the small particle size. The successive thermal treatment at 400 °C induces a particle growth, and accordingly, the second shell signal intensity increases. In the HY sample, being the particle size bigger already at room temperature, this effect is not evident. The contribution of the oxide portion does not significantly affect the curves, since it is only a few atomic percent points, as evident in data reported in Table 3. The oxide contribution, on the other hand, becomes significant for samples treated at 500 °C. In both specimens, the first shell signals are split in two components, a lower one corresponding to the Zn−O distance, the higher one to Zn−S. At 600 °C, the curves closely resemble the one recorded for wurtzite-phase ZnO.

Comparing the composition obtained from both XRD and XAS analysis for the sample treated at 500 °C, it is evident that XAS estimates a much larger amount of oxide for the HY sample, while the results obtained for the ME samples are similar.

Since XRD requires long-range order in the material to generate a detectable signal, it is unsuited to identifying amorphous phases. On the contrary, the XAS techniques can be applied also to noncrystalline phases. For this reason, the noticeable difference between the two calculated compositions could be related to the presence of amorphous/disordered phases in the sample, being formed during the conversion from crystalline ZnS sphalerite to crystalline ZnO wurtzite.

In this case, the oxidation process is not only a substitution of anions in the crystal lattice, but also requires the rearrangement of the crystal structure from cubic to hexagonal. At the same time, if the oxidation starts from ZnS wurtzite, the structural evolution of the system could be in principle limited to a shrinkage of the cell as the anions are replaced. Therefore, it appears reasonable to speculate that, in the case of the ME samples, when the temperature and the particle size allow the conversion to ZnS wurtzite prior to the oxidation, the oxide is easily formed directly in a crystalline phase, while, for the bigger HY particles, the conversion goes through a more complicated mechanism, which is likely to encompass the formation of an amorphous oxide before the crystalline phase is formed. This observation is somewhat in agreement with the known difference between the oxidation of bulk ZnS wurtzite, which was reported by Schultze et al.[50] to allow the direct conversion from ZnS to ZnO. In comparison, the bulk ZnS sphalerite is characterized by a much more complicated mechanism that encompasses the formation of bulk sulfates.

The oxidation process and the coexistence of ZnS and ZnO were also observable by Raman spectroscopy (Figure 6a),

Table 3. Samples Composition as Weight Percentages Obtained from XRD and XAS Analysis

	ME				HY			
	%ZnS[a]		%ZnO		%ZnS[a]		%ZnO	
T (°C)	XRD	XAS	XRD	XAS	XRD	XAS	XRD	XAS
as-syn.	100	100	0	0	100	100	0	0
400	100	97	0	3	100	98	0	2
500	34	44	66	56	65	42	35	58
600	0	0	100	100	0	0	100	100
700	0	0	100	100	0	0	100	100
800	0	0	100	100	0	0	100	100

[a]Sum of ZnS sphalerite and wurtzite phases in XRD.

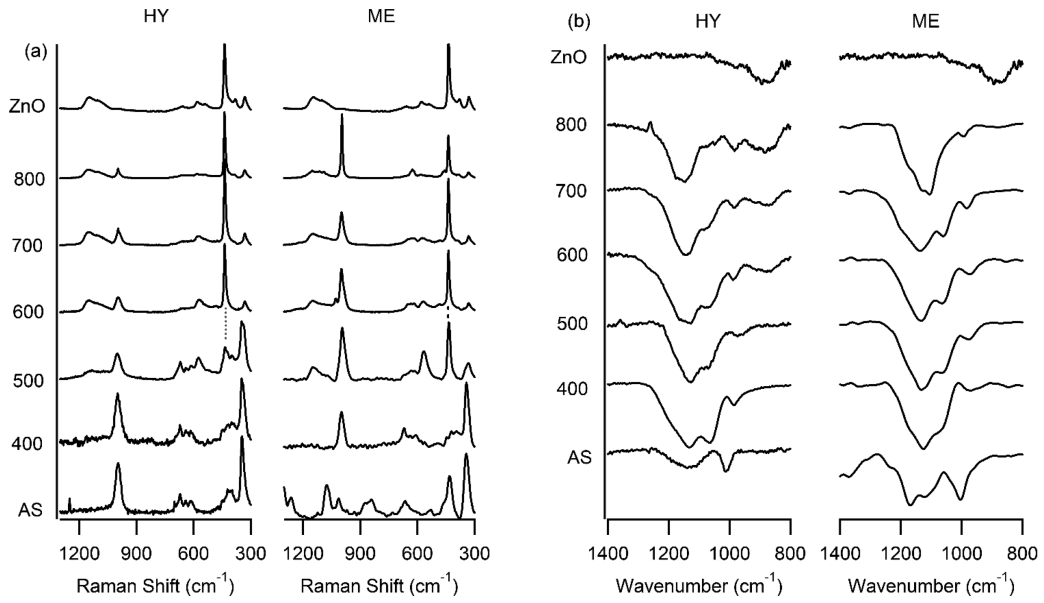

Figure 6. (a) Evolution of the Raman spectra at different calcination temperatures. The dotted lines are emphasizing the main spectral feature of ZnO. The peaks at ca. 1000 cm^{-1} are not related to ZnS or ZnO themselves, but are attributed to the presence of surface sulfate moieties instead. (b) Evolution of the FT-IR spectra at different calcination temperatures. ZnO Raman and FT-IR spectra are added as comparison in both figures. AS = as-synthesized. Temperatures are indicated in Celsius degrees.

DOI: 10.1021/acs.inorgchem.8b01101
Inorg. Chem. 2018, 57, 13104−13114

further confirming the already discussed deductions. The strongest signal at 438 cm^{-1} is typical of the ZnO phononic pattern, which is indeed visible in the 500 °C treated samples, while the ZnS pattern is not visible after the 600 °C treatment. In these spectra, the sharp signal at around 1000 cm^{-1} is associated with sulfate moieties. This peak is present in all the thermally treated samples, as well as in the as-synthesized HY ZnS. In the spectrum of untreated ME ZnS, the pattern arising from the material is not visible due to the presence of stronger signals arising from residual surfactant on the surface, which is readily eliminated after the first thermal treatment at 400 °C.

The presence of oxidized sulfur is particularly evident in the FT-IR spectra (Figure 6b), as the strong peak detected in all sample spectra at about 1136 cm^{-1} and its various shoulders (1068 and 970 cm^{-1}) are to be ascribed to sulfate moieties.[17] An increase in the intensity of these features was also observed after treatment at 300 °C, suggesting a fast increase of the presence of the sulfate on the material. Further increasing the calcination temperature does not significantly alter the signal intensity. Since there is no evidence of bulk sulfates in the XRD patterns, the observed signals were ascribed to species formed only on the nanostructures surface.

In this regard, the surface chemistry of the samples was specifically investigated by XPS spectroscopy (Figure 7).

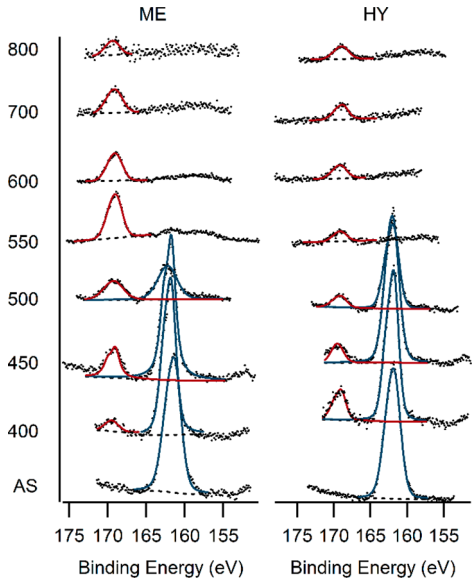

Figure 7. Evolution of XPS S 2p peaks of sulfide (blue) and sulfate (red) at different calcination temperatures. The dotted lines are used for the Shirley-type background. AS = as-synthesized. Temperatures are indicated in Celsius degrees.

While, in the untreated samples, the S 2p peak related to the sulfide[51,52] at 161.8 eV is the only one observed, in the treated ones, a second peak appears at 169.0 eV. This latter signal is diagnostic of sulfur in its highest oxidation state, such as in sulfate.[53] By increasing the treatment temperature, the sulfide peak disappears, while the sulfate remains as the only sulfur-related signal in the spectra, starting from the samples treated at 550 °C. Semiquantitative analysis obtained by fitting the S 2p components for the 400 °C treated samples gives a sulfate/sulfide molar ratio of 0.20:1 for the HY sample, while the same ratio is 0.07:1 for the ME sample. Therefore, a comparison of the two synthetic methods shows an increased tendency of the HY samples to produce sulfates, despite the bigger particle size and possibly smaller available surface area. It is also possible to infer that the presence of sulfates is probably related to a mechanistic difference in the oxidation of wurtzitic ZnS in comparison with sphaleritic ZnS, as previously suggested. In fact, the tendency of the hexagonal phase to directly produce ZnO without the previous formation of intermediates was also remarked by Schultze et al. while studying bulk materials.[50] As opposed to this, the thermal treatment of sphaleritic ZnS produces sulfates as an intermediate moiety in the oxidation to ZnO. Remarkably, the sulfate appears to be formed only on the surface of the nanoparticles, since no XRD pattern compatible with sulfates was observed.

It is also worth noticing that, while weak sulfate signals are visible in the FT-IR spectra of both as-synthesized samples, the same moiety is detectable by XPS only after a thermal treatment that is likely to increase its concentration on the surface to a detectable concentration. Because of this, the surface properties of the samples could be altered significantly even after mildly heating the samples.

Optical and Catalytic Changes. Both ZnS and ZnO are well-known white materials. Interestingly, some of the treated samples were instead obtained as yellow powders. The color is already visible after a 450 °C treatment, and gets more intense at 500 °C, while becoming more and more dull at higher calcination temperatures. This phenomenon was also previously observed for different ZnS-ZnO nanostrucutres.[30−32,34]

Remarkably, the material did not turn white as soon as the composition was determined to be entirely ZnO (calcination over 600 °C), but a stable yellowish form of ZnO was rather obtained. Due to this observation, the color is unlikely to arise solely from the coexistence of the ZnS and ZnO, but possibly due to the presence of stable color centers in the crystal structure. In fact, a transient yellow form of ZnO is known to be formed by annealing the material at a high temperature, because of the release of oxygen from the structure and the consequent formation of large amounts of defects acting as color centers.[9] The coloration rapidly disappears when the system is cooled down in air, as oxygen is allowed to enter the material to restore the original stoichiometry. A stable form of yellow ZnO was also obtained by calcining at 500 °C ZnS nanorods[40] or Zn(OH)F.[54]

To quantitatively describe the phenomenon, the absorption spectra in diffuse reflectance were measured. The as-synthesized materials show the typical absorption edge of ZnS (Figure 8a,b) at 340 nm, corresponding to a band gap of 3.6 eV. Upon thermal treatment at 400 °C, in both cases, a distinct absorption shoulder develops, even extending into the visible light range (Figure 8 insets). At 450 and 500 °C, two discrete absorption shoulders can be seen in each spectrum, indicating a mixture of ZnS and ZnO. From 550 °C, absorption spectra only show ZnO absorption at around 380 nm; the transformation seems complete. However, a strong tailing into the visible light region is still apparent, indicating a large amount of surface and bulk defects. This tailing gradually lessens with increasing temperature treatment, due to improved crystallization and decreasing numbers of defects. The absorption edge shows the least amount of defects after 800 °C.

Since zinc sulfide and zinc oxide are prominent absorbers for solar energy conversion, representative samples have been investigated regarding their performance toward photocatalytic hydrogen production. Figure 9 shows the results for the two

DOI: 10.1021/acs.inorgchem.8b01101
Inorg. Chem. 2018, 57, 13104−13114

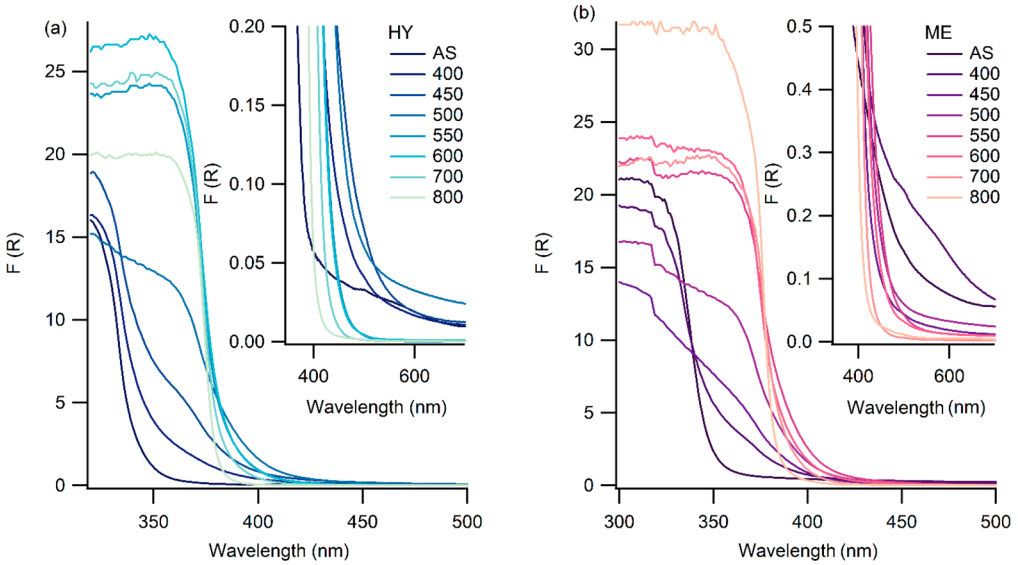

Figure 8. UV−vis spectra of (a) HY and (b) ME samples. A zoomed-in view of lower absorption range values is proposed in the insets. AS = as-synthesized. Temperatures are indicated in Celsius degrees.

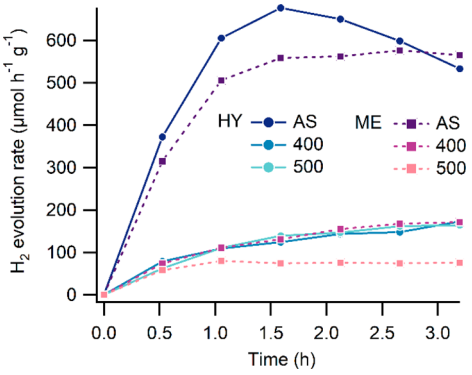

Figure 9. UV−vis spectra of (a) HY and (b) ME samples. A zoom of lower values in the absorption range is proposed the insets. AS = as-synthesized. Temperatures are indicated in Celsius degrees.

as-synthesized samples compared to samples calcined at 400 and 500 °C, respectively.

Interestingly, the best performance in hydrogen production can be observed for the as-synthesized samples. While the sample after hydrothermal synthesis shows a decline in activity after 2 h, the miniemulsion-derived sample shows stable hydrogen evolution rates after the same time span. The two phase-pure ZnS samples have the highest surface area among all samples (BET data available in Table S3 in the Supporting Information) due to their small crystallite size; thus it is unsurprising that the as-synthesized samples yielded the highest activity. However, they also exhibit the lowest crystallinity, which usually influences photocatalytic activity negatively by more defects in the crystal structure as recombination centers. For the cubic ZnS phase, the (110) surface was calculated to be the most stable one[46] and it was determined to be the only facet being exposed in nanoparticles as small as 2.6 nm.[49] Therefore, assuming the (110) surface is also responsible for the photocatalytic behavior of the sample, smaller particles having larger specific surface area should also lead to improved catalytic performances, as the density of active sites increase. However, is evident how as-synthesized HY samples show the best performance. This implies that the available surface area is not the only relevant parameter to consider, while the crystallinity of the sample may also play an important role. After calcination, the activity of both samples drops to similar values despite the difference in specific surface area and despite the increase in crystallinity observed by XRD, leaving the occurrence of ZnO as the most relevant feature influencing the photocatalytic properties of the sample. The results partially agree with the observations made by Jang et al., who also found that the photocatalytic performances drop after the oxidation of ZnS, but also pointed out that a slight oxidation obtained at 500 °C markedly enhanced the H_2 evolution rate of the material.[31] However, bearing in mind that, in that case, nanoporous platelets were employed, the limited oxidation of the material was possibly producing a larger specific surface area through some contraction of the crystallites, without completely affecting the residual ZnS phase. If the reference reaction is changed, and therefore different electronic structure requirements are to be met in order to promote a photocatalytic reaction, the presence of the ZnS/ZnO heterojuction could be beneficial, as discussed by Nasi et al.,[34] as long as the chemical stability of the material is not negatively affected in the framework of the specific process.

CONCLUSIONS

In this work, two different synthetic methods were used, namely a hydrothermal and a miniemulsion route, for the preparation of nanostructured zinc sulfide. Both methods led to the formation of pure sphalerite phase ZnS, with average crystallites dimensions of 21 nm (HY) and 7 nm (ME), respectively. The calculated sizes were found to be reasonably in agreement to the particle size observed in the TEM micrographs. By thermally treating the samples at various temperatures, different oxidation phenomena were observed, together with the general increase in particle size. In both samples, the treatment at a temperature as low as 400 °C led to the formations of a significant amount of sulfates anchored on the surface of the particles, detectable by FT-IR, Raman spectroscopy, and XPS. In particular, HY samples showed an increased tendency to form these moieties. The first traces of ZnO were already visible at 400 °C in the XAS spectra, while

DOI: 10.1021/acs.inorgchem.8b01101
Inorg. Chem. 2018, 57, 13104−13114

the complete conversion was achieved at 550 °C for both samples, according to the XRD data. Depending on the sample type (and therefore on the particles dimensions), the oxidation process was slightly different. In the case of the bigger HY samples, the obtainment of crystalline ZnO is slower, and according to the discrepancies between the XRD and XAS data, it may involve an intermediate amorphization of the material. On the other hand, the process appears to be faster for the smaller ME particles, since, in this case, the formation of ZnS in its hexagonal phase wurzite was also evident at 450 and 500 °C treated samples together with the oxidation. We propose that this structural transformation between the two ZnS polymorphs could lead to a different oxidation path, where the amorphization is unnecessary because of the structural compatibility between wurzitic ZnS and wurzitic ZnO. The samples with mixed ZnS/ZnO composition were characterized by an atypical yellow color, which does not normally belong to either of the involved phases. Indeed, the UV−vis spectra showed an extension of the absorption edge in the visible region for the mixed materials. The samples gradually turned white again upon increasing the calcination temperature. Despite the increased light absorption capabilities, the likely formation of the ZnS−ZnO heterojunction leads to the transport of excited photoelectrons to the ZnO phase and consequently to a substantial decrease in the photocatalytic activity for the H_2 evolution reaction. Therefore, avoiding such oxidation is apparently a crucial point to increase the lifetime of a ZnS-based photocatalyst for this application.

EXPERIMENTAL SECTION

Chemicals. Zinc nitrate hexahydrate ($Zn(NO_3)_2{\cdot}6H_2O$), sodium sulfide nonahydrate ($Na_2S{\cdot}9H_20$), zinc acetylacetonate hydrate ($Zn(acac)_2{\cdot}10H_2O$), and sodium hexachlororhodate(III) (Na_3RhCl_6) were purchased by Sigma-Aldrich; cyclohexane (C_6H_{12}) was purchased from Alfa-Aesar. Polyglycerol polyricinoleate (PGPR) was kindly gifted from Palsgaard. All chemicals were used without further purification.

Miniemulsion Route (ME). Two identical mixtures were prepared by dispersing PGPR (0.16 g) in cyclohexane (16 g); then 3 mL of an aqueous 0.5 M solution of $Zn(NO_3)_2{\cdot}6H_2O$ (0.8 mmol) was added to one mixture and 3 mL of an aqueous 1 M solution of $Na_2S{\cdot}9H_20$ (2.8 mmol) was added to the other. The corresponding miniemulsions were obtained by sonication of the starting suspensions for 3 min, by using a Sartorious Stedim LabsonicP homogenizer, mounting a 3 mm titanium tip, and operating at an amplitude of 70% (which corresponds to an acoustic power of 280 W/cm^2). The as-obtained miniemulsions were mixed together and sonicated with unchanged time and amplitude. The resulting white miniemulsion was mechanically stirred at room temperature for 4 h. Then, the powder product was separated by centrifugation (12 000 rpm, 10 min) and washed five times with acetone and deionized water. The white solid was dried at 80 °C for 4 h.

Hydrothermal Route (HY). In a typical hydrothermal synthesis of ZnS, $Zn(acac)_2{\cdot}10H_2O$ (0.276 g, 0.369 mmol) was dissolved in deionized water (10 mL) in a 23 mL A255AC PTFE cup (Parr Instrument Company) under constant stirring. $Na_2S{\cdot}9H_20$ (0.389 g, 1.619 mmol) was then added to the solution, followed by vigorous stirring for 10 min. The resulting suspension was sealed in the PTFE cup and placed in a stainless steel 4745 General Purpose Acid-Digestion Bomb (Parr Instrument Company), heated at 135 °C for 24 h, and then let to cool down to room temperature. The resulting solid powders were isolated by centrifugation, washed four times with deionized water, and dried at 80 °C in an open air oven.

Thermal Treatments. ZnS was thermally treated in air at different temperatures (400, 450, 500, 550, 600, 700, and 800 °C). Each sample was annealed only at one temperature, cooled at RT, and then analyzed. In a typical procedure, the calcination of ZnS in a muffle oven (Carbolite CWF 1200 with a Eurotherm 3216 temperature controller) consisted in a temperature ramp with a heating rate of 6 °C/min to the final value, a plateau of 4 h at constant temperature, and finally the sample was inertially cooled to room temperature.

XPS Spectroscopy. Powder samples were investigated by XPS with a Perkin−Elmer φ 5600ci instrument using Al−Kα radiation (1486.6 eV), operating at 350 W. The working pressure was less than $5{\cdot}10^{-8}$ Pa. The calibration was based on the binding energy (BE) of the Au $4f_{7/2}$ line at 83.9 eV with respect to the Fermi level. The standard deviation for the BE values was 0.15 eV. Reported BEs were corrected for charging effects, and the BE value of 284.6 eV was assigned to the C 1s line of carbon. Survey scans were obtained in the 0−1350 eV range (pass energy 187.5 eV, 1.0 eV step^{-1}, 25 ms step^{-1}). Detailed scans (29.35 eV pass energy, 0.1 eV step^{-1}, 50−150 ms step^{-1}) were recorded for O 1s, C 1s, Zn 2p, ZnLMM, S 2p, and S 2s. The atomic composition, after a Shirley-type background subtraction,[55] was evaluated using sensitivity factors supplied by PerkinElmer. Peak assignment was carried out according to literature data.

XRD Diffraction. The XRD patterns on the ZnS nanostructures were collected with a Bruker D8 Advance Diffractometer equipped with a Göbel mirror by using the Cu−Kα radiation. The angular accuracy was 0.0010°, and the angular resolution was better than 0.01°. All the experimental data were analyzed by using the Material Analysis Using Diffraction (MAUD) software package,[48] to deduce quantitative crystallographic and microstructural information by using the Rietveld refinement method.

TEM Microscopy. TEM micrographs where obtained with an FEI Tecnai G12 microscope operating at 100 kV, equipped with a OSIS Veleta camera. Samples were prepared by suspending the dried powders in ethanol through sonication and then deposited on 300 mesh lacey carbon coated copper grids. Particles were manually segmented and measured using the ImageJ package.[56] The obtained projected area distributions were used to calculate the corresponding equivalent circle diameters distribution, exploiting the marked convexity of the observed objects to allow the use of a spherical approximation. This approximation is commonly used, and it is also needed if a single dimensional parameter (i.e., the equivalent sphere diameter) is required. The main descriptors of the distributions (average, standard deviation, skewness, and kurtosis) were also calculated. Each distribution was fitted using the log-normal distribution.

HRTEM Microscopy and SAED. Microscopy investigation (and SAED) has been performed by means of a field-emission transmission electron microscope (JEM-2100F UHR, JEOL) operated at 200 kV. The powder has been suspended in absolute ethanol and sonicated. The particles have been transferred onto a holey grid by dipping it into the suspension and drying.

FT-IR Spectroscopy. Infrared spectra were recorded with a NEXUS 870 FT-IR (NICOLET), equipped with an ATR (Attenuated Total Reflectance) sampling device containing ZnSe crystal, operating in the 4000−600 cm^{-1} transmission range, collecting 64 scans with a spectral resolution of 4 cm^{-1}.

Micro-Raman Spectroscopy. Micro-Raman experiments were performed with a Thermo Scientific DXR Raman microscope operating in the 100−4000 cm^{-1} range with a λ = 532 nm solid-state laser and a 10× objective.

XAS Spectroscopy. The XAS measurements were performed at XAFS beamline at Elettra Synchrotron (Trieste, Italy). A Si(311) double crystal monochromator was used for measurements at the Zn K-edge (9669 keV). The second monochromator crystal was tilted for optimal harmonic rejection. The spectra were recorded in transmission mode using ionization chambers as detectors. Energy calibration was performed with a Zn metal foil. The solid samples were pressed into self-supporting pellets using cellulose as a binder. Data evaluation started with background absorption removal from the experimental absorption spectrum by using the automated removal routine found in the Athena software.[48] The threshold energy E_0 was determined as the maximum in the first derivative spectrum. To determine the smooth part of the spectrum, a piecewise polynomial was used. It was adjusted in such a way that the low-R components of

DOI: 10.1021/acs.inorgchem.8b01101
Inorg. Chem. 2018, 57, 13104−13114

the resulting Fourier transform were minimal. After division of the background-subtracted spectrum by its smooth part, the photon energy was converted to photoelectron wavenumbers k. The resulting $\chi(k)$-function was weighted with k^3 and Fourier transformed using a Hanning window function. Data analysis was performed in k-space on unfiltered data, using the Artemis software.[48]

UV−vis Spectroscopy. UV−vis absorption was measured on a PerkinElmer Lambda 750 UV−vis−NIR spectrometer equipped with a Praying Mantis mirror unit recording the diffuse reflectance in dependence of the wavelength with a step size of 1 nm. $BaSO_4$ was utilized as standard reference, and the reflectance spectra were converted into absorption spectra applying the Kubelka−Munk function: $F(R) = (1 - R)^2/2R$.

Photocatalytic H_2 Evolution. 200 mg of photocatalyst were suspended in 200 mL of an aqueous methanol solution (10 vol. %) and filled into a homemade double-walled glass reactor. A 150 W Xe lamp (Newport) was used as light source, the reactor was cooled to 20 °C using a thermostat (LAUDA RP845). Gas evolution was measured online using a GC (Shimadzu GC2014). Argon 5.0 was used as carrier gas; the continuous gas flow was controlled by a Bronkhorst mass flow controller. The gas flow was set to 25 mL min^{-1}. All reactions were performed at 20 °C. Before photocatalytic reactions were initiated, the whole system, with the photocatalyst included, was flushed with Argon 5.0 for 1 h to remove any trace of air. Co-catalyst precursor (Na_3RhCl_6) addition for photodeposition of 0.15 wt. % Rh was done through a rubber sealing (without opening the reactor).

■ ASSOCIATED CONTENT

Supporting Information

The Supporting Information is available free of charge on the ACS Publications website at DOI: 10.1021/acs.inorgchem.8b01101.

Fitting parameters used for EXAFS data analysis and Krypton adsorption measurement for the extrapolation of the specific surface area (PDF)

■ AUTHOR INFORMATION

Corresponding Authors

*E-mail: silvia.gross@unipd.it (S.G.).
*E-mail: roland.marschall@phys.chemie.uni-giessen.de (R.M.).

ORCID

Angela F. De Fazio: 0000-0002-9733-3981
Roland Marschall: 0000-0002-1057-0459
Paolo Dolcet: 0000-0001-9583-9375
Mattia Fanetti: 0000-0002-2437-5179
Silvia Gross: 0000-0003-1860-8711

Present Address

#Karlsruhe Institute of Technology (KIT), Institut für Technische Chemie und Polymerchemie, Engesserstr. 20, 76133 Karlsruhe, Germany.

Notes

The authors declare no competing financial interest.

■ ACKNOWLEDGMENTS

We would like to acknowledge XAFS beamline at Elettra Sincrotrone Trieste (Italy) for granting access to the experimental facility and Luca Olivi and Clara Guglieri Rodriguez for technical support. Financial support was provided by the DFG via the GrK (Research training group) 2204 "Substitute Materials for sustainable Energy Technologies" and by DFG MA 5392/3-1. S.G. gratefully acknowledges DFG and the Justus-Liebig Universität Gießen for the provision of a Mercator Fellowship. Dr. Federico Caicci (Department of Biology, University of Padova) is gratefully acknowledged for the TEM measurements.

■ REFERENCES

(1) Fang, X.; Bando, Y.; Gautam, U. K.; Zhai, T.; Zeng, H.; Xu, X.; Liao, M.; Golberg, D. ZnO and ZnS Nanostructures: Ultraviolet-Light Emitters, Lasers, and Sensors. *Crit. Rev. Solid State Mater. Sci.* **2009**, *34*, 190−223.

(2) Liu, H.; Hu, L.; Watanabe, K.; Hu, X.; Dierre, B.; Kim, B.; Sekiguchi, T.; Fang, X. Cathodoluminescence Modulation of ZnS Nanostructures by Morphology, Doping, and Temperature. *Adv. Funct. Mater.* **2013**, *23*, 3701−3709.

(3) Fang, X.; Bando, Y.; Liao, M.; Gautam, U. K.; Zhi, C.; Dierre, B.; Liu, B.; Zhai, T.; Sekiguchi, T.; Koide, Y.; Golberg, D. Single-Crystalline ZnS Nanobelts as Ultraviolet-Light Sensors. *Adv. Mater.* **2009**, *21*, 2034−2039.

(4) Fang, X. S.; Bando, Y.; Shen, G. Z.; Ye, C. H.; Gautam, U. K.; Costa, P. M. F. J.; Zhi, C. Y.; Tang, C. C.; Golberg, D. Ultrafine ZnS Nanobelts as Field Emitters. *Adv. Mater.* **2007**, *19*, 2593−2596.

(5) Fang, X.; Wu, L.; Hu, L. ZnS Nanostructure Arrays: A Developing Material Star. *Adv. Mater.* **2011**, *23*, 585−598.

(6) Fang, X.; Bando, Y.; Liao, M.; Zhai, T.; Gautam, U. K.; Li, L.; Koide, Y.; Golberg, D. An Efficient Way to Assemble ZnS Nanobelts as Ultraviolet-Light Sensors with Enhanced Photocurrent and Stability. *Adv. Funct. Mater.* **2010**, *20*, 500−508.

(7) Fang, X. S.; Ye, C. H.; Zhang, L. D.; Wang, Y. H.; Wu, Y. C. Temperature-Controlled Catalytic Growth of ZnS Nanostructures by the Evaporation of ZnS Nanopowders. *Adv. Funct. Mater.* **2005**, *15*, 63−68.

(8) Fang, X.; Zhai, T.; Gautam, U. K.; Li, L.; Wu, L.; Bando, Y.; Golberg, D. ZnS Nanostructures: From Synthesis to Applications. *Prog. Mater. Sci.* **2011**, *56*, 175−287.

(9) Wiberg, N.; Holleman, A. F.; Wiberg, E. *Inorganic Chemistry*; Academic Press: New York, 2001.

(10) Ves, S.; Schwarz, U.; Christensen, N. E.; Syassen, K.; Cardona, M. Cubic ZnS under Pressure: Optical-Absorption Edge, Phase Transition, and Calculated Equation of State. *Phys. Rev. B: Condens. Matter Mater. Phys.* **1990**, *42*, 9113−9118.

(11) Desgreniers, S.; Beaulieu, L.; Lepage, I. Pressure-Induced Structural Changes in ZnS. *Phys. Rev. B: Condens. Matter Mater. Phys.* **2000**, *61*, 8726−8733.

(12) Morgan, B. J. First-Principles Study of Epitaxial Strain as a Method of B 4 → B C T Stabilization in ZnO, ZnS, and CdS. *Phys. Rev. B: Condens. Matter Mater. Phys.* **2010**, *82*, 153408.

(13) Tiwary, C. S.; Kumbhakar, P.; Mondal, A. K.; Mitra, A. K. Synthesis and Enhanced Green Photoluminescence Emission from BCT ZnS Nanocrystals. *Phys. Status Solidi A* **2010**, *207*, 1874−1879.

(14) Schultze, D.; Steinike, U.; Kussin, J.; Kretzschmar, U. Thermal Oxidation of ZnS Modifications Sphalerite and Wurtzite. *Cryst. Res. Technol.* **1995**, *30*, 553−558.

(15) Siriwardane, R. V.; Woodruff, S. In Situ Fourier Transform Infrared Characterization of Sulfur Species Resulting from the Reaction of Water Vapor and Oxygen with Zinc Sulfide. *Ind. Eng. Chem. Res.* **1997**, *36*, 5277−5281.

(16) Sofekun, O. A.; Doraiswamy, L. K. High-Temperature Oxidation of Zinc Sulfide: Kinetic Modeling under Conditions of Strict Kinetic Control. *Ind. Eng. Chem. Res.* **1996**, *35*, 3163−3170.

(17) Siriwardane, R. V.; Woodruff, S. FTIR Characterization of the Interaction of Oxygen with Zinc Sulfide. *Ind. Eng. Chem. Res.* **1995**, *34*, 699−702.

(18) Hertl, W. Surface Chemical Properties of Zinc Sulfide. *Langmuir* **1988**, *4*, 594−598.

(19) Hu, J.-S.; Ren, L.-L.; Guo, Y.-G.; Liang, H.-P.; Cao, A.-M.; Wan, L.-J.; Bai, C.-L. Mass Production and High Photocatalytic Activity of ZnS Nanoporous Nanoparticles. *Angew. Chem., Int. Ed.* **2005**, *44*, 1269−1273.

(20) Wang, G.; Huang, B.; Li, Z.; Lou, Z.; Wang, Z.; Dai, Y.; Whangbo, M.-H. Synthesis and Characterization of ZnS with

DOI: 10.1021/acs.inorgchem.8b01101
Inorg. Chem. 2018, 57, 13104−13114

Controlled Amount of S Vacancies for Photocatalytic H2 Production under Visible Light. *Sci. Rep.* **2015**, *5*, 8544.
(21) Yu, X.; Yu, J.; Cheng, B.; Huang, B. One-Pot Template-Free Synthesis of Monodisperse Zinc Sulfide Hollow Spheres and Their Photocatalytic Properties. *Chem. - Eur. J.* **2009**, *15*, 6731−6739.
(22) Zhou, R.; Guzman, M. I. CO $_2$ Reduction under Periodic Illumination of ZnS. *J. Phys. Chem. C* **2014**, *118*, 11649−11656.
(23) Baran, T.; Wojtyła, S.; Dibenedetto, A.; Aresta, M.; Macyk, W. Zinc Sulfide Functionalized with Ruthenium Nanoparticles for Photocatalytic Reduction of CO2. *Appl. Catal., B* **2015**, *178*, 170−176.
(24) Zhang, J.; Yu, J.; Zhang, Y.; Li, Q.; Gong, J. R. Visible Light Photocatalytic H $_2$ -Production Activity of CuS/ZnS Porous Nanosheets Based on Photoinduced Interfacial Charge Transfer. *Nano Lett.* **2011**, *11*, 4774−4779.
(25) Qadri, S. B.; Skelton, E. F.; Hsu, D.; Dinsmore, A. D.; Yang, J.; Gray, H. F.; Ratna, B. R. Size-Induced Transition-Temperature Reduction in Nanoparticles of ZnS. *Phys. Rev. B: Condens. Matter Mater. Phys.* **1999**, *60*, 9191−9193.
(26) Akiyama, T.; Sano, K.; Nakamura, K.; Ito, T. An Empirical Interatomic Potential Approach to Structural Stability of ZnS and ZnSe Nanowires. *Jpn. J. Appl. Phys.* **2007**, *46*, 1783−1787.
(27) Kole, A. K.; Kumbhakar, P. Cubic-to-Hexagonal Phase Transition and Optical Properties of Chemically Synthesized ZnS Nanocrystals. *Results Phys.* **2012**, *2*, 150−155.
(28) Khalkhali, M.; Liu, Q.; Zeng, H.; Zhang, H. A Size-Dependent Structural Evolution of ZnS Nanoparticles. *Sci. Rep.* **2015**, *5*, 14267.
(29) Zhao, X.; Li, M.; Lou, X. Enhanced Photocatalytic Activity of Zinc Oxide Synthesized by Calcination of Zinc Sulfide Precursor. *Mater. Sci. Semicond. Process.* **2013**, *16*, 489−494.
(30) Kole, A. K.; Tiwary, C. S.; Kumbhakar, P. Ethylenediamine Assisted Synthesis of Wurtzite Zinc Sulphide Nanosheets and Porous Zinc Oxide Nanostructures: Near White Light Photoluminescence Emission and Photocatalytic Activity under Visible Light Irradiation. *CrystEngComm* **2013**, *15*, 5515.
(31) Jang, J. S.; Yu, C.-J.; Choi, S. H.; Ji, S. M.; Kim, E. S.; Lee, J. S. Topotactic Synthesis of Mesoporous ZnS and ZnO Nanoplates and Their Photocatalytic Activity. *J. Catal.* **2008**, *254*, 144−155.
(32) Li, X.; Li, X.; Zhu, B.; Wang, J.; Lan, H.; Chen, X. Synthesis of Porous ZnS, ZnO and ZnS/ZnO Nanosheets and Their Photocatalytic Properties. *RSC Adv.* **2017**, *7*, 30956−30962.
(33) Ma, H.; Han, J.; Fu, Y.; Song, Y.; Yu, C.; Dong, X. Synthesis of Visible Light Responsive ZnO−ZnS/C Photocatalyst by Simple Carbothermal Reduction. *Appl. Catal., B* **2011**, *102*, 417−423.
(34) Nasi, L.; Calestani, D.; Besagni, T.; Ferro, P.; Fabbri, F.; Licci, F.; Mosca, R. ZnS and ZnO Nanosheets from ZnS(En) $_{0.5}$ Precursor: Nanoscale Structure and Photocatalytic Properties. *J. Phys. Chem. C* **2012**, *116*, 6960−6965.
(35) Kole, A. K.; Kumbhakar, P.; Chatterjee, U. Observations on Nonlinear Optical Properties of ZnS Nanosheet, ZnS−ZnO Composite Nanosheet and Porous ZnO Nanostructures Dispersed in Aqueous Medium. *Chem. Phys. Lett.* **2014**, *591*, 93−98.
(36) Liu, D.; Li, X.; Shi, Z.; Zhu, B.; Chen, X.; Yang, J. Synthesis of Porous ZnS/ZnSe Nanosheets for Enhanced Visible Light Photocatalytic Activity. *J. Mater. Sci.: Mater. Electron.* **2018**, *29*, 11605−11612.
(37) Jing, M.; Chen, Z.; Li, Z.; Li, F.; Chen, M.; Zhou, M.; He, B.; Chen, L.; Hou, Z.; Chen, X. Facile Synthesis of ZnS/N,S Co-Doped Carbon Composite from Zinc Metal Complex for High-Performance Sodium-Ion Batteries. *ACS Appl. Mater. Interfaces* **2018**, *10*, 704−712.
(38) Kanti Kole, A.; Sekhar Tiwary, C.; Kumbhakar, P. Morphology Controlled Synthesis of Wurtzite ZnS Nanostructures through Simple Hydrothermal Method and Observation of White Light Emission from ZnO Obtained by Annealing the Synthesized ZnS Nanostructures. *J. Mater. Chem. C* **2014**, *2*, 4338−4346.
(39) Wu, X.; Li, K.; Wang, H. Facile Fabrication of Porous ZnO Microspheres by Thermal Treatment of ZnS Microspheres. *J. Hazard. Mater.* **2010**, *174*, 573−580.
(40) Emin, S.; Lisjak, D.; Pitcher, M.; Valant, M. Structural and Morphological Transformations of Textural Porous Zinc Sulfide Microspheres. *Microporous Mesoporous Mater.* **2013**, *165*, 185−192.
(41) Kanti Kole, A.; Sekhar Tiwary, C.; Kumbhakar, P. Morphology Controlled Synthesis of Wurtzite ZnS Nanostructures through Simple Hydrothermal Method and Observation of White Light Emission from ZnO Obtained by Annealing the Synthesized ZnS Nanostructures. *J. Mater. Chem. C* **2014**, *2*, 4338−4346.
(42) Murugadoss, G. Synthesis, Optical, Structural and Thermal Characterization of Mn2+ Doped ZnS Nanoparticles Using Reverse Micelle Method. *J. Lumin.* **2011**, *131*, 2216−2223.
(43) Lee, G.-J.; Wu, J. J. Recent Developments in ZnS Photocatalysts from Synthesis to Photocatalytic Applications — A Review. *Powder Technol.* **2017**, *318*, 8−22.
(44) Wang, Z.; Cao, S.-W.; Loo, S. C. J.; Xue, C. Nanoparticle Heterojunctions in ZnS−ZnO Hybrid Nanowires for Visible-Light-Driven Photocatalytic Hydrogen Generation. *CrystEngComm* **2013**, *15*, 5688.
(45) Baran, M. P.; Korsunskaya, N. E.; Stara, T. R.; Venger, Y. E.; Kryshtab, T. G.; Stroyuk, O. L.; Raevskaya, A. L.; Korzhak, G. V.; Kuchmiy, S. Y. Graded ZnS/ZnSxO1−x Heterostructures Produced by Oxidative Photolysis of Zinc Sulfide: Structure, Optical Properties and Photocatalytic Evolution of Molecular Hydrogen. *J. Photochem. Photobiol., A* **2016**, *329*, 213−220.
(46) Hamad, S.; Cristol, S.; Catlow, C. R. A. Surface Structures and Crystal Morphology of ZnS: Computational Study. *J. Phys. Chem. B* **2002**, *106*, 11002−11008.
(47) Skinner, B. J. Unit-Cell Edges of Natural and Synthetic Sphalerites. *Am. Mineral.* **1961**, *46*, 1399−1411.
(48) Lutterotti, L. Total Pattern Fitting for the Combined Size−strain−stress−texture Determination in Thin Film Diffraction. *Nucl. Instrum. Methods Phys. Res., Sect. B* **2010**, *268*, 334−340.
(49) Balantseva, E.; Berlier, G.; Camino, B.; Lessio, M.; Ferrari, A. M. Surface Properties of ZnS Nanoparticles: A Combined DFT and Experimental Study. *J. Phys. Chem. C* **2014**, *118*, 23853−23862.
(50) Zhang, H.; Chen, B.; Gilbert, B.; Banfield, J. F. Kinetically Controlled Formation of a Novel Nanoparticulate ZnS with Mixed Cubic and Hexagonal Stacking. *J. Mater. Chem.* **2006**, *16*, 249−254.
(51) Brion. Etude Par Spectroscopie de Photoelectrons de La Degradation Superficielle de FeS2, CuFeS2, ZnS et PbS a l'air et Dans l'eau. *Appl. Surf. Sci.* **1980**, *5*, 133−152.
(52) Agostinelli, E.; Battistoni, C.; Fiorani, D.; Mattogno, G.; Nogues, M. An XPS Study of the Electronic Structure of the ZnxCd1−xCr2(X = S, Se) Spinel System. *J. Phys. Chem. Solids* **1989**, *50*, 269−272.
(53) Siriwardane, R. V.; Poston, J. A. Interaction of H2S with Zinc Titanate in the Presence of H2 and CO. *Appl. Surf. Sci.* **1990**, *45*, 131−139.
(54) Peng, Y.; Wang, Y.; Chen, Q.-G.; Zhu, Q.; Xu, A. W. Stable Yellow ZnO Mesocrystals with Efficient Visible-Light Photocatalytic Activity. *CrystEngComm* **2014**, *16*, 7906−7913.
(55) Shirley, D. A. High-Resolution X-Ray Photoemission Spectrum of the Valence Bands of Gold. *Phys. Rev. B* **1972**, *5*, 4709−4714.
(56) Schneider, C. A.; Rasband, W. S.; Eliceiri, K. W. NIH Image to ImageJ: 25 Years of Image Analysis. *Nat. Methods* **2012**, *9*, 671−675.

DOI: 10.1021/acs.inorgchem.8b01101
Inorg. Chem. 2018, 57, 13104−13114

Chapter 7.

Experimental details

7.1 Chemicals

All the syntheses were carried out using milli-Q quality water. All the chemical were used without further purification.

Table 7.1 Employed chemicals.

Chemical	Formula	Molar Mass (g/mol)	CAS Number	Supplier
Ammonium sulfide (20 wt. in water)	$(NH_4)_2S$	68.14	12135-76-1	Sigma-Aldrich
Chromium(III) nitrate nonahydrate	$Cr(NO_3)_3{\cdot}9H_2O$	400.15	7789-02-8	Sigma-Aldrich
Cobalt(II) chloride hexahydrate	$CoCl_2{\cdot}6H_2O$	129.84	7791-13-1	Sigma-Aldrich
Copper(II) chloride dihydrate	$CuCl_2{\cdot}2H_2O$	170.48	10125-13-0	Sigma-Aldrich
Europium (III) chloride hexahydrate	$EuCl_3{\cdot}6H_2O$	366.41	13759-92-7	Sigma-Aldrich
Gadolinium(III) nitrate hexahydrate	$Gd(NO_3)_3{\cdot}6H_2O$	451.36	19598-90-4	Sigma-Aldrich
Iron(II) sulfate heptahydrate	$FeSO_4{\cdot}7H_2O$	278.01	7782-63-0	Sigma-Aldrich
Lead(II) nitrate	$Pb(NO_3)_2$	331.21	233-245-9	Sigma-Aldrich
Manganese(II) chloride tetrahydrate	$MnCl_2{\cdot}4H_2O$	197.91	13446-34-9	Sigma-Aldrich
Neodymium(III) nitrate hexahydrate	$Nd(NO_3)_3{\cdot}6H_2O$	438.35	16454-60-7	Sigma-Aldrich
Nickel(II) chloride hexahydrate	$NiCl_2{\cdot}6H_2O$	237.69	7791-20-0	Fluka
Silver(I) nitrate	$AgNO_3$	169.87	7761-88-8	Sigma-Aldrich
Sodium hydrogen sulfide	NaHS	56.06	207683-19-0	Sigma-Aldrich
Sodium sulfide nonahydrate	$Na_2S{\cdot}9H_2O$	204.18	1313-84-4	Alfa Aesar
Thiourea	S=C(NH2)2	76.12	62-56-6	Sigma-Aldrich
Tin(II) chloride	$SnCl_2$	189.62	7772-99-8	Sigma-Aldrich
Titanium(IV) oxysulfate	$TiOSO_4$	159.93	13825-74-6	Sigma-Aldrich
Ytterbium(III) chloride hexahydrate[a]	$YbCl_3{\cdot}6H_2O$	387.49	10361-91-8	Sigma-Aldrich
Ytterbium(III) nitrate hexahydrate[b]	$Yb(NO_3)_3{\cdot}6H_2O$	467.15	35725-34-9	Sigma-Aldrich
Zinc(II) nitrate hexahydrate[a]	$Zn(NO_3)_2{\cdot}6H_2O$	297.49	10196-18-6	Fluka
Zinc(II) nitrate hexahydrate[b]	$Zn(NO_3)_2{\cdot}6H_2O$	297.49	10196-18-6	Sigma-Aldrich

(a) Chemical employed for batch and microfluidic syntheses. (b) Chemical employed for CHFS syntheses.

7.2 Batch syntheses

In a typical batch synthesis of a metal sulfide, a proper quantity the sulfur precursor ($Na_2S·9H_2O$, NaHS or $(NH_4)_2S$) was weighted and dissolved in 25 ml of water to obtain a 0.2 M solution. This solution was quantitatively transferred in a 100 ml round-bottom flask. The sulfur precursor flask was left closed as much as possible to prevent the loss sulfur to the atmosphere as H_2S. The metal precursor was weighted in a proper quantity and dissolved in 25 ml of water to obtain a two-fold molar excess of the 0.2 M of the sulfur precursor (e.g. 0.1 M solution for ZnS, or a 0.067 M solution for Ln_2S_3). Both solutions where cooled with an ice bath thermostat, then the metal solution was added dropwise to the vigorously stirred sulfur precursor solution. Afterwards, the obtained slurry was kept stirred for approx. 1h and then let settle down. Once the product was settled, the clear solution above was carefully removed and the product was recovered washing the flask with water. The product was isolated though centrifugation (5 min, 10 000 rpm), then it was washed by adding water and sonicating the suspension for 15 min prior to isolate the product again by centrifugation (5 - 15 min, 12 500 rpm). This washing cycle was repeated four times. In the case of the formation of stable suspension (e.g. ZnS), many additional cycles of centrifugation were necessary to isolate the material, and part of the product was commonly lost in the washing water. The clean product was dried in vacuum at room temperature using a desiccator, then grinded and stored in common Eppendorf vials.

7.3 Microfluidic syntheses

The microfluidic syntheses were performed at the laboratories of Prof. Michele Maggini, Università degli Studi di Padova (Padova, IT).

In a typical microfluidic synthesis of ZnS, a proper quantity of $Na_2S·9H_2O$ was weighted and dissolved in 500 ml of water to obtain a 0.2 M or a 0.05 M solution. A proper quantity of $Zn(NO_3)_2·6H_2O$ was then weighted and dissolved in 500 ml of water to obtain a 1:2 Zn:S molar ratio with respect to the zinc precursor solution. In the case of the doped samples, the dopant precursor was directly dissolved in the zinc nitrate solution in the proper quantity that allowed to realize the same nominal M:Zn molar ratio targeted for the final product. The two solutions were used to feed the microfluidic setup schematized in Figure 4.1. The solutions were pumped using two reciprocating syringe pumps (Asia Syringe Pump, Syrris) operated at either at 2.0 or 1.2 ml/min. 0.63 mm PTFE tubing and a custom-made stainless-steel T-junction mixer were used to realize the flow setup. The solutions were fed

asymmetrically to the mixer, having the zinc solution connected in the position aligned with the mixer outlet and the sulfur solution connected at 90° with respect to both the zinc precursor and the outlet positions (cross-flow T-junction). The product was collected in an ice bath-cooled stirred vessel pre-filled with approx. 20 ml of water. Once the targeted amount of product was obtained, the setup was flowed with water before the pumps were shuttled down, to prevent the occlusion of the mixer. The obtained slurry was kept stirred for approx. 1h and then let settle down. Once the product was settled, the clear solution above was carefully removed and the product was recovered washing the flask with fresh water. The product was isolated though centrifugation (5 min, 10 000 rpm), then it was washed by adding fresh water and sonicating the suspension for 15 min prior to isolate the product again by centrifugation (5 - 15 min, 12 500 rpm). This washing cycle was repeated four times. Since ZnS NPs showed the tendency to form stable colloids during the washing procedure, many additional cycles of centrifugation were sometimes necessary to isolate the material, and part of the product was commonly lost in the washing water. The clean product was dried in vacuum at room temperature using a desiccator, then grinded and stored in common Eppendorf vials.

7.4 CHFS syntheses

The reactor schematics are reported in Figure 5.1. CHFS syntheses were performed with a lab-scale CHFS reactor in the laboratories of Prof. Jawwad Darr, UCL (London, UK). The reactor was made from off-the-shelf Swagelok™ parts and equipped with two patented confined jet mixer.[77] The mixers were fed by three Primeroyal K diaphragm pumps (Milton Roy, Pont-Saint-Pierre, France, pressurized to 24.1 MPa). Pump 1 was employed for the supercritical water line at 80 ml/min, where water was heated in line at 450 °C using a custom-made 7 kW heater. Pump 2 was used to feed the thiourea solution to the first mixer at 40 ml/min, to allow its thermal decomposition leading to the production *in-situ* of HS^- at 380 °C.[80] Pump 3 was then used to pump a $Zn(NO_3)_2 \cdot 6H_2O$ solution to the second mixer, allowing the precipitation of ZnS from the mixing with the SH^- solution. The residence time between the first and the second mixer was 2.28 s.

For the undoped CH1-CH9 samples, the reaction temperature was changed from 241 to 335 °C by tuning the flow rate of pump 3 according to Table 7.2. The zinc solution was kept fixed at 0.1 M, while the thiourea solution concentration was adjusted to maintain a Zn:S molar ratio of 1:2 at the second mixer.

For the doped ZnS samples, a flow rate of 60 ml/min was used for pump 3, corresponding to a reaction temperature of 307 °C. The concentration of the zinc precursor was 0.2 M, while the concentration of

the thiourea solution was 0.6 M. The concentration for the sulfur and the zinc precursor at the second mixer was 0.13 M and 0.07 M respectively. The dopants precursors were dissolved in the zinc nitrate solution by adding the correct quantity to realize in the solution the targeted nominal Ln:Z molar ratio of the final material.

The products were collected as slurries in a simple flask. Once the product was settled, the clear solution above was carefully removed and the product was recovered washing the flask with fresh water. The product was isolated though centrifugation (10 min, 10 000 rpm), then it was washed by adding fresh water and isolated again though centrifugation (10 min, 10 000 rpm) for four times. As a stable suspension was sometimes obtained during the washing cycles, a prolonged centrifugation time was sometimes necessary to isolate the material. The clean products were freeze-dried, grinded and stored in common Falcon tubes.

Table 7.2 Thiourea concentration, pump 3 (P3) flow rates, temperature obtained at the second mixer (M2) and concentrations at the second mixer of the zinc and the sulfur precursors.

Sample	Conc. Thiourea M	P3 Flow Rate ml/min	M2 Temp °C	M2 Zn Conc M	M2 S Conc. M
CH1	0.600	120	241	0.050	0.100
CH2	0.550	110	251	0.048	0.096
CH3	0.500	100	260	0.045	0.091
CH4	0.450	90	271	0.043	0.086
CH5	0.400	80	282	0.040	0.080
CH6	0.350	70	294	0.037	0.074
CH7	0.300	60	307	0.033	0.067
CH8	0.250	50	321	0.029	0.059
CH9	0.200	40	335	0.025	0.050

Chapter 8.

Characterization methods

All the characterizations here reported were performed in-house if not differently specified.

8.1 X-Ray Diffraction (XRD)

XRD patterns were collected with a Bruker D8 Advance Diffractometer equipped with a Göbel mirror by using the Cu-Kα radiation. The angular accuracy was 0.0010° and the angular resolution was better than 0.01°.

The Whole Pattern Profile Fitting (WPPF) method implemented in MAUD[84] was employed to obtain crystallographic information from the refinement of the XRD profiles. This approach is Rieteveld-based, thus all the reflections from a determined crystal structure are fitted to the data, also allowing the analysis of overlapping reflections. In MAUD, the formula for the calculated profile intensity ${I_i}^{calc}(2\theta_i)$ at each point i of the pattern can be expressed by the following equation.[84]

(8.1)

$$ {I_i}^{calc}(2\theta_i) = bkg_i + I_0 \cdot Lp(2\theta_i) \cdot \sum_{n=1}^{Nphases} \frac{f_n}{V_n^2} \times \sum_{k=1}^{Nhkl_n} m_{k,n} \cdot \left|F_{k,n}\right|^2 \cdot S_{k,n}\left(2\theta_i - 2\theta_{k,n}\right) \cdot P_{k,n} $$

Here, bkg_i is the background contribution, I_0 is a scale factor proportional to the incident beam intensity, $Lp(2\theta_i)$ is the Lorentz–polarization correction, $Nphases$ is the number of phases in the pattern, $Nhkl_n$ is the number of reflections for the n-th phase, f_n is the volume fraction of the n-th phase, V_n is the cell volume, $m_{k,n}$ is the multiplicity factor, $F_{k,n}$ is the structure factor, $S_{k,n}\left(2\theta_i - 2\theta_{k,n}\right)$ is the profile function for the reflection at the position $2\theta_{k,n}$ and $P_{k,n}$ is the texture weight.

Pseudo-Voigt functions were used to fit the reflections. Despite these functions only empirically describes the reflections shape, physically meaningful results can still be obtained since the reflections

position, intensities, width and shape are constrained by a physical model.[250] Reflections positions and intensities are adapted to the pattern directly refining the structural model. Constrains in reflections width and shape as a function of the scattering angle are also applied by using the Caglioti formula.[331] Microstructural information was obtained from the reflection broadening thought the simultaneous analysis of size and strain effects developed by Lutterotti and Scardi.[332] For the calculation of lognormal size distributions from the XRD patterns, the method developed by Popa and Balzar was used,[333] while the presence of stacking faults in ZnS was included using the Warren model.[89] In the case of anisotropic particles, the model for the anisotropic broadening developed by Popa was employed, which calculates an equivalent crystallite shape by using spherical harmonics in order to allow different size and strain effects to be applied to different crystallographic directions.[154] In the case relevant texturing effects (i.e. preferred orientation in the crystallites) were observed, the harmonic texture model proposed by Von Dreele was employed.[334] In general, to ensure that meaningful data were retrieved, the fittings were aided by orthogonal information, like particle size, morphology or the tendency to assume a preferred orientation, observed at the TEM analyses. In the fittings, a polynomial function on 2θ was used for the background. Refined parameters always included the incident beam intensity, the background coefficients, the unit cell parameters and thermal Debye-Waller factors. For the latter, only a single value was used for all the atoms in the unit cell to reduce the number of fitted parameters. Different Debye-Waller factors were only refined along with the atomic positions in the unit cells when an investigation on the crystal structure was performed (e.g. Ag_2S sample in Chapter 3.4).

The Debye Scattering Equation (DSE)-based method coded in the DebUsSy suite[254] was used with XRD data obtained by microfluidic samples. DSE allows to calculate the scattering that originates from isotropic samples without presuming any periodicity on the underlying structure and is therefore applicable even to liquids or amorphous material.[253] The great advantage of this method, in opposition to more conventional Bragg and Laue type of approaches, is that information can be retrieved from the entire pattern profile and is not limited to the parameters that regulates shape, intensity and position of Bragg peaks.[253] Applied to nanomaterials, the DSE analysis allows to take advantage of the diffuse scattering (i.e. off-Bragg scattering) without constraining the analysis to the chosen functions to model the reflections. However, the DSE calculates the scattering intensity as a sum of contributions from all the atoms in the sample, accounting for the mutual interference of the scattered radiation of all the atoms with each other, as in equation (8.2) (even though, in practice, the evaluation of the interference with neighbor atoms is normally limited for practical reasons).

$$I(q) = \sum_{j=1}^{N} f_j(q)^2 \, o_j^2 + 2 \sum_{j>i=1}^{N} f_j(q) f_i(q) T_j(q) T_i(q) o_j o_i \frac{sen(q d_{ij})}{q d_{ij}} \qquad (8.2)$$

Here, the scattering intensity $I(q)$ is calculated from two terms, where the first represent the term from zero distance between an atom and itself, and the second the interference contribution of the atom i and the atom j. f_i is the atomic form factor, T_i is the thermal Debye-Waller factor, o_i is the occupancy factor and d_{ij} is the interatomic distance between atoms i and atom j.

Consequently, this method requires to build an atomistic model of the sample. In the case of ZnS, particles where small enough to model all the relevant particle sizes, starting from a single unit cell. The layer-by-layer approach implemented in the DebUsSy suite[254] was used for both modelling the particles and sample the pair atomic distances for the DSE-based calculation. Once the database of the pair interatomic distances for each particle size was obtained, the corresponding diffraction pattern was calculated by DSE. Finally, with this approach, the pattern was fitted using a weighted sum of the calculated single-size patterns, where the relative contributions are constrained by a lognormal size distribution.

In the performed DSE-based analyses, ZnS model particles were built layer-by-layer, starting from the ZnS sphalerite structure and using a spherical morphology, up to a maximum size of 25 nm, corresponding to 60 different sizes. In the final fittings, microstrain and a size-dependent single Debye-Waller factor for all the atoms were also refined.

8.2 Transmission Electron Microscopy (TEM)

Images of the NPs were acquired using a Philips CM12 electron microscope, operated at 120 kV. Samples were prepared for TEM observations by suspending a small amount of powder either in water, methanol or a 1 mM solution of oleylamine in hexane. A drop of the suspension was deposited onto a carbon-coated holey gold grid. The oleylamine approach led to in the formation of small dark droplets of a few hundreds of nm on the TEM grid. Small NPs were observed to be trapped in the droplets, that could result in the separation of aggregated particles at the cost of a slightly less clear and defined image. Images obtained using this method were background-subtracted to remove from the image the smooth contribution of the droplet. When the samples were already available as suspensions, the TEM grid was directly dipped in the colloid.

The HRTEM observations were performed in collaboration with the workgroup of Prof. Jawwad Darr, UCL (London, UK). Micrographs were acquired with a JEOL JEM 2100 equipped with a LaB_6 filament and a Gatan Orius digital camera. Samples were dispersed in methanol via ultrasonication. A drop of suspension was than deposited onto a 300-mesh copper film grid (Agar Scientific, Stansted, UK).

The dimensional analysis on the obtained micrographs was performed using ImageJ.[335] For isomorphic particles a spherical approximation was employed. In the case of aggregated particles, a manual segmentation method was employed, while a semi-automated approach was used when particles were sufficiently separated. With the latter method, a suitable thresholding algorithm was applied to convert the greyscale image to a binary one. From the binary image, the automatic particle counter procedure included in ImageJ was employed to identify the projected area of each particle. Dimensional and circularity thresholds were carefully employed to avoid the inclusion of aggregates in the particle detection procedure. From the projected area values obtained, the corresponding equivalent circular diameters were calculated (i.e. the diameter of a circle having the same area of the one measured for a particle projection). From the obtained distribution of equivalent diameters, relevant statistical descriptors were obtained. Histograms obtained from the equivalent diameter populations were fitted to a log-normal distribution using the software Igor Pro.

In the case of anisomorphic particles, a manual measurement was always performed. For squared particles, a rectangular projection was considered to retrieve long and short dimensions of each particles as two dimensional descriptors. Therefore, two distributions were retrieved in this case. For plate-like shapes, a cylindrical approximation was employed, where only the base diameter was obtainable from the images using the maximum Feret diameter value (i.e. the maximum traceable diameter).

8.3 X-ray Photoelectron Spectroscopy (XPS)

XPS measurements were performed with a Perkin–Elmer ϕ 5600ci instrument using Al-K_α radiation (1486.6 eV), operating at 350 W. The working pressure was less than $5 \cdot 10^{-8}$ Pa. The calibration was based on the binding energy (BE) of the Au $4f_{7/2}$ line at 84.0 eV with respect to the Fermi level. The standard deviation for the BE values was 0.15 eV. Reported BEs were corrected for charging effects and the BE value of 284.6 eV was assigned to the C1s line of carbon. Survey scans were obtained in the 0–1350 eV range (pass energy 187.85 eV, 1.0 eV step–1, 25 ms $step^{-1}$). High resolution scans (23.50 eV pass energy, 0.1 eV $step^{-1}$, 150 ms $step^{-1}$) were recorded for relevant regions of the spectra. The semi-quantitative analysis was performed after a Shirley-type background subtraction using sensitivity factors supplied by Perkin–Elmer. Peak assignment was carried out according to literature data. Peak fittings were performed using the software XPSPeak4.1.

8.4 Fourier Transform Infrared Spectroscopy (FTIR)

FTIR experiments were performed with a Nicolet Nexus 870 FTIR equipped with an Attenuated Total Reflectance (ATR) accessory using a diamond ATR crystal. FTIR spectra were acquired in the 4000 – 400 cm^{-1} range, collecting 1024 scans with spectral resolution of 4 cm^{-1}. The background subtraction was performed interpolating the obtained spectra with a cubic spline function implemented in the software Igor Pro.

8.5 Raman Spectroscopy

Raman spectra were collected using a Thermo Scientific DXR Raman micro-Spectrometer equipped with a 532 nm laser and using a 10x LWD. The spectral range was 100 – 3500 cm^{-1}. Alternatively, a 780 nm laser was also employed. The laser power was adjusted to obtain the maximum signal and simultaneously avoid samples photodegradation, when possible.

The analyses of the CH1-CH9 samples series in Chapter 5 were performed in cooperation with the workgroup of Prof. Peter Klar, Justus-Liebig-Universität Gießen – JLU (Gießen, DE). The Raman spectra were obtained at room temperature in a backscattering geometry using a Renishaw In-Via Raman microscope system. The 514 nm line of an Ar-ion laser nm was used for excitation. The excitation light was linearly polarized, but no polarization optics were used for detection. The principal component analysis of the Raman spectra was performed using the corresponding routines of the software package Origin 2018b.

8.6 In-situ Small Angle X-Ray Scattering (SAXS)

The *in-situ* SAXS experiment was performed at the SAXS beamline of the Elettra synchrotron facility in Trieste (Italy), in cooperation with Prof. Heinz Amenitsch and Dr. Barbara Sartori (Graz University of Technology, Austria).

The experimental setup was composed of a thermostated glass reaction vessel, equipped with a stirrer, a thermometer and a circulating flow system. The reaction mixture was circulated though the tubing using a peristaltic pump through a quartz measuring capillary mounted on the SAXS beamline. The total residence time in the flow system was 6 s. A sketch of the realized setup is depicted in Figure 2.7. The X-Ray beam entered the capillary perpendicularly. X-rays extracted from the synchrotron ring were

monochromated at 16 eV and focused with a double toroidal mirror on the measuring quartz capillary. The final reciprocal space window available ranged from 0.1 to 6 nm^{-1}. SAXS profiles were collected with a 10 s time step with 8 s acquisition time. Pure water flowed through the measuring capillary was used as background. The zinc precursor was injected in the reaction vessel at a rate of 2 ml/min while keeping a vigorous stirring to simulate the procedure commonly employed during the synthesis of sample ZnS1. The obtained SAXS profiles where background-subtracted by using the profiles obtained from pure water. The radiation absorption was accounted thank to the transmittance values retrieve by a photodiode mounted on the beamstop of the SAXS detector. The Porod invariant $\tilde{Q}_{inv}$ and the integrated intensities were calculated from the corrected SAXS profiles, as in equation (8.3), where $I(q)$ is the recorded scattering intensity in q.[336]

$$\tilde{Q}_{inv} = \int_0^\infty q^2 I(q)\, dq \tag{8.3}$$

Then, the correlation length $\langle l \rangle$ was obtained as follows.

$$\langle l \rangle = \frac{\pi}{\tilde{Q}_{inv}} \int_0^\infty q\, I(q)\, dq \tag{8.4}$$

From the correlation length, the $D_{4,3}$ average of the NPs was obtained as follows.[120]

$$D_{4,3} = \frac{2}{3}\langle l \rangle \tag{8.5}$$

The mass fractal dimension at every time step was obtained fitting the corresponding linear region in the log-log plot of the SAXS profile.[118] SAXS profiles simulations where obtained using a spherical shape factor[337] and the hard-sphere model for the structure factor.[338]

8.7 Dynamic Light Scattering (DLS) and ζ potential

DLS and ζ potential analyses on NPs suspension were carried out using a Malvern Zetasizer Nano, mounting a He-Ne laser (λ = 633 nm) operated in backscattering mode (175°). Suspensions were thermostated at 20 °C.

8.8 Isothermal Titration Calorimetry (ITC)

The ITC analysis was performed in cooperation with the workgroup of Prof. Yitzhak Mastai, Bar-Ilan University (Ramat Gan, IL). The measurements were performed with a VP-ITC calorimeter (MicroCal Inc., Northampton, MA). ZnS suspensions were titrated via ITC using ammonia, methylamine, pyridine, methanol, and furan water solutions. The measurements were optimized adjusting the sample and the titrant concentration. The typical concentration of a ZnS suspension was between 3.0 and 0.5 mg/ml, while the concentration of the titrants was varied between 5 and 100 mM. The injection heat contribution was measured periodically with water-water titrations and subtracted from the data, while the reference cell was always filled with water. Reference blank titrations on water (using only the titrant solution) were performed prior to every measurement to assess the heat contributions arising from their dilution and from acid-base equilibria. Titrations were performed in overfill mode using a 1.442 ml cell thermostated at 20 °C, while stirring the suspension at 300 rpm. In a typical titration, 28 injection of 10 µl each of the titrant solution were used. Injections were separated by a 300 s interval. The retrieved thermograms were reconstructed using the software NITPIC[339] to remove high and low frequency noise contributions, while all the data plotting and processing was carried out on Igor Pro.

In ITC, the relation between the variation of concentration of a specie after an injection and the enthalpy of interaction is given by the following equation.

$$Q = \sum_{k=1}^{n} \Delta H_k^0 \Delta \mathrm{C_k} V \tag{8.6}$$

Here, Q is the heat evolved after an injection of titrant, ΔH_k^0 is the enthalpy of the k-th contribution to the total heat exchanged, $\Delta \mathrm{C_k}$ is the change of concentration of the k-th specie and V is the cell volume. Since Q is measured, by modelling the variation of concentration $\Delta \mathrm{C_k}$ relative to al the n significative contributions in the measuring volume (the chemical equilibria in the solution or suspension), the ΔH_k^0 values can be obtain by a least-squares minimization routine. Since the fitting requires to model the equilibria in solution, the relative equilibrium constants K_k of each equilibria are also determined, that can be directly converted in the free energy values ΔG_k.

8.9 Photoluminescence (PL)

PL spectra were recorded on powders using a spectrofluorometer JASCO FP8200, in cooperation with the workgroup of Prof. Adolfo Speghini (Università degli Studi di Verona, Verona, Italy).

8.9 Inductively Coupled Plasma – Mass Spectrometry (ICP-MS)

The ICP-MS analyses were performed in cooperation with Prof. Denis Badocco, Università degli Studi di Padova. Samples (50 mg) were placed in a 15 ml digestion vials and digested with 2.5 ml of 69% HNO_3. Vials were heated at 80 °C for 45 min. A PTFE cap was used to minimize sample loss from the vial. Vials were then cooled, and the obtained solutions were diluted to 50 g with milliQ water. All the elements were measured by using inductively coupled plasma coupled to mass spectrometer Agilent Technologies 7700x ICP-MS system (Agilent Technologies International Japan, Ltd., Tokyo, Japan), equipped with an octupole collision cell. The instruments were optimized daily to achieve optimum sensitivity and stability according to manufacturer recommendations. All parameters were checked daily using an in-house optimization program.

8.10 N_2 physisorption measurements

N_2 adsorption/desorption isotherms were recorded at 77 K by using a Micromeritics ASAP 2020 instrument. The specific surface area of the samples was calculated by a multipoint BET analysis.

8.11 Hydrogen Evolution Reaction (HER)

The photocatalytic assessments on ZnS NPs for the hydrogen evolution reaction were performed in cooperation with the workgroup of Prof. Emiel Hensen, Eindhoven University of Technology – TU/e (Eindhoven, NL).

All photocatalytic experiments were performed in a home-built air-tight photocatalytic setup in a side-illuminated PEEK cell. A 500 W Hg (Xe) lamp was used as the light source, and the amount of H_2 produced during the experiments was detected with an online GC-TCD (ShinCarbon column) with N_2 as the carrier gas. The amount of produced H_2 was determined as a function of time to compare the photocatalytic activities among samples. In a typical test, 10 mg photocatalyst was dispersed under

sonication in 50 mL sacrificial agents solution (0.25 M Na_2S and 0.35 M Na_2SO_3) and transferred into the PEEK cell to generate a photocatalyst loading of 0.2 g/l. Before each test, air in the system was removed by evacuation three times. Then the activity measurements were carried out under constant stirring with automated sampling of the gaseous products with 12 min intervals. The temperature of the solution was maintained at 20°C.

8.12 MTS Assay

Preliminary MTS assays for the assessment of NPs cytotoxicity were performed by Prof. Maddalena Mognato (Università degli Studi di Padova, Padova, IT) using human A549 cells (lung adenocarcinoma) purchased from American Type Culture Collection (ATCC n. CCL-185) and cultured in Ham's F12-K Nutrient Mixture (Invitrogen Life Technologies, Carlsbad, CA, USA) supplemented with 10% heat inactivated fetal bovine serum (FBS, BIOCHROM, Berlin, Germany), 38 units/mL streptomycin, and 100 units/mL penicillin G, in T75 cm2 flasks (FALCON). Cells were kept at 37 °C in a humidified atmosphere of 95% air and 5% CO_2. The cells were seeded and maintained for 24 h in complete culture medium before starting the treatment with NPs. Then, cells were incubated for 24 h with increasing concentrations of NPs (0.01–0.1 mg/ml). After incubation with NPs, the medium containing NPs was removed, and the cells were incubated for 60–90 min in the dark with 20 µL of the MTS reagent diluted in 100 µL of serum-free medium. As reference for the MTS assay, group of cells underwent the same steps of treated cells, except for NPs exposure.

Cytotoxicity induced by the samples was evaluated by the MTS assay, which is a colorimetric assay based on the reduction of tetrazolium salts of 3-(4,5-diMethylthiazol-2-yl)-5-(3-carboxymethoxyphenyl)-2-(4-sulfophenyl)-2H to formazan product. The measure of cell viability is based on the intracellular reduction of MTS, which is primarily attributable to mitochondrial dehydrogenases. After the incubation time, the medium containing NPs was removed, and the cells were incubated for 60–90 min in the dark with 20 µL of the MTS reagent diluted in 100 µL of serum-free medium. The absorbance of formazan product was recorded at 490 nm with a microplate reader (Spectramax 190, Molecular Device®). Cell viability was determined by comparing the absorbance values of the treated with NPs with those of untreated cells, that was taken as reference values as 100 %.

8.13 Computational Details

The DFT-based computation of the phonon dispersion and DOS for ZnS sphalerite and wurtzite, in the context of the Raman analysis of the CH1-CH9 samples series in Chapter 5, was performed in cooperation with the workgroup of Prof. Peter Klar, Justus-Liebig-Universität Gießen – JLU (Gießen, DE).

The phonon dispersions and the densities of states of wurtzite and sphalerite ZnS were derived on the basis of density functional theory using a pseudopotential method and a plane-wave expansion. The interatomic force constants (ifcs) were calculated with the code package ABINIT.[340] The local density approximation (LDA) was used for the exchange correlation potential. The Troullier-Martins scheme was employed to represent the pseudopotentials.[296] A perturbation method was used to derive the dynamical matrix on a discrete grid in the 1st Brillouin zone and then the ifcs by a discrete inverse Fourier transformation of the discrete dynamical matrix. With the knowledge of the ifcs the dynamical matrix was derived for the entire Brillouin zone. Similarly, the dielectric permittivity tensor and the Born effective charges were calculated. These are essential for decomposing the ifcs in a long range part which describes the dipole-dipole interaction and a short range part which describes the electronic contribution to the interaction.[341,342] Ground state calculations and cell shape optimization were performed for wurtzite and sphalerite ZnS using a *k*-point sampling of 6 × 6 × 3 and of 6 × 6 × 6, respectively. In both cases, a cutoff energy of 60 Hartree was used for the plane wave expansion. Using these parameters, the lattice constants are converged within 0.1%.

Chapter 9.

Conclusions and perspectives

The aim of this work was to investigate the synthesis of metal sulfides nanostructures prepared using aqueous-based ligands-free methods. The motivation was not only limited to study of a simplified and eco-friendly approach to the synthesis of metal sulfides semiconductors, but also to take advantage of the ligand-free conditions to gain insights on the mechanisms that control the growth of these materials in water solution and study the properties and the oxidation of the exposed surface without the influence of adsorbed ligands.

A very simple batch method was tested with Zn^{2+}, Ni^{2+}, Co^{2+}, Cr^{3+}, Fe^{2+}, Sn^{2+}, Ti^{4+}, Nd^{3+}, Yb^{3+}, Gd^{3+}, Eu^{3+} ions, while simple sulfide salts solutions were used as sulfur precursors. Crystalline compounds free of secondary products were obtained for ZnS, CuS, PbS, MnS and Ag_2S, despite the syntheses were conducted without preliminary degassing steps and were performed at a temperature near 0 °C.

The best results were obtained for ZnS, for which 7.8 and 18 nm NPs having a narrow size distribution (16% and 21% respectively) were obtained using the batch approach by simply changing the sulfide salt used as precursor, and consequently the reaction pH. Thus, a remarkable influence on NPs size of the pH was observed, since lowering the pH from 13.0 to 11.3 resulted in an 230% increase in the retrieved average NPs diameter. An analogous, but less dramatic, pH dependence of the NPs dimensions was observed for CuS nanoplateletes and PbS nanocubes, where the employment of a lower pH also resulted in increased NPs size. In the case of MnS and Ag_2S larger (> 100 nm) and more polydispersed particles were obtained. In the case of MnS, a mixture of the metastable β-MnS or γ-MnS was obtained. Therefore, it is possible to hypothesize that further optimizations of this water-based approach may lead to the obtainment both β-MnS or γ-MnS as a single-phase product.

The surface assessment of the naked NPs was mainly based on XPS and FTIR. ZnS was found to be insensitive to oxidation phenomena at room temperature, while PbS showed clear traces of oxidation only after an extensive period of storage at open-air. The presence of oxidation was mainly visible as the formation of SO_x species, along with the formation of metal oxides for CuS, PbS and MnS. The oxidation phenomena on ZnS was also studied in detail, by performing a size-dependent (7 nm and 21 nm) assessment of the effect of open-air thermal treatments at temperature from 400 °C to 800 °C. A

transition towards ZnO was already observed at 400 °C and was complete at 550 °C. The full conversion to the oxide was preceded by the formation of sulfates and by a partial transition from ZnS sphalerite to ZnS wurtzite in the case of the 7 nm NPS. The formation of ZnO was observed to impair the photocatalytic activity of the hydrogen evolution reaction of the NPs. Overall, ZnS was observed to be stable against oxidation in comparison to the other analyzed metal sulfides, but it is advisable to not heat the material to avoid the formation of oxidation products.

An *in-situ* SAXS analysis was performed for the ligands-free batch synthesis of ZnS, that indicated that a size increase on NPs occurred in the first tenths of seconds of the reaction. This evidence was rationalized as a consequence of the successive additions of the zinc precursor in the reaction mixture. This was confirmed converting the precipitation method from a batch to a microfluidic one. In the latter case, a minimum average size of 4.8 nm was retrieved, that further extended the versatility of the ligand-free coprecipitation approach. The refinement of XRD data revealed that the NPs size was not the only feature that varied using different reaction conditions, as particles showed a stacking fault probability that increased from 0.01 (ZnS2, 18 nm) to ~0.14% (ZnS MF1, 5.1 nm) as a function of the size. This evidence was coherent with the decrease of the energy difference between the ZnS sphalerite and wurtzite polymorphs as NPs size is lowered,[97] possibly leading to the increase of stacking disorder during the growth of the NPs.

Another interesting aspect of the synthetized ZnS NPs was the obtainment of stable water suspensions from the purification stages of the material, despite the absence of stabilizing agents. The suspensions were observed to maintain their stability up to a few weeks, while DLS measurements and the SAXS *in-situ* analysis indicated that fractal aggregates were formed in the suspension. The reason of the colloidal stability was elucidated from the basic pH of the suspension and from the measured z potential value of -41 mV, indicating an electrostatic stabilization. This was attributed to the adsorption of SH- ions on the surface of the NPs. ZnS NPs were also characterized by a very large SSA, reaching the value of almost 300 $m^2 g^{-1}$ in sample ZnS MF1.

The photocatalytic properties of the ZnS NPs were tested, showing that NPs were active for the hydrogen evolution reaction, however without a clear correlation to the retrieved dimensional and structural properties of the NPs could be evidenced. The microfluidic approach was also employed for the syntheses of samples doped with Mn^{2+}, Cu^{2+}, Ni^{2+}, Eu^{3+}, Sm^{3+}, Nd^{3+} and Yb^{3+}. The inclusion of the dopants was clearly seen for Mn-doped NPs, which showed the presence of charge transfer from the ZnS matrix to the Mn^{2+}, resulting in an orange emission at 596 nm upon excitation at 293 nm. Preliminary tests based on the MTS assay also pointed out the low cytotoxicity of the particles, that might become a candidate system for the development of bioimaging applications.

Overall, the low temperature water-based and ligands-free method, either batch or microfluidic, allowed to obtain interesting results, showing an unexpected versatility in terms of size control for the synthesis of ZnS, while encouraging results were also obtained for CuS, PbS, MnS and Ag_2S.

ZnS NPs were also synthetized using the continuous flow hydrothermal synthesis (CHFS). A new setup was developed in order to achieve a good control over the thermal decomposition of thiourea, used as sulfur precursor, and over the reaction temperature. XRD, TEM, HRTEM and Raman analysis showed that highly defective ZnS NPs of ~20 nm were obtained. A hybrid cubic-hexagonal phase was evidenced by the XRD analysis, as a consequence of stacking disorder. The wurtzitic content was linearly dependent on the reaction temperature, as evidenced by the Raman analysis. Since highly defective NPs are an emerging class of materials the field of photocatalysis,[263] the NPs were also tested as photocatalysts. Preliminary results indicated that an increased activity was obtained as a function of the increasing wurzitic content on the samples. Lanthanides-doped ZnS NPs where also synthetized by CHFS, resulting in a good uptake of dopants in the 0.5% – 3% doping level range. The assessment of PL properties indicated the absence of energy transfer from the ZnS matrix to the dopant, but the presence of energy transfer from Nd^{3+} to Yb^{3+} in co-doped Yb,Nd:ZnS samples.

Planar defects were retrieved in the crystal structure of all the synthetized ZnS samples. Remarkably, different methods and conditions led to different defect probabilities. The lowest staking faults probability was estimated at 1% for the ZnS2 sample obtained using the low temperature batch approach. The presence of these defects was then found to be generally increased in smaller NPs obtained both by batch (sample ZnS1) and microfluidic conditions. By using the CHFS approach, the obtained concentration of planar defects in the samples was found to be too high to be estimated with the employed XRD refinement approach. In these latter samples, the possibility to control the structural defectivity by tuning the synthetic conditions was evidenced from both the qualitative analysis of the XRD patterns and the principal component analysis performed on the retrieved Raman spectra. Thus, the employed synthetic approaches for ZnS not only disclosed new possibilities to control the NPs size, but also to control their structural defectivity, which is relevant also for different functional properties (e.g. catalytic ones).

The synergy of different analytical techniques was found to be crucial to precisely identify dimensional, structural and compositional features of the samples, clearly showing the potential of using orthogonal information in the characterization of (nano)materials.

Many new open opportunities were left to explore, ranging from the further optimization of the syntheses (e.g. the isolation of single metastable phases in MnS or a wider exploration of synthesis parameters for the microfluidic synthesis of ZnS), to the development of promising applications (e.g. in-depth studies of the inclusion of dopants in CHFS synthetized ZnS NPs or the clarification of the

effect of stacking faults and other structural features over the ZnS photocatalytic activity), but also for the development of analytical techniques dedicated to colloidal nanocrystals (e.g. the application of ITC to probe interactions at the liquid/solid interface).

Bibliography

(1) Feynman's Talk There's Plenty of Room at the Bottom http://www.zyvex.com/nanotech/feynman.html (accessed Sep 28, 2019).

(2) Taniguchi, N. On the Basic Concept of Nanotechnology. *Proc. Int. Conf. Prod. Eng.* **1974**, 18–23.

(3) Shi, D.; Guo, Z.; Bedford, N. *Nanomaterials and Devices*; William Andrew Publishing: Oxford, 2015.

(4) Alivisatos, A. P. Semiconductor Clusters, Nanocrystals, and Quantum Dots. *Science* **1996**, *271*, 933–937.

(5) Dowling, A.; Clift, R.; Grobert, N.; Hutton, D. *Nanoscience and Nanotechnologies: Opportunities and Uncertainties*; The Royal Society of Chemistry, 2004.

(6) Hu, X.; Li, G.; Yu, J. C. Design, Fabrication, and Modification of Nanostructured Semiconductor Materials for Environmental and Energy Applications. *Langmuir* **2010**, *26*, 3031–3039.

(7) van Embden, J.; Chesman, A. S. R.; Jasieniak, J. J. The Heat-Up Synthesis of Colloidal Nanocrystals. *Chem. Mater.* **2015**, *27*, 2246–2285.

(8) Cozzoli, P. D.; Pellegrino, T.; Manna, L. Synthesis, Properties and Perspectives of Hybrid Nanocrystal Structures. *Chem. Soc. Rev.* **2006**, *35*, 1195.

(9) Weller, H. Colloidal Semiconductor Q-Particles: Chemistry in the Transition Region Between Solid State and Molecules. *Angew. Chemie Int. Ed. English* **1993**, *32*, 41–53.

(10) Kovalenko, M. V.; Manna, L.; Cabot, A.; Hens, Z.; Talapin, D. V.; Kagan, C. R.; Klimov, V. I.; Rogach, A. L.; Reiss, P.; Milliron, D. J.; Guyot-Sionnnest, P.; Konstantatos, G.; Parak, W. J.; Hyeon, T.; Korgel, B. A.; Murray, C. B.; Heiss, W. Prospects of Nanoscience with Nanocrystals. *ACS Nano* **2015**, *9*, 1012–1057.

(11) Kwon, S. G.; Hyeon, T. Formation Mechanisms of Uniform Nanocrystals via Hot-Injection and Heat-Up Methods. *Small* **2011**, *7*, 2685–2702.

(12) Donegá, C. de M. Synthesis and Properties of Colloidal Heteronanocrystals. *Chem. Soc. Rev.*

2011, *40*, 1512–1546.

(13) El-Sayed, M. A. Small Is Different: Shape-, Size-, and Composition-Dependent Properties of Some Colloidal Semiconductor Nanocrystals. *Acc. Chem. Res.* **2004**, *37*, 326–333.

(14) Murray, C. B.; Kagan, C. R.; Bawendi, M. G. Synthesis and Characterization of Monodisperse Nanocrystals and Close-Packed Nanocrystal Assemblies. *Annu. Rev. Mater. Sci.* **2000**, *30*, 545–610.

(15) LaMer, V. K.; Dinegar, R. H. Theory, Production and Mechanism of Formation of Monodispersed Hydrosols. *J. Am. Chem. Soc.* **1950**, *72*, 4847–4854.

(16) Chu, D. B. K.; Owen, J. S.; Peters, B. Nucleation and Growth Kinetics from LaMer Burst Data. *J. Phys. Chem. A* **2017**, *121*, 7511–7517.

(17) Ostwald, W. Studien Über Die Bildung Und Umwandlung Fester Körper. *Zeitschrift für Phys. Chemie* **1897**, *22U*, 289–330.

(18) Lifshitz, I. M.; Slyozov, V. V. The Kinetics of Precipitation from Supersaturated Solid Solutions. *J. Phys. Chem. Solids* **1961**, *19*, 35–50.

(19) Baronov, A.; Bufkin, K.; Shaw, D. W.; Johnson, B. L.; Patrick, D. L. A Simple Model of Burst Nucleation. *Phys. Chem. Chem. Phys.* **2015**, *17*, 20846–20852.

(20) Sun, Y. Controlled Synthesis of Colloidal Silver Nanoparticles in Organic Solutions: Empirical Rules for Nucleation Engineering. *Chem. Soc. Rev.* **2013**, *42*, 2497–2511.

(21) Gebauer, D.; Völkel, A.; Cölfen, H. Stable Prenucleation Calcium Carbonate Clusters. *Science* **2008**, *322*, 1819–1822.

(22) Sugimoto, T.; Sugimoto, T. Control of Particle Characteristics. *Monodispersed Part.* **2001**, 368–452.

(23) Sugimoto, T. Spontaneous Nucleation of Monodisperse Silver Halide Particles from Homogeneous Gelatin Solution I: Silver Chloride. *Colloids Surfaces A Physicochem. Eng. Asp.* **2000**, *164*, 183–203.

(24) Schubert, U.; Hüsing, N. *Synthesis of Inorganic Materials*; Wiley-VCH, 2012.

(25) Wang, J. Nanomaterial-Based Electrochemical Biosensors. *Analyst* **2005**, *130*, 421.

(26) Smet, P. F.; Moreels, I.; Hens, Z.; Poelman, D. Luminescence in Sulfides: A Rich History and a Bright Future. *Materials (Basel).* **2010**, *3*, 2834–2883.

(27) Costa-Fernández, J. M.; Pereiro, R.; Sanz-Medel, A. The Use of Luminescent Quantum Dots for Optical Sensing. *TrAC Trends Anal. Chem.* **2006**, *25*, 207–218.

(28) Wu, P.; Yan, X.-P. Doped Quantum Dots for Chemo/Biosensing and Bioimaging. *Chem. Soc. Rev.* **2013**, *42*, 5489.

(29) Hendricks, M. P.; Campos, M. P.; Cleveland, G. T.; Jen-La Plante, I.; Owen, J. S. A Tunable Library of Substituted Thiourea Precursors to Metal Sulfide Nanocrystals. *Science* **2015**, *348*, 1226–1230.

(30) Hamachi, L. S.; Jen-La Plante, I.; Coryell, A. C.; De Roo, J.; Owen, J. S. Kinetic Control over CdS Nanocrystal Nucleation Using a Library of Thiocarbonates, Thiocarbamates, and Thioureas. *Chem. Mater.* **2017**, *29*, 8711–8719.

(31) Mourdikoudis, S.; Liz-Marzán, L. M. Oleylamine in Nanoparticle Synthesis. *Chem. Mater.* **2013**, *25*, 1465–1476.

(32) Wiles, C.; Watts, P. Continuous-Flow Organic Synthesis: A Tool for the Modern Medicinal Chemist. *Future Med. Chem.* **2009**, *1*, 1593–1612.

(33) Anastas, P.; Eghbali, N. Green Chemistry: Principles and Practice. *Chem. Soc. Rev.* **2010**, *39*, 301–312.

(34) Dengo, N.; De Fazio, A. F.; Weiss, M.; Marschall, R.; Dolcet, P.; Fanetti, M.; Gross, S. Thermal Evolution of ZnS Nanostructures: Effect of Oxidation Phenomena on Structural Features and Photocatalytical Performances. *Inorg. Chem.* **2018**, *57*, 13104–13114.

(35) Boles, M. A.; Ling, D.; Hyeon, T.; Talapin, D. V. The Surface Science of Nanocrystals. *Nat. Mater.* **2016**, *15*, 141–153.

(36) Jing, L.; Kershaw, S. V.; Li, Y.; Huang, X.; Li, Y.; Rogach, A. L.; Gao, M. Aqueous Based Semiconductor Nanocrystals. *Chem. Rev.* **2016**, *116*, 10623–10730.

(37) Parr, R. G.; Pearson, R. G. Absolute Hardness: Companion Parameter to Absolute Electronegativity. *J. Am. Chem. Soc.* **1983**, *105*, 7512–7516.

(38) Pearson, G. Hard and Soft Acids and Bases. *J. Am. Chem. Soc.* **1963**, *85*, 3533–3539.

(39) Tomasulo, M.; Yildiz, I.; Kaanumalle, S. L.; Raymo, F. M. PH-Sensitive Ligand for Luminescent Quantum Dots. *Langmuir* **2006**, *22*, 10284–10290.

(40) Cheng, T.; Li, D.; Li, J.; Ren, B.; Wang, G.; Cheng, J. Aqueous Synthesis of High-Fluorescence ZnTe Quantum Dots. *J. Mater. Sci. Mater. Electron.* **2015**, *26*, 4062–4068.

(41) Xu, S.; Wang, C.; Xu, Q.; Zhang, H.; Li, R.; Shao, H.; Lei, W.; Cui, Y. Key Roles of Solution PH and Ligands in the Synthesis of Aqueous ZnTe Nanoparticles. *Chem. Mater.* **2010**, *22*, 5838–5844.

(42) Myers, R. J. The New Low Value for the Second Dissociation Constant for H_2S: Its History, Its Best Value, and Its Impact on the Teaching of Sulfide Equilibria. *J. Chem. Educ.* **1986**, *63*, 687.

(43) Patnaik, P.; Dean, J. A. *Dean's Analytical Chemistry Handbook*; McGraw-Hill, 2004.

(44) May, P. M.; Batka, D.; Hefter, G.; Königsberger, E.; Rowland, D. Goodbye to S^{2-} in Aqueous Solution. *Chem. Commun.* **2018**, *54*, 1980–1983.

(45) Greenwood, A. N.; Earnshaw, N. *Chimica Degli Elementi*; Piccin: Padova, 1991.

(46) Zhang, H.; Zhou, Z.; Yang, B.; Gao, M. The Influence of Carboxyl Groups on the Photoluminescence of Mercaptocarboxylic Acid-Stabilized CdTe Nanoparticles. *J. Phys. Chem. B* **2003**, *107*, 8–13.

(47) Gao, M.; Kirstein, S.; Möhwald, H.; Rogach, A. L.; Kornowski, A.; Eychmüller, A.; Weller, H. Strongly Photoluminescent CdTe Nanocrystals by Proper Surface Modification. *J. Phys. Chem. B* **1998**, *102*, 8360–8363.

(48) Li, L.; Walda, J.; Manna, L.; Alivisatos, A. P. Semiconductor Nanorod Liquid Crystals. *Nano Lett.* **2002**, *2*, 557–560.

(49) Peng, X.; Wickham, J.; Alivisatos, A. P. Kinetics of II-VI and III-V Colloidal Semiconductor Nanocrystal Growth: "Focusing" of Size Distributions. *J. Am. Chem. Soc.* **1998**, *120*, 5343–5344.

(50) Peng, X.; Manna, L.; Yang, W.; Wickham, J.; Scher, E.; Kadavanich, A.; Alivisatos, A. P. Shape Control of CdSe Nanocrystals. *Nature* **2000**, *404*, 59–61.

(51) Talapin, D. V.; Rogach, A. L.; Haase, M.; Weller, H. Evolution of an Ensemble of Nanoparticles in a Colloidal Solution: Theoretical Study. *J. Phys. Chem. B* **2001**, *105*, 12278–12285.

(52) Xie, R.; Li, Z.; Peng, X. Nucleation Kinetics vs Chemical Kinetics in the Initial Formation of Semiconductor Nanocrystals. *J. Am. Chem. Soc.* **2009**, *131*, 15457–15466.

(53) van Embden, J.; Sader, J. E.; Davidson, M.; Mulvaney, P. Evolution of Colloidal Nanocrystals: Theory and Modeling of Their Nucleation and Growth. *J. Phys. Chem. C* **2009**, *113*, 16342–16355.

(54) Yin, Y.; Alivisatos, A. P. Colloidal Nanocrystal Synthesis and the Organic–Inorganic Interface. *Nature* **2005**, *437*, 664–670.

(55) Talapin, D. V.; Rogach, A. L.; Shevchenko, E. V.; Kornowski, A.; Haase, M.; Weller, H. Dynamic Distribution of Growth Rates within the Ensembles of Colloidal II−VI and III−V Semiconductor Nanocrystals as a Factor Governing Their Photoluminescence Efficiency. *J. Am. Chem. Soc.* **2002**, *124*, 5782–5790.

(56) Whitesides, G. M. The Origins and the Future of Microfluidics. *Nature* **2006**, *442*, 368–373.

(57) Wegner, J.; Ceylan, S.; Kirschning, A. Ten Key Issues in Modern Flow Chemistry. *Chem. Commun.* **2011**, *47*, 4583–4592.

(58) Schmidt, W.; Bussian, P.; Lindén, M.; Amenitsch, H.; Agren, P.; Tiemann, M.; Schüth, F. Accessing Ultrashort Reaction Times in Particle Formation with SAXS Experiments: ZnS Precipitation on the Microsecond Time Scale. *J. Am. Chem. Soc.* **2010**, *132*, 6822–6826.

(59) Weierstall, U. Liquid Sample Delivery Techniques for Serial Femtosecond Crystallography. *Philos. Trans. R. Soc. B Biol. Sci.* **2014**, *369*, 20130337.

(60) Elvira, K. S.; i Solvas, X. C.; Wootton, R. C. R.; DeMello, A. J. The Past, Present and Potential for Microfluidic Reactor Technology in Chemical Synthesis. *Nat. Chem.* **2013**, *5*, 905–915.

(61) Darr, J. A.; Zhang, J.; Makwana, N. M.; Weng, X. Continuous Hydrothermal Synthesis of Inorganic Nanoparticles: Applications and Future Directions. *Chem. Rev.* **2017**, *117*, 11125–11238.

(62) Phillips, T. W.; Lignos, I. G.; Maceiczyk, R. M.; deMello, A. J.; deMello, J. C. Nanocrystal Synthesis in Microfluidic Reactors: Where Next? *Lab Chip* **2014**, *14*, 3172–3180.

(63) Song, Y.; Hormes, J.; Kumar, C. S. S. R. Microfluidic Synthesis of Nanomaterials. *Small* **2008**, *4*, 698–711.

(64) Erdem, E. Y. Microfluidic Reactors for the Controlled Synthesis of Nanoparticles, 2013.

(65) Ward, K.; Fan, Z. H. Mixing in Microfluidic Devices and Enhancement Methods. *J. Micromechanics Microengineering* **2015**, *25*, 094001.

(66) Lee, C. Y.; Chang, C. L.; Wang, Y. N.; Fu, L. M. Microfluidic Mixing: A Review. *Int J Mol Sci* **2011**, *12*, 3263–3287.

(67) Benito-Lopez, F.; Verboom, W.; Kakuta, M.; Gardeniers, J. (Han) G. E.; Egberink, R. J. M.; Oosterbroek, E. R.; van den Berg, A.; Reinhoudt, D. N. Optical Fiber-Based on-Line UV/Vis Spectroscopic Monitoring of Chemical Reaction Kinetics under High Pressure in a Capillary Microreactor. *Chem. Commun.* **2005**, No. 22, 2857.

(68) Ferstl, W.; Klahn, T.; Schweikert, W.; Billeb, G.; Schwarzer, M.; Loebbecke, S. Inline Analysis in Microreaction Technology: A Suitable Tool for Process Screening and Optimization. *Chem. Eng. Technol.* **2007**, *30*, 370–378.

(69) Carter, C. F.; Lange, H.; Ley, S. V.; Baxendale, I. R.; Wittkamp, B.; Goode, J. G.; Gaunt, N. L. ReactIR Flow Cell: A New Analytical Tool for Continuous Flow Chemical Processing. *Org. Process Res. Dev.* **2010**, *14*, 393–404.

(70) Mozharov, S.; Nordon, A.; Littlejohn, D.; Wiles, C.; Watts, P.; Dallin, P.; Girkin, J. M. Improved Method for Kinetic Studies in Microreactors Using Flow Manipulation and Noninvasive Raman Spectrometry. *J. Am. Chem. Soc.* **2011**, *133*, 3601–3608.

(71) Sans, V.; Porwol, L.; Dragone, V.; Cronin, L. A Self Optimizing Synthetic Organic Reactor System Using Real-Time in-Line NMR Spectroscopy. *Chem. Sci.* **2015**, *6*, 1258–1264.

(72) Lignos, I.; Stavrakis, S.; Kilaj, A.; deMello, A. J. Millisecond-Timescale Monitoring of PbS Nanoparticle Nucleation and Growth Using Droplet-Based Microfluidics. *Small* **2015**, *11*, 4009–4017.

(73) Edel, J. B.; Fortt, R.; deMello, J. C.; deMello, A. J. Microfluidic Routes to the Controlled Production of Nanoparticles. *Chem. Commun.* **2002**, No. 10, 1136–1137.

(74) Yang, H.; Fan, N.; Luan, W.; Tu, S. Synthesis of Monodisperse Nanocrystals via Microreaction: Open-to-Air Synthesis with Oleylamine as a Coligand. *Nanoscale Res. Lett.* **2009**, *4*, 344–352.

(75) Fernández, D. P.; Mulev, Y.; Goodwin, A. R. H.; Sengers, J. M. H. L. A Database for the Static Dielectric Constant of Water and Steam. *J. Phys. Chem. Ref. Data* **1995**, *24*, 33–70.

(76) Chaudhry, A. A.; Knowles, J. C.; Rehman, I.; Darr, J. A. Rapid Hydrothermal Flow Synthesis and Characterisation of Carbonate- and Silicate-Substituted Calcium Phosphates. *J. Biomater. Appl.* **2013**, *28*, 448–461.

(77) Gruar, R. I.; Tighe, C. J.; Darr, J. A. Scaling-up a Confined Jet Reactor for the Continuous Hydrothermal Manufacture of Nanomaterials. *Ind. Eng. Chem. Res.* **2013**, *52*, 5270–5281.

(78) Dunne, P. W.; Starkey, C. L.; Gimeno-Fabra, M.; Lester, E. H.; Wang, X.; Qian, Y.; Calvino-Gámez, J. J.; González-Calbet, J. M.; Green, P. F.; Kotov, N. A. The Rapid Size- and Shape-Controlled Continuous Hydrothermal Synthesis of Metal Sulphide Nanomaterials. *Nanoscale* **2014**, *6*, 2406–2418.

(79) Chaudhry, A. A.; Haque, S.; Kellici, S.; Boldrin, P.; Rehman, I.; Khalid, F. A.; Darr, J. A. Instant Nano-Hydroxyapatite: A Continuous and Rapid Hydrothermal Synthesis. *Chem. Commun.*

2006, No. 21, 2286.

(80) Wang, Z. D.; Yoshida, M.; George, B. Theoretical Study on the Thermal Decomposition of Thiourea. *Comput. Theor. Chem.* **2013**, *1017*, 91–98.

(81) Conde, J.; Dias, J. T.; GrazÃº, V.; Moros, M.; Baptista, P. V; de la Fuente, J. M. Revisiting 30 Years of Biofunctionalization and Surface Chemistry of Inorganic Nanoparticles for Nanomedicine. *Front. Chem.* **2014**, *2*.

(82) Sapsford, K. E.; Algar, W. R.; Berti, L.; Gemmill, K. B.; Casey, B. J.; Oh, E.; Stewart, M. H.; Medintz, I. L. Functionalizing Nanoparticles with Biological Molecules: Developing Chemistries That Facilitate Nanotechnology. *Chem. Rev.* **2013**, *113*, 1904–2074.

(83) Ullah, M. H.; Kim, I.; Ha, C.-S. pH Selective Synthesis of ZnS Nanocrystals and Their Growth and Photoluminescence. *Mater. Lett.* **2007**, *61*, 4267–4271.

(84) Lutterotti, L. Total Pattern Fitting for the Combined Size-Strain-Stress-Texture Determination in Thin Film Diffraction. *Nucl. Instruments Methods Phys. Res. Sect. B* **2010**, *268*, 334–340.

(85) Balzar, D.; Popa, N. C. Crystallite Size and Residual Strain/Stress Modeling in Rietveld Refinement. In *Diffraction Analysis of the Microstructure of Materials*; 2004; pp 125–145.

(86) Skinner, B. J. Unit-Cell Edges of Natural and Synthetic Sphalerites. *Am. Mineral.* **1961**, *46*, 1399–1411.

(87) Zhang, H.; Chen, B.; Gilbert, B.; Banfield, J. F. Kinetically Controlled Formation of a Novel Nanoparticulate ZnS with Mixed Cubic and Hexagonal Stacking. *J. Mater. Chem.* **2006**, *16*, 249–254.

(88) Yan, J.; Wang, Z.; Zhang, L. Effect of Stacking Fault on the Formation of the Saw-Teeth of ZnS Nanosaws. *Cryst. Growth Des.* **2008**, *8*, 1723–1726.

(89) Warren, B. E. X-Ray Measurement of Stacking Fault Widths in Fcc Metals. *J. Appl. Phys.* **1961**, *32*, 2428–2431.

(90) Toby, B. H. R Factors in Rietveld Analysis: How Good Is Good Enough? *Powder Diffr.* **2006**, *21*, 67–70.

(91) Corrado, C.; Jiang, Y.; Oba, F.; Kozina, M.; Bridges, F.; Zhang, J. Z. Synthesis, Structural, and Optical Properties of Stable ZnS:Cu,Cl Nanocrystals. *J. Phys. Chem. A* **2009**, *113*, 3830–3839.

(92) Lu, S. W.; Lee, B. I.; Wang, Z. L.; Tong, W.; Wagner, B. K.; Park, W.; Summers, C. J. Synthesis and Photoluminescence Enhancement of Mn2+-Doped ZnS Nanocrystals. *J. Lumin.* **2000**, *92*,

73–78.

(93) Ghosh, G.; Kanti Naskar, M.; Patra, A.; Chatterjee, M. Synthesis and Characterization of PVP-Encapsulated ZnS Nanoparticles. *Opt. Mater. (Amst).* **2006**, *28*, 1047–1053.

(94) Ma, Y.; Qi, L.; Ma, J.; Cheng, H. Facile Synthesis of Hollow ZnS Nanospheres in Block Copolymer Solutions. *Langmuir* **2003**, *19*, 4040–4042.

(95) Suyver, J. F.; Wuister, S. F.; Kelly, J. J.; Meijerink, A. Synthesis and Photoluminescence of Nanocrystalline ZnS:Mn 2+. *Nano Lett.* **2001**, *1*, 429–433.

(96) Khalkhali, M.; Liu, Q.; Zeng, H.; Zhang, H. A Size-Dependent Structural Evolution of ZnS Nanoparticles. *Sci. Rep.* **2015**, *5*, 14267.

(97) Qadri, S. B.; Skelton, E. F.; Hsu, D.; Dinsmore, A. D.; Yang, J.; Gray, H. F.; Ratna, B. R.; Matter, C.; Physics, M.; Reports, B. Size-Induced Transition-Temperature Reduction in Nanoparticles of ZnS. *Phys. Rev. B* **1999**, *60*, 9191–9193.

(98) Sperling, R. A.; Parak, W. J. Surface Modification, Functionalization and Bioconjugation of Colloidal Inorganic Nanoparticles. *Philos. Trans. R. Soc. A Math. Phys. Eng. Sci.* **2010**, *368*, 1333–1383.

(99) NIST X-ray Photoelectron Spectroscopy Database, Version 4.1 http://srdata.nist.gov/xps/.

(100) Barr, T. L.; Seal, S. Nature of the Use of Adventitious Carbon as a Binding Energy Standard. *J. Vac. Sci. Technol. A* **1995**, *13*, 1239–1246.

(101) Wang, X.; Shi, J.; Feng, Z.; Li, M.; Li, C. Visible Emission Characteristics from Different Defects of ZnS Nanocrystals. *Phys. Chem. Chem. Phys.* **2011**, *13*, 4715–4723.

(102) De Fazio, A. F.; Morgese, G.; Mognato, M.; Piotto, C.; Pedron, D.; Ischia, G.; Causin, V.; Rosenboom, J.-G.; Benetti, E. M.; Gross, S. Robust and Biocompatible Functionalization of ZnS Nanoparticles by Catechol-Bearing Poly(2-Methyl-2-Oxazoline)S. *Langmuir* **2018**, *34*, 11534–11543.

(103) Dengo, N.; Vittadini, A.; Natile, M. M.; Gross, S. In-Depth Study of ZnS Nanoparticles Surface Properties with a Combined Experimental and Theoretical Approach. *Submitted*.

(104) Nakamoto, K. *Infrared and Raman Spectra of Inorganic and Coordination Compounds, Part A, Theory and Applications in Inorganic Chemistry, 6th Edition*; John Wiley & Sons, 2009.

(105) Hug, S. J. In Situ Fourier Transform Infrared Measurements of Sulfate Adsorption on Hematite in Aqueous Solutions. *J. Colloid Interface Sci.* **1997**, *188*, 415–422.

(106) Peak, D.; Ford, R.; Sparks, D. An in Situ ATR-FTIR Investigation of Sulfate Bonding Mechanisms on Goethite. *J. Colloid Interface Sci.* **1999**, *218*, 289–299.

(107) Busca, G.; Lorenzelli, V. Infrared Spectroscopic Identification of Species Arising from Reactive Adsorption of Carbon Oxides on Metal Oxide Surfaces. *Mater. Chem.* **1982**, *7*, 89–126.

(108) Busca, G. Bases and Basic Materials in Chemical and Environmental Processes. Liquid versus Solid Basicity. *Chem. Rev.* **2010**, *110*, 2217–2249.

(109) Cheng, Y. C.; Jin, C. Q.; Gao, F.; Wu, X. L.; Zhong, W.; Li, S. H.; Chu, P. K. Raman Scattering Study of Zinc Blende and Wurtzite ZnS. *J. Appl. Phys.* **2009**, *106*, 123505–123510.

(110) Karar, N.; Singh, F.; Mehta, B. R. Structure and Photoluminescence Studies on ZnS:Mn Nanoparticles. *J. Appl. Phys.* **2004**, *95*, 656–660.

(111) Luo, Y. Y.; Duan, G. T.; Li, G. H. Resonant Raman Scattering and Surface Phonon Modes of Hollow ZnS Microspheres. *Appl. Phys. Lett.* **2007**, *90*, 201911.

(112) Nilsen, W. G. Raman Spectrum of Cubic ZnS. *Phys. Rev.* **1969**, *182*, 838–850.

(113) Yoshioka, A.; Nagata, K. Raman Spectrum of Sulfur under High Pressure. *J. Phys. Chem. Solids* **1995**, *56*, 581–584.

(114) Li, T.; Senesi, A. J.; Lee, B. Small Angle X-Ray Scattering for Nanoparticle Research. *Chem. Rev.* **2016**, *116*, 11128–11180.

(115) Polizzi, S.; Spinozzi, F. Small Angle X-Ray Scattering (SAXS) with Synchrotron Radiation Sources. In *Synchrotron Radiation*; Springer Berlin Heidelberg: Berlin, Heidelberg, 2015; pp 337–359.

(116) Mandelbrot, B. B.; Wheeler, J. A. The Fractal Geometry of Nature. *Am. J. Phys.* **1983**, *51*, 286–287.

(117) Reich, M. .; Russo, S. .; Snook, I. .; Wagenfeld, H. . The Application of SAXS to Determine the Fractal Properties of Porous Carbon-Based Materials. *J. Colloid Interface Sci.* **1990**, *135*, 353–362.

(118) Anitas, E. M. Small-Angle Scattering from Mass and Surface Fractals. In *Complexity in Biological and Physical Systems - Bifurcations, Solitons and Fractals*; InTech, 2018.

(119) Boldon, L.; Laliberte, F.; Liu, L. Review of the Fundamental Theories behind Small Angle X-Ray Scattering, Molecular Dynamics Simulations, and Relevant Integrated Application. *Nano Rev.* **2015**, *6*, 25661.

(120) Paradies, H. H. Particle Size Distribution and Determination of Characteristic Properties of Colloidal Bismuth—Silica Compounds by Small-Angle X-Ray Scattering and Inelastic Light Scattering. *Colloids Surfaces A Physicochem. Eng. Asp.* **1993**, *74*, 57–69.

(121) Segets, D.; Komada, S.; Butz, B.; Spiecker, E.; Mori, Y.; Peukert, W. Quantitative Evaluation of Size Selective Precipitation of Mn-Doped ZnS Quantum Dots by Size Distributions Calculated from UV/Vis Absorbance Spectra. *J. Nanoparticle Res.* **2013**, *15*, 1486.

(122) Jiang, J.; Oberdörster, G.; Biswas, P. Characterization of Size, Surface Charge, and Agglomeration State of Nanoparticle Dispersions for Toxicological Studies. *J. Nanoparticle Res.* **2009**, *11*, 77–89.

(123) Thordarson, P. Determining Association Constants from Titration Experiments in Supramolecular Chemistry. *Chem. Soc. Rev.* **2011**, *40*, 1305–1323.

(124) Chakraborty, S.; Joshi, P.; Shanker, V.; Ansari, Z. A.; Singh, S. P.; Chakrabarti, P. Contrasting Effect of Gold Nanoparticles and Nanorods with Different Surface Modifications on the Structure and Activity of Bovine Serum Albumin. *Langmuir* **2011**, *27*, 7722–7731.

(125) Chakraborti, S.; Joshi, P.; Chakravarty, D.; Shanker, V.; Ansari, Z. A.; Singh, S. P.; Chakrabarti, P. Interaction of Polyethyleneimine-Functionalized ZnO Nanoparticles with Bovine Serum Albumin. *Langmuir* **2012**, *28*, 11142–11152.

(126) Joshi, H.; Shirude, P. S.; Bansal, V.; Ganesh, K. N.; Sastry, M. Isothermal Titration Calorimetry Studies on the Binding of Amino Acids to Gold Nanoparticles. *J. Phys. Chem. B* **2004**, *108*, 11535–11540.

(127) Bekdemir, A.; Liao, S.; Stellacci, F. On the Effect of Ligand Shell Heterogeneity on Nanoparticle/Protein Binding Thermodynamics. *Colloids Surfaces B Biointerfaces* **2019**, *174*, 367–373.

(128) Lin, W.; Schmidt, J.; Mahler, M.; Schindler, T.; Unruh, T.; Meyer, B.; Peukert, W.; Segets, D. Influence of Tail Groups during Functionalization of ZnO Nanoparticles on Binding Enthalpies and Photoluminescence. *Langmuir* **2017**, *33*, 13581–13589.

(129) Shval, A.; Mastai, Y. Isothermal Titration Calorimetry as a New Tool to Investigate Chiral Interactions at Crystal Surfaces. *Chem. Commun.* **2011**, *47*, 5735.

(130) Fedin, I.; Talapin, D. V. Probing the Surface of Colloidal Nanomaterials with Potentiometry *in Situ*. *J. Am. Chem. Soc.* **2014**, *136*, 11228–11231.

(131) Parfitt, G. D.; Rochester, C. H. *Adsorption from Solution at the Solid/Liquid Interface*; Academic

Press, 1983.

(132) Lombardo, S.; Thielemans, W. Thermodynamics of Adsorption on Nanocellulose Surfaces. *Cellulose* **2019**, *26*, 249–279.

(133) Giles, C. H.; Smith, D.; Huitson, A. A General Treatment and Classification of the Solute Adsorption Isotherm. I. Theoretical. *J. Colloid Interface Sci.* **1974**, *47*, 755–765.

(134) Li, Z.; Ma, J.; Zong, Y.; Men, Y. ZnS Nanoparticles for High-Sensitive Fluorescent Detection of Pyridine Compounds. *J. Alloys Compd.* **2013**, *559*, 39–44.

(135) Sun, S.; Li, P.; Liang, S.; Yang, Z. Diversified Copper Sulfide ($Cu_{2-x}S$) Micro-/Nanostructures: A Comprehensive Review on Synthesis, Modifications and Applications. *Nanoscale* **2017**, *9*, 11357–11404.

(136) Morgese, G.; Dolcet, P.; Feis, A.; Gellini, C.; Gialanella, S.; Speghini, A.; Badocco, D.; Pastore, P.; Casarin, M.; Gross, S. Room-Temperature Crystallization of CuS Nanostructures for Photothermal Applications through a Nanoreactor Approach. *Eur. J. Inorg. Chem.* **2017**, *2017*, 2745–2754.

(137) Goel, S.; Chen, F.; Cai, W. Synthesis and Biomedical Applications of Copper Sulfide Nanoparticles: From Sensors to Theranostics. *Small* **2014**, *10*, 631–645.

(138) Li, Y.; Lu, W.; Huang, Q.; Li, C.; Chen, W. Copper Sulfide Nanoparticles for Photothermal Ablation of Tumor Cells. *Nanomedicine* **2010**, *5*, 1161–1171.

(139) Roy, P.; Srivastava, S. K. Nanostructured Copper Sulfides: Synthesis, Properties and Applications. *CrystEngComm* **2015**, *17*, 7801–7815.

(140) Ku, G.; Zhou, M.; Song, S.; Huang, Q.; Hazle, J.; Li, C. Copper Sulfide Nanoparticles As a New Class of Photoacoustic Contrast Agent for Deep Tissue Imaging at 1064 Nm. *ACS Nano* **2012**, *6*, 7489–7496.

(141) Lai, C.-H.; Huang, K.-W.; Cheng, J.-H.; Lee, C.-Y.; Hwang, B.-J.; Chen, L.-J. Direct Growth of High-Rate Capability and High Capacity Copper Sulfide Nanowire Array Cathodes for Lithium-Ion Batteries. *J. Mater. Chem.* **2010**, *20*, 6638.

(142) Tseng, Y.-H.; He, Y.; Que, L. Ultrasensitive Thin Film Infrared Sensors Enabled by Hybrid Nanomaterials. *Analyst* **2013**, *138*, 3053.

(143) Dutta, A. K.; Das, S.; Samanta, S.; Samanta, P. K.; Adhikary, B.; Biswas, P. CuS Nanoparticles as a Mimic Peroxidase for Colorimetric Estimation of Human Blood Glucose Level. *Talanta* **2013**,

107, 361–367.

(144) Lu, Q.; Gao, F.; Zhao, D. One-Step Synthesis and Assembly of Copper Sulfide Nanoparticles to Nanowires, Nanotubes, and Nanovesicles by a Simple Organic Amine-Assisted Hydrothermal Process. *Nano Lett.* **2002**, *2*, 725–728.

(145) Han, W.; Yi, L.; Zhao, N.; Tang, A.; Gao, M.; Tang, Z. Synthesis and Shape-Tailoring of Copper Sulfide/Indium Sulfide-Based Nanocrystals. *J. Am. Chem. Soc.* **2008**, *130*, 13152–13161.

(146) Yi, L.; Tang, A.; Niu, M.; Han, W.; Hou, Y.; Gao, M. Synthesis and Self-Assembly of Cu1.94S–ZnS Heterostructured Nanorods. *CrystEngComm* **2010**, *12*, 4124.

(147) Kristl, M.; Hojnik, N.; Gyergyek, S.; Drofenik, M. Sonochemical Preparation of Copper Sulfides with Different Phases in Aqueous Solutions. *Mater. Res. Bull.* **2013**, *48*, 1184–1188.

(148) Zhang, X.; Wang, G.; Gu, A.; Wei, Y.; Fang, B. CuS Nanotubes for Ultrasensitive Nonenzymatic Glucose Sensors. *Chem. Commun.* **2008**, No. 45, 5945.

(149) Gao, L.; Wang, E.; Lian, S.; Kang, Z.; Lan, Y.; Wu, D. Microemulsion-Directed Synthesis of Different CuS Nanocrystals. *Solid State Commun.* **2004**, *130*, 309–312.

(150) Solanki, J. N.; Sengupta, R.; Murthy, Z. V. P. Synthesis of Copper Sulphide and Copper Nanoparticles with Microemulsion Method. *Solid State Sci.* **2010**, *12*, 1560–1566.

(151) Morgese, G.; Dolcet, P.; Feis, A.; Gellini, C.; Gialanella, S.; Speghini, A.; Badocco, D.; Pastore, P.; Casarin, M.; Gross, S. Room-Temperature Crystallization of CuS Nanostructures for Photothermal Applications through a Nanoreactor Approach. *Eur. J. Inorg. Chem.* **2017**, *2017*, 2745–2754.

(152) Di Benedetto, F.; Borgheresi, M.; Caneschi, A.; Chastanet, G.; Cipriani, C.; Gatteschi, D.; Pratesi, G.; Romanelli, M.; Sessoli, R. First Evidence of Natural Superconductivity: Covellite. *Eur. J. Mineral.* **2006**, *18*, 283–287.

(153) Liang, W.; Whangbo, M.-H. Conductivity Anisotropy and Structural Phase Transition in Covellite CuS. *Solid State Commun.* **1993**, *85*, 405–408.

(154) Popa, N. C. The (Hkl) Dependence of Diffraction-Line Broadening Caused by Strain and Size for All Laue Groups in Rietveld Refinement. *J. Appl. Crystallogr.* **1998**, *31*, 176–180.

(155) Ratanatawanate, C.; Bui, A.; Vu, K.; Balkus, K. J. Low-Temperature Synthesis of Copper(II) Sulfide Quantum Dot Decorated TiO_2 Nanotubes and Their Photocatalytic Properties. *J. Phys. Chem. C* **2011**, *115*, 6175–6180.

(156) Todd, E. .; Sherman, D. .; Purton, J. . Surface Oxidation of Chalcopyrite (CuFeS2) under Ambient Atmospheric and Aqueous (PH 2-10) Conditions: Cu, Fe L- and O K-Edge X-Ray Spectroscopy. *Geochim. Cosmochim. Acta* **2003**, *67*, 2137–2146.

(157) Luther, G. W.; Theberge, S. M.; Rozan, T. F.; Rickard, D.; Rowlands, C. C.; Oldroyd, A. Aqueous Copper Sulfide Clusters as Intermediates during Copper Sulfide Formation. *Environ. Sci. Technol.* **2002**, *36*, 394–402.

(158) Folmer, J. C. .; Jellinek, F. The Valence of Copper in Sulphides and Selenides: An X-Ray Photoelectron Spectroscopy Study. *J. Less Common Met.* **1980**, *76*, 153–162.

(159) Goh, S. W.; Buckley, A. N.; Lamb, R. N. Copper(II) Sulfide? *Miner. Eng.* **2006**, *19*, 204–208.

(160) Fjellvåg, H.; Grønvold, F.; Stølen, S.; Andresen, A. F.; Müller-Käfer, R.; Simon, A. Low-Temperature Structural Distortion in CuS. *Zeitschrift für Krist.* **1988**, *184*, 111–121.

(161) Kumar, P.; Nagarajan, R.; Sarangi, R. Quantitative X-Ray Absorption and Emission Spectroscopies: Electronic Structure Elucidation of Cu2S and CuS. *J. Mater. Chem. C* **2013**, *1*, 2448.

(162) Morales-García, A.; Soares, A. L.; Dos Santos, E. C.; de Abreu, H. A.; Duarte, H. A. First-Principles Calculations and Electron Density Topological Analysis of Covellite (CuS). *J. Phys. Chem. A* **2014**, *118*, 5823–5831.

(163) Gainov, R. R.; Dooglav, A. V.; Pen'kov, I. N.; Mukhamedshin, I. R.; Mozgova, N. N.; Evlampiev, I. A.; Bryzgalov, I. A. Phase Transition and Anomalous Electronic Behavior in the Layered Superconductor CuS Probed by NQR. *Phys. Rev. B* **2009**, *79*, 075115.

(164) Cabrera-German, D.; García-Valenzuela, J. A.; Martínez-Gil, M.; Suárez-Campos, G.; Montiel-González, Z.; Sotelo-Lerma, M.; Cota-Leal, M. Assessing the Chemical State of Chemically Deposited Copper Sulfide: A Quantitative Analysis of the X-Ray Photoelectron Spectra of the Amorphous-to-Covellite Transition Phases. *Appl. Surf. Sci.* **2019**, *481*, 281–295.

(165) Biesinger, M. C. Advanced Analysis of Copper X-Ray Photoelectron Spectra. *Surf. Interface Anal.* **2017**, *49*, 1325–1334.

(166) *Core-Level Spectroscopy in Condensed Systems*; Kanamori, J., Kotani, A., Eds.; Springer Series in Solid-State Sciences; Springer Berlin Heidelberg: Berlin, Heidelberg, 1988; Vol. 81.

(167) Folmer, J. C. W.; Jellinek, F.; Calis, G. H. M. The Electronic Structure of Pyrites, Particularly CuS2 and Fe1−xCuxSe2: An XPS and Mössbauer Study. *J. Solid State Chem.* **1988**, *72*, 137–144.

(168) Sacher, E. Asymmetries in Transition Metal XPS Spectra: Metal Nanoparticle Structure, and Interaction with the Graphene-Structured Substrate Surface. *Langmuir* **2010**, *26*, 3807–3814.

(169) Pratt, A. .; Muir, I. .; Nesbitt, H. . X-Ray Photoelectron and Auger Electron Spectroscopic Studies of Pyrrhotite and Mechanism of Air Oxidation. *Geochim. Cosmochim. Acta* **1994**, *58*, 827–841.

(170) Dunn, J. .; Muzenda, C. Thermal Oxidation of Covellite (CuS). *Thermochim. Acta* **2001**, *369*, 117–123.

(171) Tarachand, T.; Hussain, S.; Lalla, N. P.; Kuo, Y.-K.; Lakhani, A.; Sathe, V. G.; Deshpande, U.; Okram, G. S. Thermoelectric Properties of Ag-Doped CuS Nanocomposites Synthesized by a Facile Polyol Method. *Phys. Chem. Chem. Phys.* **2018**, *20*, 5926–5935.

(172) Banyai, L.; Hu, Y. Z.; Lindberg, M.; Koch, S. W. Third-Order Optical Nonlinearities in Semiconductor Microstructures. *Phys. Rev. B* **1988**, *38*, 8142–8153.

(173) Akhtar, J.; Azad Malik, M.; O'Brien, P.; Wijayantha, K. G. U.; Dharmadasa, R.; Hardman, S. J. O.; Graham, D. M.; Spencer, B. F.; Stubbs, S. K.; Flavell, W. R.; Binks, D. J.; Sirotti, F.; El Kazzi, M.; Silly, M. A Greener Route to Photoelectrochemically Active PbS Nanoparticles. *J. Mater. Chem.* **2010**, *20*, 2336.

(174) Cao, H.; Wang, G.; Zhang, S.; Zhang, X. Growth and Photoluminescence Properties of PbS Nanocubes. *Nanotechnology* **2006**, *17*, 3280–3287.

(175) Zhao, N.; Osedach, T. P.; Chang, L.-Y.; Geyer, S. M.; Wanger, D.; Binda, M. T.; Arango, A. C.; Bawendi, M. G.; Bulovic, V. Colloidal PbS Quantum Dot Solar Cells with High Fill Factor. *ACS Nano* **2010**, *4*, 3743–3752.

(176) Nozik, A. J. Nanoscience and Nanostructures for Photovoltaics and Solar Fuels. *Nano Lett.* **2010**, *10*, 2735–2741.

(177) Pattantyus-Abraham, A. G.; Kramer, I. J.; Barkhouse, A. R.; Wang, X.; Konstantatos, G.; Debnath, R.; Levina, L.; Raabe, I.; Nazeeruddin, M. K.; Grätzel, M.; Sargent, E. H. Depleted-Heterojunction Colloidal Quantum Dot Solar Cells. *ACS Nano* **2010**, *4*, 3374–3380.

(178) Nair, G.; Geyer, S. M.; Chang, L.-Y.; Bawendi, M. G. Carrier Multiplication Yields in PbS and PbSe Nanocrystals Measured by Transient Photoluminescence. *Phys. Rev. B* **2008**, *78*, 125325.

(179) Ellingson, R. J.; Beard, M. C.; Johnson, J. C.; Yu, P.; Micic, O. I.; Nozik, A. J.; Shabaev, A.; Efros, A. L. Highly Efficient Multiple Exciton Generation in Colloidal PbSe and PbS Quantum Dots. *Nano Lett.* **2005**, *5*, 865–871.

(180) Hardman, S. J. O.; Graham, D. M.; Stubbs, S. K.; Spencer, B. F.; Seddon, E. A.; Fung, H.-T.; Gardonio, S.; Sirotti, F.; Silly, M. G.; Akhtar, J.; O'Brien, P.; Binks, D. J.; Flavell, W. R. Electronic and Surface Properties of PbS Nanoparticles Exhibiting Efficient Multiple Exciton Generation. *Phys. Chem. Chem. Phys.* **2011**, *13*, 20275.

(181) Cant, D. J. H.; Syres, K. L.; Lunt, P. J. B.; Radtke, H.; Treacy, J.; Thomas, P. J.; Lewis, E. A.; Haigh, S. J.; O'Brien, P.; Schulte, K.; Bondino, F.; Magnano, E.; Flavell, W. R. Surface Properties of Nanocrystalline PbS Films Deposited at the Water–Oil Interface: A Study of Atmospheric Aging. *Langmuir* **2015**, *31*, 1445–1453.

(182) Sykora, M.; Koposov, A. Y.; McGuire, J. A.; Schulze, R. K.; Tretiak, O.; Pietryga, J. M.; Klimov, V. I. Effect of Air Exposure on Surface Properties, Electronic Structure, and Carrier Relaxation in PbSe Nanocrystals. *ACS Nano* **2010**, *4*, 2021–2034.

(183) Jiao, Y.; Gao, X.; Lu, J.; Chen, Y.; Zhou, J.; Li, X. A Novel Method for PbS Quantum Dot Synthesis. *Mater. Lett.* **2012**, *72*, 116–118.

(184) Chakraborty, I.; Moulik, S. P. On PbS Nanoparticles Formed in the Compartments of Water/AOT/n-Heptane Microemulsion. *J. Nanoparticle Res.* **2005**, *7*, 237–247.

(185) Sadovnikov, S. I.; Kuznetsova, Y. V.; Rempel, A. A. Synthesis of a Stable Colloidal Solution of PbS Nanoparticles. *Inorg. Mater.* **2014**, *50*, 969–975.

(186) Gaiduk, A. P.; Gaiduk, P. I.; Larsen, A. N. Chemical Bath Deposition of PbS Nanocrystals: Effect of Substrate. *Thin Solid Films* **2008**, *516*, 3791–3795.

(187) Hampton, M. A.; Plackowski, C.; Nguyen, A. V. Physical and Chemical Analysis of Elemental Sulfur Formation during Galena Surface Oxidation. *Langmuir* **2011**, *27*, 4190–4201.

(188) Nowak, P.; Laajalehto, K. Oxidation of Galena Surface – an XPS Study of the Formation of Sulfoxy Species. *Appl. Surf. Sci.* **2000**, *157*, 101–111.

(189) Buckley, A. N.; Woods, R. An X-Ray Photoelectron Spectroscopic Study of the Oxidation of Galena. *Appl. Surf. Sci.* **1984**, *17*, 401–414.

(190) Beygi, H.; Sajjadi, S. A.; Babakhani, A.; Young, J. F.; van Veggel, F. C. J. M. Surface Chemistry of As-Synthesized and Air-Oxidized PbS Quantum Dots. *Appl. Surf. Sci.* **2018**, *457*, 1–10.

(191) Ramis, G.; Busca, G.; Lorenzelli, V. Low-Temperature CO_2 Adsorption on Metal Oxides: Spectroscopic Characterization of Some Weakly Adsorbed Species. *Mater. Chem. Phys.* **1991**, *29*, 425–435.

(192) Siriwardane, R. V.; Woodruff, S. In Situ Fourier Transform Infrared Characterization of Sulfur Species Resulting from the Reaction of Water Vapor and Oxygen with Zinc Sulfide. *Ind. Eng. Chem. Res.* **1997**, *36*, 5277–5281.

(193) Lutz, H. D.; El-Suradi, S. M.; Engelen, B. Zur Kenntnis Der Sulfite Und Sulfithydrate Des Zinks, Mangans, Magnesiums Und Cobalts — Röntgenographische, Spektroskopische Und Thermoanalytische Untersuchungen / Sulfites and Sulfite Hydrates of Zinc, Manganese, Magnesium and Cobalt-X-Ray, Spectroscopic and Thermoanalytical Data. *Zeitschrift für Naturforsch. B* **1977**, *32*, 1230–1238.

(194) Hertl, W. Surface Chemical Properties of Zinc Sulfide. *Langmuir* **1988**, *4*, 594–598.

(195) Shapter, J. .; Brooker, M. .; Skinner, W. . Observation of the Oxidation of Galena Using Raman Spectroscopy. *Int. J. Miner. Process.* **2000**, *60*, 199–211.

(196) Lokhande, C. D.; Ennaoui, A.; Patil, P. S.; Giersig, M.; Muller, M.; Diesner, K.; Tributsch, H. Process and Characterisation of Chemical Bath Deposited Manganese Sulphide (MnS) Thin Films. *Thin Solid Films* **1998**, *330*, 70–75.

(197) Danielian, A.; Stevens, K. W. H. Exchange Interactions in the Polymorphic Forms of MnS. *Proc. Phys. Soc.* **1961**, *77*, 124–128.

(198) Zhang, X. V.; Martin, S. T.; Friend, C. M.; Schoonen, M. A. A.; Holland, H. D. Mineral-Assisted Pathways in Prebiotic Synthesis: Photoelectrochemical Reduction of Carbon(+IV) by Manganese Sulfide. *J. Am. Chem. Soc.* **2004**, *126*, 11247–11253.

(199) Meng, J.; Zhao, Y.; Li, Z.; Wang, L.; Tian, Y. Phase Transfer Preparation of Ultrasmall MnS Nanocrystals with a High Performance MRI Contrast Agent. *RSC Adv.* **2016**, *6*, 6878–6887.

(200) Viswanath, R.; Bhojya Naik, H. S.; Yashavanth Kumar, G. S.; Prashanth Kumar, P. N.; Harish, K. N.; Prabhakara, M. C. Luminescence Properties of Blue–Red Emitting Multilayer Coated Single Structure ZnS/MnS/ZnS Nanocomposites. *Spectrochim. Acta Part A Mol. Biomol. Spectrosc.* **2014**, *125*, 222–227.

(201) Ferretti, A. M.; Mondini, S.; Ponti, A. Manganese Sulfide (MnS) Nanocrystals: Synthesis, Properties, and Applications. In *Advances in Colloid Science*; InTech, 2016.

(202) Ha, D.-H.; Ly, T.; Caron, J. M.; Zhang, H.; Fritz, K. E.; Robinson, R. D. A General Method for High-Performance Li-Ion Battery Electrodes from Colloidal Nanoparticles without the Introduction of Binders or Conductive-Carbon Additives: The Cases of MnS, $Cu_{2-x}S$, and Ge. *ACS Appl. Mater. Interfaces* **2015**, *7*, 25053–25060.

(203) Chen, D.; Quan, H.; Wang, G.-S.; Guo, L. Hollow α-MnS Spheres and Their Hybrids with Reduced Graphene Oxide: Synthesis, Microwave Absorption, and Lithium Storage Properties. *Chempluschem* **2013**, *78*, 843–851.

(204) Beltran-Huarac, J.; Resto, O.; Carpena-Nuñez, J.; Jadwisienczak, W. M.; Fonseca, L. F.; Weiner, B. R.; Morell, G. Single-Crystal γ-MnS Nanowires Conformally Coated with Carbon. *ACS Appl. Mater. Interfaces* **2014**, *6*, 1180–1186.

(205) Kan, S.; Felner, I.; Banin, U. Synthesis, Characterization, and Magnetic Properties of α-MnS Nanocrystals. *Isr. J. Chem.* **2001**, *41*, 55–62.

(206) Michel, F. M.; Schoonen, M. A. A.; Zhang, X. V.; Martin, S. T.; Parise, J. B. Hydrothermal Synthesis of Pure α-Phase Manganese(II) Sulfide without the Use of Organic Reagents. *Chem. Mater.* **2006**, *18*, 1726–1736.

(207) Pradhan, N.; Katz, B.; Efrima, S. Synthesis of High-Quality Metal Sulfide Nanoparticles from Alkyl Xanthate Single Precursors in Alkylamine Solvents. *J. Phys. Chem. B* **2003**, *107*, 13843–13854.

(208) Yang, X.; Wang, Y.; Sui, Y.; Huang, X.; Cui, T.; Wang, C.; Liu, B.; Zou, G.; Zou, B. Size-Controlled Synthesis of Bifunctional Magnetic and Ultraviolet Optical Rock-Salt MnS Nanocube Superlattices. *Langmuir* **2012**, *28*, 17811–17816.

(209) Sun, W.; Ceder, G. Efficient Creation and Convergence of Surface Slabs. *Surf. Sci.* **2013**, *617*, 53–59.

(210) Veeramanikandasamy, T.; Rajendran, K.; Sambath, K. Influence of Mn/S Molar Ratio on the Microstructure and Optical Properties of MnS Nanocrystals Synthesized by Wet Chemical Technique. *J. Mater. Sci. Mater. Electron.* **2014**, *25*, 3383–3388.

(211) Mrowec, S.; JANOWSKI, J. Similarities and Differences in Defect Dependent Properties of Transition Metal Sulphides and Oxides. *Stud. Inorg. Chem.* **1989**, *9*, 55–99.

(212) Taguchi, M.; Uozumi, T.; Kotani, A. Theory of X-Ray Photoemission and X-Ray Emission Spectra in Mn Compounds. *J. Phys. Soc. Japan* **1997**, *66*, 247–256.

(213) Bagus, P. S.; Broer, R.; de Jong, W. A.; Nieuwpoort, W. C.; Parmigiani, F.; Sangaletti, L. Atomic Many-Body Effects for the p -Shell Photoelectron Spectra of Transition Metals. *Phys. Rev. Lett.* **2000**, *84*, 2259–2262.

(214) Liang, X.; Hart, C.; Pang, Q.; Garsuch, A.; Weiss, T.; Nazar, L. F. A Highly Efficient Polysulfide Mediator for Lithium–Sulfur Batteries. *Nat. Commun.* **2015**, *6*, 5682.

(215) Chen, H.; Wang, M. Q.; Yu, Y.; Liu, H.; Lu, S.-Y.; Bao, S.-J.; Xu, M. Assembling Hollow Cobalt Sulfide Nanocages Array on Graphene-like Manganese Dioxide Nanosheets for Superior Electrochemical Capacitors. *ACS Appl. Mater. Interfaces* **2017**, *9*, 35040–35047.

(216) Kumbhar, V. S.; Lee, Y. R.; Ra, C. S.; Tuma, D.; Min, B.-K.; Shim, J.-J. Modified Chemical Synthesis of MnS Nanoclusters on Nickel Foam for High Performance All-Solid-State Asymmetric Supercapacitors. *RSC Adv.* **2017**, *7*, 16348–16359.

(217) Tiwari, P.; Malik, G.; Chandra, R. Phase-Dependent Structural and Electrochemical Properties of Single Crystalline MnS Thin Films Deposited by DC Reactive Sputtering. *J. Appl. Phys.* **2018**, *124*, 195106.

(218) Ramachandran, R.; Saranya, M.; Grace, A. N.; Wang, F. MnS Nanocomposites Based on Doped Graphene: Simple Synthesis by a Wet Chemical Route and Improved Electrochemical Properties as an Electrode Material for Supercapacitors. *RSC Adv.* **2017**, *7*, 2249–2257.

(219) Cerrato, J. M.; Hochella, M. F.; Knocke, W. R.; Dietrich, A. M.; Cromer, T. F. Use of XPS to Identify the Oxidation State of Mn in Solid Surfaces of Filtration Media Oxide Samples from Drinking Water Treatment Plants. *Environ. Sci. Technol.* **2010**, *44*, 5881–5886.

(220) Nelson, A. J.; Reynolds, J. G.; Christou, G. Spin-State Effects on the Outer Core-Level Multiplet Structures for High-Spin Mn Molecular Clusters. *J. Appl. Phys.* **2003**, *93*, 2536–2539.

(221) Hermsmeier, B.; Osterwalder, J.; Friedman, D. J.; Sinkovic, B.; Tran, T.; Fadley, C. S. Spin-Polarized Photoelectron Diffraction and Valence-Band Photoemission from MnO(001). *Phys. Rev. B* **1990**, *42*, 11895–11913.

(222) Nesbitt, H. W.; Banerjee, D. Interpretation of XPS Mn(2p) Spectra of Mn Oxyhydroxides and Constraints on the Mechanism of MnO 2 Precipitation. *Am. Mineral.* **1998**, *83*, 305–315.

(223) Strohmeier, B. R.; Hercules, D. M. Surface Spectroscopic Characterization of Manganese/Aluminum Oxide Catalysts. *J. Phys. Chem.* **1984**, *88*, 4922–4929.

(224) Franzen, H.; Sterner, C. The X-Ray Photoelectron Spectra of MnS, MnSe, and MnTe. *J. Solid State Chem.* **1978**, *25*, 227–230.

(225) Oku, M.; Hirokawa, K.; Ikeda, S. X-Ray Photoelectron Spectroscopy of Manganese—Oxygen Systems. *J. Electron Spectros. Relat. Phenomena* **1975**, *7*, 465–473.

(226) Lafuente, B.; Downs, R. T.; Yang, H.; Stone, N. 1. The Power of Databases: The RRUFF Project. In *Highlights in Mineralogical Crystallography*; DE GRUYTER: Berlin, München, Boston, 2016; pp 1–30.

(227) Avril, C.; Malavergne, V.; Caracas, R.; Zanda, B.; Reynard, B.; Charon, E.; Bobocioiu, E.; Brunet, F.; Borensztajn, S.; Pont, S.; Tarrida, M.; Guyot, F. Raman Spectroscopic Properties and Raman Identification of CaS-MgS-MnS-FeS-Cr $_2$ FeS $_4$ Sulfides in Meteorites and Reduced Sulfur-Rich Systems. *Meteorit. Planet. Sci.* **2013**, *48*, 1415–1426.

(228) Zhang, L.; You, S.; Zuo, M.; Yang, Q. Solution Synthesis of Nonequilibrium Zincblende MnS Nanowires. *Inorg. Chem.* **2017**, *56*, 7679–7686.

(229) Akamatsu, K.; Takei, S.; Mizuhata, M.; Kajinami, A.; Deki, S.; Takeoka, S.; Fujii, M.; Hayashi, S.; Yamamoto, K. Preparation and Characterization of Polymer Thin Films Containing Silver and Silver Sulfide Nanoparticles. *Thin Solid Films* **2000**, *359*, 55–60.

(230) Ma, L.; Li, L.; Li, X.; Deng, L.; Zheng, H.; Zhang, Y.; Zhang, J.; Yin, Q.; Bui, B.; Chen, W. Silver Sulfide Nanoparticles as Photothermal Transducing Agents for Cancer Treatment. *J. Nanomater. Mol. Nanotechnol.* **2016**, *05*.

(231) Hildebrandt, B.; Wust, P.; Ahlers, O.; Dieing, A.; Sreenivasa, G.; Kerner, T.; Felix, R.; Riess, H. The Cellular and Molecular Basis of Hyperthermia. *Crit. Rev. Oncol. Hematol.* **2002**, *43*, 33–56.

(232) van der Zee, J. Heating the Patient: A Promising Approach? *Ann. Oncol.* **2002**, *13*, 1173–1184.

(233) Fu, H.; Duan, X. Highly Sensitive and Colorimetric Detection of Hydrogen Sulphide by in Situ Formation of Ag_2S@Ag Nanoparticles in Polyelectrolyte Multilayer Film. *RSC Adv.* **2015**, *5*, 3508–3511.

(234) Sadovnikov, S. I.; Gusev, A. I. Recent Progress in Nanostructured Silver Sulfide: From Synthesis and Nonstoichiometry to Properties. *J. Mater. Chem. A* **2017**, *5*, 17676–17704.

(235) Zamiri, R.; Abbastabar Ahangar, H.; Zakaria, A.; Zamiri, G.; Shabani, M.; Singh, B.; Ferreira, J. M. F. The Structural and Optical Constants of Ag2S Semiconductor Nanostructure in the Far-Infrared. *Chem. Cent. J.* **2015**, *9*, 28.

(236) Sadanaga, R.; Sueno, S. X-Ray Study On The A-B Transition Of Ag_2S. *Mineral. J.* **1967**, *5*, 124–143.

(237) Romand, M.; Roubin, M.; Deloume, J. P. ESCA Studies of Some Copper and Silver Selenides. *J. Electron Spectros. Relat. Phenomena* **1978**, *13*, 229–242.

(238) Hota, G.; Idage, S. B.; Khilar, K. C. Characterization of Nano-Sized CdS–Ag_2S Core-Shell Nanoparticles Using XPS Technique. *Colloids Surfaces A Physicochem. Eng. Asp.* **2007**, *293*, 5–12.

(239) Ferraria, A. M.; Carapeto, A. P.; Botelho do Rego, A. M. X-Ray Photoelectron Spectroscopy: Silver Salts Revisited. *Vacuum* **2012**, *86*, 1988–1991.

(240) Klauber, C.; Parker, A.; van Bronswijk, W.; Watling, H. Sulphur Speciation of Leached Chalcopyrite Surfaces as Determined by X-Ray Photoelectron Spectroscopy. *Int. J. Miner. Process.* **2001**, *62*, 65–94.

(241) Smart, R. S. C.; Skinner, W. M.; Gerson, A. R. XPS of Sulphide Mineral Surfaces: Metal-Deficient, Polysulphides, Defects and Elemental Sulphur. *Surf. Interface Anal.* **1999**, *28*, 101–105.

(242) Tang, J.; Brzozowski, L.; Barkhouse, D. A. R.; Wang, X.; Debnath, R.; Wolowiec, R.; Palmiano, E.; Levina, L.; Pattantyus-Abraham, A. G.; Jamakosmanovic, D.; Sargent, E. H. Quantum Dot Photovoltaics in the Extreme Quantum Confinement Regime: The Surface-Chemical Origins of Exceptional Air- and Light-Stability. *ACS Nano* **2010**, *4*, 869–878.

(243) Kim, Y.-Y.; Walsh, D. Metal Sulfidenanoparticles Synthesized via Enzyme Treatment of Biopolymer Stabilized Nanosuspensions. *Nanoscale* **2010**, *2*, 240–247.

(244) Alekperov, O.; Jahangirli, Z.; Paucar, R. First-Principles Lattice Dynamics and Raman Scattering in Ionic Conductor β-Ag_2S. *Phys. status solidi* **2016**, *253*, 2049–2055.

(245) Martina, I.; Wiesinger, R.; Jembrih-Simbürger, D.; Schreiner, M. *Micro-Raman Characterization of Silver Corrosion Products: Instrumental Set-up and Reference Database*.

(246) Faulkner, E. B.; Schwartz, R. J. *High Performance Pigments*; Smith, H. M., Ed.; Wiley, 2001.

(247) Squires, T. M.; Quake, S. R. Microfluidics: Fluid Physics at the Nanoliter Scale. *Rev. Mod. Phys.* **2005**, *77*, 977–1026.

(248) Saber, M.; Commenge, J. M.; Falk, L. Microreactor Numbering-up in Multi-Scale Networks for Industrial-Scale Applications: Impact of Flow Maldistribution on the Reactor Performances. *Chem. Eng. Sci.* **2010**, *65*, 372–379.

(249) Qiu, M.; Zha, L.; Song, Y.; Xiang, L.; Su, Y. Numbering-up of Capillary Microreactors for Homogeneous Processes and Its Application in Free Radical Polymerization. *React. Chem. Eng.* **2019**, *4*, 351–361.

(250) Mittemeijer, E. J.; Scardi, P. *Diffraction Analysis of the Microstructure of Materials*; Mittemeijer, E. J., Scardi, P., Eds.; Springer Series in Materials Science; Springer Berlin Heidelberg: Berlin, Heidelberg, 2004; Vol. 68.

(251) LaMer, V. K. Nucleation in Phase Transitions. *Ind. Eng. Chem.* **1952**, *44*, 1270–1277.

(252) Gilbert, B. Nanoparticles: Strained and Stiff. *Science* **2004**, *305*, 651–654.

(253) Scardi, P.; Billinge, S. J. L.; Neder, R.; Cervellino, A. Celebrating 100 Years of the Debye Scattering Equation. *Acta Crystallogr. Sect. A Found. Adv.* **2016**, *72*, 589–590.

(254) Cervellino, A.; Frison, R.; Bertolotti, F.; Guagliardi, A.; IUCr. *DEBUSSY 2.0* : The New Release of a Debye User System for Nanocrystalline and/or Disordered Materials. *J. Appl. Crystallogr.* **2015**, *48*, 2026–2032.

(255) Hiemenz, P. C.; Rajagopalan, R. *Principles of Colloid and Surface Chemistry*; CRC Press: Boca Raton, 1997.

(256) Khalkhali, M.; Zeng, H.; Liu, Q.; Zhang, H. Structural Evolutions of ZnS Nanoparticles in Hydrated and Bare States. *J. Phys. Chem. C* **2016**, *120*, 7870–7884.

(257) Balantseva, E.; Berlier, G.; Camino, B.; Lessio, M.; Ferrari, A. M. Surface Properties of ZnS Nanoparticles: A Combined DFT and Experimental Study. *J. Phys. Chem. C* **2014**, *118*, 23853–23862.

(258) He, P.; Greenway, G.; Haswell, S. J. The On-Line Synthesis of Enzyme Functionalized Silica Nanoparticles in a Microfluidic Reactor Using Polyethylenimine Polymer and R5 Peptide. *Nanotechnology* **2008**, *19*, 315603.

(259) Lee, G.-J.; Wu, J. J. Recent Developments in ZnS Photocatalysts from Synthesis to Photocatalytic Applications — A Review. *Powder Technol.* **2017**, *318*, 8–22.

(260) Wang, G.; Huang, B.; Li, Z.; Lou, Z.; Wang, Z.; Dai, Y.; Whangbo, M.-H. Synthesis and Characterization of ZnS with Controlled Amount of S Vacancies for Photocatalytic H2 Production under Visible Light. *Sci. Rep.* **2015**, *5*, 8544.

(261) Liu, M.; Wang, L.; (Max) Lu, G.; Yao, X.; Guo, L. Twins in $Cd_{1-x}Zn_xS$ Solid Solution: Highly Efficient Photocatalyst for Hydrogen Generation from Water. *Energy Environ. Sci.* **2011**, *4*, 1372.

(262) Brunauer, S.; Emmett, P. H.; Teller, E. Adsorption of Gases in Multimolecular Layers. *J. Am. Chem. Soc.* **1938**, *60*, 309–319.

(263) Liu, M.; Jing, D.; Zhou, Z.; Guo, L. Twin-Induced One-Dimensional Homojunctions Yield High Quantum Efficiency for Solar Hydrogen Generation. *Nat. Commun.* **2013**, *4*, 2278.

(264) Fang, X.; Zhai, T.; Gautam, U. K.; Li, L.; Wu, L.; Bando, Y.; Golberg, D. ZnS Nanostructures: From

Synthesis to Applications. *Prog. Mater. Sci.* **2011**, *56*, 175–287.

(265) Hu, H.; Zhang, W. Synthesis and Properties of Transition Metals and Rare-Earth Metals Doped ZnS Nanoparticles. *Opt. Mater. (Amst).* **2006**, *28*, 536–550.

(266) Shannon, R. D. Revised Effective Ionic Radii and Systematic Studies of Interatomie Distances in Halides and Chaleogenides. *Acta Crystallogr.* **1976**, *32*, 751–767.

(267) Kennedy, T. A.; Glaser, E. R.; Klein, P. B.; Bhargava, R. N. Symmetry and Electronic Structure of the Mn Impurity in ZnS Nanocrystals. *Phys. Rev. B* **1995**, *52*, R14356–R14359.

(268) Borse, P. H.; Srinivas, D.; Shinde, R. F.; Date, S. K.; Vogel, W.; Kulkarni, S. K. Effect of Mn^{2+} Concentration in ZnS Nanoparticles on Photoluminescence and Electron Spin Resonance Spectra. *Phys. Rev. B* **1999**, *60*, 8659–8664.

(269) Yu, I.; Isobe, T.; Senna, M.; Takahashi, S. Optical Properties and Characteristics of ZnS:Mn Prepared by Mn Coating Method. *Mater. Sci. Eng. B* **1996**, *38*, 177–181.

(270) Morales-García, Á.; He, J.; Soares, A. L.; Duarte, H. A. Surfaces and Morphologies of Covellite (CuS) Nanoparticles by Means of Ab Initio Atomistic Thermodynamics. *CrystEngComm* **2017**, *19*, 3078–3084.

(271) Yang, P.; Lü, M.; Xü, D.; Yuan, D.; Chang, J.; Zhou, G.; Pan, M. Strong Green Luminescence of Ni 2+ -Doped ZnS Nanocrystals. *Appl. Phys. A Mater. Sci. Process.* **2002**, *74*, 257–259.

(272) Yang, P.; Lü, M.; Xu, D.; Yuan, D.; Song, C.; Liu, S.; Cheng, X. Luminescence Characteristics of ZnS Nanoparticles Co-Doped with Ni2+ and Mn2+. *Opt. Mater. (Amst).* **2003**, *24*, 497–502.

(273) Khosravi, A. A.; Kundu, M.; Jatwa, L.; Deshpande, S. K.; Bhagwat, U. A.; Sastry, M.; Kulkarni, S. K. Green Luminescence from Copper Doped Zinc Sulphide Quantum Particles. *Appl. Phys. Lett.* **1995**, *67*, 2702–2704.

(274) Bol, A. A.; Ferwerda, J.; Bergwerff, J. A.; Meijerink, A. Luminescence of Nanocrystalline ZnS:Cu2+. *J. Lumin.* **2002**, *99*, 325–334.

(275) Bol, A. A.; van Beek, R.; Meijerink, A. On the Incorporation of Trivalent Rare Earth Ions in II−VI Semiconductor Nanocrystals. *Chem. Mater.* **2002**, *14*, 1121–1126.

(276) Bhargava, R. N.; Gallagher, D.; Hong, X.; Nurmikko, A. Optical Properties of Manganese-Doped Nanocrystals of ZnS. *Phys. Rev. Lett.* **1994**, *72*, 416–419.

(277) De Visschere, P.; Neyts, K. Concentration Quenching and Luminescent Decay in AC Thin-Film ZnS:Mn Electroluminescent Devices. *J. Lumin.* **1992**, *52*, 313–323.

(278) Soo, Y. L.; Ming, Z. H.; Huang, S. W.; Kao, Y. H.; Bhargava, R. N.; Gallagher, D. Local Structures around Mn Luminescent Centers in Mn-Doped Nanocrystals of ZnS. *Phys. Rev. B* **1994**, *50*, 7602–7607.

(279) Tuan, N. T.; Trung, D. Q.; Quang, N. V.; Hung, N. D.; Khoi, N. T.; Huy, P. T.; Smet, P. F.; Meert, K. W.; Poelman, D. Excitation Energy Dependence of the Life Time of Orange Emission from Mn-Doped ZnS Nanocrystals. *J. Lumin.* **2018**, *199*, 39–44.

(280) Binnemans, K. Interpretation of Europium(III) Spectra. *Coord. Chem. Rev.* **2015**, *295*, 1–45.

(281) Hänninen, P.; Härmä, H.; Ala-Kleme, T. *Lanthanide Luminescence*; Hänninen, P., Härmä, H., Eds.; Springer Series on Fluorescence; Springer Berlin Heidelberg: Berlin, Heidelberg, 2011; Vol. 7.

(282) Villa, I.; Vedda, A.; Cantarelli, I. X.; Pedroni, M.; Piccinelli, F.; Bettinelli, M.; Speghini, A.; Quintanilla, M.; Vetrone, F.; Rocha, U.; et al. 1.3 Mm Emitting SrF_2:Nd^{3+} Nanoparticles for High Contrast in Vivo Imaging in the Second Biological Window. *Nano Res.* **2015**, *8*, 649–665.

(283) Dunne, P. W.; Munn, A. S.; Starkey, C. L.; Huddle, T. A.; Lester, E. H. Continuous-Flow Hydrothermal Synthesis for the Production of Inorganic Nanomaterials. *Philos. Trans. R. Soc. A Math. Phys. Eng. Sci.* **2015**, *373*, 20150015.

(284) Adschiri, T.; Hakuta, Y.; Arai, K. Hydrothermal Synthesis of Metal Oxide Fine Particles at Supercritical Conditions. *Ind. Eng. Chem. Res.* **2000**, *39*, 4901–4907.

(285) Shaw, W. H. R.; Walker, D. G. The Decomposition of Thiourea in Water Solutions. *J. Am. Chem. Soc.* **1956**, *78*, 5769–5772.

(286) Yu, S.-H.; Shu, L.; Yang, J.; Han, Z.-H.; Qian, Y.-T.; Zhang, Y.-H. A Solvothermal Decomposition Process for Fabrication and Particle Sizes Control of Bi_2S_3 Nanowires. *J. Mater. Res.* **1999**, *14*, 4157–4162.

(287) Shen, G.; Chen, D.; Tang, K.; Liu, X.; Huang, L.; Qian, Y. General Synthesis of Metal Sulfides Nanocrystallines via a Simple Polyol Route. *J. Solid State Chem.* **2003**, *173*, 232–235.

(288) Dong, W.; Wang, X.; Li, B.; Wang, L.; Chen, B.; Li, C.; Li, X.; Zhang, T.; Shi, Z. Hydrothermal Synthesis and Structure Evolution of Hierarchical Cobalt Sulfidenanostructures. *Dalt. Trans.* **2011**, *40*, 243–248.

(289) Takeuchi, S.; Suzuki, K. Stacking Fault Energies of Tetrahedrally Coordinated Crystals. *Phys. status solidi* **1999**, *171*, 99–103.

(290) Zhang, H.; Gilbert, B.; Huang, F.; Banfield, J. F. Water-Driven Structure Transformation in Nanoparticles at Room Temperature. *Nature* **2003**, *424*, 1025–1029.

(291) Goodell, C. M.; Gilbert, B.; Weigand, S. J.; Banfield, J. F. Kinetics of Water Adsorption-Driven Structural Transformation of ZnS Nanoparticles. *J. Phys. Chem. C* **2008**, *112*, 4791–4796.

(292) Smith, F. G. Structure of Zinc Sulphide Minerals. *Am. Mineral.* **1955**, *40*, 658–675.

(293) Zhang, H.; Huang, F.; Gilbert, B.; Banfield, J. F. Molecular Dynamics Simulations, Thermodynamic Analysis, and Experimental Study of Phase Stability of Zinc Sulfide Nanoparticles. *J. Phys. Chem. B* **2003**, *107*, 13051–13060.

(294) Moscheni, D.; Bertolotti, F.; Piveteau, L.; Protesescu, L.; Dirin, D. N.; Kovalenko, M. V.; Cervellino, A.; Pedersen, J. S.; Masciocchi, N.; Guagliardi, A. Size-Dependent Fault-Driven Relaxation and Faceting in Zincblende CdSe Colloidal Quantum Dots. *ACS Nano* **2018**, *12*, 12558–12570.

(295) Zhang, H.; Banfield, J. F. Identification and Growth Mechanism of ZnS Nanoparticles with Mixed Cubic and Hexagonal Stacking. *J. Phys. Chem. C* **2009**, *113*, 9681–9687.

(296) Troullier, N.; Martins, J. L. Efficient Pseudopotentials for Plane-Wave Calculations. *Phys. Rev. B* **1991**, *43*, 1993–2006.

(297) Gonze, X.; Lee, C. Dynamical Matrices, Born Effective Charges, Dielectric Permittivity Tensors, and Interatomic Force Constants from Density-Functional Perturbation Theory. *Phys. Rev. B* **1997**, *55*, 10355–10368.

(298) Serrano, J.; Cantarero, A.; Cardona, M.; Garro, N.; Lauck, R.; Tallman, R.; Ritter, T.; Weinstein, B. Raman Scattering in β-ZnS. *Phys. Rev. B* **2004**, *69*, 1–11.

(299) Zhang, H.; Wei, B.; Zhu, L.; Yu, J.; Sun, W.; Xu, L. Cation Exchange Synthesis of ZnS–Ag_2S Microspheric Composites with Enhanced Photocatalytic Activity. *Appl. Surf. Sci.* **2013**, *270*, 133–138.

(300) Chen, G.; Li, F.; Fan, Y.; Luo, Y.; Li, D.; Meng, Q. A Novel Noble Metal-Free ZnS–WS_2/CdS Composite Photocatalyst for H2 Evolution under Visible Light Irradiation. *Catal. Commun.* **2013**, *40*, 51–54.

(301) Chen, M.; Wu, P.; Zhu, Y.; Yang, S.; Lu, Y.; Lin, Z. Enhanced Photocatalytic H2 Production Activity of CdZnS with Stacking Faults Structure Assisted by Ethylenediamine and NiS. *Int. J. Hydrogen Energy* **2018**, *43*, 10938–10949.

(302) He, K.; Wang, M.; Guo, L. Novel-CdS-Nanorod with Stacking Fault Structures: Preparation and Properties of Visible-Light-Driven Photocatalytic Hydrogen Production from Water. *Chem. Eng. J.* **2015**, *279*, 747–756.

(303) Litke, A.; Hofmann, J. P.; Weber, T.; Hensen, E. J. M. On the Formation of Cd–Zn Sulfide Photocatalysts from Insoluble Hydroxide Precursors. *Inorg. Chem.* **2015**, *54*, 9491–9498.

(304) Pellegrino, F.; Pellutiè, L.; Sordello, F.; Minero, C.; Ortel, E.; Hodoroaba, V.-D.; Maurino, V. Influence of Agglomeration and Aggregation on the Photocatalytic Activity of TiO_2 Nanoparticles. *Appl. Catal. B Environ.* **2017**, *216*, 80–87.

(305) del Rosal, B.; Pérez-Delgado, A.; Misiak, M.; Bednarkiewicz, A.; Vanetsev, A. S.; Orlovskii, Y.; Jovanović, D. J.; Dramićanin, M. D.; Rocha, U.; Upendra Kumar, K.; Jacinto, C.; Navarro, E.; Martín Rodríguez, E.; Pedroni, M.; Speghini, A.; Hirata, G. A.; Martín, I. R.; Jaque, D. Neodymium-Doped Nanoparticles for Infrared Fluorescence Bioimaging: The Role of the Host. *J. Appl. Phys.* **2015**, *118*, 143104.

(306) Górska, M.; Anderson, J. R.; Kido, G.; Green, S. M.; Gol/acki, Z. Exchange Interaction in Rare-Earth-Doped IV-VI Diluted Magnetic Semiconductors. *Phys. Rev. B* **1992**, *45*, 11702–11708.

(307) Furdyna, J. K. Diluted Magnetic Semiconductors. *J. Appl. Phys.* **1988**, *64*, R29–R64.

(308) Wang, S.; Westcott, S.; Chen, W. Nanoparticle Luminescence Thermometry. *J. Phys. Chem. B* **2002**, *106*, 11203–11209.

(309) Weber, M. J. Optical Properties of Yb^{3+} and Nd^{3+} - Yb^{3+} Energy Transfer in $YAlO_3$. *Phys. Rev. B* **1971**, *4*, 3153–3159.

(310) Manzoor, K.; Johny, S.; Thomas, D.; Setua, S.; Menon, D.; Nair, S. Bio-Conjugated Luminescent Quantum Dots of Doped ZnS: A Cyto-Friendly System for Targeted Cancer Imaging. *Nanotechnology* **2009**, *20*, 65102–65155.

(311) Vegard, L. Die Konstitution Der Mischkristalle Und Die Raumfüllung Der Atome. *Zeitschrift für Phys.* **1921**, *5*, 17–26.

(312) Derfus, A. M.; Chan, W. C. W.; Bhatia, S. N. Probing the Cytotoxicity of Semiconductor Quantum Dots. *Nano Lett.* **2004**, *4*, 11–18.

(313) Miller, J. E.; Sharp, E. J. Optical Properties and Energy Transfer in $LiYF_4$:Nd_{3+}, Yb_{3+}. *J. Appl. Phys.* **1970**, *41*, 4718–4722.

(314) Peterson, G. E.; Bridenbaugh, P. M. Study of Relaxation Processes in Nd Using Pulsed

Excitation. *J. Opt. Soc. Am.* **1964**, *54*, 644.

(315) Tiwari, A.; Dhoble, S. J. Critical Analysis of Phase Evolution, Morphological Control, Growth Mechanism and Photophysical Applications of ZnS Nanostructures (Zero-Dimensional to Three-Dimensional): A Review. *Cryst. Growth Des.* **2017**, *17*, 381–407.

(316) Fang, X.; Wu, L.; Hu, L. ZnS Nanostructure Arrays: A Developing Material Star. *Adv. Mater.* **2011**, *23*, 585–598.

(317) Fang, X.; Bando, Y.; Liao, M.; Zhai, T.; Gautam, U. K.; Li, L.; Koide, Y.; Golberg, D. An Efficient Way to Assemble ZnS Nanobelts as Ultraviolet-Light Sensors with Enhanced Photocurrent and Stability. *Adv. Funct. Mater.* **2010**, *20*, 500–508.

(318) Fang, X.; Bando, Y.; Liao, M.; Gautam, U. K.; Zhi, C.; Dierre, B.; Liu, B.; Zhai, T.; Sekiguchi, T.; Koide, Y.; Golberg, D. Single-Crystalline ZnS Nanobelts as Ultraviolet-Light Sensors. *Adv. Mater.* **2009**, *21*, 2034–2039.

(319) Liu, H.; Hu, L.; Watanabe, K.; Hu, X.; Dierre, B.; Kim, B.; Sekiguchi, T.; Fang, X. Cathodoluminescence Modulation of ZnS Nanostructures by Morphology, Doping, and Temperature. *Adv. Funct. Mater.* **2013**, *23*, 3701–3709.

(320) Zhang, J.; Yu, J.; Zhang, Y.; Li, Q.; Gong, J. R. Visible Light Photocatalytic H_2 -Production Activity of CuS/ZnS Porous Nanosheets Based on Photoinduced Interfacial Charge Transfer. *Nano Lett.* **2011**, *11*, 4774–4779.

(321) Hu, J.-S.; Ren, L.-L.; Guo, Y.-G.; Liang, H.-P.; Cao, A.-M.; Wan, L.-J.; Bai, C.-L. Mass Production and High Photocatalytic Activity of ZnS Nanoporous Nanoparticles. *Angew. Chemie Int. Ed.* **2005**, *44*, 1269–1273.

(322) Yu, X.; Yu, J.; Cheng, B.; Huang, B. One-Pot Template-Free Synthesis of Monodisperse Zinc Sulfide Hollow Spheres and Their Photocatalytic Properties. *Chem. - A Eur. J.* **2009**, *15*, 6731–6739.

(323) Zhou, R.; Guzman, M. I. CO_2 Reduction under Periodic Illumination of ZnS. *J. Phys. Chem. C* **2014**, *118*, 11649–11656.

(324) Baran, T.; Wojtyła, S.; Dibenedetto, A.; Aresta, M.; Macyk, W. Zinc Sulfide Functionalized with Ruthenium Nanoparticles for Photocatalytic Reduction of CO_2. *Appl. Catal. B Environ.* **2015**, *178*, 170–176.

(325) Schultze, D.; Steinike, U.; Kussin, J.; Kretzschmar, U. Thermal Oxidation of ZnS Modifications Sphalerite and Wurtzite. *Cryst. Res. Technol.* **1995**, *30*, 553–558.

(326) Zhao, X.; Li, M.; Lou, X. Enhanced Photocatalytic Activity of Zinc Oxide Synthesized by Calcination of Zinc Sulfide Precursor. *Mater. Sci. Semicond. Process.* **2013**, *16*, 489–494.

(327) Kole, A. K.; Kumbhakar, P.; Chatterjee, U. Observations on Nonlinear Optical Properties of ZnS Nanosheet, ZnS–ZnO Composite Nanosheet and Porous ZnO Nanostructures Dispersed in Aqueous Medium. *Chem. Phys. Lett.* **2014**, *591*, 93–98.

(328) Jang, J. S.; Yu, C.-J.; Choi, S. H.; Ji, S. M.; Kim, E. S.; Lee, J. S. Topotactic Synthesis of Mesoporous ZnS and ZnO Nanoplates and Their Photocatalytic Activity. *J. Catal.* **2008**, *254*, 144–155.

(329) Li, X.; Li, X.; Zhu, B.; Wang, J.; Lan, H.; Chen, X. Synthesis of Porous ZnS, ZnO and ZnS/ZnO Nanosheets and Their Photocatalytic Properties. *RSC Adv.* **2017**, *7*, 30956–30962.

(330) Ma, H.; Han, J.; Fu, Y.; Song, Y.; Yu, C.; Dong, X. Synthesis of Visible Light Responsive ZnO–ZnS/C Photocatalyst by Simple Carbothermal Reduction. *Appl. Catal. B Environ.* **2011**, *102*, 417–423.

(331) Caglioti, G.; Paoletti, A.; Ricci, F. P. Choice of Collimators for a Crystal Spectrometer for Neutron Diffraction. *Nucl. Instruments* **1958**, *3*, 223–228.

(332) Lutterotti, L.; Scardi, P. Simultaneous Structure and Size–Strain Refinement by the Rietveld Method. *J. Appl. Crystallogr.* **1990**, *23*, 246–252.

(333) Popa, N. C.; Balzar, D. An Analytical Approximation for a Size-Broadened Profile given by the Lognormal and Gamma Distributions. *J. Appl. Crystallogr.* **2002**, *35*, 338–346.

(334) Von Dreele, R. B. Quantitative Texture Analysis by Rietveld Refinement. *J. Appl. Crystallogr.* **1997**, *30*, 517–525.

(335) Schneider, C. A.; Rasband, W. S.; Eliceiri, K. W. NIH Image to ImageJ: 25 Years of Image Analysis. *Nat. Methods* **2012**, *9*, 671–675.

(336) Glatter, O.; Kratky, O. *Small Angle X-Ray Scattering*; Academic Press: New York, 1982.

(337) Guinier, A.; Fournet, G. *Small-Angle Scattering of X-Rays*; John Wiley & Sons: New York, 1955.

(338) Percus, J. K.; Yevick, G. J. Analysis of Classical Statistical Mechanics by Means of Collective Coordinates. *Phys. Rev.* **1958**, *110*, 1–13.

(339) Brautigam, C. A.; Zhao, H.; Vargas, C.; Keller, S.; Schuck, P. Integration and Global Analysis of Isothermal Titration Calorimetry Data for Studying Macromolecular Interactions. *Nat. Protoc.* **2016**, *11*, 882–894.

(340) Gonze, X. A Brief Introduction to the ABINIT Software Package. *Zeitschrift für Krist. - Cryst. Mater.* **2005**, *220*, 558–562.

(341) Gonze, X.; Lee, C. Dynamical Matrices, Born Effective Charges, Dielectric Permittivity Tensors, and Interatomic Force Constants from Density-Functional Perturbation Theory. *Phys. Rev. B* **1997**, *55*, 10355–10368.

(342) Gonze, X. First-Principles Responses of Solids to Atomic Displacements and Homogeneous Electric Fields: Implementation of a Conjugate-Gradient Algorithm. *Phys. Rev. B* **1997**, *55*, 10337–10354.

Publications

Functionalisation of Colloidal Transition Metal Sulphides Nanocrystals: A Fascinating and Challenging Playground for the Chemist

Silvia Gross, Andrea Vittadini, and Nicola Dengo

Published on Crystals, **2017**, 7(4), 110; doi:10.3390/cryst7040110

Thermal Evolution of ZnS Nanostructures: Effect of Oxidation Phenomena on Structural Features and Photocatalytical Performances

Nicola Dengo, Angela Federica De Fazio, Morten Weiss, Roland Marchall, Paolo Dolcet, Mattia Fanetti, and Silvia Gross

Published on Inorganic Chemistry, **2018**, 57, 21, 13104-13114; doi: 10.1021/acs.inorgchem.8b01101

Exploring the Phase-Selective, Green Hydrothermal Synthesis of Upconverting Doped Sodium Yttrium Fluoride: Effects of Temperature, Time and Precursors

Nora Jannsen, Stefano Diodati, Nicola Dengo, Francesca Tajoli, Nicola Vicentini, Giacomo Lucchini, Adolfo Speghini, Denis Badocco, Paolo Pastore, and Silvia Gross

Published on Chemistry – A European Journal, **2019**, doi: 10.1002/chem.201903261

Quaternary ferrites by batch and continuous flow hydrothermal synthesis: a comparison

Michele Bastianello, Stefano Diodati, Nicola Dengo, Liam McCafferty, Charles Footer, Denis Badocco, Paolo Pastore, Jawwad Darr and Silvia Gross

Published on CrystEngComm, **2019**, 21, 6801 – 6809; doi: 10.1039/C9CE01462D

The role of the synthetic pathways on properties of Ag_2S nanoparticles for photothermal therapy

Jessica Munaro, Paolo Dolcet, Silvia Nappini, Elena Magnano, Nicola Dengo, Giacomo Lucchini, Adolfo Speghini and Silvia Gross

Under revision in Applied Surface Science

In-depth study of ZnS nanoparticles surface properties with a combined experimental and theoretical approach

Nicola Dengo, Andrea Vittadini, Marta Maria Natile and Silvia Gross

Submitted to Nanoscale

Acknowledgments

First, I am deeply and sincerely grateful to my supervisor, Prof. Silvia Gross, not only for giving me the opportunity to undertake this Ph.D., but also for everything she taught me over the last three years, for every occasion of personal and scientific growth I had under her supervision, and for the immense trust she had in my capabilities.

Ministero dell'Istruzione, dell'Università e della Ricerca, Scuola di Dottorato in Scienze Molecolari (Dip. Scienze Chimiche, Università degli Studi di Padova) and the Royal Society of Chemistry are thanked for the financial support.

My most sincere thanks also go to Prof. Michele Maggini (Università degli Studi di Padova), who inspired me in the development of the microfluidic approach and allowed me to use his laboratory and his equipment. Prof. Tommaso Carofiglio and Dr. Andrea Faresin are also kindly acknowledged for the help and the precious advices.

Grateful thanks also go to Prof. Jawwad Darr (UCL – University College London, United Kingdom) for letting me join his workgroup for a total of over one month, for allowing me to use his CHFS setup and instrumentation and to the warm welcome I've always received from him and his workgroup. I also want to thanks Dr. Liam McCafferty, Dr. Chris Starkey and M.Sc Charles Footer for all the support over the course of my staying in London.

I very thankful to Prof. Yitzhak Mastai (Bar Ilan University, Israel) to allowing me in his group to perform the ITC measurements for three months, and for all the unconditioned support I received from him. I'm also very obligated to Dr. Liora Verber and Dr. Ortal Lidor-Shalev for all the scientific help and the warm and friendly hospitality they reserved to me during my staying.

Prof. Emiel Hensen (TU/e – Eindhoven Technical University, The Netherlands) is kindly acknowledged for HER measurements. Prof. Jan Philipp Hofmann and Dr. Longfei Wu are also acknowledged for their work and their insightful advices.

I am very thankful to Prof. Adolfo Speghini (Università degli Studi di Verona), for his work on the PL of my samples, and for the insightful conversations. I am also thankful to Dr. Giacomo Lucchini for his precious help.

Prof. Heinz Amenitsch (Graz University of Technology, Austria) is acknowledged for his support and his precious advices for the realization of the SAXS *in-situ* setup and setting up the data analysis. Dr. Barbara Sartori and M.Sc. Marco Bogar are gratefully acknowledged for their fundamental support on the SAXS experiments.

I am very thankful to Prof. Peter Klar, Dr. Christian Heiliger and Dr. Limei Chen (JLU - Justus-Liebig University of Giessen, Germany) for their Raman analysis and the computational work.

I am also very obligated to Dr. Marco Bersani (UCL – University College London, United Kingdom; Particular Materials SRL, Italy) for the HRTEM pictures he helped me to obtain in London, but also for the countless precious conversation and hints he gave me over the course of the last three years, and lastly for the all the great time.

I would also like to acknowledge all the people in the University of Padova which helped me by carrying out some analyses on my samples. In particular, Prof. Paolo Pastore and Prof. Denis Badocco, who performed ICP-MS measurements, Prof. Maddalena Mognato for the MTS assays.

I'm also thankful for the help that Prof. Andrea Vittadini and Dr. Marta Maria Natile (Università degli Studi di Padova) gave me for the characterization of the interactions at the gat/solid interface.

Finally, I am very thankful for all the people of my workgroup. Firstly, I thank Paolo, Francesca, Lucia and Marco, who actively helped me in this work. I also warmly thanks Stefano, Michele, Nicola, Giacomo, Federico, Jasica, Chiara, Elisa, Giulia, Marina and Anna for the daily cooperation and the all the great time inside and outside the lab we had together.